Universidade Estadual Paulista “Júlio de Mesquita Filho”
UNESP
Universiteit Antwerpen - UAntwerpen

Leonardo Rodrigues Cadorim

Numerical Investigation of the Vortex Matter in Superconducting Systems: Fundamental Properties and Applications

Bauru
2024

LEONARDO RODRIGUES CADORIM

Numerical Investigation of the Vortex Matter in Superconducting Systems: Fundamental Properties and Applications

Thesis presented to the Universidade Estadual Paulista "Júlio de Mesquita Filho" – Programa de Pós-Graduação em Ciência e Tecnologia de Materiais and Universiteit Antwerpen – Doctoral Study Program as a partial requirement to award a joint degree of Doctor in Science and Materials Technology and Physics, under the supervision of Prof. Dr. Edson Sardella and Prof. Dr. Milorad V. Milošević.

Bauru, 2024

To the loving memory of my father.

Acknowledgements

Over the years of preparing this thesis, I have received support from many people in various ways.

First and foremost, I wish to thank my supervisors, Prof. Edson Sardella and Prof. Milorad Milošević. Prof. Sardella introduced me to the field of superconductivity seven years ago and, through the countless analytical and numerical calculations we carried out together, educated me about the physics of vortices and scientific computing. During my time in Antwerp, I was fortunate to engage in frequent scientific discussions with Prof. Milošević, which greatly enriched my understanding of superconductivity and condensed matter physics as a whole. I will always be profoundly grateful to both of them for their guidance, patience, and availability throughout these past five years. On a personal note, I was also lucky to share many laughs and enjoyable moments with both, memories I will always look back on with great fondness.

I would also like to extend my gratitude to my collaborators: Lucas Veneziani, Jorge Berger, Clécio Clemente de Souza Silva, Mauro Doria, Antonio Romaguera, Isaías de Oliveira, Rafael Zadorosny, Wilson Ortiz, and Daniel Domínguez. Their insights and suggestions were invaluable to the work presented in this thesis, contributing significantly to its development.

I'm also deeply grateful to my mother and father for their unconditional love and support during my entire life.

Finally, I want to thank the Brazilian Agency FAPESP (Grant No. 20/03947-2) and the Special Research Funds of the University of Antwerp (BOF-UA) for financial support during the development of this thesis.

Resumo

Materiais supercondutores têm despertado uma atividade significativa de pesquisa nos últimos anos, especialmente no desenvolvimento de dispositivos eletrônicos. Esses dispositivos já são utilizados ou espera-se que sejam aplicados em breve em várias áreas, como detectores de campo de alta precisão e baixo custo, detectores de fóton único ultrasensíveis, diodos supercondutores, tecnologias de memória e comunicação, neurônios artificiais e até mesmo na computação quântica, onde podem servir como plataformas para qubits. O interesse em dispositivos supercondutores foi renovado com a descoberta da supercondutividade em materiais atomicamente finos, permitindo o desenvolvimento de dispositivos supercondutores menores, mais leves e, portanto, mais acessíveis. Além disso, a descoberta de supercondutores multicomponentes—materiais descritos por mais de um condensado—abriu caminho para novos e ricos fenômenos emergentes, de interesse tanto fundamental quanto prático. Dado que o comportamento dos vórtices supercondutores sob campos magnéticos ou elétricos aplicados pode tanto melhorar quanto prejudicar o desempenho de um dispositivo, compreender a dinâmica dos vórtices em diferentes condições físicas é crucial para otimizar a funcionalidade dos dispositivos. Nesta tese, investigamos as propriedades de equilíbrio e dinâmicas dos supercondutores convencionais de uma única banda de emparelhamento s-wave, assim como de sistemas multicomponentes com simetria de onda s e d, resolvendo numericamente as equações de Ginzburg-Landau dependentes do tempo. Na primeira parte, exploramos supercondutores mesoscópicos, onde a resposta do sistema a um campo magnético aplicado apresenta características únicas devido à pequena razão volume-área, desafiando a classificação convencional dos materiais em tipo I e tipo II. Em seguida, examinamos o processo de criação e aniquilação de vórtice-antivórtice em um filme supercondutor que transporta corrente, demonstrando que, em filmes suficientemente espessos, temos um novo estado dinâmico—"loop de vórtice fechado"—onde as linhas de vórtice e antivórtice formam um único loop antes da aniquilação. Também propomos possíveis assinaturas experimentais desse estado. Por fim, propomos um diodo supercondutor, onde um filme supercondutor central é flanqueado por dois fios supercondutores que transportam correntes contínuas. Ao otimizar o perfil do campo magnético criado por essas correntes, identificamos as condições para máxima eficiência do diodo e mostramos que o dispositivo pode funcionar como um retificador de meia onda. Na segunda parte, desenvolvemos um método semianalítico para avaliar a estabilidade dos estados de fluxo em anéis supercondutores de duas bandas. Após validar esse modelo com simulações numéricas, exploramos a possibilidade de estados de solitons. Finalmente, estudamos a matéria de vórtices em bicamadas rotacionadas com simetria de onda d, revelando a emergência de dois estados distintos de skyrmions em diferentes ângulos de rotação. Mostramos como o perfil do campo magnético desses estados pode servir como um indício claro para a detecção de estados topológicos em tais heteroestruturas.

Abstract

Superconducting materials have sparked significant research activity in recent years, particularly in the development of electronic devices. These devices are currently used or are expected to soon be applied in various areas, such as highly precise and low-cost field detectors, ultra-sensitive single-photon detectors, superconducting diodes, memory and communication technologies, artificial neurons, and even quantum computing, where they could serve as platforms for qubits. Interest in such devices has been renewed by the discovery of superconductivity in atomically thin materials, enabling the design of smaller, lighter, and more affordable superconducting devices. Moreover, the discovery of multicomponent superconductors—materials described by more than one condensate—has opened the door to new, rich emergent phenomena with both fundamental and practical significance. Given that the behavior of superconducting vortices under applied magnetic or electric fields can either enhance or impair device performance, understanding vortex dynamics under different conditions is crucial for optimizing device functionality. In this thesis, we investigate the equilibrium and dynamic properties of conventional single-band s-wave superconductors, as well as multicomponent systems with s- and d-wave pairing, by numerically solving the time-dependent Ginzburg-Landau equations. In the first part, we explore mesoscopic superconductors, where the system's response to an applied magnetic field exhibits unique features due to the small volume-to-area ratio, challenging the conventional classification into type I and type II materials. We then examine the vortex-antivortex creation and annihilation process in a superconducting film carrying a transport current, demonstrating that in sufficiently thick films, a new dynamical state—termed the "closed vortex loop"—emerges, where vortex and antivortex lines form a single loop before annihilation. We also propose possible experimental signatures of this state. Finally, we present a superconducting diode design, where a central superconducting film is flanked by two superconducting wires carrying DC currents. By optimizing the magnetic field profile from these currents, we identify conditions for maximum diode efficiency and show that the device can function as a half-wave rectifier. In the second part, we develop a semi-analytical method to assess the stability of flux states in two-band superconducting rings. After validating this model with numerical simulations, we explore the possibility of soliton states. Lastly, we study vortex matter in twisted bilayers with d-wave superconducting pairing, revealing the emergence of two distinct skyrmionic states at different twist angles. We demonstrate how their magnetic field profiles could serve as key indicators for detecting topological states in such heterostructures.

Abstract - Nederlandse versie

Supergeleidende materialen hebben de afgelopen jaren veel onderzoek aangewakkerd, met name op het gebied van de ontwikkeling van elektronische apparaten. Deze apparaten worden momenteel gebruikt of zullen naar verwachting binnenkort worden toegepast in verschillende gebieden, zoals uiterst nauwkeurige en goedkope magnetische-veld-sensoren (cfr. SQUID), ultra-gevoelige een-foton detectors, supergeleidende diodes, geheugen- en communicatietechnologieën, kunstmatige neuronen en zelfs in quantumcomputing, waar ze kunnen dienen als qubits. De interesse in dergelijke apparaten is nieuw leven ingeblazen door de ontdekking van supergeleiding in atomair dunne materialen, wat het ontwerp van kleinere, lichtere en goedkopere supergeleidende apparaten mogelijk maakt. Bovendien heeft de ontdekking van multicomponent-supergeleiders—materialen die worden beschreven door meer dan één condensaat—de deur geopend naar nieuwe verschijnselen die zowel fundamenteel als praktisch van belang zijn. Aangezien het gedrag van supergeleidende vortices onder aangelegde magnetische of elektrische velden de prestaties van een apparaat kan verbeteren of juist belemmeren, is het essentieel om de dynamiek van vortices onder verschillende omstandigheden te begrijpen om de functionaliteit van apparaten te kunnen optimaliseren. In deze thesis, onderzoeken we de evenwichts- en dynamische eigenschappen van conventionele enkelbandige s-golf supergeleiders, evenals multicomponent-systemen met s- en d-golf paring, door de tijdsafhankelijke Ginzburg-Landau-vergelijkingen numeriek op te lossen. In het eerste deel van de thesis, verkennen we mesoscopische supergeleiders, waar de respons van het systeem op een aangelegd magnetisch veld unieke kenmerken vertoont vanwege de kleine volume-oppervlakteverhouding, wat de conventionele indeling in type-I en type-II materialen uitdaagt. Vervolgens onderzoeken we het proces van vortex-antivortex creatie en annihilatie in een supergeleidende film met transportstroom. We tonen aan dat in voldoende dikke films een nieuwe dynamische toestand ontstaat, de zogenaamde "gesloten vortexlus," waarbij vortex- en antivortexlijnen samen een enkele lus vormen voordat ze annihileren. We stellen ook mogelijke experimentele signalen voor om deze toestand te detecteren. Ten slotte presenteren we een ontwerp voor een supergeleidende diode, waarbij een centrale supergeleidende film wordt geflankeerd door twee supergeleidende draden met gelijkstroom (DC). Door het magnetische veldprofiel van deze stromen te optimaliseren, identificeren we de voorwaarden voor maximale diode-efficiëntie en laten we zien dat het systeem kan functioneren als een halfgolf-rectificator. In het tweede deel van de thesis, ontwikkelen we een semianalytische methode om de stabiliteit van fluxtoestanden in tweebandige supergeleidende ringen te beoordelen. Na het valideren van dit model met numerieke simulaties, verkennen we de mogelijkheid van solitontoestanden. Ten slotte bestuderen we vortexmaterie in gedraaide bilagen met d-golf supergeleidende paring, waarbij we de opkomst van twee verschillende skyrmiontoestanden bij verschillende draaigraden onthullen. We tonen aan

hoe hun magnetische veldprofielen kunnen dienen als aanwijzingen voor het detecteren van topologische toestanden in dergelijke heterostructuren.

List of Publications in the Period

Published papers discussed in this thesis:

1. **Cadorim, L. R.**, Romaguera, A. R. D. C., De Oliveira, I. G., Gomes, R. R., Doria, M. M., Sardella, E. Intermediate type-I superconductors in the mesoscopic scale. Physical Review B, 103(1), 014504. (2021). The results of this paper are discussed in **Chapter 2** of this thesis.

2. **Cadorim, L. R.**, De Toledo, L. V., Ortiz, W. A., Berger, J., Sardella, E. Closed vortex state in three-dimensional mesoscopic superconducting films under an applied transport current. Physical Review B, 107(9), 094515. (2023). The results of this paper are discussed in **Chapter 3** of this thesis.

3. **Cadorim, L. R.**, Sardella, E., Silva, C. C. D. S. Harnessing the superconducting diode effect through inhomogeneous magnetic fields. Physical Review Applied, 21(5), 054040. (2024). The results of this paper are discussed in **Chapter 4** of this thesis.

4. **Cadorim, L. R.**, Sardella, E., Dominguez, D., Berger, J. Stability limits of flux states in two-band superconductor rings. Physical Review B, 110(14), 144513. (2024). The results of this paper are discussed in **Chapter 5** of this thesis.

5. **Cadorim, L. R.**, Sardella, E., Milošević, M. V. Vortical versus skyrmionic states in the topological phase of a twisted bilayer with d-wave superconducting pairing. Physical Review B, 110(6), 064508. (2024). The results of this paper are discussed in **Chapter 6** of this thesis.

Published papers not discussed in this thesis:

1. **Cadorim, L. R.**, de Oliveira Junior, A., Sardella, E. Ultra-fast kinematic vortices in mesoscopic superconductors: the effect of the self-field. Scientific reports, 10(1), 18662. (2020).

2. de Toledo, L. V., Presotto, A., **Cadorim, L. R.**, Filenga, D., Zadorosny, R., Sardella, E. Clusters of vortices induced by thermal gradient in mesoscopic superconductors. Physics Letters A, 406, 127449. (2021).

3. de Oliveira, I. G., **Cadorim, L. R.**, Romaguera, A. R. D. C., Sardella, E., Gomes, R. R., Doria, M. M. The spike state in type-I mesoscopic superconductor. Physics Letters A, 406, 127457. (2021).

4. **Cadorim, L. R.**, de Toledo, L. V., Sardella, E. Describing heat dissipation in the resistive state of three-dimensional superconductors. Physica C: Superconductivity and its Applications, 622, 1354531. (2024).

List of Figures

Contents

1 Introduction

Superconductivity was first discovered by Heike Kamerlingh Onnes, a Dutch physicist, in 1911. At that time, Onnes was studying the behavior of materials at very low temperatures [2], particularly when using liquefied helium to cool metals. In a landmark experiment, Onnes observed that the electrical resistance of mercury dropped abruptly to zero when it cooled below 4.2 K, a phenomenon that became known as superconductivity [3]. This discovery won Onnes the Nobel Prize in Physics in 1913, and it opened a new field in low-temperature physics.

For the next few decades, the primary focus in superconductivity research was the identification of other materials that exhibited this property and the development of theories to explain it. Many metals and alloys were found to become superconducting at low temperatures, but the theoretical understanding of this phenomenon was elusive.

In the early 1930s, Walther Meissner and Robert Ochsenfeld made a significant discovery when they demonstrated the Meissner effect, which showed that superconductors could expel magnetic fields from their interior when transitioning into the superconducting state [4, 5]. This discovery established that superconductivity was not just about zero electrical resistance but also involved unique magnetic properties, paving the way to the development of the first phenomenological theories of superconductivity (discussed in detail in the next section). The most successful of them was the Ginzburg-Landau theory, proposed in 1950 by the Russian physicists Lev Landau and Vitaly Ginzburg [6]. Based on the Landau theory of second order phase transitions, the theory provided a mathematical framework for describing the macroscopic behavior of superconductors without explaining the microscopic mechanism.

The fully microscopic description of superconductivity would only come after the discovery of the so-called isotope effect. Two independent research groups, one led by Emil Maxwell and another by Cochran and Reynolds, found that the critical temperature (Tc) of certain superconductors varied depending on the isotope of the metal used. This isotope effect suggested that superconductivity was related to lattice vibrations (phonons), linking it to quantum mechanics. Based on this, in 1957, John Bardeen, Leon Cooper, and Robert Schrieffer published their seminal BCS theory, where it is proposed that at low temperatures, electrons in a superconductor form pairs (Cooper pairs) because of an attractive interaction mediated by phonons (vibrations in the crystal lattice). These Cooper pairs move through the material without scattering, leading to zero resistance. The BCS theory was a major success, explaining not only the phenomenon of superconductivity but also predicting the critical temperature of many materials. The trio received the

Nobel Prize in Physics in 1972 for their work. This theory became the cornerstone of understanding superconductors and guided research for the next few decades [7, 8].

For several decades after the development of BCS theory, progress in the field of superconductivity was relatively slow. By the mid-20th century, superconductors were known to exist only at very low temperatures, typically below 30 Kelvin, which severely limited their practical applications. Liquid helium, used for cooling, was expensive and difficult to handle, restricting the widespread use of superconducting technologies. This changed dramatically in 1986 when two IBM researchers, Johannes Georg Bednorz and Karl Alexander Müller, discovered a new class of superconducting materials: cuprates (compounds containing copper and oxygen). They found that lanthanum barium copper oxide became superconducting at 35 K, far above the previously established temperature limits for superconductors [9].

This breakthrough led to a surge of research, and in 1987, another team of researchers, led by Paul Ching Wu Chu at the University of Houston, discovered a new material, yttrium barium copper oxide), which exhibited superconductivity at an even higher temperature of 92 K [10]. This discovery was critical because it brought superconductivity above the temperature of liquid nitrogen), a much cheaper and easier coolant than liquid helium. These materials were called high-temperature superconductors.

The discovery of high-Tc superconductors was revolutionary. Not only did it expand the theoretical understanding of superconductivity, it also opened the door to new practical applications, such as magnetic levitation (maglev) trains, medical imaging technologies (MRI), and improvements in power transmission. Bednorz and Müller were awarded the Nobel Prize in Physics in 1987 for their pioneering work. However, the exact mechanism that allowed these cuprate materials to become superconducting at such high temperatures was not explained by BCS theory. This prompted intense theoretical and experimental efforts to uncover the nature of high-Tc superconductors, leading to the development of new models and the exploration of other types of materials that exhibited unconventional forms of superconductivity. These materials often did not fit the conventional BCS framework and included a wide variety of compounds with unique properties [11].

As one example of such materials we can cit the iron-based superconductors. First reported in 2008, these materials exhibited superconductivity at temperatures as high as 56 Kelvin, sparking excitement because they provided a second family of high-temperature superconductors, alongside the cuprates. However, iron-based superconductors involved a mechanism different from that of cuprates, and researchers are still working to fully understand the physics behind them [12]. Non-conventional superconductivity also exists outside the family of high-temperature, for example, heavy fermion superconductors are materials where electron-electron interactions are particularly strong [13]. These mate-

rials exhibit superconductivity at very low temperatures, and their unusual electronic properties, including large effective electron masses, challenge traditional superconducting theories. They often exhibit multiple competing quantum states, such as magnetism and superconductivity, providing valuable insight into the interplay between these forces.

More recently, materials known as topological superconductors have garnered attention. These are materials that host Majorana fermions, particles that could be their own antiparticles, potentially useful for quantum computing [14, 15]. Superconductors such as Sr_2RuO4 and engineered superconducting heterostructures are being studied for their exotic topological properties and potential applications in robust quantum information storage. One of the most recent breakthroughs in superconductivity came in the 2010s when researchers began exploring superhydrides (such as H_3S) under extremely high pressures. In 2015, it was discovered that hydrogen sulfide (H_2S), when subjected to pressures of 150 gigapascals, exhibited superconductivity at 203 K, making it the highest T_c superconductor at that time. Later, in 2020, a compound known as carbonaceous sulfur hydride broke this record with superconductivity at 287 K, under even higher pressures. While these materials require extreme conditions, they offer tantalizing hints that room-temperature superconductivity might one day be possible [16, 17].

1.1 Theories of Superconductivity

1.1.1 London Theory

The first theory to describe both the zero electrical resistance and the perfect diamagnetism of superconductors was the London theory. To derive the equation of the London theory that governs the behavior of the magnetic field inside a superconductor, we start by separating the electrons into two components: the normal and superconducting parts. In this case, the total energy of the system can be written as the sum of three contributions:

$$F = F_n + F_{kin} + F_{mag} \ , \tag{1.1}$$

where F_n comes from the normal contribution, F_{kin} is the kinetic energy associated with the superelectrons and F_{mag} is the energy stored in the magnetic field.

With the velocity of the superelectrons given by $\mathbf{v} = \mathbf{j}/ne$, with e being the electric charge of the electron and n the density of superelectrons and recalling that from Ampère's law we have $\mathbf{j} = (c/4\pi)\boldsymbol{\nabla} \times \mathbf{h}$, the kinetic energy can be written as:

With the velocity of the superelectrons given by $\mathbf{v} = \mathbf{j}/ne$, where e is the electric charge of the electron and n is the density of superelectrons, and recalling that from Ampère's law we have $\mathbf{j} = (c/4\pi)\boldsymbol{\nabla} \times \mathbf{h}$, the kinetic energy can be written as:

$$F_{kin} = \frac{1}{8\pi} \int \frac{mc^2}{4\pi ne^2} \left|\boldsymbol{\nabla} \times \mathbf{h}(\mathbf{r})\right|^2 d^3r \ , \tag{1.2}$$

while the local magnetic field term takes the usual form:

$$F_{mag} = \frac{1}{8\pi} \int h^2(\mathbf{r}) d^3r \ . \tag{1.3}$$

With Eqs. 1.2 and 1.3, we minimize Eq. 1.1 to obtain:

$$\boldsymbol{\nabla} \times (\boldsymbol{\nabla} \times \mathbf{h}) + \frac{1}{\lambda_L^2} \mathbf{h} = 0 \ , \tag{1.4}$$

where we have defined the London penetration length $\lambda_L^2 = mc^2/(4\pi ne^2)$. Eq. 1.4 is known as the second London equation.

To gain insight into what this equation tells us about the behavior of the local magnetic field inside a superconductor, suppose we have a superconductor/insulator interface at $x = 0$, with a parallel applied magnetic field $\mathbf{h} = H\hat{\mathbf{z}}$. Making use of the Maxwell equation $\boldsymbol{\nabla} \cdot \mathbf{h} = 0$, Eq. 1.4 can be written as:

$$\nabla^2 \mathbf{h} - \frac{1}{\lambda_L^2} \mathbf{h} = 0 \ , \tag{1.5}$$

which, in this case, has the solution:

$$\mathbf{h} = He^{-x/\lambda_L} \hat{\mathbf{z}} \ . \tag{1.6}$$

As we can see, Eq. 1.6 states that the applied magnetic field penetrates the superconductor only to a length λ_L, going to zero in the bulk of the superconductor, thus accounting for the perfect diamagnetism observed in superconductors.

Now, let us see how the London theory accounts for the zero electron resistance in the superconducting state. For this, we start from Drude's model for the electron motion in a metal:

$$m \left(\frac{\partial \mathbf{v}}{\partial t} + \frac{\mathbf{v}}{\tau} \right) = e\mathbf{E} \ , \tag{1.7}$$

where τ denotes the mean free time between two collisions of the electron with an ion.

For superconducting electron, τ goes to infinity and, bearing in mind that $\mathbf{v} = \mathbf{j}/ne$, we have what it is known as the first London equation:

$$\frac{\partial \mathbf{j}}{\partial t} = \frac{ne^2}{m} \mathbf{E} \ . \tag{1.8}$$

As can be seen, this equation describes the perfect conductivity of the superconducting state, since it allows for the presence of a constant and finite current even in the absence of an applied electric field.

The second London equation, Eq. 1.4, can be obtained from Eq. 1.7. To see this, we take the curl and the time derivative of Ampère's law to obtain:

$$\boldsymbol{\nabla} \times \left(\boldsymbol{\nabla} \times \frac{\partial \mathbf{h}}{\partial t} \right) = \frac{4\pi}{c} \boldsymbol{\nabla} \times \frac{\partial \mathbf{j}}{\partial t} \, . \tag{1.9}$$

With the use of Eq. 1.8 and the Faraday's law of induction, Eq. 1.9 can be written as:

$$\boldsymbol{\nabla} \times \left(\boldsymbol{\nabla} \times \frac{\partial \mathbf{h}}{\partial t} \right) + \frac{1}{\lambda_L^2} \frac{\partial \mathbf{h}}{\partial t} = 0 \, , \tag{1.10}$$

which, as can be easily seen, describes the response of a perfect conductor to the application of a time-varying magnetic field. To correctly describe the observed properties of the superconducting state, we must drop the time derivatives in Eq. 1.9, recovering the second London equation detailed above.

1.1.2 Ginzburg-Landau Theory of Superconductivity

1.1.2.1 The Ginzburg-Landau Equations

The Ginzburg-Landau free energy density to describe the superconducting state is given by:

$$F = \alpha(T)|\psi|^2 + \frac{\beta}{2}|\psi|^4 + \frac{1}{2m^*} \left| \left(-\mathrm{i}\hbar \boldsymbol{\nabla} - \frac{e^*}{c} \mathbf{A} \right) \psi \right|^2 + \frac{1}{8\pi} \left| \boldsymbol{\nabla} \times \mathbf{A} \right|^2 \, , \tag{1.11}$$

where $\alpha(T)$ and β are phenomenological parameters; m^* is the effective mass; ψ is the superconducting order parameter and $\mathbf{A}$ is the vector potential.

The first two terms on the right-hand side of Eq. 1.11 represent the condensation energy of the superconducting electron pairs. The third term comes from the contribution of superconducting currents present in the system, or in other words, the kinetic energy of the superconductor. Lastly, the final term takes into account the magnetic energy of the system.

To describe the transition from normal to superconducting state, the phenomenological constant β is taken to be always positive, while the temperature dependence of the constant $\alpha(T)$ is given as $\alpha(T) = -\alpha_0(T_c - T)$, where T_c is the critical temperature of the superconductor and α_0 is a positive phenomenological constant.

Fig. 1 shows the profile of the free energy density of a homogeneous superconductor in the absence of external fields. In this case, the only nonzero terms come from the condensation energy. The dashed line represents the case of a temperature higher than the critical temperature. Since in this case both $\alpha(T)$ and β are positive, Eq. 1.11 shows that the minimum energy state occurs for $|\psi| = 0$, *i.e.*, there is no superconductivity and the system resides at the normal state. On the other hand, for $T < T_c$, $\alpha(T)$ is negative and the minimum energy now occurs for a finite $|\psi|$, namely $|\psi| = n_s = \sqrt{\alpha_0(T_c - T)/\beta}$.

To understand how the theory explains the transition to the normal state under the influence of an applied magnetic field, let us consider a boundless superconductor subjected to a homogeneous magnetic field of magnitude H. From Eq. 1.11 and the conclusion of the previous paragraph, it is clear that the system transitions to the normal state when the field reaches a critical value, which is given by:

$$\frac{H_c^2}{8\pi} = \frac{\alpha^2(T)}{2\beta} = \frac{\alpha_0^2(T_c - T)^2}{2\beta} \,, \tag{1.12}$$

where H_c is known as the thermodynamic critical field.

In a more general scenario, for finite superconductors exposed to external fields, the superconducting system is characterized by an order parameter that minimizes the Ginzburg-Landau free energy. In this context, the stationary state is governed by the following equations:

$$\begin{aligned} \frac{\delta F}{\delta \psi^*} &= 0 \,, \\ \frac{\delta F}{\delta \mathbf{A}} &= 0 \,. \end{aligned} \tag{1.13}$$

By substituting Eq.1.11 into Eq.1.13, we derive the following two coupled partial differential equations for the order parameter and the vector potential:

$$\begin{aligned} \alpha(T)\psi + \beta|\psi|^2\psi + \frac{1}{2m^*}\left(-\mathrm{i}\hbar\boldsymbol{\nabla} - \frac{e^*}{c}\mathbf{A}\right)^2\psi &= 0 \\ \frac{c}{4\pi}\boldsymbol{\nabla}\times\mathbf{h} &= \mathbf{J}_s \,, \end{aligned} \tag{1.14}$$

where $\mathbf{h} = \boldsymbol{\nabla}\times\mathbf{A}$ and $\mathbf{J}_s$ is the superconducting current density flowing in the material, which is given by:

$$\mathbf{J}_s = \frac{e^*}{m^*}\mathrm{Re}\left[\psi^*\left(-\mathrm{i}\hbar\boldsymbol{\nabla} - \frac{e^*}{c}\mathbf{A}\right)\psi\right] \,. \tag{1.15}$$

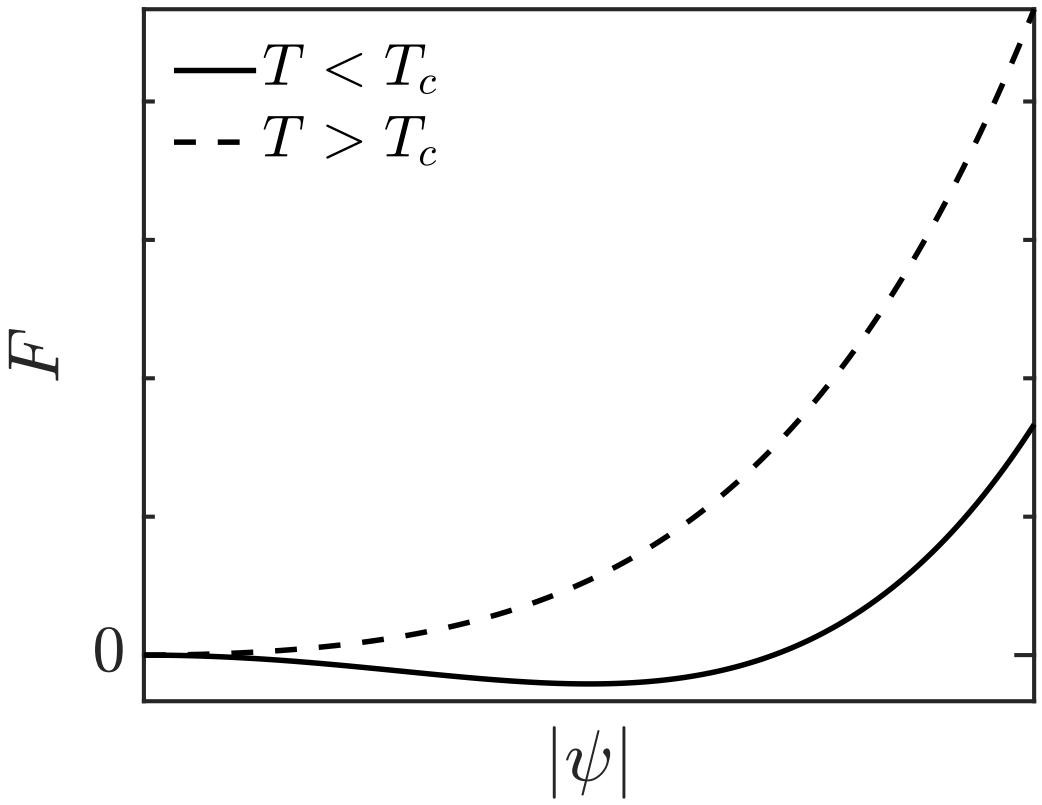

Figure 1 *– Profile of the free energy density for $T < T_c$ (solid line) and $T < T_c$ (dashed line).*

Eqs. 1.14 are the famous Ginzburg-Landau equations of superconductivity. To solve for ψ and $\mathbf{A}$ in a finite system, one must specify suitable boundary conditions. The most common ones are the following:

$$\hat{\mathbf{n}} \cdot \left(-i\hbar \boldsymbol{\nabla} - \frac{e^*}{c} \mathbf{A} \right) = 0 \, , \tag{1.16}$$

which ensure that the superconducting current does not leave the system, while the local field is assumed to match the externally applied field $\mathbf{H}_a$ at points far from the superconductor, i.e., $\boldsymbol{\nabla} \times \mathbf{A} = \mathbf{H}_a$.

To gain insight into the workings of the model, let us consider the example of a superconductor/normal metal interface in the absence of any fields or currents. In this situation, the order parameter can be assumed to be real without any loss of generality, and the first Ginzburg-Landau equation simplifies to an ordinary differential equation, written as:

$$\alpha(T)\psi + \beta\psi^3 - \frac{\hbar^2}{2m^*} \frac{d^2\psi}{dx^2} = 0 \, . \tag{1.17}$$

Let us assume that the interface is located at $x = 0$, with the semi-infinite super-

conductor on the positive x axis. If we now take the order parameter as $\tilde{\psi} = \psi/\sqrt{\alpha(T)/\beta}$, such that $\tilde{\psi} = 0$ at $x = 0$ and $\tilde{\psi} = 1$ for $x \to \infty$, Eq. 1.17 can be rewritten as:

$$-\psi + \psi^3 - \frac{\hbar^2}{2m^*|\alpha(T)|}\frac{d^2\psi}{dx^2} = 0 \ , \tag{1.18}$$

where we have dropped the tildes.

Multiplying each side of Eq. 1.18 by $\frac{d\psi}{dx}$ and defining $\xi^2(T) = \frac{\hbar^2}{2m^*|\alpha(T)|}$, we have:

$$\frac{d}{dx}\left(-\frac{\xi^2(T)}{2}\left(\frac{d\psi}{dx}\right)^2 - \frac{1}{2}\psi^2 + \frac{1}{4}\psi^4\right) = 0 \ . \tag{1.19}$$

The solution of Eq. 1.19 which obeys our boundary conditions is:

$$\psi = \tanh\left(\frac{x}{\sqrt{2}\xi(T)}\right) \ . \tag{1.20}$$

As seen from Eq. 1.20, $\xi(T)$ represents the distance over which the order parameter recovers its bulk value. $\xi(T)$ is known as the Ginzburg-Landau coherence length.

This illustrates how the Ginzburg-Landau theory describes the variation of the order parameter in a simple case. Similarly, we can analyze the behavior of the magnetic field profile. Consider again a superconductor/insulator interface, with a small magnetic field applied parallel to the surface. For a sufficiently small field, we can assume the order parameter is constant and equal to its bulk value, $\psi = |\psi(T)|$. With this, the supercurrent in Eq. 1.15 can be written as:

$$\mathbf{J}_s = -\frac{e^{*2}}{m^*c}|\psi(T)|^2\mathbf{A} \ . \tag{1.21}$$

Taking the curl on both sides of Eq. 1.21 and using the Ampère law in Eq. 1.14, we have:

$$\frac{c}{4\pi}\boldsymbol{\nabla}\times(\boldsymbol{\nabla}\times\mathbf{h}) = -\frac{e^{*2}}{m^*c}|\psi(T)|^2\mathbf{h} \ . \tag{1.22}$$

Remembering the London theory, Eq. 1.22 can be simplified as:

$$\nabla^2\mathbf{h} - \frac{1}{\lambda^2}\mathbf{h} = 0 \ , \tag{1.23}$$

with the penetration depth of Ginzburg-Landau theory given by $\lambda^2(T) = m^*c^2/(4\pi|\psi(T)|^2e^{*2})$. The ratio $\kappa = \lambda(T)/\xi(T)$ is called the Ginzburg-Landau parameter and will have a significant role in our subsequent analysis.

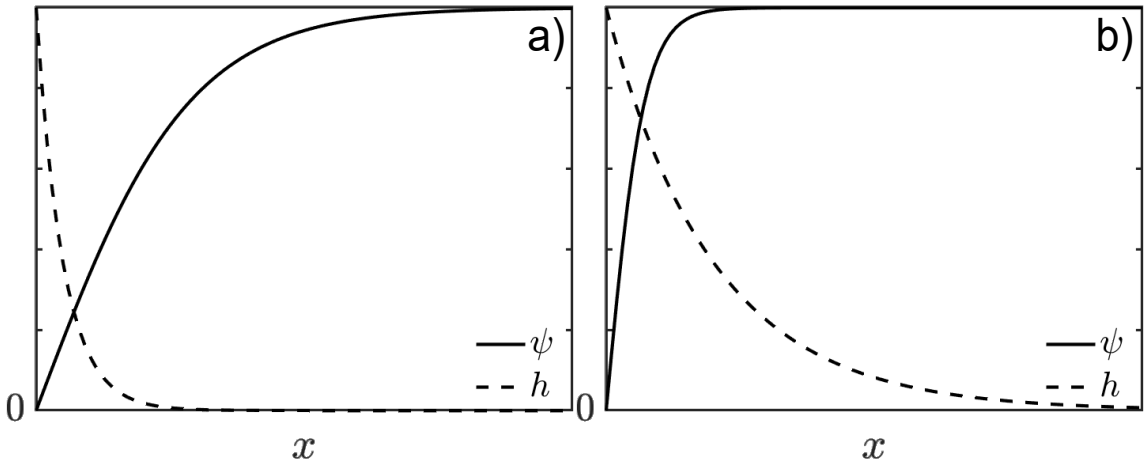

Figure 2 *– Profile of the of order parameter (solid line) and local magnetic field (dashed line) for $\kappa << 1$ (panel a)) and for $\kappa >> 1$ (panel b)).*

1.1.2.2 Energy of a Superconductor/Normal Metal Surface

Next, we calculate the energy of a domain wall separating a superconductor from a normal metal. To do this, we first rewrite the Ginzburg-Landau free energy of the system in dimensionless units. In these units, lengths are scaled by the penetration length λ, the magnetic field is given in units of $\sqrt{2}H_c$, with H_c being the thermodynamic critical field, the order parameter in units of $\sqrt{\alpha_0(T_c - T)/\beta}$ and the free energy in units of $H_c^2/4\pi$. With this, we can write Eq. 1.11 as:

$$F_s = F_{n0} - |\psi|^2 + \frac{1}{2}|\psi|^4 + \left|\left(-\frac{\mathrm{i}}{\kappa}\boldsymbol{\nabla} - \mathbf{A}\right)\psi\right|^2 + |\boldsymbol{\nabla}\times\mathbf{A}|^2 \ , \tag{1.24}$$

with the Ginzburg-Landau Eqs.1.14 being given by:

$$\begin{aligned} -\psi + |\psi|^2\psi + \left(-\frac{\mathrm{i}}{\kappa}\boldsymbol{\nabla} - \mathbf{A}\right)^2\psi &= 0 \\ \boldsymbol{\nabla}\times\mathbf{h} &= \mathbf{J}_s \ , \end{aligned} \tag{1.25}$$

where the new supercurrent density is:

$$\mathbf{J}_s = \mathrm{Re}\left[\psi^*\left(-\frac{\mathrm{i}}{\kappa}\boldsymbol{\nabla} - \mathbf{A}\right)\psi\right] \ . \tag{1.26}$$

In Eq. 1.24, to facilitate our following analysis, we have explicitly included the free energy of the normal state at zero applied magnetic field F_{n0}, which was arbitrarily taken as zero in the previous calculations. It is evident from our previous definition that the free energies of the superconducting and normal state at zero field relate as $F_{n0} - Fs0 = H_c^2/8\pi$.

Let us begin by assuming the domain wall is located at $x = 0$ and spans the entire yz plane. This reduces the problem to one dimension, allowing us to take $\mathbf{h} = h(x)\hat{\mathbf{z}}$ and $\mathbf{A} = A(x)\hat{\mathbf{y}}$. h and ψ must obey the following boundary conditions:

$$\begin{aligned} \psi(x) &= 0 \quad h(x) = 1/\sqrt{2} \qquad \text{for } x \to -\infty \\ \psi(x) &= 1 \quad h(x) = 0 \qquad\quad \text{for } x \to \infty \ . \end{aligned} \tag{1.27}$$

Since we are working with a fixed applied field, it is more convenient to use the Gibbs free energy density $G = G - hH/4\pi$. For $x \to -\infty$ the system is at the normal state and the Gibbs free energy becomes:

$$G_n = F_{n0} + \frac{H_c^2}{8\pi} - \frac{H_c^2}{4\pi} \ , \tag{1.28}$$

where we have used the boundary condition that $\psi(x) = 0$ and $h(x) = 0$ as $x \to -\infty$.

As we can see, the Gibbs free energy density deep in the normal state is equal to the the superconducting free energy at zero field F_{s0}. Since for $x \to \infty$ h goes to zero, we have that the Gibbs free energy of the system asymptotically approaches the same value on both sides of the domain wall. The surface energy (per unit area) σ_{ns} is then defined as the difference between this value and the actual value calculated in the system:

$$\sigma_{ns} = \int_{-\infty}^{\infty} \left(F_s - \frac{hH_c}{4\pi} - F_{s0} \right) dx \ . \tag{1.29}$$

Using Eq. 1.24 and the definition of the thermodynamic critical field, we have :

$$\sigma_{ns} = \int_{-\infty}^{\infty} \left(-|\psi|^2 + \frac{1}{2}|\psi|^4 + \left| \left(-\frac{\mathrm{i}}{\kappa}\boldsymbol{\nabla} - \mathbf{A} \right) \psi \right|^2 + (h - 1/\sqrt{2})^2 \right) dx \ . \tag{1.30}$$

Multiplying both sides of the first GL equation by ψ^* and integrating over all space, Eq. 1.30 can be simplified as:

$$\sigma_{ns} = \int_{-\infty}^{\infty} \left(-\frac{1}{2}|\psi|^4 + \left[h - 1/\sqrt{2} \right]^2 \right) dx \ . \tag{1.31}$$

For certain cases, it is possible to exactly obtain σ_{ns}. As the calculations are intricate, we will only reproduce the results obtained in the literature. For $\kappa << 1$ the surface energy is given by $\sigma_{ns} = 4\sqrt{2}/3\kappa$, whereas for $\kappa >> 1$, $\sigma_{ns} = -8(\sqrt{2} - 1)/3$.

To understand these results, we show the profile of the order parameter and of the local magnetic field for both κ limits in Fig. 2. As we can see, for $\kappa << 1$, there is a region

of the superconductor where the energy increases due to the expulsion of the magnetic field, while the superconducting state is not fully recovered, thus not contributing with the condensation energy. On the other hand, for $\kappa >> 1$, not only superconductivity recovers in a shorter space, but the magnetic field also penetrates the system over a much larger length.

1.1.2.3 Small ψ Limit of the Ginzburg-Landau Equation

If we assume that the order parameter is very small, we can disregard the cubic term in Eq. 1.14 and assume that the local magnetic field is equal to the applied field, since the supercurrent is negligible. The first Ginzburg-Landau equation can then be written as:

$$\alpha(T)\psi + \frac{1}{2m^*}\left(-\mathrm{i}\hbar\boldsymbol{\nabla} - \frac{e^*}{c}\mathbf{A}\right)^2\psi = 0\ . \tag{1.32}$$

Using the definition of the magnetic flux quantum $\Phi_0 = hc/2e$, we have:

$$\alpha(T)\psi + \frac{\hbar^2}{2m^*}\left(-\mathrm{i}\boldsymbol{\nabla} - \frac{2\pi}{\Phi_0}\mathbf{A}\right)^2\psi = 0\ , \tag{1.33}$$

Let us now assume we have an infinite superconductor with an external magnetic field $\mathbf{h} = H\hat{\mathbf{z}}$. Without loss of generality, we take the vector potential to be $\mathbf{A} = Hx\hat{\mathbf{y}}$. Eq. 1.33 then becomes:

$$\alpha(T)\psi + \frac{\hbar^2}{2m^*}\left(-\nabla^2 + \frac{4\pi\mathrm{i}Hx}{\Phi_0}\frac{\partial}{\partial y} + \left(\frac{2\pi H}{\Phi_0}\right)^2 x^2\right)^2\psi = 0\ . \tag{1.34}$$

Our aim is to find the highest value of H at which the order parameter is finite, *i.e.*, at which superconductivity is not completely destroyed. Note that this is not the same as the thermodynamic critical field H_c, since H_c is the highest possible value of external field that the superconducting state can completely expel without being destroyed, whereas in our new scenario the field penetrates the system.

Given the form of the potential observed in Eq. 1.34, we choose an ansatz to facilitate the solving of the problem:

$$\psi = e^{\mathrm{i}k_y y}e^{k_z z}f(x)\ , \tag{1.35}$$

after substituting this on Eq. 1.34 we get:

$$\left(\alpha(T)+\frac{\hbar^2k_z^2}{2m^*}\right)f(x)-\frac{\hbar^2}{2m^*}\frac{d^2f(x)}{dx^2}+\frac{\hbar^2}{2m^*}\left(k_y^2-\frac{4\pi H}{\Phi_0}k_yx+\left(\frac{2\pi H}{\Phi_0}\right)^2x^2\right)f(x)=0\ , \tag{1.36}$$

we can further simplify Eq. 1.36 to:

$$-\frac{\hbar^2}{2m^*}\frac{d^2f(x)}{dx^2}+\frac{m^*}{2}\left(\frac{2\pi\hbar H}{m^*\Phi_0}\right)^2\left(x-\frac{\Phi_0k_y}{2\pi H}\right)^2f(x)=-\left(\alpha(T)+\frac{\hbar^2k_z^2}{2m^*}\right)f(x)\ . \tag{1.37}$$

As can be seen, Eq. 1.37 is just the Schrödinger equation for a harmonic oscillator with a minimum energy at $x_0 = \Phi_0 k_y/2\pi H$, frequency $\omega = 2\pi\hbar H/m^*\Phi_0$ and energy $E = -\alpha(T) - \hbar^2k_z^2/2m^*$. The solution of this problem is widely known, with the energy being equal to:

$$E=\left(n+\frac{1}{2}\right)\hbar\omega\ . \tag{1.38}$$

To obtain the highest possible value of H we see that we must set $n = 0$ and $k_y = 0$ in Eq. 1.38, which gives:

$$H=\frac{m^*|\alpha(T)|\Phi_0}{4\pi\hbar^2}=\frac{\Phi_0}{2\pi\xi(T)^2}\ . \tag{1.39}$$

The field H is known as the upper critical field H_{c2}.

It is interesting to relate the upper critical field to the thermodynamic critical field H_c. To do so, we point out that, from the definition of the penetration length, the ratio $|\alpha(T)|/\beta$ can be expressed as:

$$\frac{|\alpha(T)|}{\beta}=|\phi_0|^2=\frac{e^{*2}}{m^*c^2}H_c^2\lambda^2(T)\ . \tag{1.40}$$

If we Eq. 1.40 in the definition of the coherence length, it is easy to see that:

$$\begin{aligned}\xi(T) &= \frac{\Phi_0}{2\sqrt{2}\pi}\frac{1}{H_c(T)\lambda(T)}\\ \kappa &= \frac{2\sqrt{2}\pi H_c(T)\lambda^2(T)}{\Phi_0}\ .\end{aligned} \tag{1.41}$$

Finally, using Eq. 1.41 on the expression for the upper critical field, we have:

$$H_{c2}(T)=\frac{4\pi H_c^2(T)\lambda^2(T)}{\Phi_0}=\sqrt{2}\kappa H_c(T)\ . \tag{1.42}$$

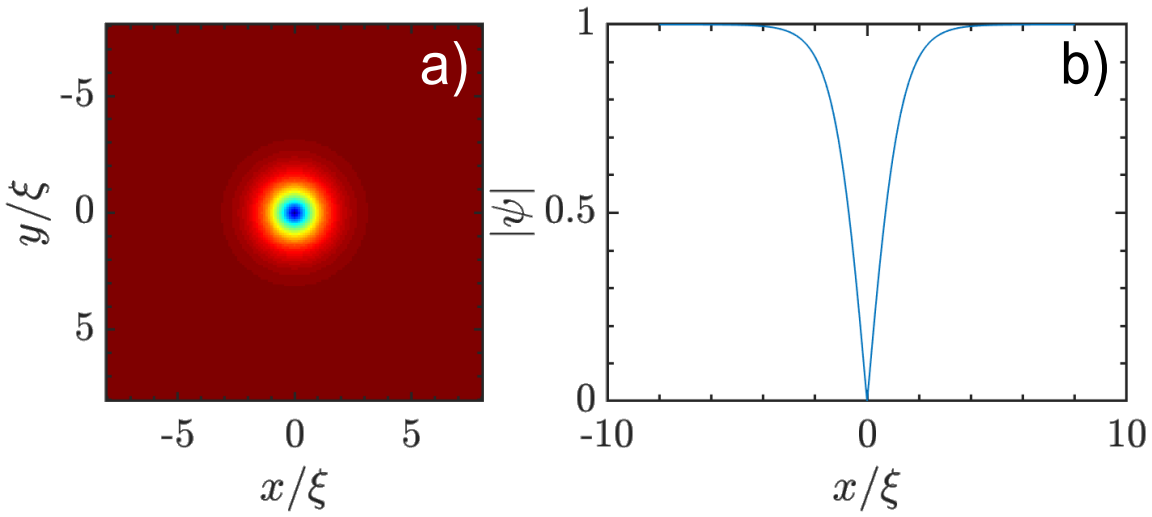

Figure 3 – *Panel a) shows the color plot of the modulus of the order parameter with a vortex at the center (blue means $|\psi| = 0$ and red $|\psi| = 1$). Panel b) shows the modulus of the order parameter as a function of x for $y = 0$, i.e., passing through the center of the vortex.*

1.1.2.4 The Two Types of Superconductors

As detailed in the previous subsections, the Ginzburg-Landau parameter $\kappa = 1/\sqrt{2}$ appears as a limiting value in two situations. In the first of them, $\kappa = 1/\sqrt{2}$ is the exact value at which the surface energy of a superconductor/normal domain wall is zero. In the second situation, we saw that, at $\kappa = 1/\sqrt{2}$, the upper critical field H_{c2} is equal to the thermodynamic critical field H_c.

These two cases are not coincidental and highlight the existence of two distinct groups of superconducting materials found in nature. The first group, known as type I superconductors, remains in the Meissner state as the applied magnetic field increases, up to the thermodynamic critical field. Above H_c, superconductivity is completely destroyed and the system goes to the normal state.

On the other hand, for materials with $\kappa > 1/\sqrt{2}$, known as type II superconductors, the evolution of the superconducting state as the external field increases is remarkably different. In this case, above a certain critical field, the system leaves the Meissner state but does not transition directly to the normal state. Instead, the superconductor enters a phase known as the mixed state, where magnetic flux penetrates the interior of the superconductor through the formation of normal regions.

Since the surface energy of a superconductor/normal interface is negative for $\kappa > 1/\sqrt{2}$, it becomes energetically favorable for the system to maximize the area of such interfaces, causing the normal regions to divide into small circular structures. To gain insight into the flux carried by these entities, we can take the expression for the

supercurrent in Eq. 1.15 and integrate it over a closed path surrounding one of these objects:

$$\oint \mathbf{J}_s \cdot \boldsymbol{ds} = \oint \frac{e^*}{m^*} \mathrm{Re}\left[\psi^* \left(-\mathrm{i}\hbar\boldsymbol{\nabla} - \frac{e^*}{c}\mathbf{A}\right)\psi\right] \cdot d\mathbf{r} \ . \tag{1.43}$$

Far from the normal region and deep in the superconducting state, we expect the supercurrent to be zero. Furthermore, it is reasonable to take the order parameter with a constant modulus and of the form $\psi = |\psi_0|e^{i\theta}$, where θ is a phase factor. With this, Eq. 1.43 becomes:

$$\oint \left(\hbar\boldsymbol{\nabla}\theta - \frac{e^*}{c}\mathbf{A}\right) \cdot d\mathbf{r} = 0 \ , \tag{1.44}$$

noticing the path integral of $\mathbf{A}$ is just the flux Φ enclosed by this path, we have:

$$\Phi = \frac{\Phi_0}{2\pi} \oint \boldsymbol{\nabla}\theta \cdot d\mathbf{r} \ . \tag{1.45}$$

Given that the superconductor order parameter must be a single-valued function, one can see that the path integral in Eq. 1.45 must be an integer multiple of 2π. Thus, we have that the flux carried by the normal region is given by:

$$\Phi = n\Phi_0 \ , \tag{1.46}$$

this is, a multiple of the magnetic flux quantum. As we will see later, it is energetically favorable for the system to have $n = 1$. It is important to note that the flux quantization is valid for both type I and type II superconductors.

This normal region with a phase winding of 2π around it is known as a superconducting vortex. The discontinuity in phase signals a circular flow of supercurrent around it, thus the name vortex. In Fig. 3, panel *a*), we show the color plot of the order parameter with a vortex present in its center. As described earlier, the vortex has a circular shape, with the order parameter recovering in a radius ξ from its center. This region is known as the core of the vortex. Panel *b*) helps the visualization of the order parameter profile. As we can see, ψ goes to zero at its center, where the discontinuity in phase takes place, and then monotonically recovers until it reaches its value in the Meissner state.

In Fig. 4, we show the profile of the z component of the local magnetic field for the same vortex. As we can see, the peak of the field occurs at the center of the vortex, with the field gradually going to zero away from it. In this example, we have set $\kappa = 1$, so the magnetic field extends over the same radius as the vortex core described above.

Finally, in Fig. 5 we show the behavior of the supercurrent in the superconductor. Panel *a*) displays the vector plot of the current, illustrating the circulation around the

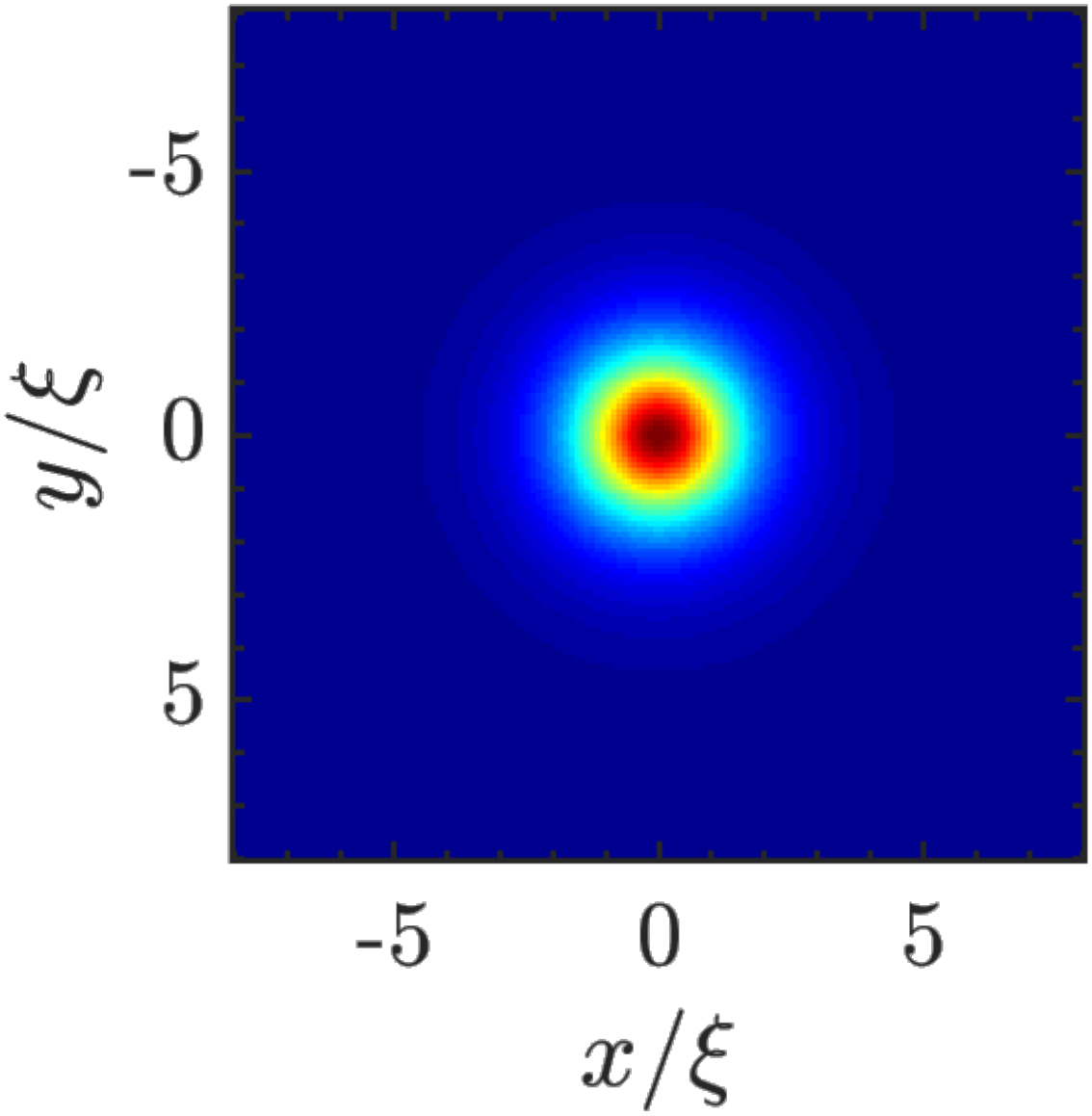

Figure 4 – *Color plot of the z component of the magnetic field profile of a superconductor with a vortex at its the center (blue means $h_z = 0$ and red the maximum value of the field).*

center of the vortex, which produces the magnetic field profile observed earlier. To understand how the current is distributed throughout the superconductor, Panel *b*) presents a color plot of the current's magnitude. It is evident that the current reaches its maximum just outside the vortex core, which is a consequence of the fact that it is energetically favorable for currents to flow in regions of robust superconductivity, where the resistance is lower than in the normal region at the vortex core.

1.1.2.5 Vortices in a Type II Superconductor

Let us now examine how vortices behave in a type II superconductor. Previously, we demonstrated that in these materials, superconductivity can persist above H_c by al-

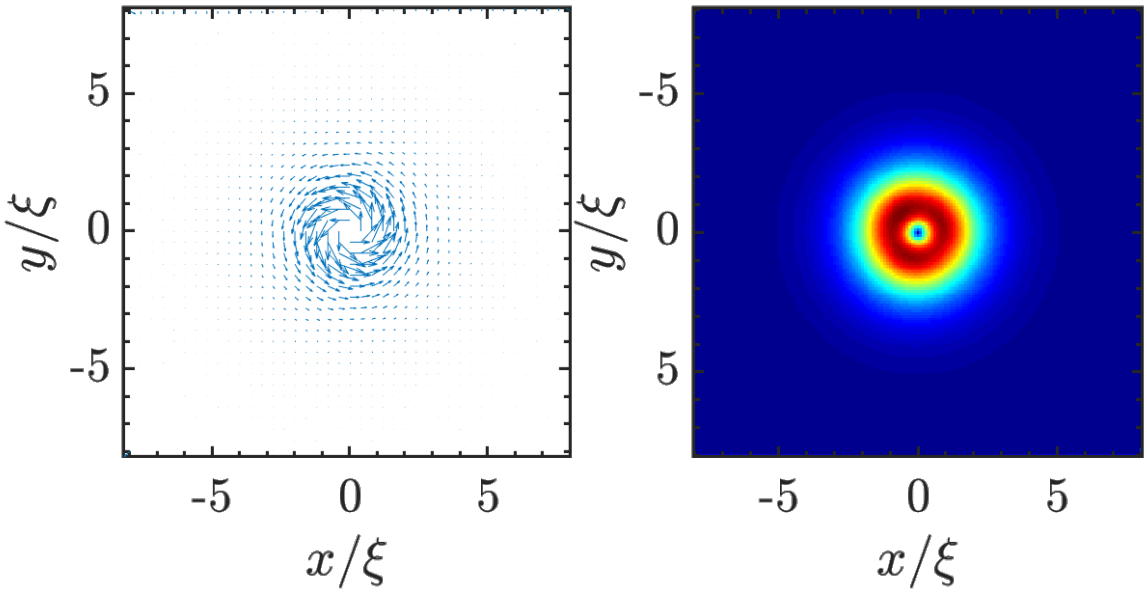

Figure 5 – *Vector plot of the supercurrent of a superconductor with a vortex at its center (panel a)). Color plot of the modulus of this supercurrent (panel b)).*

lowing the penetration of magnetic flux in the form of superconducting vortices. However, we have not specified the applied field at which the system exits the Meissner state and enters the mixed state. This critical field is known as the lower critical field, H_{c1}. To determine its value, we start by noting that, in this regime, vortices are spaced far apart from each other, allowing us to assume they do not interact. In this case, we can treat the system as if only one vortex is present, and the following expression must hold true at H_{c1}:

$$G_{\text{Meissner}} = G_{\text{One vortex}} \ , \tag{1.47}$$

where G_{Meissner} is the Gibbs free energy of the superconductor in the Meissner state and $G_{\text{One vortex}}$ is the free energy of the system when one vortex is present.

The Gibbs free energy for a superconductor with a vortex can be written as:

$$G_{Onevortex} = F_s + \epsilon_v L - \frac{H_{c1} \int h dV}{4\pi} \ , \tag{1.48}$$

where F_s is the free energy of the Meissner state, ϵ_v is the free energy per unit length of a vortex and L is the length of the vortex line.

As we saw, the flux carried by a vortex is equal to the magnetic flux quantum. Also remembering that $G_{\text{Meissner}} = F_s$, we have:

$$H_{c1} = \frac{4\pi\epsilon_v}{\Phi_0} \ . \tag{1.49}$$

Our task, then, is to find the free energy per unit length ϵ_v. To do this for a general value of κ would require the numerical solution of the Ginzburg-Landau equations for each value of the parameter. Instead, we focus on a the high κ limit, where the London model can be used and a simple solution for H_{c1} is possible to be obtained.

The problem is then to calculate the magnetic field profile produced by a vortex, which is here described as a small core of radius $\xi << \lambda$. Outside the core region, the London equation for the local field holds. Due to the symmetries of the problem, $\mathbf{h} = h_z(r)\hat{\mathbf{z}}$, with h_z given by:

$$\nabla^2 h_z(r) - \frac{1}{\lambda^2} h_z(r) = 0 \ . \tag{1.50}$$

Such equation has a well known solution and, since $h_z(r)$ must go to zero as $r \to \infty$, the local magnetic field is promptly obtained:

$$h_z(r) = C K_0 \left(\frac{r}{\lambda}\right) \ , \tag{1.51}$$

where K_0 is the modified Bessel function of the second kind. Since $\lambda >> \xi$, we can assume the field as a constant at the vortex core, hence, for $r < \xi$ the magnetic field profile is:

$$h_z(r) = C K_0 \left(\frac{\xi}{\lambda}\right) \ . \tag{1.52}$$

We now need to determine the constant C. To do so, we calculate the total flux produced by the vortex and impose it to be equal to Φ_0. We calculate the fluxoid in a path far away from the vortex, such that J_s is zero and we can use Eq. 1.44:

$$\int h_z da = \Phi_0 \ , \tag{1.53}$$

substituting the expression for the field:

$$C \left(2\pi K_0 \left(\frac{\xi}{\lambda}\right) \int_0^{\xi} r dr + \int_{\xi}^{\infty} 2\pi K_0 \left(\frac{r}{\lambda}\right) r dr \right) = \Phi_0 \ . \tag{1.54}$$

Since the integral involving the Bessel function is known, we can express C as:

$$C = \frac{\Phi_0}{2\pi\lambda^2} \left(\frac{1}{2\kappa^2} K_0 \left(\frac{\xi}{\lambda}\right) + \frac{1}{\kappa} K_1 \left(\frac{\xi}{\lambda}\right) \right)^{-1} \ . \tag{1.55}$$

We can further simplify this by noting these two limits involving the modified Bessel functions hold:

$$\begin{aligned} \lim_{\kappa\to\infty} \frac{1}{\kappa^2} K_0\left(\frac{1}{\kappa}\right) &= 0 \\ \lim_{\kappa\to\infty} \frac{1}{\kappa} K_1\left(\frac{1}{\kappa}\right) &= 1 \,, \end{aligned} \tag{1.56}$$

which means that, since $\lambda >> \xi$, the flux through the vortex core is negligible and the whole flux comes from the regions outside the vortex core.

With this result, we can finally write the local magnetic field of a vortex in the high κ limit as:

$$\begin{aligned} h_z(r) &= \frac{\Phi_0}{2\pi\lambda^2} K_0\left(\frac{r}{\lambda}\right) \qquad \text{for } r \geq \xi \\ h_z(r) &= \frac{\Phi_0}{2\pi\lambda^2} K_0\left(\frac{\xi}{\lambda}\right) \qquad \text{for } r < \xi \,. \end{aligned} \tag{1.57}$$

It is useful for the following discussions to point out that this same expression for the local field can be obtained through the solution of a modified version of the London model to include the presence of the vortex. The new equation is given by:

$$\nabla^2 h_z(r) - \frac{1}{\lambda^2} h_z(r) = -\frac{\Phi_0}{\lambda^2} \delta_2(r)\hat{\mathbf{z}} \,. \tag{1.58}$$

Once we have the magnetic field profile, we can obtain the free energy per unit length of a vortex ϵ_v, thus finding a closed expression for H_{c1}. The energy for the system, according to the London model, is given by:

$$\epsilon_v = \frac{1}{8\pi} \int \left(\mathbf{h}^2 + \lambda^2 |\boldsymbol{\nabla} \times \mathbf{h}|^2\right) dA \,, \tag{1.59}$$

where we are integrating over the superconducting area excluding the vortex core, thus neglecting the energy coming from the suppression of the superconducting state at the core, since ξ is very small.

Using Eq. 1.58 and a vector identity on the second term of the integral, we have:

$$\epsilon_v = \frac{1}{8\pi} \int h_z(r)\Phi_0 \delta_2(\mathbf{r}) da + \frac{\lambda^2}{8\pi} \oint \mathbf{h} \times (\boldsymbol{\nabla} \times \mathbf{h}) \cdot \boldsymbol{ds} \,. \tag{1.60}$$

Since we are excluding the core region in our integration, the delta function at the first term is always zero and this term can be dropped. To obtain ϵ we then need to solve the line integrals of the second term over the two contours. The first of them is at $r \to \infty$, which does not contribute to the energy, as the magnetic field goes to zero at this limit. The other line integral is performed at $r = \xi$ and here we use the approximation $K_0(r) = \ln(1/r)$ for this value of radius. With this, we finally obtain:

$$\epsilon_v = \left(\frac{\Phi_0}{4\pi\lambda}\right)^2 \ln(\kappa) \ . \tag{1.61}$$

Now that we know ϵ_v, we can obtain the lower critical field from Eq. 1.49:

$$H_{c1} = \frac{4\pi}{\Phi_0}\left(\frac{\Phi_0}{4\pi\lambda}\right)^2 \ln(\kappa) = \frac{\Phi_0}{4\pi\lambda^2}\ln(\kappa) = \frac{H_c}{\sqrt{2}\kappa}\ln(\kappa) \ . \tag{1.62}$$

Once we know at which field vortices start to penetrate bulk superconductors, it is interesting to investigate how they interact with each other when there is more than one vortex in the system. To do so, we calculate the force between two vortices located at $\mathbf{r}_1$ and $\mathbf{r}_2$, respectively. The profile of the local magnetic field of these two vortices can then be decomposed as:

$$h_{z2v}(\mathbf{r}) = h_z\left(|\mathbf{r}-\mathbf{r}_1|\right) + h_z\left(|\mathbf{r}-\mathbf{r}_2|\right) \ , \tag{1.63}$$

where h_z is the same field calculated above and given by Eq. 1.57.

Using Eq. 1.63 to calculate the energy of this configuration in the same manner that was done by a single vortex, it is simple to see that the free energy per unit length of the two vortex system is given by:

$$\epsilon_{2v} = \frac{\Phi_0}{8\pi}\left(h_{z1}(\mathbf{r}_1) + h_{z1}(\mathbf{r}_2) + h_{z2}(\mathbf{r}_1) + h_{z2}(\mathbf{r}_2)\right) \ , \tag{1.64}$$

with $H_{zi}(\mathbf{r})$ being the field of the ith vortex calculated at position $\mathbf{r}$.

Since h_{z1} and h_{z2} are completely symmetric, this can be simplified as:

$$\epsilon_{2v} = \frac{\Phi_0}{8\pi}\left(h_{z1}(\mathbf{r}_1) + h_{z1}(\mathbf{r}_2)\right) \ . \tag{1.65}$$

We can see that the first term is the energy of two isolated vortices, while the second term gives the increment in energy due to their interaction. With the previous definition of h_z, we see that the interaction energy between two vortices E_I is given by:

$$E_I = \frac{\Phi_0^2}{8\pi^2\lambda^2} K_0\left(\frac{|\mathbf{r}_1-\mathbf{r}_2|}{\lambda}\right) \ . \tag{1.66}$$

The Bessel function monotonically decays as the distance between the vortices increases, which means the interaction between two vortices is always repulsive. On the other hand, if the two vortices have different polarity, *i.e.*, current flowing in opposite directions, the interaction is attractive and the two vortices become gradually closer until they annihilate each other. A vortex with opposite polarity is known as an antivortex.

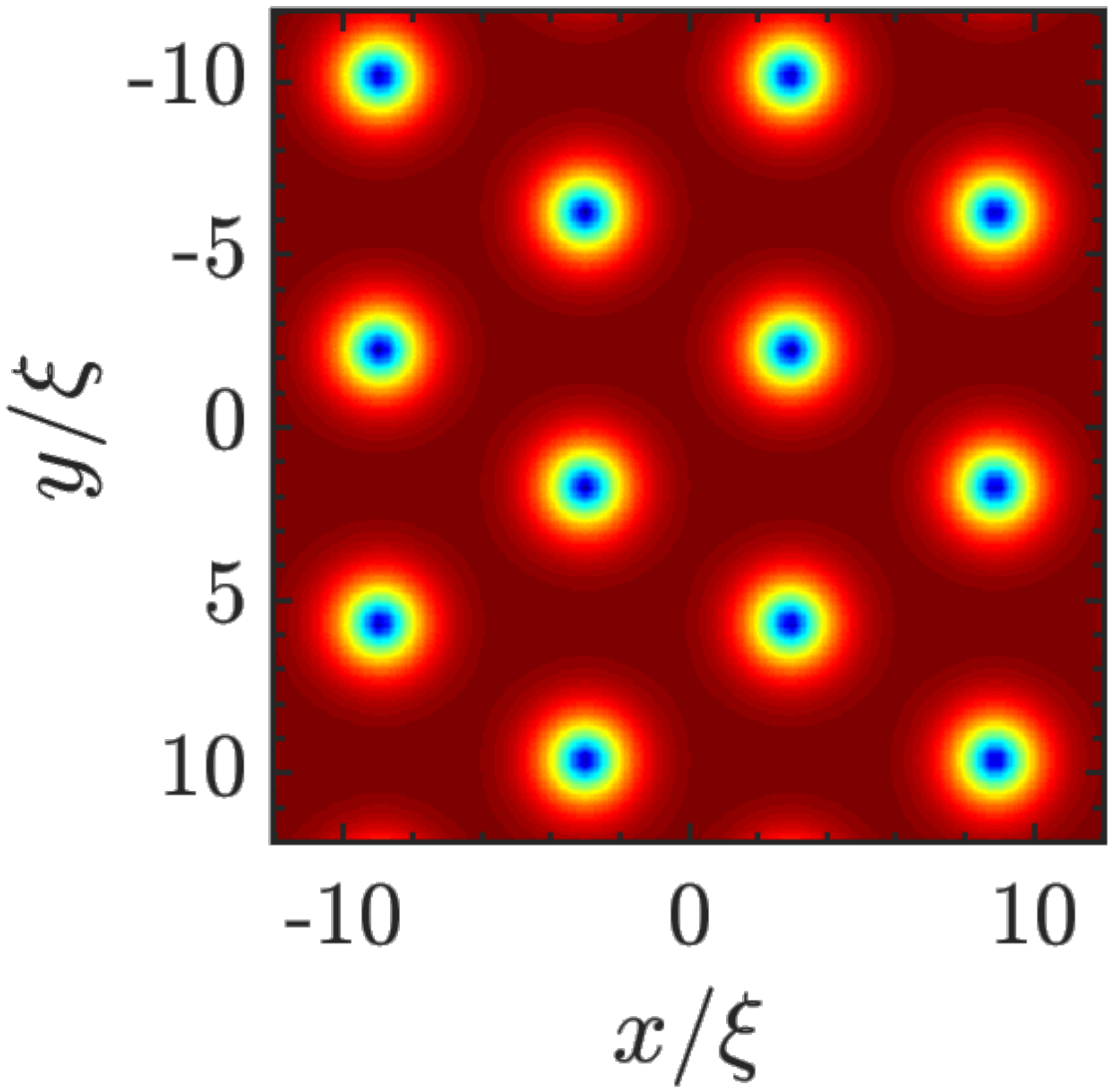

Figure 6 – *Color plot of the modulus of the order parameter in a region of a superconducting system containing* 12 *vortices. A quasi-hexagonal structure is clearly seen. Distortion from perfect hexagonal lattice is due to boundary condition.*

Given that vortices tend to repel one another, it is an interesting problem to investigate in which structure they organize themselves when the applied field is large enough to allow the penetration of several vortices in a bulk superconductor. It was shown by Abrikosov in his seminal paper that a hexagonal lattice is the configuration with the smallest energy. To see this, we numerically solve the Ginzburg-Landau equations for a system with 12 vortices and periodic boundary conditions. Fig. 6 shows the color plot of the modulus of the order parameter for this system, where the hexagonal pattern predicted by Abrikosov can be promptly identified.

1.1.2.6 Flux Flow

The ability to carry electrical current with no energy dissipation makes superconductor materials natural candidates to a series of applications from electronic devices of nanoscale used in computers and other communication systems to large magnetic field generators. The zero resistance, though, does not depend solely on the capacity of the superconductor to support the generated fields, but also on the behavior of the vortices present in the sample.

In the presence of an applied current density $\mathbf{J}$, a vortex feels a force given by:

$$\mathbf{F} = \mathbf{J} \times \frac{\Phi_0 \hat{\mathbf{z}}}{c} , \tag{1.67}$$

where we see that the force is perpendicular to the applied current.

Now, assuming this force is sufficient to set the vortex in motion, an induced electric field parallel to the current density will emerge. This indicates that the motion of the vortex is accompanied by energy dissipation, which poses a significant challenge to achieve zero resistance in devices based on superconducting materials.

To mitigate this issue, pinning techniques were developed, whereby vortices are attracted to specific small areas of the superconductor (typically in the order of ξ). his increases the applied current required to set them in motion. If this pinning is very strong, finite resistance emerges only when the current is sufficient to induce a vortex jump from one pinning site to another, in a phenomenon known as flux creep. Conversely, weak pinning results in smooth vortex motion, referred to as flux flow, which we will explore below.

Suppose the vortex, driven by the Lorentz force, moves with a constant velocity, due to the action of a viscous drag caused by the superconducting medium. Eq. 1.67 gives the following expression:

$$\eta \mathbf{v} = \mathbf{F} = \mathbf{J} \times \frac{\Phi_0 \hat{\mathbf{z}}}{c} , \tag{1.68}$$

where η is the viscosity coefficient of the medium.

The electric field associated with this motion can be expressed as:

$$\mathbf{E} = \mathbf{h} \times \frac{\mathbf{v}}{c} . \tag{1.69}$$

Combining Eqs. 1.68 and 1.69 and already taking into account the direction of the vectors as discussed above, we have:

$$\rho_f = \frac{E}{J} = \frac{h\Phi_0}{\eta c^2} , \tag{1.70}$$

with ρ_f being the resistivity that arises from the vortex motion.

To conclude this analysis and find the flux flow resistivity, we then need to obtain the value of the viscosity coefficient. Although this demands a detailed analysis of the evolution of the order parameter with the time-dependent Ginzburg-Landau theory, a simpler model was developed by Bardeen and Stephan [18] which gives us an expression for η, as well as an understanding of its origin. In this model, dissipation arises from normal currents that exist in the vortex core solely due to its motion. Through straightforward calculations using the London model, which can be found in Ref. [19], η can be expressed as:

$$\eta = \frac{\Phi_0 H_{c2}}{\rho_n c^2} \,, \tag{1.71}$$

where ρ_n is the resistivity of the normal state.

1.1.3 BCS theory

1.1.3.1 Cooper Pairs

So far, we have introduced the phenomenological theories that describe the phenomenon of superconductivity. Let us now briefly discuss how the emergence of the superconducting state can be explained from a microscopic perspective. To do this, we begin by illustrating how two electrons can form a bound state when placed in a Fermi sea. This explanation, along with the subsequent discussion on BCS theory, is inspired by the topics presented in Refs. [19, 20, 21, 22].

We assume that the two electrons wave function depends only on the relative position of the electrons and can be written as:

$$\psi(\mathbf{r}_1 - \mathbf{r}_2) = \sum_{\mathbf{k}} g(\mathbf{k}) e^{\mathrm{i}\mathbf{k}\cdot(\mathbf{r}_1 - \mathbf{r}_2)} \,, \tag{1.72}$$

where we have assumed that the total momentum of the electron pair is zero. As the two electrons are placed in a Fermi sea, the amplitude $g(\mathbf{k})$ must be zero for $k < k_F$.

The Schrödinger equation for our system is given by:

$$-\frac{\hbar^2}{2m}\left(\nabla_1^2 + \nabla_2^2\right)\psi(\mathbf{r}_1 - \mathbf{r}_2) + V(\mathbf{r}_1, \mathbf{r}_2)\psi(\mathbf{r}_1 - \mathbf{r}_2) = E'\psi(\mathbf{r}_1 - \mathbf{r}_2) \,, \tag{1.73}$$

with $V(\mathbf{r}_1, \mathbf{r}_2)$ representing the electron-electron interaction. In momentum space, this interaction can be written as:

$$V_{\mathbf{k},\mathbf{k}'} = \frac{1}{L^3}\int V(\mathbf{r}) e^{-\mathrm{i}(\mathbf{k}-\mathbf{k}')\cdot\mathbf{r}} d^3\mathbf{r} \,, \tag{1.74}$$

$\mathbf{r}$ being the relative position between the electrons and L^3 is the volume of our system.

To facilitate our discussion, let us redefine the energy in Eq. 1.73 as $E' \to E + \frac{\hbar^2 k_F^2}{m}$, where $2E_F = \frac{\hbar^2 k_F^2}{m}$ is the energy of two free electrons at the Fermi surface. In this case, a negative value of E means the formation of a two electrons bound state and the breaking of the normal state. Substituting Eqs. 1.72 and 1.74 on Eq. 1.73, we have:

$$\frac{\hbar^2 k^2}{2m} g(\mathbf{k}) + \sum_{\mathbf{k}'} g(\mathbf{k}') V_{\mathbf{k},\mathbf{k}'} = (E + 2E_F) g(\mathbf{k}) \ , \tag{1.75}$$

to get this result, one need to multiply Eq. 1.73 by $e^{-i\mathbf{q}\cdot\mathbf{r}}$ and integrate over $\mathbf{r}$.

In Eq. 1.75, the energy E is positive for all repulsive form of the interaction $V_{\mathbf{k},\mathbf{k}'}$. Our goal is to show that an attractive interaction between the electrons can lead to negative values of E. To facilitate our analysis, let us assume the interaction is nonzero and equal to $V_{\mathbf{k},\mathbf{k}'} = -V/L^3$ only at a small region above the Fermi surface such that $\hbar^2 k^2/2m < E_F + \hbar\omega_D$ and $\hbar^2 k'^2/2m < E_F + \hbar\omega_D$.

Substituting this interaction in Eq. 1.75 and rearranging the terms, we have:

$$\left(-\frac{\hbar^2 k^2}{2m} + E + 2E_F \right) g(\mathbf{k}) = -\frac{V}{L^3} \sum_{\mathbf{k}'} g(\mathbf{k}') \ , \tag{1.76}$$

where the sum must be over $E_F < \hbar^2 k'^2/2m < E_F + \hbar\omega_D$, given the form of the interaction potential and the existence of the Fermi sea.

Eq. 1.76 can only be true if the following condition also holds:

$$1 = \frac{V}{L^3} \sum_{\mathbf{k}'} \frac{1}{\frac{\hbar^2 k'^2}{m} - E - 2E_F} \ . \tag{1.77}$$

To find the value of E, it is more convenient to go from the discrete sum to an integral formulation of Eq. 1.77. To do this, we define $\epsilon = \hbar^2 k'^2/2m - E_F$ and the density of state relating k' to ϵ $N(\epsilon) = (2\pi)^{-3} 4\pi k'^2 dk'/d\epsilon$. Eq. 1.77 can then be expressed as:

$$1 = V \int_0^{\hbar\omega_D} d\epsilon N(\epsilon) \frac{1}{2\epsilon - E} \ , \tag{1.78}$$

to obtain a closed expression for E, we approximate $N(\epsilon) \to N(0)$. The integral then becomes trivial and we obtain:

$$\begin{aligned} 1 &= \frac{N(0)V}{2} \ln\left(\frac{E - 2\hbar\omega_D}{E} \right) \\ \left(e^{2/N(0)V} - 1\right) E &= -2\hbar\omega_D \\ E &= -2\hbar\omega_D e^{-2/N(0)V} \ , \end{aligned} \tag{1.79}$$

where, to obtain the last line, we have assumed $N(0)V$ is very small and performed a Taylor expansion of the exponential in the second line. As we can see from the final result, a small attractive interaction between two electrons placed in a background Fermi sea is sufficient to break the normal state and form a bound state, the so called Copper pair. In conventional superconducting materials, the attractive interaction has origin in the electron-phonon interaction.

1.1.3.2 BCS Ground State

Now that we have established the possibility of Copper pair formation, let us discuss the ground state of many Cooper pairs. We will limit ourselves to show how the ground state of our system exhibits a finite energy gap below the critical temperature for the transition to the superconducting state, referring the reader to the above cited books for the discussion about the magnetic response of this ground state and the origin of the Meissner state.

We start by defining our model Hamiltonian, which takes into account all the important interactions for the emergence of the superconducting state:

$$H = \sum_{\mathbf{k}\sigma} \epsilon_{\mathbf{k}} c^{\dagger}_{\mathbf{k}\sigma} c_{\mathbf{k}\sigma} + \sum_{\mathbf{k},\mathbf{k}'} V_{\mathbf{k},\mathbf{k}'} c^{\dagger}_{\mathbf{k}\uparrow} c^{\dagger}_{-\mathbf{k}\downarrow} c_{-\mathbf{k}'\downarrow} c_{\mathbf{k}'\uparrow} \,, \tag{1.80}$$

where σ refers to the electron spin and $\epsilon_{\mathbf{k}} = \hbar^2 k^2/2m - \mu$, with μ being the chemical potential of our system.

To treat Eq. 1.80, we perform a mean field approximation, introducing:

$$b^*_{\mathbf{k}} = \left\langle c^{\dagger}_{\mathbf{k}\uparrow} c^{\dagger}_{-\mathbf{k}\downarrow} \right\rangle \,. \tag{1.81}$$

With this, $c^{\dagger}_{\mathbf{k}\uparrow} c^{\dagger}_{-\mathbf{k}\downarrow}$ can be written as the sum of the average value defined in Eq. 1.81 and a small correction, such as:

$$c^{\dagger}_{\mathbf{k}\uparrow} c^{\dagger}_{-\mathbf{k}\downarrow} = b^*_{\mathbf{k}} + \left(c^{\dagger}_{\mathbf{k}\uparrow} c^{\dagger}_{-\mathbf{k}\downarrow} - b^*_{\mathbf{k}} \right) \,, \tag{1.82}$$

and the product appearing in Eq. 1.80 can be linearly approximated, disregarding the product between the terms inside the parenthesis. Our model Hamiltonian can then be simplified as:

$$H = \sum_{\mathbf{k}\sigma} \epsilon_{\mathbf{k}} c^{\dagger}_{\mathbf{k}\sigma} c_{\mathbf{k}\sigma} + \sum_{\mathbf{k},\mathbf{k}'} V_{\mathbf{k},\mathbf{k}'} \left(c^{\dagger}_{\mathbf{k}\uparrow} c^{\dagger}_{-\mathbf{k}\downarrow} b_{\mathbf{k}'} + c_{-\mathbf{k}'\downarrow} c_{\mathbf{k}'\uparrow} b^*_{\mathbf{k}} - b^*_{\mathbf{k}} b_{\mathbf{k}'} \right) \,. \tag{1.83}$$

Proceeding, we now define the superconducting gap:

$$\Delta_{\mathbf{k}} = -\sum_{\mathbf{k}'} V_{\mathbf{k},\mathbf{k}'} \left\langle c_{-\mathbf{k}'\downarrow} c_{\mathbf{k}'\uparrow} \right\rangle \ , \tag{1.84}$$

and the Hamiltonian becomes:

$$H = \sum_{\mathbf{k}\sigma} \epsilon_{\mathbf{k}} c^{\dagger}_{\mathbf{k}\sigma} c_{\mathbf{k}\sigma} - \sum_{\mathbf{k}} \left(c^{\dagger}_{\mathbf{k}\uparrow} c^{\dagger}_{-\mathbf{k}\downarrow} \Delta_{\mathbf{k}} + c_{-\mathbf{k}\downarrow} c_{\mathbf{k}\uparrow} \Delta^{*}_{\mathbf{k}} - b_{\mathbf{k}} \Delta^{*}_{\mathbf{k}} \right) \ . \tag{1.85}$$

To solve this Hamiltonian, we now need to perform a transformation to obtain an expression which is linear in the creation and annihilation operators. The suitable transformation for this is:

$$\begin{aligned} c_{\mathbf{k}\uparrow} &= u^{*}_{\mathbf{k}} \gamma_{\mathbf{k}0} - v_{\mathbf{k}} \gamma^{\dagger}_{-\mathbf{k}1} \\ c^{\dagger}_{-\mathbf{k}\downarrow} &= v^{*}_{\mathbf{k}} \gamma_{\mathbf{k}0} + u_{\mathbf{k}} \gamma^{\dagger}_{-\mathbf{k}1} \ . \end{aligned} \tag{1.86}$$

To find the expressions for $u_{\mathbf{k}}$ and $v_{\mathbf{k}}$, we must impose that the transformed Hamiltonian is linear with respect to the new operators. Which means that terms containing cross products of $\gamma^{\dagger}_{\mathbf{k}0}\gamma^{\dagger}_{\mathbf{k}1}$, $\gamma_{\mathbf{k}0}\gamma_{\mathbf{k}1}$, $\gamma^{\dagger}_{\mathbf{k}0}\gamma_{\mathbf{k}1}$ and $\gamma^{\dagger}_{\mathbf{k}1}\gamma_{\mathbf{k}0}$ to vanish. Substituting Eq. 1.86 on the Hamiltonian of Eq. 1.85, we obtain:

$$\begin{aligned} H &= \sum_{\mathbf{k}} \left(\epsilon_{\mathbf{k}} \left(|u_{\mathbf{k}}|^2 - |v_{\mathbf{k}}|^2 \right) + u^{*}_{\mathbf{k}} v^{*}_{\mathbf{k}} \Delta_{\mathbf{k}} + u_{\mathbf{k}} v_{\mathbf{k}} \Delta^{*}_{\mathbf{k}} \right) \left(\gamma^{\dagger}_{\mathbf{k}0}\gamma_{\mathbf{k}0} + \gamma^{\dagger}_{\mathbf{k}1}\gamma_{\mathbf{k}1} \right) \\ &+ \sum_{\mathbf{k}} \left(2\epsilon_{\mathbf{k}} u^{*}_{\mathbf{k}} v_{\mathbf{k}} - u^{*2}_{\mathbf{k}} \Delta_{\mathbf{k}} + v^{2}_{\mathbf{k}} \Delta^{*}_{\mathbf{k}} \right) \gamma^{\dagger}_{\mathbf{k}0}\gamma^{\dagger}_{\mathbf{k}1} \\ &+ \sum_{\mathbf{k}} \left(2\epsilon_{\mathbf{k}} u_{\mathbf{k}} v^{*}_{\mathbf{k}} - u^{2}_{\mathbf{k}} \Delta^{*}_{\mathbf{k}} + v^{*2}_{\mathbf{k}} \Delta_{\mathbf{k}} \right) \gamma_{\mathbf{k}1}\gamma_{\mathbf{k}0} \\ &+ 2\epsilon_{\mathbf{k}} |v_{\mathbf{k}}|^2 - u_{\mathbf{k}} v^{*}_{\mathbf{k}} \Delta_{\mathbf{k}} - u^{*}_{\mathbf{k}} v_{\mathbf{k}} \Delta^{*}_{\mathbf{k}} + b_{\mathbf{k}} \Delta^{*}_{\mathbf{k}} \ . \end{aligned} \tag{1.87}$$

As can be seen, to make the Hamiltonian diagonal, second and third lines must be taken out. This can be guaranteed by imposing the following relationship:

$$2\epsilon_{\mathbf{k}} u_{\mathbf{k}} v^{*}_{\mathbf{k}} - u^{2}_{\mathbf{k}} \Delta^{*}_{\mathbf{k}} + v^{*2}_{\mathbf{k}} \Delta_{\mathbf{k}} = 0 \ , \tag{1.88}$$

which must be combined with the imposition that $\{\gamma^{\dagger}_{\mathbf{k}0}, \gamma_{\mathbf{k}0}\} = \{\gamma^{\dagger}_{\mathbf{k}1}, \gamma_{\mathbf{k}1}\} = 1$, which leads to the following relationship:

$$|u_{\mathbf{k}}|^2 + |v_{\mathbf{k}}|^2 = 1 \ , \tag{1.89}$$

we can then write $u_{\mathbf{k}}$ and $v_{\mathbf{k}}$ as:

$$\begin{aligned} u_{\mathbf{k}} &= e^{\mathrm{i}\varphi}\cos(\theta/2) \\ v_{\mathbf{k}} &= e^{\mathrm{i}\varphi}\sin(\theta/2)\ , \end{aligned} \tag{1.90}$$

from Eq. 1.89, one can see that we must have $\Delta_{\mathbf{k}} = |\Delta_{\mathbf{k}}|e^{2\mathrm{i}\varphi}$.

Substituting these expressions in Eq. 1.88 and using the appropriate trigonometric relationships, we obtain:

$$\epsilon_{\mathbf{k}}\sin(\theta) - |\Delta_{\mathbf{k}}|\cos(\theta) = 0\ , \tag{1.91}$$

from this, we have:

$$\begin{aligned} \sin^2(\theta) + \cos^2(\theta) &= 1 \\ \left(1 + \frac{|\Delta_{\mathbf{k}}|^2}{\epsilon_{\mathbf{k}}^2}\right)\cos^2(\theta) &= 1 \\ \cos(\theta) &= \frac{\epsilon_{\mathbf{k}}}{\sqrt{|\Delta_{\mathbf{k}}|^2 + \epsilon_{\mathbf{k}}^2}}\ , \end{aligned} \tag{1.92}$$

and consequently:

$$\sin(\theta) = \frac{|\Delta_{\mathbf{k}}|}{\sqrt{|\Delta_{\mathbf{k}}|^2 + \epsilon_{\mathbf{k}}^2}}\ . \tag{1.93}$$

Again using trigonometric identities, we can finally write closed expressions for $|u_{\mathbf{k}}|^2$ and $|v_{\mathbf{k}}|^2$:

$$\begin{aligned} |u_{\mathbf{k}}|^2 &= \frac{1}{2}\left(1 + \frac{\epsilon_{\mathbf{k}}}{E_{\mathbf{k}}}\right) \\ |v_{\mathbf{k}}|^2 &= \frac{1}{2}\left(1 - \frac{\epsilon_{\mathbf{k}}}{E_{\mathbf{k}}}\right)\ , \end{aligned} \tag{1.94}$$

where we have introduced $E_{\mathbf{k}} = |\Delta_{\mathbf{k}}|^2 + \epsilon_{\mathbf{k}}^2$. Hereafter, we take the positive root solution for both $u_{\mathbf{k}}$ and $v_{\mathbf{k}}$ in the equation above.

Substituting this in Eq. 1.87, we obtain our final model Hamiltonian:

$$H = \sum_{\mathbf{k}} E_{\mathbf{k}}\left(\gamma_{\mathbf{k}0}^{\dagger}\gamma_{\mathbf{k}0} + \gamma_{\mathbf{k}1}^{\dagger}\gamma_{\mathbf{k}1}\right) + E_0\ , \tag{1.95}$$

where E_0 denotes a constant energy term.

We are now able to evaluate the superconducting gap defined in Eq. 1.84:

$$\Delta_{\mathbf{k}} = -\sum_{\mathbf{k}'} V_{\mathbf{k},\mathbf{k}'} \left\langle c_{-\mathbf{k}'\downarrow} c_{\mathbf{k}'\uparrow} \right\rangle = -\sum_{\mathbf{k}'} \frac{V_{\mathbf{k},\mathbf{k}'}\Delta_{\mathbf{k}'}}{2E_{\mathbf{k}'}} \tanh\left(\frac{E_{\mathbf{k}'}}{2k_B T}\right) , \tag{1.96}$$

where we have used the transformations given by Eq. 1.86 and statistical mechanics to calculate the averages involving the operators.

To proceed, we must make an assumption about the form of the interaction potential. Again, we take it to be **k** independent and only nonzero within a finite energy range:

$$\begin{aligned} V_{\mathbf{k},\mathbf{k}'} &= -V \qquad \text{if} \qquad |\epsilon_{\mathbf{k}}| \, , \, |\epsilon_{\mathbf{k}'}| \, < \, \hbar\omega_D \\ V_{\mathbf{k},\mathbf{k}'} &= 0 \qquad \text{if} \qquad |\epsilon_{\mathbf{k}}| \, , \, |\epsilon_{\mathbf{k}'}| \, > \, \hbar\omega_D \, . \end{aligned} \tag{1.97}$$

As a consequence, the superconducting gap must also be nonzero only in this same energy interval, which gives us:

$$\begin{aligned} \Delta_{\mathbf{k}} &= \Delta \qquad \text{if} \qquad |\epsilon_{\mathbf{k}}| \, , \, |\epsilon_{\mathbf{k}'}| \, < \, \hbar\omega_D \\ \Delta_{\mathbf{k}} &= 0 \qquad \text{if} \qquad |\epsilon_{\mathbf{k}}| \, , \, |\epsilon_{\mathbf{k}'}| \, > \, \hbar\omega_D \, . \end{aligned} \tag{1.98}$$

Eq. 1.96 then becomes:

$$1 = V \sum_{\mathbf{k}'} \frac{1}{2E_{\mathbf{k}'}} \tanh\left(\frac{E_{\mathbf{k}'}}{2k_B T}\right) . \tag{1.99}$$

Converting the sum to an integral, we have:

$$1 = N(0)V \int_0^{\hbar\omega_D} d\epsilon \frac{1}{\sqrt{\Delta^2 + \epsilon^2}} \tanh\left(\frac{\sqrt{\Delta^2 + \epsilon^2}}{2k_B T}\right) , \tag{1.100}$$

where we have again approximated the density of states for its value at the Fermi surface.

To gain some insight, let us set the temperature to zero and calculate the resulting superconducting gap. From Eq. 1.100 we have:

$$1 = N(0)V \int_0^{\hbar\omega_D} d\epsilon \frac{1}{\sqrt{\Delta^2 + \epsilon^2}} = N(0)V \sinh^{-1}\left(\frac{\hbar\omega_D}{\Delta}\right) . \tag{1.101}$$

If we consider that $N(0)V$ is very small, this can be rewritten as:

$$\Delta(0) = 2\hbar\omega_D e^{-1/N(0)V} . \tag{1.102}$$

Eq. 1.101 shows us that a weak attractive interaction between the electrons leads to formation of a superconducting state and to the formation of an energy gap. From Eq. 1.100 we can also determine the critical temperature T_c above which there is no superconductivity. To do so, we substitute $\Delta = 0$ in this equation. We then have:

$$\begin{aligned} 1 &= N(0)V \int_0^{\hbar\omega_D} d\epsilon \frac{1}{\epsilon} \tanh\left(\frac{\epsilon}{2k_B T_c}\right) \\ 1 &= N(0)V \int_0^{\hbar\omega_D/2k_B T_c} dx \frac{\tanh(x)}{x} , \end{aligned} \tag{1.103}$$

where in the second line we have substituted $\epsilon = 2k_B T_c x$. The last integral is tabulated and we can write the final result as:

$$\begin{aligned} 1 &= N(0)V \ln\left(\frac{2e^{\gamma}\hbar\omega_D}{\pi k_B T_c}\right) \\ k_B T_c &= 1.13\hbar\omega_D e^{-1/N(0)V} . \end{aligned} \tag{1.104}$$

where $\gamma = 0.577$ and $2e^{\gamma}/\pi \approx 1.13$.

Comparing Eqs. 1.102 and 1.104, we reach an important result of the BCS theory:

$$\frac{\Delta(0)}{k_B T_c} = 1.764 , \tag{1.105}$$

which has excellent agreement with experimental results.

1.1.4 Microscopic Derivation of the Ginzburg-Landau Equations

Previously, we have obtained the Ginzburg-Landau equations that describe the superconducting state of a conventional s-wave superconductor through phenomenological arguments. In what follows, we will show that this equation can be derived directly from the BCS theory in the limit $T \to T_c$, as it was first shown by Gor'kov [23].

We start the description, based on the derivation given by Refs. [22, 21], by writing the grand canonical Hamiltonian for our system:

$$\begin{aligned} \hat{K} &= \int d^3\mathbf{r}\, \hat{\psi}(\mathbf{r})^{\dagger}_{\alpha} \left[\frac{1}{2m}\left(-i\hbar\boldsymbol{\nabla} + \frac{e\mathbf{A}(\mathbf{r})}{c}\right)^2 - \mu\right] \hat{\psi}(\mathbf{r})_{\beta} \\ &- \frac{g}{2}\int d^3\mathbf{r}\, \hat{\psi}(\mathbf{r})^{\dagger}_{\alpha}\hat{\psi}(\mathbf{r})^{\dagger}_{\beta}\hat{\psi}(\mathbf{r})_{\beta}\hat{\psi}(\mathbf{r})_{\alpha} . \end{aligned} \tag{1.106}$$

If we consider the normal state as a free electron gas and use the Hartree-Fock approximation to treat the formation of the Cooper pairs, we get:

$$\begin{aligned}\hat{K}_{eff} = &= \int d^3\mathbf{r}\,\hat{\psi}(\mathbf{r})^\dagger_\alpha \left[\frac{1}{2m}\left(-\mathrm{i}\hbar\boldsymbol{\nabla} + \frac{e\mathbf{A}(\mathbf{r})}{c}\right)^2 - \mu\right]\hat{\psi}(\mathbf{r})_\beta \\ &- g\int d^3\mathbf{r}\left[\left\langle\hat{\psi}(\mathbf{r})^\dagger_\downarrow\hat{\psi}(\mathbf{r})^\dagger_\uparrow\right\rangle\hat{\psi}(\mathbf{r})_\uparrow\hat{\psi}(\mathbf{r})_\downarrow + \hat{\psi}(\mathbf{r})^\dagger_\downarrow\hat{\psi}(\mathbf{r})^\dagger_\uparrow\left\langle\hat{\psi}(\mathbf{r})_\uparrow\hat{\psi}(\mathbf{r})_\downarrow\right\rangle\right] \quad (1.107)\end{aligned}$$

where the averages above are given by:

$$\left\langle\hat{\psi}(\mathbf{r})^\dagger_\downarrow\hat{\psi}(\mathbf{r})^\dagger_\uparrow\right\rangle = \frac{\mathrm{Tr}\left[e^{-\beta\hat{K}_{eff}}\hat{\psi}(\mathbf{r})^\dagger_\downarrow\hat{\psi}(\mathbf{r})^\dagger_\uparrow\right]}{\mathrm{Tr}e^{-\beta\hat{K}_{eff}}}\ . \quad (1.108)$$

We now define the Heisenberg operators:

$$\begin{aligned}\hat{\psi}_{K\uparrow}(\mathbf{r},\tau) &= e^{\hat{K}_{eff}\tau/\hbar}\hat{\psi}_\uparrow(\mathbf{r})e^{-\hat{K}_{eff}\tau/\hbar} \\ \hat{\psi}^\dagger_{K\downarrow}(\mathbf{r},\tau) &= e^{\hat{K}_{eff}\tau/\hbar}\hat{\psi}^\dagger_\downarrow(\mathbf{r})e^{-\hat{K}_{eff}\tau/\hbar}\ , \quad (1.109)\end{aligned}$$

which satisfies the following equations of motion:

$$\begin{aligned}\hbar\frac{\partial\hat{\psi}_{K\uparrow}}{\partial\tau} &= -\left[\frac{1}{2m}\left(-\mathrm{i}\hbar\boldsymbol{\nabla} + \frac{e\mathbf{A}(\mathbf{r})}{c}\right)^2 - \mu\right]\hat{\psi}_{K\uparrow} - g\left\langle\hat{\psi}_\uparrow\hat{\psi}_\downarrow\right\rangle\hat{\psi}^\dagger_{K\downarrow} \\ \hbar\frac{\partial\hat{\psi}^\dagger_{K\downarrow}}{\partial\tau} &= \left[\frac{1}{2m}\left(-\mathrm{i}\hbar\boldsymbol{\nabla} + \frac{e\mathbf{A}(\mathbf{r})}{c}\right)^2 - \mu\right]\hat{\psi}^\dagger_{K\downarrow} - g\left\langle\hat{\psi}^\dagger_\downarrow\hat{\psi}^\dagger_\uparrow\right\rangle\hat{\psi}_{K\uparrow}\ . \quad (1.110)\end{aligned}$$

We are now ready to define the Green's function:

$$G(\mathbf{r}\tau,\mathbf{r}'\tau') = -\left\langle\mathrm{T}_\tau\left[\hat{\psi}_{K\uparrow}(\mathbf{r}\tau)\hat{\psi}^\dagger_{K\uparrow}(\mathbf{r}'\tau')\right]\right\rangle\ , \quad (1.111)$$

where T_τ indicates the time ordered product of the operators.

Deriving with respect to τ, we obtain:

$$\begin{aligned}\hbar\frac{\partial G(\mathbf{r}\tau,\mathbf{r}'\tau')}{\partial\tau} &= -\hbar\delta(\tau-\tau')\delta(\mathbf{r}-\mathbf{r}') \\ &- \left[\frac{1}{2m}\left(-\mathrm{i}\hbar\boldsymbol{\nabla} + \frac{e\mathbf{A}(\mathbf{r})}{c}\right)^2 - \mu\right]G(\mathbf{r}\tau,\mathbf{r}'\tau') \\ &+ g\left\langle\hat{\psi}_\uparrow(\mathbf{r})\hat{\psi}_\downarrow(\mathbf{r})\right\rangle\left\langle\mathrm{T}_\tau\left[\hat{\psi}^\dagger_{K\downarrow}(\mathbf{r}\tau)\hat{\psi}^\dagger_{K\uparrow}(\mathbf{r}'\tau')\right]\right\rangle\ . \quad (1.112)\end{aligned}$$

To simplify this equation, we define an anomalous Green's function:

$$\begin{aligned} F(\mathbf{r}\tau,\mathbf{r}'\tau') &= -\left\langle \mathrm{T}_\tau\left[\hat{\psi}_{K\uparrow}(\mathbf{r}\tau)\hat{\psi}_{K\downarrow}(\mathbf{r}'\tau')\right]\right\rangle \\ F^\dagger(\mathbf{r}\tau,\mathbf{r}'\tau') &= -\left\langle \mathrm{T}_\tau\left[\hat{\psi}^\dagger_{K\downarrow}(\mathbf{r}\tau)\hat{\psi}^\dagger_{K\uparrow}(\mathbf{r}'\tau')\right]\right\rangle , \end{aligned} \tag{1.113}$$

and the gap function:

$$\Delta((\mathbf{r}) = gF(\mathbf{r}\tau^+,\mathbf{r}\tau) = -g\left\langle \hat{\psi}_\uparrow(\mathbf{r})\hat{\psi}_\downarrow(\mathbf{r})\right\rangle . \tag{1.114}$$

With this, Eq. 1.112 can be rewritten as:

$$\left[-\hbar\frac{\partial}{\partial t} - \frac{1}{2m}\left(-\mathrm{i}\hbar\boldsymbol{\nabla} + \frac{e\mathbf{A}(\mathbf{r})}{c}\right)^2 + \mu\right] G(\mathbf{r}\tau,\mathbf{r}'\tau') + \Delta((\mathbf{r})F^\dagger(\mathbf{r}\tau,\mathbf{r}'\tau') = \hbar\delta(\tau-\tau')\delta(\mathbf{r}-\mathbf{r}') . \tag{1.115}$$

If we carry out the same procedure for the anomalous functions defined in Eq. 1.113, we obtain the following set of equations:

$$\begin{aligned} \left[-\hbar\frac{\partial}{\partial t} - \frac{1}{2m}\left(-\mathrm{i}\hbar\boldsymbol{\nabla} + \frac{e\mathbf{A}(\mathbf{r})}{c}\right)^2 + \mu\right] F(\mathbf{r}\tau,\mathbf{r}'\tau') &= \Delta((\mathbf{r})G(\mathbf{r}\tau,\mathbf{r}'\tau') \\ \left[\hbar\frac{\partial}{\partial t} - \frac{1}{2m}\left(\mathrm{i}\hbar\boldsymbol{\nabla} + \frac{e\mathbf{A}(\mathbf{r})}{c}\right)^2 + \mu\right] F^\dagger(\mathbf{r}\tau,\mathbf{r}'\tau') &= \Delta^*((\mathbf{r})G(\mathbf{r}\tau,\mathbf{r}'\tau') . \end{aligned} \tag{1.116}$$

Suppose now that our Hamiltonian does not depend on time, which means our Green's functions are functions of $(\tau-\tau')$. Which allows us to use a Fourier transformation with the Matsubara frequencies:

$$\begin{aligned} G(\mathbf{r}\tau,\mathbf{r}'\tau') &= (\beta\hbar)^{-1}\sum_n e^{-\mathrm{i}\omega_n(\tau-\tau')}G(\mathbf{r},\mathbf{r}',\omega_n) \\ F^\dagger(\mathbf{r}\tau,\mathbf{r}'\tau') &= (\beta\hbar)^{-1}\sum_n e^{-\mathrm{i}\omega_n(\tau-\tau')}F^\dagger(\mathbf{r},\mathbf{r}',\omega_n) , \end{aligned} \tag{1.117}$$

where $\omega_n = (2n+1)\pi/(\beta\hbar)$.

In the same manner, the gap function is given by:

$$\Delta(\mathbf{r}) = \frac{g}{\beta\hbar}\sum_n F^\dagger(\mathbf{r},\mathbf{r}',\omega_n) . \tag{1.118}$$

With these new definitions, the equations of motion for the Green's functions in the new representation are given by:

$$\left[\mathrm{i}\hbar\omega_n - \frac{1}{2m}\left(-\mathrm{i}\hbar\boldsymbol{\nabla} + \frac{e\mathbf{A}(\mathbf{r})}{c}\right)^2 + \mu\right] G(\mathbf{r},\mathbf{r}',\omega_n) + \Delta(\mathbf{r})F^\dagger(\mathbf{r},\mathbf{r},\omega_n) = \hbar\delta(\mathbf{r}-\mathbf{r}')$$
$$\left[-\mathrm{i}\hbar\omega_n - \frac{1}{2m}\left(\mathrm{i}\hbar\boldsymbol{\nabla} + \frac{e\mathbf{A}(\mathbf{r})}{c}\right)^2 + \mu\right] F^\dagger(\mathbf{r},\mathbf{r}',\omega_n) - \Delta^*(\mathbf{r})G(\mathbf{r},\mathbf{r}',\omega_n) = 0\,. \quad (1.119)$$

To proceed, we define the normal state Green's function $G^0(\mathbf{r},\mathbf{r}',\omega_n)$, obtained with $\Delta(\mathbf{r}) = 0$:

$$\left[\mathrm{i}\hbar\omega_n - \frac{1}{2m}\left(-\mathrm{i}\hbar\boldsymbol{\nabla} + \frac{e\mathbf{A}(\mathbf{r})}{c}\right)^2 + \mu\right] G^0(\mathbf{r},\mathbf{r}',\omega_n) = \hbar\delta(\mathbf{r}-\mathbf{r}')\,. \quad (1.120)$$

The definition of the normal state Green's function allows us to rewrite Eqs.1.119 in an integral form. These equations are given by:

$$G(\mathbf{r},\mathbf{r}',\omega_n) = G^0(\mathbf{r},\mathbf{r}',\omega_n) - \hbar^{-1}\int d^3\mathbf{r}_1\, G^0(\mathbf{r},\mathbf{r}_1,\omega_n)\Delta(\mathbf{r}_1)F^\dagger(\mathbf{r}_1,\mathbf{r}',\omega_n)\,, \quad (1.121)$$

and:

$$F^\dagger(\mathbf{r},\mathbf{r}',\omega_n) = \hbar^{-1}\int d^3\mathbf{r}_1\, G^0(\mathbf{r}_1,\mathbf{r},-\omega_n)\Delta^*(\mathbf{r}_1)G(\mathbf{r}_1,\mathbf{r}',\omega_n)\,, \quad (1.122)$$

Finally, substituting Eq. 1.122 on Eq. 1.121 and Eq. 1.121 on Eq. 1.122, we can separate these two equations and obtain one integral equation for the Green's function and another for the anomalous Green's function:

$$\begin{aligned} G(\mathbf{r},\mathbf{r}',\omega_n) &= G^0(\mathbf{r},\mathbf{r}',\omega_n) - \hbar^{-2}\int\int d^3\mathbf{r}_1 d^3\mathbf{r}_2\, G^0(\mathbf{r},\mathbf{r}_1,\omega_n)\Delta(\mathbf{r}_1)G^0(\mathbf{r}_2,\mathbf{r}_1,-\omega_n) \\ &\quad \Delta^*(\mathbf{r}_2)G(\mathbf{r}_2,\mathbf{r}',\omega_n) \\ F^\dagger(\mathbf{r},\mathbf{r}',\omega_n) &= \hbar^{-1}\int d^3\mathbf{r}_1\, G^0(\mathbf{r}_1,\mathbf{r},-\omega_n)\Delta^*(\mathbf{r}_1)G^0(\mathbf{r}_1,\mathbf{r}',\omega_n) \\ &\quad - \hbar^{-2}\int\int d^3\mathbf{r}_1\, d^3\mathbf{r}_2\, G^0(\mathbf{r}_1,\mathbf{r},-\omega_n)\Delta^*(\mathbf{r}_1)G^0(\mathbf{r}_1,\mathbf{r}_2,\omega_n) \\ &\quad \Delta(\mathbf{r}_2)F^\dagger(\mathbf{r}_2,\mathbf{r}',\omega_n)\,. \end{aligned} \quad (1.123)$$

With these equations, we make the first assumption to go to the Ginzburg-Landau limit, which is that the superconducting gap is small. With Eq. 1.123 and this approximation, we can write the gap given in Eq. 1.118, up to third order, as:

$$\begin{aligned}\Delta^*(\mathbf{r}) &= (\beta\hbar^2)^{-1}\sum_n \int d^3\mathbf{r}_1\, G^0(\mathbf{r}_1,\mathbf{r},-\omega_n)G^0(\mathbf{r}_1,\mathbf{r},\omega_n)\Delta^*(\mathbf{r}_1) \\ &- (\beta\hbar^4)\sum_n \int\int\int d^3\mathbf{r}_1\, d^3\mathbf{r}_2 d^3\mathbf{r}_3\, G^0(\mathbf{r}_1,\mathbf{r},-\omega_n)G^0(\mathbf{r}_1,\mathbf{r}_2,\omega_n)G^0(\mathbf{r}_3,\mathbf{r}_2,-\omega_n) \\ &\quad G^0(\mathbf{r}_3,\mathbf{r},\omega_n)\times \\ &\times \Delta^*(\mathbf{r}_1)\Delta(\mathbf{r}_2)\Delta^*(\mathbf{r}_3)\,. \end{aligned} \tag{1.124}$$

To proceed, we need to know the normal state Green's function. As a matter of condensed matter theory, this function is widely known when there is no applied magnetic field in the system. In this case, the Green's function is given by:

$$G^0(\mathbf{r}-\mathbf{r}',\omega_n) = \frac{\hbar}{2\pi^3}\int d^3k \frac{e^{\mathrm{i}\boldsymbol{k}\cdot(\mathbf{r}-\mathbf{r}')}}{\mathrm{i}\hbar\omega_n - \hbar^2k^2/2m}\,. \tag{1.125}$$

The next step is the second assumption to the Ginzburg-Landau limit, which is that the temperature of the system is close to T_c. In this region, the gap function and the vector potential are slow varying functions when compared to the Green's functions. In this scenario, we can write the normal state Green's function in the presence of an applied field as an eikonal expansion of the following form:

$$G^0(\mathbf{r},\mathbf{r}',\omega_n) = e^{\mathrm{i}\phi(\mathbf{r}-\mathbf{r}')}G^0(\mathbf{r}-\mathbf{r}',\omega_n)\,, \tag{1.126}$$

where the phase factor is given by:

$$\phi(\mathbf{r}-\mathbf{r}') = -\frac{e}{2\hbar c}\left[\mathbf{A}(\mathbf{r})+\mathbf{A}(\mathbf{r}')\right]\cdot(\mathbf{r}-\mathbf{r}')\,. \tag{1.127}$$

The final form of the Ginzburg-Landau equation is recovered by applying Eq. 1.126 in Eq. 1.124, solving the sums and the integrals, with the use of a Fourier transformation and the assumption that the Fermi surface is a sphere. After this procedure, the phenomenological constants that appear in the Ginzburg-Landau equations can be expressed in terms of microscopic parameters of the superconductor material as fallows:

$$\begin{aligned}\alpha &= -\frac{6\pi^2T_c^2}{7\zeta(3)\epsilon_F}\left(1-\frac{T}{T_c}\right) \\ \beta &= \frac{6\pi^2T_c^2}{7\zeta(3)\epsilon_F n}\,, \end{aligned} \tag{1.128}$$

where ϵ_F is the Fermi energy and n is the electron density.

1.1.5 Superconductors Described by More than One Condensate

In some materials, where Cooper pair formation occurs in multiple electronic bands, the superconducting state is, phenomenologically, correctly described by more than one order parameter. In this subsection, we discuss some of the characteristic features of such systems. To do so, we focus on the simple case of a superconductor with two condensates. As we are mainly interested in the macroscopic properties of superconductors, such as their vortex matter, we simplify the microscopic properties of the system and simply assume that each condensate relates to an electronic band. With this simplification, hereafter we often refer to the order parameters as being of band 1 or band 2.

The Ginzburg-Landau equations for a two-band superconductor are given by Ref. [24]:

$$-\left(-i\boldsymbol{\nabla}-\mathbf{A}\right)^2\Delta_1+\left(\chi_1-|\Delta_1|^2\right)\Delta_1+\gamma\Delta_2 = 0, \tag{1.129}$$

$$-\frac{D_2}{D_1}\left(-i\boldsymbol{\nabla}-\mathbf{A}\right)^2\Delta_2+\left(\chi_2-|\Delta_2|^2\right)\Delta_2+\frac{n_1}{n_2}\gamma\Delta_1 = 0, \tag{1.130}$$

where Δ_i is the order parameter correspondent to band i, with D_i and n_i being the diffusion coefficient and partial density of states of such band. Given the matrix of coupling constants of our two-band system:

$$\hat{\Lambda}=\begin{pmatrix} n_1\lambda_{11} & n_2\lambda_{12} \\ n_1\lambda_{12} & n_2\lambda_{22}\end{pmatrix}, \tag{1.131}$$

the parameters χ_i in Eq.1.130 are given by:

$$\begin{aligned}\chi_1 &= 1-T+S-\lambda_{22}/n_1\delta \\ \chi_2 &= 1-T+S-\lambda_{11}/n_2\delta,\end{aligned} \tag{1.132}$$

where S is the minimum positive eigenvalue of the matrix $\hat{\Lambda}^{-1}$ and $\delta=\lambda_{11}\lambda_{22}-\lambda_{12}^2$. Finally, the coupling between the two equations is given by $\gamma=\lambda_{12}/n_1\delta$.

To understand the behavior of the solution of Eqs.1.130, we investigate the simple case of homogeneous superconductivity in the absence of external fields. To do this, we choose $\lambda_{11}=2.0$, $\lambda_{22}=1.03$, $\lambda_{12}=0.005$, $n_1=0.355$. The dependence of the order parameter with temperature is shown in Fig. 7 for the first band (blue curve) and second band (red curve). For this set of microscopic parameters, the second band is active up to $T_{c2}=0.9T_c$ and remains superconducting for $T>T_{c2}$ exclusively due to the coupling with the first band. Here, we should note that the Ginzburg-Landau theory is only valid very near T_c, in a region where the system effectively behaves as a single-band superconductor. In order to investigate the interplay between two active order parameters (an order parameter is considered active if its critical temperature is higher than the system

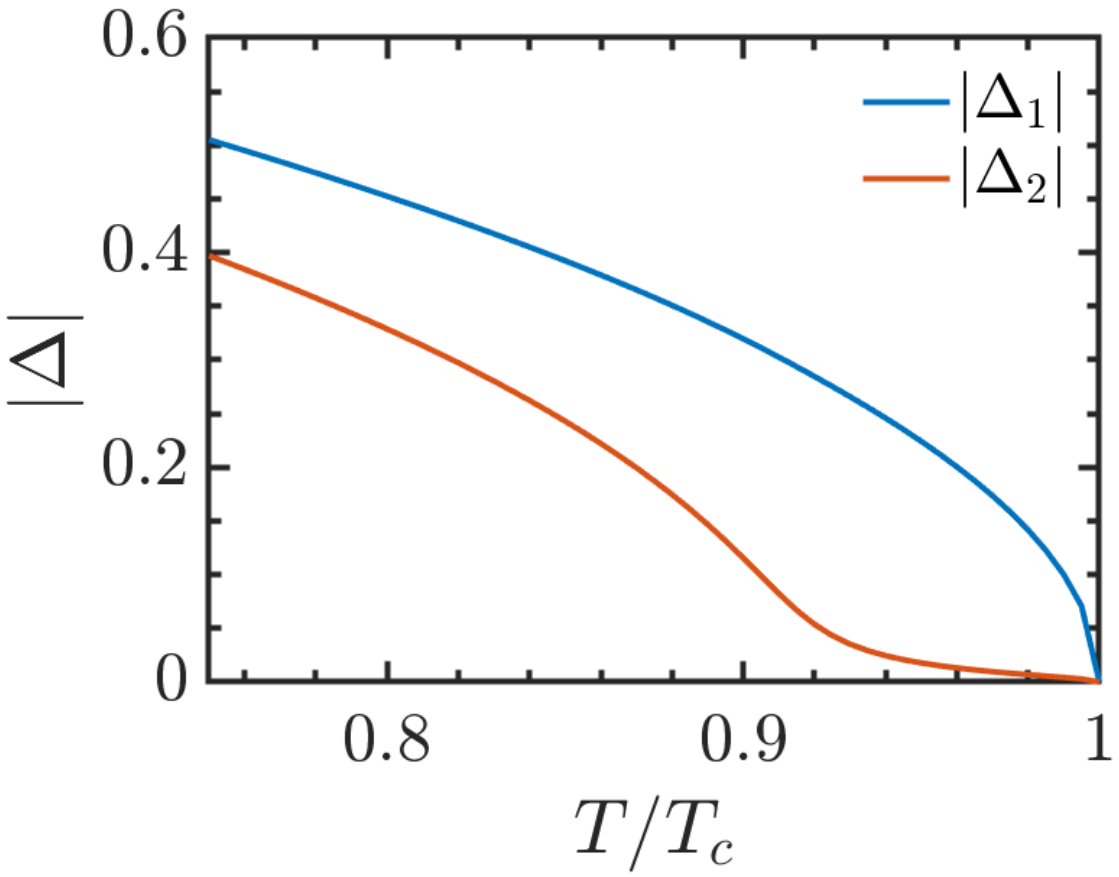

Figure 7 – *Equilibrium order parameter as a function of temperature for the first band (blue curve) and second band (red curve). Here,* $\lambda_{11} = 2.0$, $\lambda_{22} = 1.03$, $\lambda_{12} = 0.005$ *and* $n_1 = 0.355$. *Curves were obtained through the numerical solution of Eqs.1.130.*

temperature) and the interesting physical phenomena that emerge from it, we push the theory to lower temperatures. Though not mathematically precise, it has been shown by comparison with microscopic theory that this gives correct physical results [25].

Let us now introduce the external magnetic field in our analysis and investigate the behavior of a vortex in this two-band system. To do this, we introduce the supercurrent density and the Ampère law:

$$\begin{aligned} &\mathbf{J}_s - \kappa_1^2 \boldsymbol{\nabla} \times \mathbf{h} = 0 \\ &\mathbf{J}_s = \sum_{j=1}^{2} \frac{n_j}{n_1} \frac{D_j}{D_1} \mathrm{Re}\left[\Delta_j^* \left(-\mathrm{i}\boldsymbol{\nabla} - \mathbf{A}\right) \Delta_j\right], \end{aligned} \tag{1.133}$$

where κ_1 is the Ginzburg-Landau parameter of the first band.

Fig.8 shows the order parameters of both bands for a system with one vortex and D_1/D_2 and $T = 0.8T_c$. We can note that the coherence length of the second condensate is

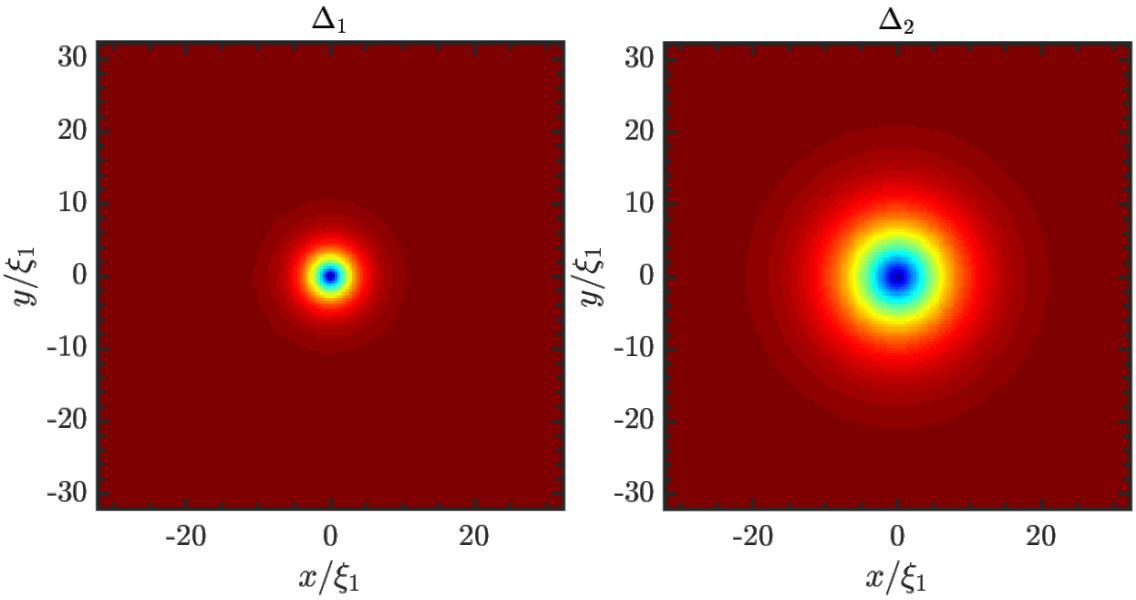

Figure 8 *– Color plot of the order parameter of the first (left panel) and second (right panel) bands for a superconductor carrying one vortex. Here,* $D_1/D_2 = 0.25$.

larger. This occurs for two reasons. First, as can be seen from Eqs. 1.130, ξ_2 increases as the ratio D_1/D_2 decreases. Second, since the second band is the weaker one in our system, our working temperature is closer to the critical temperature above which it becomes passive, which increases its coherence length [26].

Having seen how the order parameters behave in a system with a vortex, we now proceed to show how fluxoid quantization occurs in this case. From the expression for the supercurrent density in Eq. 1.133, we have:

$$\begin{aligned}\mathbf{J}_s = &- \mathrm{i}\left(\Delta_1^*\boldsymbol{\nabla}\Delta_1 - \Delta_1\boldsymbol{\nabla}\Delta_1^*\right) - 2\mathbf{A}|\Delta_1|^2 \\ &- \mathrm{i}\frac{n_2D_2}{n_1D_1}\left(\Delta_2^*\boldsymbol{\nabla}\Delta_2 - \Delta_2\boldsymbol{\nabla}\Delta_2^*\right) - 2\frac{n_2D_2}{n_1D_1}\mathbf{A}|\Delta_2|^2.\end{aligned} \tag{1.134}$$

Substituting $\Delta_1 = a_1e^{\mathrm{i}\theta_1}$ and $\Delta_1 = a_1e^{\mathrm{i}\theta_1}$, we have:

$$\mathbf{J}_s = 2a_1^2\boldsymbol{\nabla}\theta_1 - 2a_1^2\mathbf{A} - 2a_2^2\frac{n_2D_2}{n_1D_1}\boldsymbol{\nabla}\theta_2 - 2a_2^2\mathbf{A}\frac{n_2D_2}{n_1D_1}. \tag{1.135}$$

If we now integrate both sides of Eqs. 1.135 along a closed path far enough from the vortex core where the system is in the Meissner state and $\mathbf{J}_s = 0$, we have:

$$\left(a_1^2 + a_2^2\frac{n_2D_2}{n_1D_1}\right)\Phi = 2\pi\left(n_1a_1^2 + n_2a_2^2\frac{n_2D_2}{n_1D_1}\right), \tag{1.136}$$

where $\Phi = \oint \mathbf{A}\cdot\mathbf{ds}$ and, due to the uniqueness of the order parameter, $\oint \boldsymbol{\nabla}\theta_i = 2n_i\pi$. For the case where the vorticity is the same for both bands ($n_1 = n_2 = n$), it is easy to

see that the magnetic flux is quantized as $\Phi = 2n\pi$. In natural units, this is the common expression $\Phi = n\Phi_0$.

From Eq. 1.136 it is useful to define the fraction of flux produced by the supercurrents in each band, that can be given by:

$$\begin{aligned} \Phi_1 &= \frac{2\pi a_1^2}{a_1^2 + a_2^2 n_2 D_2/(n_1 D_1)} \\ \Phi_2 &= \frac{2\pi a_2^2 n_2 D_2/(n_1 D_1)}{a_1^2 + a_2^2 n_2 D_2/(n_1 D_1)}. \end{aligned} \tag{1.137}$$

One interesting possibility that arises from these equations is the scenario of $n_1 \neq n_2$, which means the emergence of a vortex carrying a fraction of the flux quanta. Such configurations are known as fractional vortices, in opposition to composite vortices, with $n_1 = n_2$. Though mathematically possible, it has been shown that such states are energetically forbidden in bulk superconductors, but can be stabilized near the edges of superconducting samples. As we will discuss later, the application of a current can separate a composite vortex into two fractional vortices, coupled through a phase soliton.

1.1.6 *d*-wave Superconductor

In later chapters, we are also interested in describing the physics of superconducting materials with *d*-wave pairing symmetry. In such systems, the Ginzburg-Landau equations must be altered accordingly.

Unfortunately, due to symmetry, it is not possible to obtain these equations for a system with only a *d*-wave order parameter [27]. Instead, one must consider also the existence of a *s*-wave component, *i.e.*, the system is described by two order parameters, one with *s*-wave symmetry and another with *d*-wave symmetry.

The derivation of the Ginzburg-Landau equations in this case follows the same steps we have outlined for the *s*-wave case, with the difference that the attractive interaction potential between the electrons is now spatial dependent. Following the calculation developed by Ren *et. al.* [27], the Ginzburg-Landau free energy, for $d_{x^2-y^2}$ superconductors is given by:

$$\begin{aligned} F &= -2\alpha_s|\Delta_s|^2 - |\Delta_d|^2 + \frac{4}{3}|\Delta_s|^4 + \frac{1}{2}|\Delta_d|^4 \\ &\quad + \frac{8}{3}|\Delta_s|^2|\Delta_d|^2 + \frac{2}{3}(\Delta_s^{*2}\Delta_d^2 + H.c.) \\ &\quad + 2|\mathbf{\Pi}\Delta_s^*|^2 + |\mathbf{\Pi}\Delta_d^*|^2 + (\Pi_x\Delta_s^*\Pi_x^*\Delta_d \\ &\quad - \Pi_y\Delta_s^*\Pi_y^*\Delta_d + H.c.)\ , \end{aligned} \tag{1.138}$$

where α_s determines the relative strength between the s and d-wave components. We have introduced the operator $\mathbf{\Pi} = (\mathrm{i}\boldsymbol{\nabla} - \mathbf{A})$ to facilitate our notation, Δ_s and Δ_d are the s and d-wave components of the order parameter, respectively. The free energy is given here in dimensionless units such that the order parameters are in units of $\Delta_0 = \sqrt{(4/3W)\ln(T_d/T)}$; lengths in units of the coherence length $\xi = (\nu_F/2)\sqrt{W/\ln(T_d/T)}$, where ν_F is the Fermi velocity and $W = 7\xi(3)/(8\pi^2T^2)$; the magnetic field in units of H_{c2}.

To obtain the Ginzburg-Landau equations for each component of the order parameter, we need to minimize Eq. 1.138 with respect to the two components. Minimizing it with respect to Δ_s, we have:

$$\begin{aligned} &-\alpha_s\Delta_s + \frac{4}{3}|\Delta_s|^2\Delta_s + \frac{4}{3}|\Delta_d|^2\Delta_s + \frac{2}{3}\Delta_d^2\Delta_1^* \\ &+\Pi^{*2}\Delta_s + \frac{1}{2}(\Pi_x^{*2} - \Pi_y^{*2})\Delta_d = 0 \,, \end{aligned} \tag{1.139}$$

and minimizing it with respect to Δ_d, we obtain:

$$\begin{aligned} &-\Delta_d + |\Delta_d|^2\Delta_d + \frac{8}{3}|\Delta_s|^2\Delta_d + \frac{4}{3}\Delta_s^2\Delta_d^* \\ &+\Pi^{*2}\Delta_d + (\Pi_x^{*2} - \Pi_y^{*2})\Delta_s = 0 \,. \end{aligned} \tag{1.140}$$

In a rapid analysis of Eqs. 1.139 and 1.140, we can see that the solutions to such equations are no longer rotational invariant, as one would expect for a $d_{x^2-y^2}$ material. Choosing α_s such that the s component plays a small role in the dynamics of the system allows us to study superconductors with a $d_{x^2-y^2}$ pairing.

1.2 Thesis Outline

Having introduced the basics and most important theoretical topics for our discussions, we start to present the results of this thesis in the following chapters.

In **Chapter 2** we begin our investigations treating the magnetic response of type I mesoscopic superconductors. More precisely, we revisit the old problem of how the presence of an insulator/superconducting surface affects the classification of superconducting materials between type I and II. By considering systems with small volume-to-area ratio, we show that the Tinkham–de Gennes scenario is extended in the case of a mesoscopic type-I superconductor. Namely, we find additional features of the transition at the passage from the *genuine* to the *intermediate* type I. The latter has two distinct transitions, from a paramagnetic to diamagnetic response in descending field, and a *quasi*-type-II behavior as the critical coupling $1/\sqrt{2}$ is approached in ascending field. The findings reported in this chapter have been published in Ref. [28].

In **Chapter 3** we start considering the behavior of the vortex matter in the presence of a transport current. By solving the TDGL equations in a three-dimensional superconducting film, we show that, above a certain critical thickness, the dynamics of vortex-antivortex annihilation produces a closed vortex loop. This occurs because the vortices and the antivortices become curved before they annihilate each other. As they approach the center of the sample, their ends combine, producing a single closed vortex. We also determine the critical values of the thickness for which the closed vortex sets in for different values of the Ginzburg-Landau parameter and propose a model of how to detect a closed vortex experimentally. The findings reported in this chapter have been published in Ref. [29].

In **Chapter 4**, continuing our investigation on the vortex matter response to an applied current, we study the superconducting diode. More specifically, we propose a superconducting diode device comprising a central superconducting film flanked by two wires carrying an applied dc bias, suitably chosen so as to generate different asymmetric field profiles. Through the numerical solution of the TDGL equations, we show that this design is capable of efficiently breaking the reciprocity of the critical current in the central superconductor, thus promoting the diode effect in response to an applied ac. We also conduct a series of simulations to determine the conditions that facilitate the entrance of vortices and antivortices in a given polarity of the applied ac and impede their entrance in the other polarity and show that our device can behave as a superconducting half-wave rectifier, with diode efficiencies surpassing 70%. The findings reported in this chapter have been published in Ref. [30].

In **Chapter 5** we switch our focus to the study of superconducting system described by more than one order parameter. Here, we investigate the transitions between states with different winding number in two-band superconducting rings. Starting from the Ginzburg-Landau theory of a two-component superconductor, we apply linear stability theory to develop a semianalytical method that provides the critical flux for phase-slip occurrence. We then applied the developed method to investigate how the critical flux depends on physical properties, such as band parameters and temperature. In a second moment, we numerically solve the TDGL equations to study the possibility of a soliton state in our system, where the winding number of each condensate is not the same. The findings reported in this chapter have been published in Ref. [31].

In **Chapter 6** we focus on the study of the vortex matter in twisted bilayers composed of d-wave superconductors. As it was recently shown, a chiral topological phase emerges from the coupling of two twisted monolayers of superconducting Bi2Sr2CaCu2O8+δ for certain twist angles. In this chapter, we investigate how the vortex matter depends on the twist angle, showing the emergence of two skyrmionic states that characterize the chiral topological phase and argue that the distinct signatures of

their magnetic field profile can be used as a smoking gun for the experimental detection of topological states in such structures. The findings reported in this chapter have been published in Ref. [32].

Finally, in **Chapter 7** we present our concluding remarks and the outlook for future studies.

In **Appendix A** we describe in detail the numerical procedure for the solution of the Ginzburg-Landau equations for superconducting systems under different physical conditions.

2 The Intermediate type I superconductor

2.1 Introduction

So far, we have treated the properties of superconductors in a bulk system, where we have seen that superconducting materials can be divided in two groups, depending on their response to an applied magnetic field. If we consider a more real scenario, where the system under consideration has boundary surfaces, new physics emerge. Specifically, we found a new critical field for the nucleation of superconductivity near the surfaces.

For example, with the help of a variational procedure, it can be shown that, in a superconductor with an infinite plane surface, superconductivity nucleates first at the boundary in a critical field $H_{c3} = 1.695H_{c2}$. This means that, between H_{c3} and H_{c2}, superconductivity exists only near the surface, with the order parameter being null at its interior, bulk superconductivity only existing below H_{c2}.

This renders a particularly interesting consequence to type I superconductor. As we have seen, for materials with $\kappa < 1/\sqrt{2}$, we have $H_{c2} < H_c$, which means that, although superconductivity exists in an ascending field up to H_c, if the field is decreased, with the system at the normal state, superconductivity can only be nucleated at the lower field H_{c2}, which is known as supercooling.

In the presence of a surface, the scenario changes, once the supercooling is now governed by H_{c3} and no longer H_{c2}. For the plane surface discussed above, for example, $H_{c3} < H_c$ for $\kappa_c < 0.417$. Hereafter, we call this a *genuine* type I behavior, once it continues to present supercooling in a descending field. On the other hand, for $\kappa_c < \kappa < 1/\sqrt{2}$, we have the peculiar situation where $H_{c2} < H_c < H_{c3}$, which means that the system is still type I, in the sense that it continues to not allow vortices, but now it no longer presents supercooling. We refer to this as an *intermediate* type I behavior.

Although the value of κ_c depends on the geometry of the system, the transition described above reflects a pure intrinsic property of superconductors, once there will always be a κ_c for a given geometry. Experimental [33, 34, 35, 36] and theoretical [37, 38] work have been carried out in this matter, but, once the majority of superconducting materials that attracted practical interest in the last years are of type II, this question was somewhat relegated. Despite of that, some superconducting alloys have been found to, surprisingly, display type I behavior. As examples, we can name $TaSi_2$ [39], the heavily boron-doped silicon carbide [40], $YbSb_2$ [41], $YNiSi_3$ and $LuNiSi_3$ [42]. In addition, since the coherence length varies with disorder, we can control the value of κ with doping.

These new findings make it worth for us to revisit the problem of *genuine-intermediate*

transition in type I superconductors. In what follows, we study this transition in mesoscopic superconducting system, where the surface-to-volume ratio is larger, which enhances the importance of the boundaries and thus contributes to the physics responsible for the transition in question. As we will see, in the mesoscopic limit, the *intermediate* type I behavior is divided in different phases, with κ_c giving place to three different values κ_{c1}, κ_{c2} and κ_{c3}. For $\kappa < \kappa_{c1}$, the system shows the *genuine* type I behavior *i.e.* in ascending field, it goes directly from the Meissner to the normal state and, reversely, in descending field it goes from the normal to the Meissner state, with no vortices being stable at the system in any branch of field sweep. In the $\kappa_{c1} < \kappa < \kappa_{c2}$ region the behavior remains the same in the ascending field branch, but the system now supports the existence of vortices when the field is being decreased. In this region, the obtained magnetization response is always diamagnetic. For $\kappa_{c2} < \kappa < \kappa_{c3}$, the system behaves in the same manner as for the last region, but now, in the descending field branch, the magnetization switch from diamagnetic to paramagnetic regions. Finally, for $\kappa > \kappa_{c3}$, the behavior of the system dramatically changes also in the ascending field branch, which no longer is characterized by direct transition of the Meissner to the normal state. Instead, the system behavior is marked by a substantial magnetization drop and the penetration of giant vortices [43, 44] *i.e.* vortices with a vorticity larger than 1. We classified this behavior as *quasi*-type II, once vortices are able to penetrate, but not as in the mixed state characteristic of type II superconductors.

Here, it is important to emphasize that the existence of the different phases described above is a direct consequence of the Ginzburg-Landau equations for systems with mesoscopic dimensions, not depending on the system geometry. For instance, the transitions discussed in the following must not be confused with the type I/type II crossover that emerges from changing the thickness of a thin film [45, 46, 47]. Moreover, the phases discussed in the present Chapter are obtained from the standard Ginzburg-Landau theory, and therefore must not be confused with the intertype superconductivity obtained from next order corrections of the GL model.

To facilitate our analysis, let us define some important fields. First, at the ascending field branch, we define H_c', where the magnetization curve $(-M)$ reaches its maximum value and H_c'', where the the magnetization vanishes and the system goes to the normal state. For $\kappa < \kappa_{c3}$, H_c' and H_c'' are close to each other, once the Meissner state is followed by the normal state. For $\kappa > \kappa_{c3}$, the difference between the two fields becomes increasingly larger, once a region with the presence of giant vortices arises. It is important to note that both of these fields are larger than H_c, which means the superconducting state in these regions is metastable *i.e.* displays a Gibbs free energy higher than the normal state one. The final notable field, H_{c3}, is defined in the descending branch and it marks the field at which superconductivity first nucleates and the system leaves the normal state.

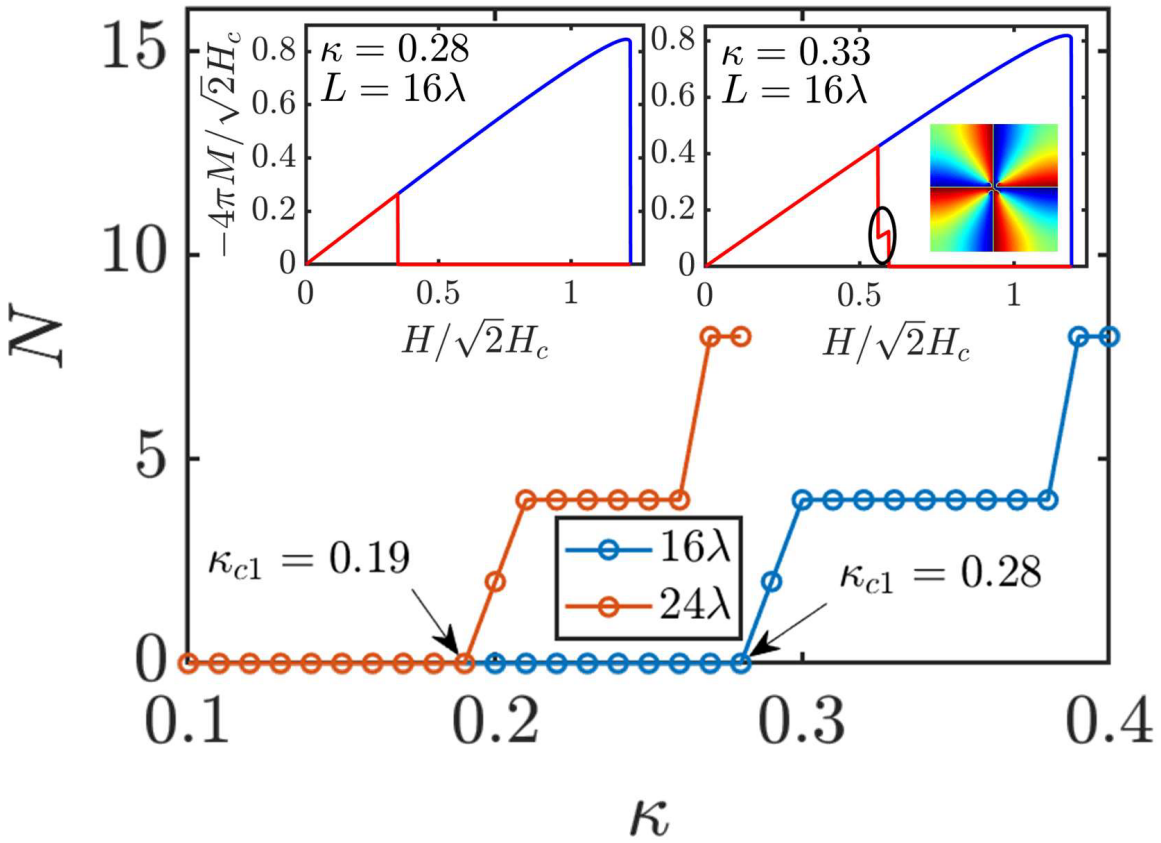

Figure 1 – *The vorticity N of the system at the field which superconductivity is first nucleated in descending field branch, H_{c3}, as a function of κ. The vorticity is displayed for $L = 16\lambda$ (blue curve) and $L = 24\lambda$ (orange curve). The insets show typical magnetization curves for $\kappa < \kappa_{c1}$ (left inset) and $\kappa > \kappa_{c1}$ (right inset). In the insets, blue and red curves represent the ascending and descending field branches, respectively. The black ellipse highlight the region where a vortex is trapped in the system.*

Our results show that the above defined fields and, consequently, the response of the system to an external field is strongly dependent of the value of κ. Our numerical analysis shows that the *genuine-intermediate* transitions in the mesoscopic scale occur for $\kappa_{c1} < \kappa_c$, with the *quasi* type II behavior starting for $\kappa < 1/\sqrt{2}$. Interestingly, we have obtained that, as the volume increases and approaches a bulk behavior, κ_{c2} asymptotically approaches κ_c. However, we have found no evidence that this result is more than just an interesting coincidence.

2.2 Theoretical Formalism

The results here presented were obtained through the numerical solution of the Ginzburg-Landau equations:

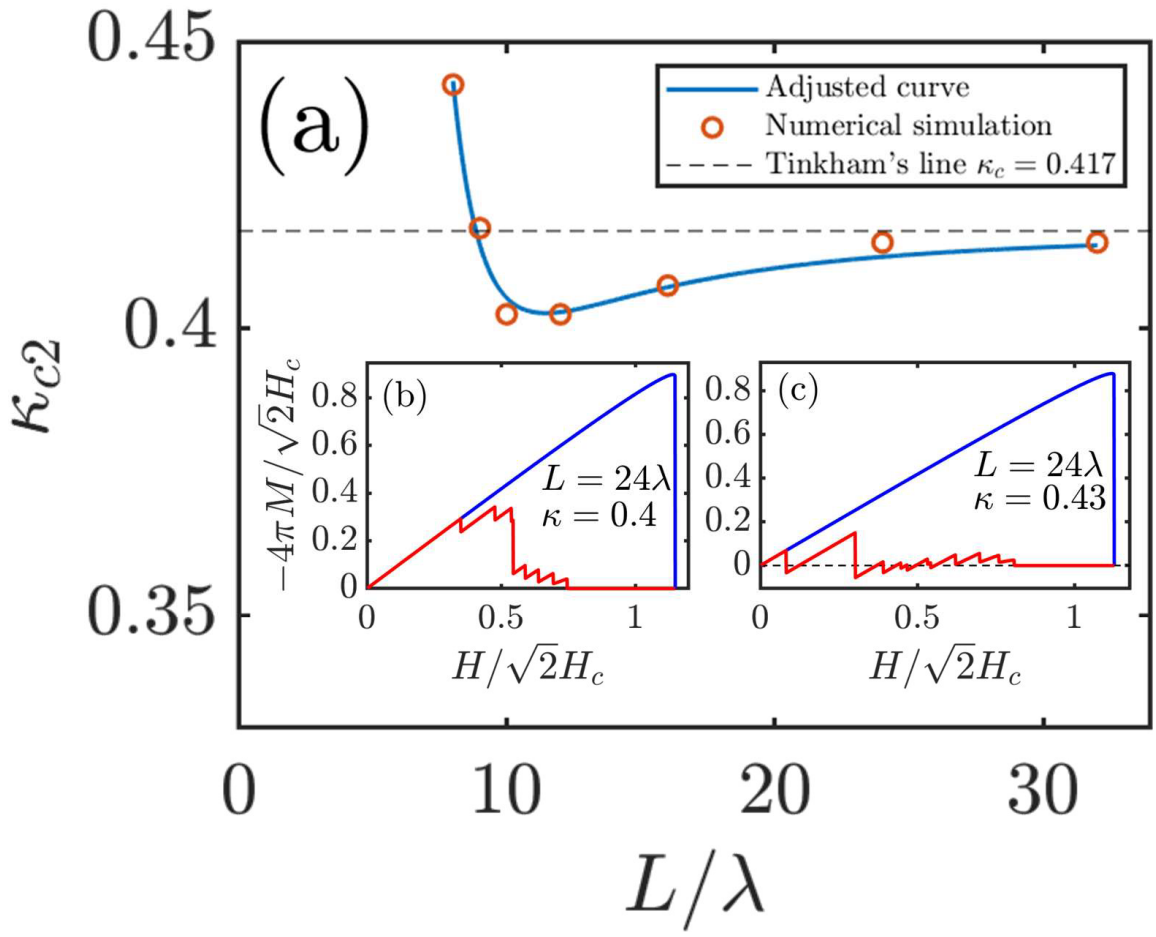

Figure 2 – *The value of κ_{c2} as a function of L. The red circles are the critical values obtained through the numerical simulations, the solid blue line gives an adjusted curve for the obtained data and the dashed black line represents the value of κ_c. Inset a) shows an example of a solely diamagnetic response obtained for $\kappa_{c1} < \kappa < \kappa_{c2}$, while inset b) exemplifies the behavior for $\kappa_{c2} < \kappa < \kappa_{c3}$.*

$$-\psi + |\psi|^2\psi + \left(-\frac{\mathrm{i}}{\kappa}\boldsymbol{\nabla} - \boldsymbol{A}\right)^2 \psi = 0$$
$$\boldsymbol{\nabla} \times \boldsymbol{h} = \boldsymbol{J}_s \,, \tag{2.1}$$

where the supercurrent is given by:

$$\boldsymbol{J}_s = \mathrm{Re}\left[\psi^* \left(-\frac{\mathrm{i}}{\kappa}\boldsymbol{\nabla} - \boldsymbol{A}\right)\psi\right] \,. \tag{2.2}$$

In these equations, lengths are units of the penetration length λ, magnetic fields in units of $\sqrt{2}H_c$ and the vector potential in units of $\sqrt{2}\lambda H_c$. Our simulations were carried in a long superconducting needle with square cross section L^2. The needle is constructed such that the top and bottom surfaces are very distant and play no role in this physics of the problem. In such manner, we can treat our system as effectively two-dimensional.

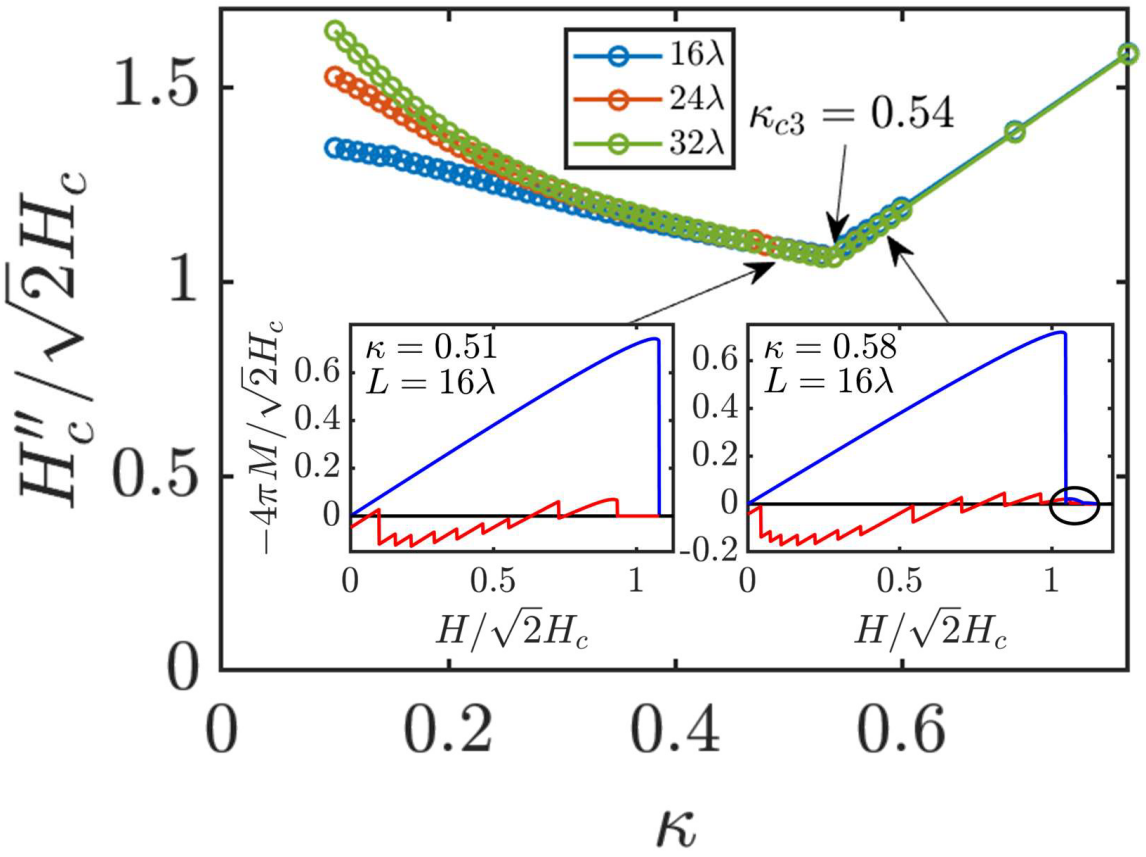

Figure 3 – *The field H_c'' as a function of κ for $L = 16\lambda$ (blue curve), $L = 24\lambda$ (red curve) and $L = 32\lambda$ (green curve). The left and right insets show typical system behavior for κ lower and higher than κ_{c3}, respectively.*

As boundary conditions, we impose that no current leaves the system and that the local magnetic field is equal to the applied field at the boundaries of the system. To study how the behavior of the system changes with system size, we simulate squares with $L = \rho\lambda$, with $\rho = 8$, 12, 16, 24 and 32. For every L, we have varied κ in steps of $\Delta\kappa = 0.01$, from $\kappa = 0.125$ to 0.8. In each case, the field was swept from zero up to the normal state at steps $\Delta H = 0.001$ and then swept back to zero. For details of the numerical method, see Chapter 2.

2.3 Results and Discussion

Let us start discussing the transition occurring at κ_{c1}. Fig. 1 shows the vorticity of the system calculated at H_{c3} as a function of κ for two values of L. As defined above, in the *genuine* type I behavior, the system goes from the normal to the Meissner state directly, therefore, the vorticity at the nucleation field H_{c3} must be zero. For an *intermediate* type I superconductor, however, vortices are trapped in the system in the moment superconductivity is recovered, rendering a non-zero N. As shown in Fig. 1, this criteria gives $\kappa_{c1} = 0.28$ for $L = 16\lambda$ and $\kappa_{c1} = 0.19$ for $L = 24\lambda$.

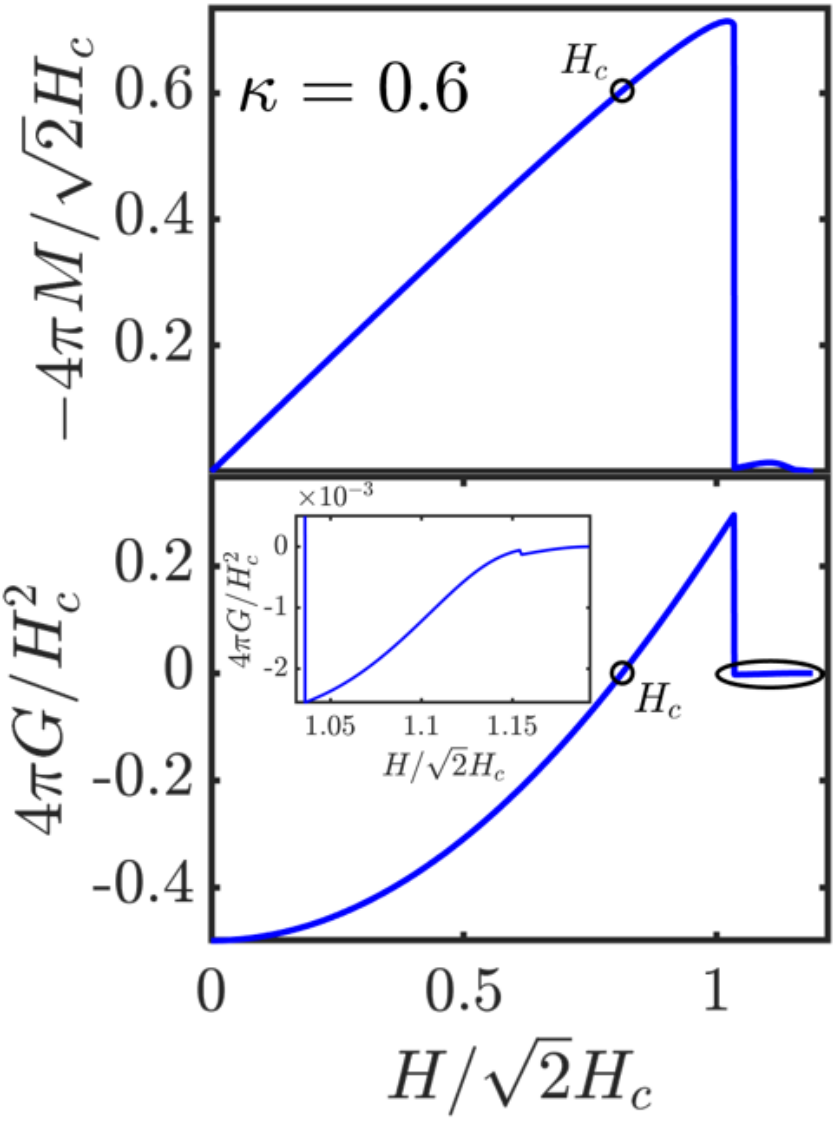

Figure 4 – *The upper panel shows the magnetization curve for $L = 16\lambda$ and $\kappa = 0.6$. The lower panel show the Gibbs free energy of the same system, as a function of the applied field. The inset in the lower panel shows the region highlighted by the black ellipse. In both panels, we denote the thermodynamic field H_c with a black circle.*

In the insets of Fig. 1, we show the magnetization curves exemplifying these two kinds of behavior. In these insets, blue and red curves give us the magnetization for the ascending and descending branches, respectively. The left inset depicts the *genuine* case, where the Meissner state is immediately recovered. In the right inset, on the other hand, we can see an example of *intermediate behavior*, with a giant vortex being trapped in the system, which leaves a characteristic mark in the magnetization curve, as highlighted by the black ellipse. The color plot inside the right insight shows the phase of the order parameter for the trapped vortex.

Fig. 2 shows how κ_{c2} changes with L. The insets mark the difference in behavior for

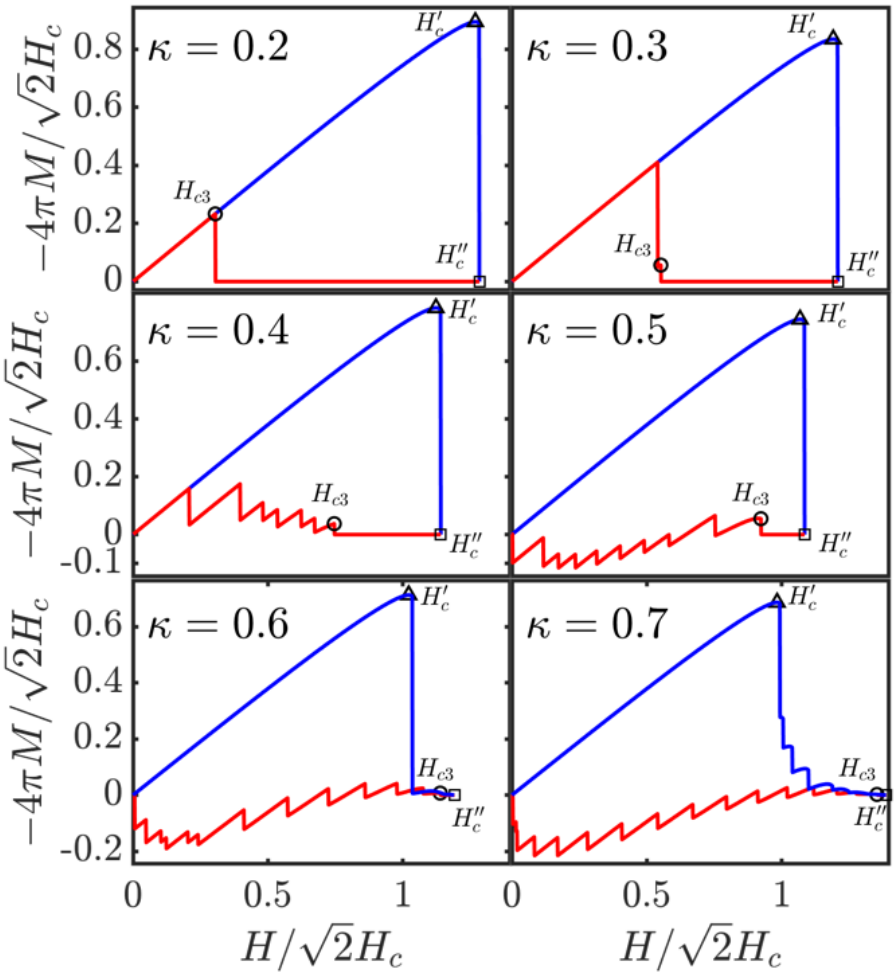

Figure 5 – *Magnetization curves for $L = 16\lambda$, with κ ranging from 0.2 to 0.7. The fields H'_c, H''_c and H_{c3} are denoted by the black triangle, square and circle, respectively.*

κ's below and above this value. As we can see in panel (b), which shows the magnetization curve for a typical case where $\kappa < \kappa_{c2}$. In such scenario, in the descending field branch, vortices are trapped inside the system when superconductivity is restored. As the field is adiabatically decreased, the vortices are gradually expelled from the superconductor, with each magnetization step marking the exit of one or more vortices. Throughout the whole process, the magnetic response of the system remains diamagnetic. For $\kappa > \kappa_{c2}$, on the other hand, at certain field ranges, the magnetic response becomes paramagnetic, as we can see in inset (c). This occurs because a high number of vortices remain trapped in the system for much lower fields. It is interesting to note that κ_{c2} presents a non-monotonic behavior with increasing L and, as mentioned before, asymptotically approaches $\kappa_c = 0.417$ for large L.

The transition to the *quasi*-type II behavior is exemplified in Fig. 3, where we show the field H''_c as a function of κ for three different values of L. As we can see, for $\kappa < \kappa_{c3}$, H''_c gradually decreases as the value of κ is increased. On the other hand, there

is a clear and sharp change of behavior at κ_{c3} above which H_c'' begins to increase with κ. This reflects the fact that, for $\kappa > \kappa_{c3}$, vortices emerge in the ascending branch of the field, which prolongs the existence of superconductivity, thus increasing the value of H_c''. The left inset in Fig. 3 shows an example of a magnetization curve before κ_{c3}, where the normal state sets in almost immediately after the system reaches the peak in magnetization at the ascending branch. Conversely, the right inset shows an example of *quasi*-type II behavior, where, after the magnetization peak, the system does not transit to the normal state, but instead, a vortex phase is encountered. This vortex phase is highlighted in the black ellipse in the inset.

As stated previously, the field H_c', which signals the peak in magnetization, occurs in a metastable energy. This can be better visualised in Fig. 4, where we show the magnetization curve (upper panel) as well as the Gibbs free energy (lower panel) for $L = 16\lambda$ and $\kappa = 0.6$. The field H_c at which the Meissner and normal states have the same energy is indicated with a black circle. As one can see, the peak of the magnetization occurs in a region with positive free energy, thus being metastable, whereas the vortex state displays a negative free energy, as shown in the inset. Contrary to this, the vortex phase found for $\kappa > \kappa_{c3}$ in the ascending branch displays a lower energy than the normal state, thus being energetically stable. For the true type II behavior case, all states are in the stable region, including the field H_c'.

The precise transition from *quasi*-type II to pure type II behavior is not our goal here, but we have verified that *quasi*-type behavior is still encountered for κ's as high as 0.8. As can be seen from Fig. 3, $\kappa_{c3} = 0.54$ is the same for all system sizes presented in the figure. In fact, for all values L investigated, we have obtained the same value for the transition. We then conclude that κ_{c3} does not depend on the size of the superconductor.

A compilation of all the physical behaviors describe above can be seen in Fig. 5, where we show magnetization curves for $L = 16\lambda$, with κ values from 0.2 to 0.7. $\kappa = 0.2$ presents the *genuine* type I behavior, where vortices are not stable for both the ascending and descending branches of the field. For $\kappa = 0.3$, we see the beginning of the *intermediate* type I behavior, where vortices can be found in the descending branch. Once we have $\kappa \approx \kappa_{c1}$ in this case, the vortex can be found only in a small region of applied field and its signature in the magnetization curve is small. On the other hand, for $\kappa = 0.4$ we can see that vortices are present for a much larger portion of the descending field branch. Once $\kappa = 0.4 < \kappa_{c2}$, our system displays a totally diamagnetic response. This changes for $\kappa = 0.5 > \kappa_{c2}$, where we now have regions of field where the magnetization response is paramagnetic. The *quasi*-type II behavior is exemplified for $\kappa = 0.6$, where we now have a vortex phase also in the ascending branch. This vortex phase becomes more visible for $\kappa = 0.7$, where its signature in the magnetization curve is much more pronounced.

In Fig. 6, we show the $\kappa - L$ phase diagram displaying the transitions described

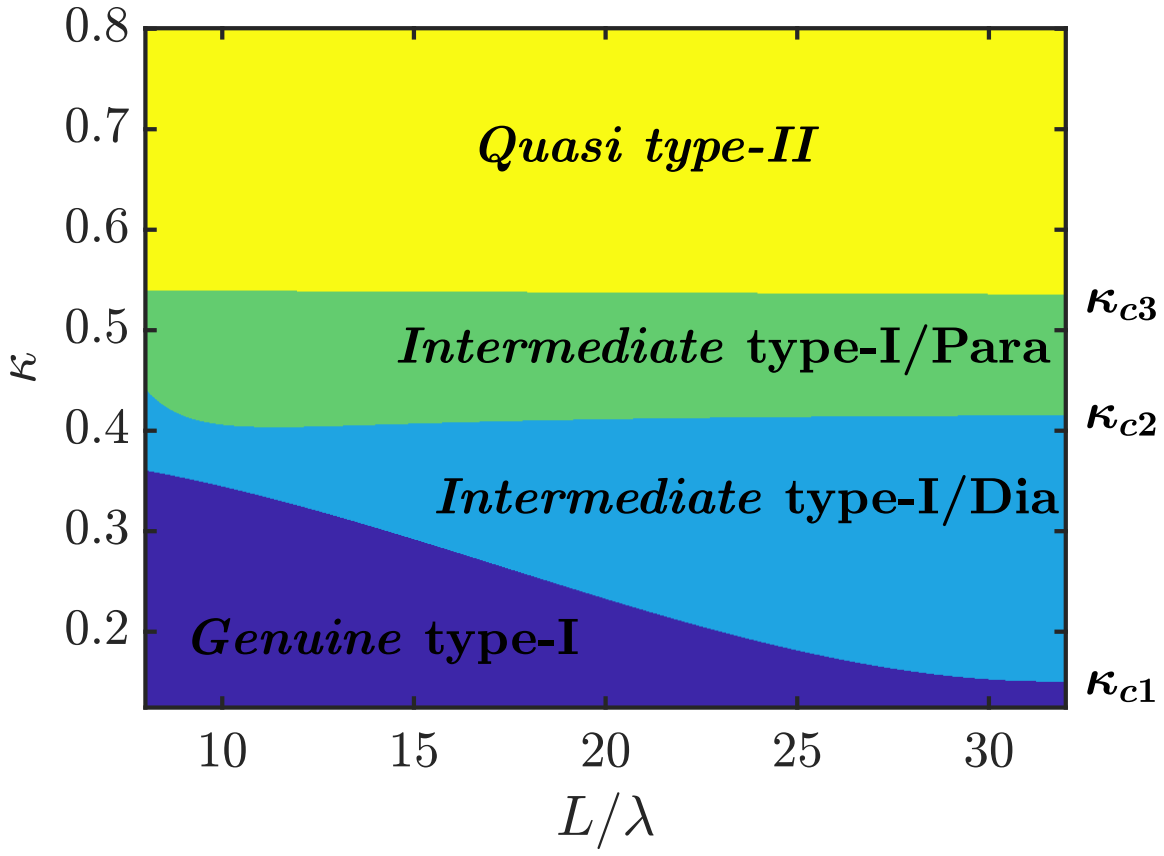

Figure 6 – *$\kappa - L$ phase diagram for the three transitions discussed above. Each color represent a different type of behavior presented by the system. The limiting curves were obtained by the adjusting the critical values of κ found in the simulations.*

above. Each limiting $\kappa_{ci}(L)$ curve was obtained through a numerical adjustment on the critical values obtained in the simulations. The purple region corresponds to the *genuine* type I behavior, for $\kappa < \kappa_{c1}(L)$. The blue region, which we have denominated *intermediate* diamagnetic type I behavior, corresponds to $\kappa_{c1}(L) < \kappa < \kappa_{c2}(L)$. In the green region, the *intermediate* paramagnetic type I behavior, with $\kappa_{c2}(L) < \kappa < \kappa_{c3}(L)$ Finally, the yellow region shows the *quasi*-type II behavior, for $\kappa_{c3}(L)$. As we can see, for certain values of κ, we can transit from one behavior to another by varying the size of our system. Also, by doping the superconductor with impurities, we can change its κ value and then obtain different magnetic behaviors for the same L.

2.4 Concluding Remarks

As we have seen, mesoscopic superconductors are a particularly suitable candidate for the study of the *genuine-intermediate* type I transition, once it introduces new layers to its physics. We emphasize that such transitions arise already in the standard level of the Ginzburg-Landau theory and are not related to the intermediate type of superconductors

which appear when one takes into account the next terms in the Ginzburg-Landau expansion of the superconducting free energy [48, 49]. Also, although the physics presented here depends on the geometry of the samples, as it is the case of other transitions reported in the literature [45, 46, 47], the *genuine-intermediate* type I transition is an intrinsic property of the materials, once it occurs for other geometries [50].

3 Closed Vortex in a Superconducting Film

3.1 Introduction

The existence of flux quantization in the so called Shubnikov phase of superconducting materials is one of the most interesting phenomena in condensed matter physics. Bulk type-II superconductors allow the penetration of magnetic flux in quantized units of $\Phi_0 = hc/2e$. such objects are known as magnetic vortices. Such vortices attract a great amount of attention due to their many possible applications, ranging from single-photon detectors to quantum information systems. In addition, once vortex motion leads to heat dissipation, the detailed knowledge of how vortices behave under different circumstances is of fundamental importance to the optimization of various superconducting based electronic devices.

From a theoretical point of view, as we have seen in previous chapters, the order parameter goes to zero at vortex core and its phase changes by a multiple of 2π when circulated around a given closed loop that encloses the vortex core. In a three-dimensional sample, the core extends over a line, which tends to be aligned with the applied magnetic field, with supercurrents circulating around this line. Hereafter, we refer this typical vortex as an Abrikosov vortex [51].

In the case of vortices induced by an applied current, though, the circularly shaped magnetic self-field induced by the current can produce a vortex with a ringlike geometry, usually known as *closed vortex*. This solution was first obtained by Kozlov and Samokhvalov [52] through the solution of the London equation and was extensively studied further in Refs. [53, 54, 55, 56, 57, 58, 59, 60, 61, 62]. In these works, the existence, dynamics and even stability of such closed vortices in the presence of inhomogeneities were studied for unbounded superconductors or superconducting samples in the shape of a cylinder. In the latter configuration, due to the matching symmetry between the system geometry and the magnetic self-field produced by the current, a vortex penetrates the sample already in the form of a closed vortex. Recently, these closed vortices were also shown to exist in a more complex geometry, such as a superconducting torus. [63]

Closed vortices were also investigated in different physical systems. For instance, the formation of closed vortices was investigated in Josephson junctions submitted to an external current [64], where it was shown that Josephson vortices can exist as vortex loops and possible mechanisms for their experimental detection were proposed. In what regards the Abrikosov closed vortices, their short life time makes their experimental observation a challenging task, not accomplished so far.

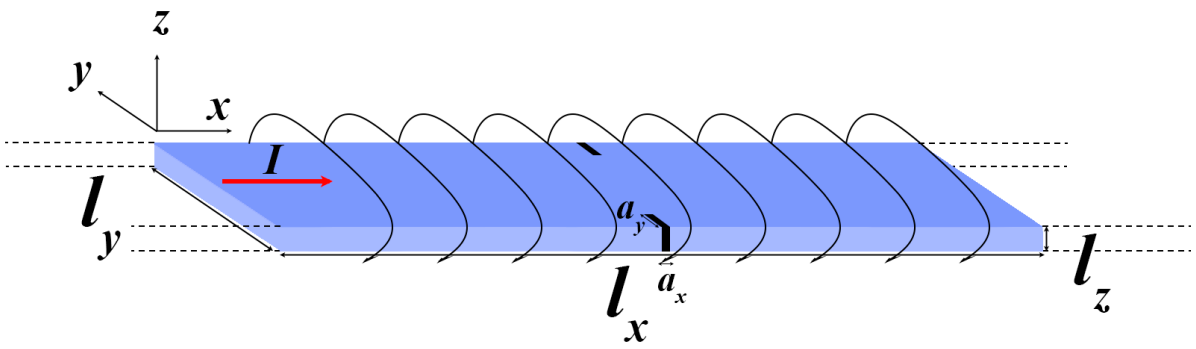

Figure 1 – *Schematic view of the system under consideration: an infinitely long superconducting sample of width l_y and thickness l_z; only one unit cell of length l_x is shown. The transport current is applied in the x direction. The encircling lines illustrate the line fields of the self-field produced by the current. Two defects are introduced at the border of the sample (black spots), in order to facilitate nucleation of v-av pairs.*

Within the framework of the microscopic theory of superconductivity, Fyhn and Linder [65] have recently proposed an experimental setup based on STM measurements for the direct observation of such closed vortices. In what follows, we propose two new methods for the indirect experimental observation of the closed vortices, which relies on the magnetic field produced by them.

In this chapter, the physics of closed vortices is studied in a different system than what is commonly used in the literature of this topic. We investigate how closed vortices are emerge and get annihilated in a superconducting film driven by an external transport current. We notice that, unlike previous works, our system geometry does not favor the creation of a closed vortex by matching the current self-field profile. In the present case, the closed vortex is formed due to the inhomogeneous action of the applied current in different parts of the vortex line. By investigating the vortex dynamics in three-dimensional superconducting films, we show that, for appropriate values of the film thickness and the Ginzburg-Landau parameter κ, a closed vortex emerges in the process of annihilation of a vortex and an antivortex pair (V-Av pair). As we discuss in the following, when approaching one another, the vortex line and the antivortex line combine, forming a closed loop. After its formation, the loop assumes the form of a quasi-ellipse, with its aspect ratio gradually decreasing, until the collapse of the loop at its center. For thick films, the loop is able to take the form of a circle before being destroyed.

The outline of this chapter is as follows. In Sec. 3.2 we present our model and the numerical method we used in order to solve the generalized Ginzburg-Landau equations [66, 67]. In Sec. 3.3 we present and discuss the results obtained in our simulations. Finally, we present our concluding remarks in Sec. 3.4.

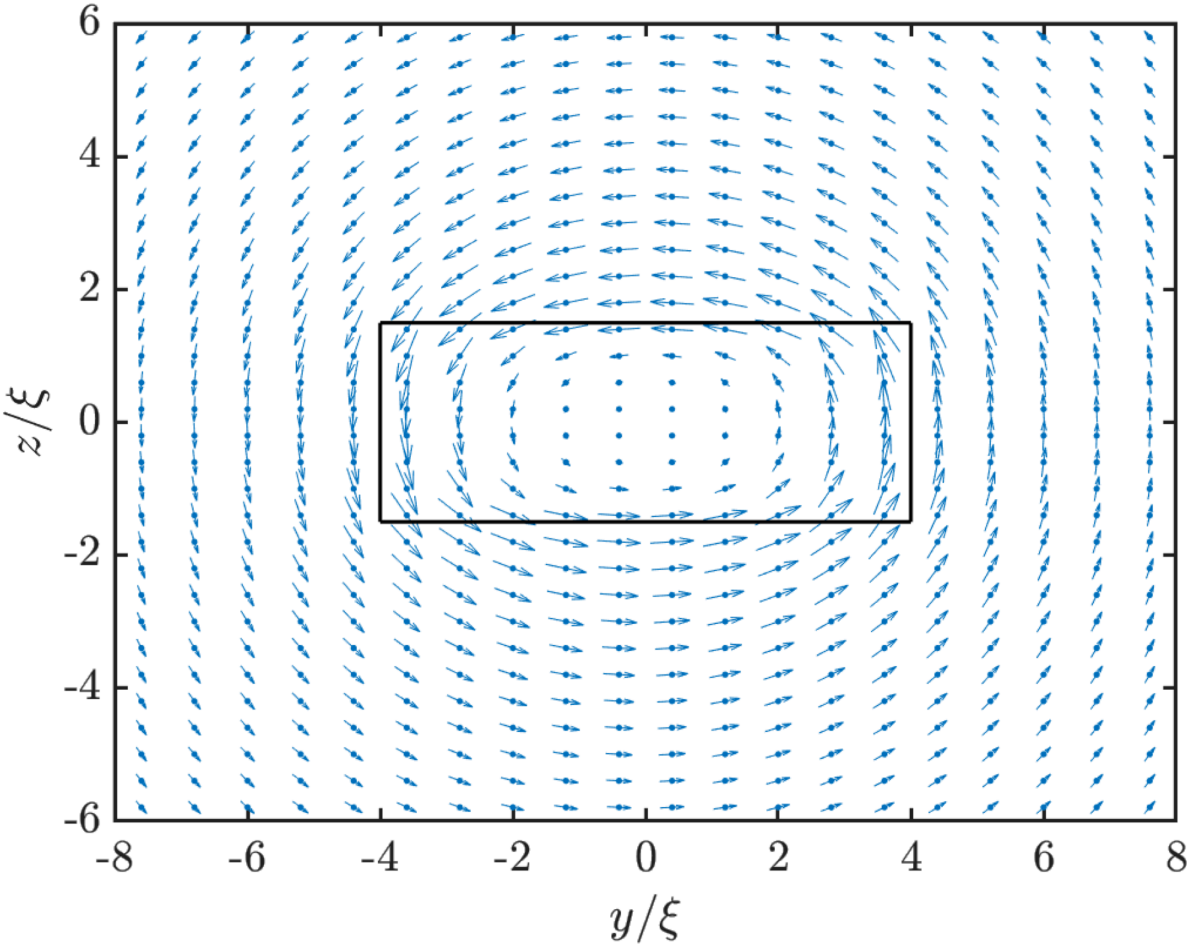

Figure 2 – *The magnetic field profile in the vertical plane $x = 0$ (parallel to the yz plane): for better visualization purposes, the arrows are not in real size; the rectangle inside is a cross section of the superconductor; this picture is for $\kappa = 1$, $l_y = 8\xi$, $l_z = 3\xi$; the value of the current density is $J_a = 0.26 J_{GL}$ just before the critical current density $J_{c1} = 0.27 J_{GL}$. The vortex (antivortex) nucleates on the right-hand side (left hand-side) of the figure.*

3.2 Theoretical Model

To investigate the dynamics of our system, we use the generalized time dependent Ginzburg-Landau (GTDGL) equation which is more suitable to describe the resitive state of dirty superconductors in the non-equilibrium state [66, 67]. In dimensionless units this equation is given by

$$\frac{u}{\sqrt{1+\gamma^2|\psi|^2}}\left[\frac{\partial}{\partial t}+\frac{1}{2}\gamma^2\frac{\partial|\psi|^2}{\partial t}\right]\psi = \\ = (\boldsymbol{\nabla}-i\mathbf{A})^2\,\psi+\psi(1-|\psi|^2), \tag{3.1}$$

coupled with Ampère's law

$$\Sigma\frac{\partial \mathbf{A}}{\partial t} = \mathbf{J}_s - \kappa^2\boldsymbol{\nabla}\times\mathbf{h}, \tag{3.2}$$

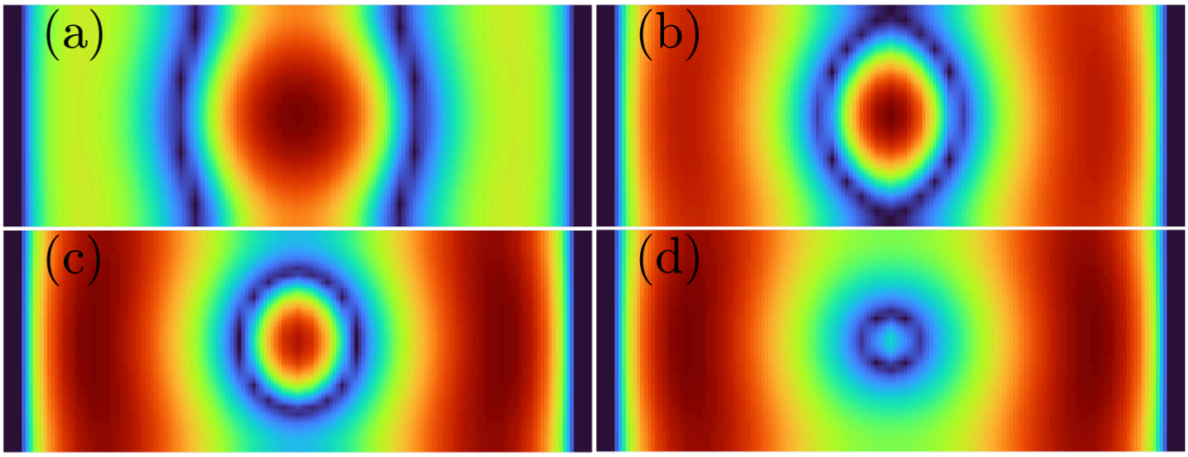

Figure 3 – *Color maps of the superconducting Cooper-pair density, $|\psi|$, for $\kappa = 1$, $l_z = 3\xi$, and $J_a = 0.27 J_{GL}$ throughout the plane $x = 0$: (a) a v-av pair of curved vortices; on the left hand-side (right hand side) is the antivortex (vortex); (b) a combination of a vortex and an antivortex producing a closed vortex; (c) a closed vortex diminishing its radius; (d) a closed vortex shrinking down at the center. The dark strips on both sides are due to the defects. These pictures correspond to the same region highlighted in Fig. 2.*

where

$$\mathbf{J}_s = Im\left[\bar{\psi}(\boldsymbol{\nabla} - i\mathbf{A})\psi\right] \tag{3.3}$$

is the superconducting current density.

Here, the temperature is in units of the critical temperature T_c; the order parameter ψ is in units of $\psi_\infty(T) = \sqrt{\alpha(T)/\beta}$, where α and β are two phenomenological constants; the distances are measured in units of the coherence length $\xi(T)$; the vector potential $\mathbf{A}$ is in units of $\xi H_{c2}(T)$, where H_{c2} is the upper critical field; the local magnetic field $\mathbf{h} = \boldsymbol{\nabla} \times \mathbf{A}$ is units of $H_{c2}(T)$; time is in units of the Ginzburg-Landau characteristic time $\tau_{GL} = \pi\hbar/8k_BTu$; the material dependent parameter $\gamma = 2\tau_E\Delta_0/\hbar$, where τ_E is the inelastic electron-collision time, and Δ_0 is the gap in the Meissner state; the constant $\Sigma = 4\pi\sigma D/c^2\xi^2(T)$, where D is the diffusion coefficient and σ is the normal state electrical conductivity; $\kappa = \lambda(T)/\xi(T)$ is the Ginzburg-Landau parameter, where $\lambda(T)$ is the London penetration depth; and finally, the constant u is equal to 5.79, which is derived from first principles [66].

Taking into account the gauge invariance of the GTDGL equations under the following transformations:

$$\begin{aligned} \psi' &= e^{-i\chi}\psi, \\ \mathbf{A}' &= \mathbf{A} - \boldsymbol{\nabla}\chi, \\ \varphi' &= \varphi + \frac{\partial\chi}{\partial t}, \end{aligned} \tag{3.4}$$

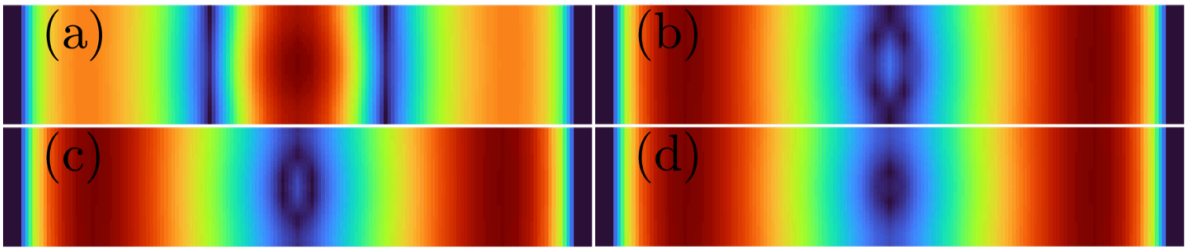

Figure 4 *– The same as in Fig.3 for* $l_z = 1.6\xi$ *and* $J_a = 0.30 J_{GL}$.

where χ is an arbitrary scalar function therefore, we conveniently use the Weyl gauge [68] in which the scalar potential is constant and equal to zero.

In this chapter, the system under consideration consists of a infinite superconducting film carrying a transport current, as illustrated in Fig. 1. For the inclusion of the transport current in our numerical simulations, we consider the following scenario. The superconducting film is driven by an external electric field which sustains a *DC* current along the x direction given by $\mathbf{J}_a = J_a\hat{\mathbf{x}}$. In the normal state, the system vector potential has only the x component. In the superconductor state, we separate the total vector potential as a combination of the normal state vector potential and the contribution coming from the diamagnetic currents that tries to expel the external field from the superconductor interior. Mathematically, in Eqs.3.1-3.3 we write:

$$\mathbf{A} = \mathbf{A}_0 + \mathbf{A}_1, \tag{3.5}$$

$$\mathbf{h} = \mathbf{h}_0 + \mathbf{h}_1, \tag{3.6}$$

where $\mathbf{A}_0$ and $\mathbf{h}_0$ satisfy the following equations:

$$\kappa^2\boldsymbol{\nabla}\times\mathbf{h}_0 = J_a\hat{\mathbf{x}}, \quad \kappa^2\nabla^2 A_{0x} = -J_a\,. \tag{3.7}$$

To obtain a closed expression for this field, we start by writing the Biot-Savart law:

$$\mathbf{h}_0(\mathbf{r}) = \frac{1}{4\pi\kappa^2}\int\frac{\mathbf{J}(\mathbf{r}')\times(\mathbf{r}-\mathbf{r}')}{|\mathbf{r}-\mathbf{r}'|^3}d^3r'\,. \tag{3.8}$$

Using $\mathbf{J} = J_a\hat{\mathbf{x}}$, we have that:

$$\mathbf{J}(\mathbf{r}')\times(\mathbf{r}-\mathbf{r}') = J_a(y-y')\hat{\mathbf{z}} - J_a(z-z')\hat{\mathbf{y}}\,, \tag{3.9}$$

substituting this result in Eq. 3.8, we have:

$$\mathbf{h}_0(\mathbf{r}) = \frac{J_a}{4\pi\kappa^2}\int_{-d/2}^{d/2}\int_{-w/2}^{w/2}\int_{-\infty}^{\infty}dz'dy'dx'\left[\hat{\mathbf{z}}\frac{(y-y')}{R^3} - \hat{\mathbf{y}}\frac{(z-z')}{R^3}\right]. \tag{3.10}$$

where $R = \left[(x-x')^2+(y-y')^2+(z-z')^2\right]^{1/2}$.

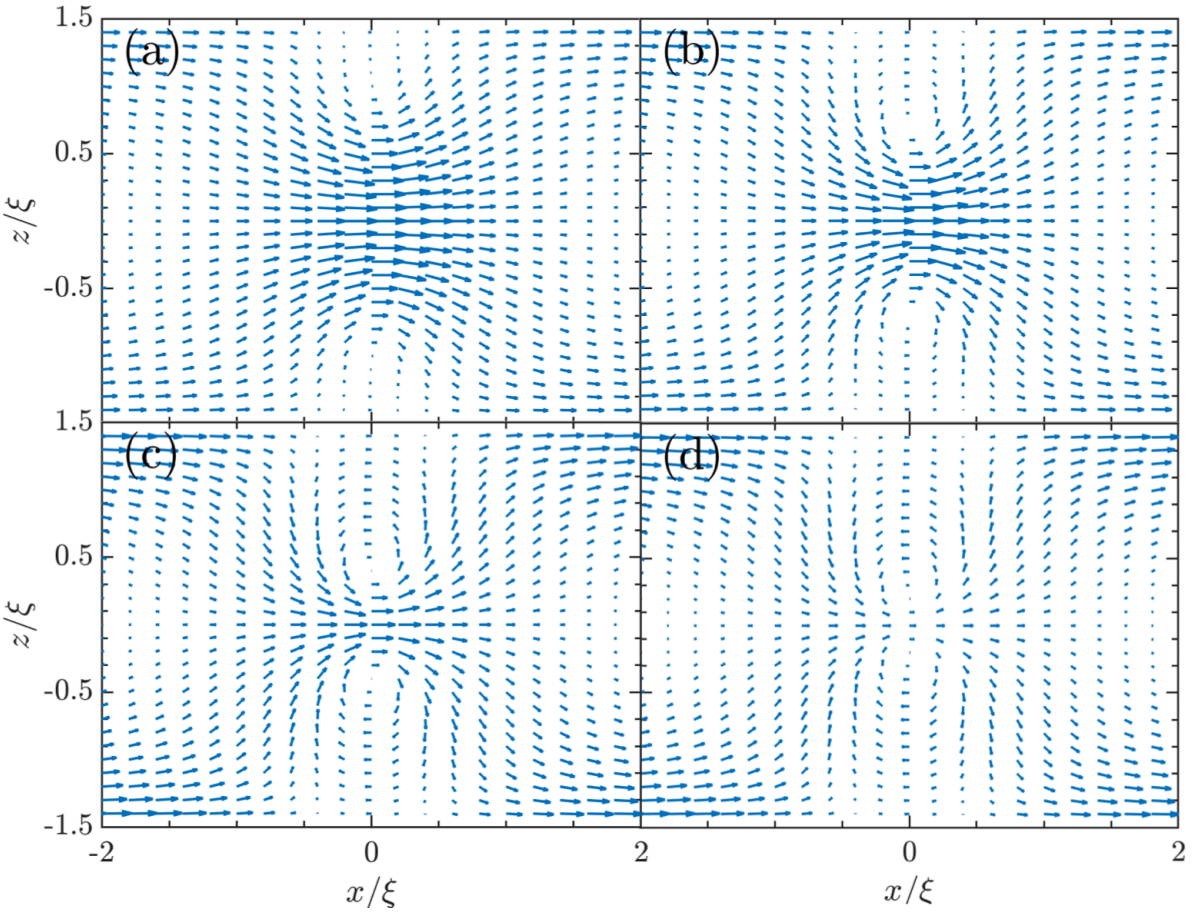

Figure 5 – *The panels show four cuts of the current distribution of the closed vortex throughout the vertical plane $y = 0$. The radius of the closed vortex diminishes from (a) to (d).*

The solution of this integral follows straightforwardly and the two non-zero components of the magnetic field can be written as:

$$h_{y0}(\mathbf{r}) = \frac{J_a}{4\pi\kappa^2}\Bigg[-(y-w/2)\ln\left[\frac{(y-w/2)^2+(z+d/2)^2}{(y-w/2)^2+(z-d/2)^2}\right]+(y+w/2)\ln\left[\frac{(y+w/2)^2+(z+d/2)^2}{(y+w/2)^2+(z-d/2)^2}\right] \tag{3.11}$$

$$+2(z-d/2)\arctan\left(\frac{(y-w/2)}{(z-d/2)}\right)-2(z-d/2)\arctan\left(\frac{(y+w/2)}{(z-d/2)}\right)- \tag{3.12}$$

$$-2(z+d/2)\arctan\left(\frac{(y-w/2)}{(z+d/2)}\right)+2(z+d/2)\arctan\left(\frac{(y+w/2)}{(z+d/2)}\right)\Bigg], \tag{3.13}$$

$$h_{z0}(\mathbf{r}) = \frac{J_a}{4\pi\kappa^2}\Bigg[(z-d/2)\ln\left[\frac{(y+w/2)^2+(z-d/2)^2}{(y-w/2)^2+(z-d/2)^2}\right]-(z+d/2)\ln\left[\frac{(y+w/2)^2+(z+d/2)^2}{(y-w/2)^2+(z+d/2)^2}\right] \tag{3.14}$$

$$-2(y-w/2)\arctan\left(\frac{(z-d/2)}{(y-w/2)}\right)+2(y-w/2)\arctan\left(\frac{(z+d/2)}{(y-w/2)}\right)+ \tag{3.15}$$

$$+2(y+w/2)\arctan\left(\frac{(z-d/2)}{(y+w/2)}\right)-2(y+w/2)\arctan\left(\frac{(z+d/2)}{(y+w/2)}\right)\Bigg]. \tag{3.16}$$

The full three-dimensional GTDGL equations are here numerically solved for a system consisting of an infinite superconducting film with finite thickness and width (see Fig. 1). To simulate the infinite film, we divide it into unit cells with dimensions (l_x, l_y, l_z). The demagnetization effects are taken into account by considering this unit cell inside a simulation box (not shown in Fig. 1) of dimensions (l_x, L_y, L_z), where (L_y, L_z) are sufficiently larger than (l_y, l_z) so that the local demagnetizing field $\mathbf{h}_1$ vanishes far away from the superconductor.

To ensure that no supercurrent flows out of the superconductor, the following boundary conditions must be fulfilled:

$$\hat{\mathbf{n}} \cdot (\boldsymbol{\nabla} - i\mathbf{A}_0 - i\mathbf{A}_1)\psi = 0, \quad \text{in } \partial\Omega_{sc}, \tag{3.17}$$

$$\boldsymbol{\nabla} \times \mathbf{A}_1 = 0, \quad \text{in } \partial\Omega, \tag{3.18}$$

where $\partial\Omega_{sc}$ and $\partial\Omega$ stand for superconducting and simulation box surfaces, respectively.

To introduce inhomogeneity in the superconducting state, we introduce deffects in our system, depicted in Fig. 1 by the two black spots. Their presence induces the nucleation of vortices and antivortices in each side of the stripe.

3.3 Results and Discussion

3.3.1 Parameters and Methodology

In the simulations, we have fixed some parameters and varied others as follows. The length and width of the unit cell are fixed as $l_x = 12\xi$ and $l_y = 8\xi$. The thickness of the sample varied from $l_z = 1\xi$ to $l_z = 3.6\xi$ in increments of 0.2ξ. We use $\kappa = 1/\sqrt{2}, 1, \sqrt{3}$ for each set of values of l_z. The grid space used is $\Delta x = \Delta y = 0.2\xi$ and $\Delta z = 0.1\xi$. The size of the simulation box was chosen sufficiently large in order to satisfy the boundary conditions (3.18); we use $l_y = 16\xi$ and $l_z = 12\xi$. The dimensions of the defects are $a_x = a_y = 0.2\xi$. The range $10 \leq \gamma \leq 20$ is suitable for most metals like Nb [66, 67, 69]; we used $\gamma = 10$.

Let us explain how we calculate the IV (current-voltage) and IR (current-resistance) characteristics, that are the measurable quantities in the resistive state. In the Weyl gauge, the electrical field is given by $\mathbf{E} = -\partial\mathbf{A}/\partial t$, so, assuming that the voltage is measured between electrodes at $z = 0$ that cover the width of the film, the voltage across a unit cell is:

$$\begin{aligned} U(t) &= -\frac{1}{n_y - 1} \sum_{j=2}^{n_y} \int_{-l_x/2}^{l_x/2} E_x(x, y_j, 0) dx \\ &= \frac{1}{n_y - 1} \sum_{j=2}^{n_y} \int_{-l_x/2}^{l_x/2} \frac{\partial A_x(x, y_j, 0)}{\partial t} dx, \end{aligned} \tag{3.19}$$

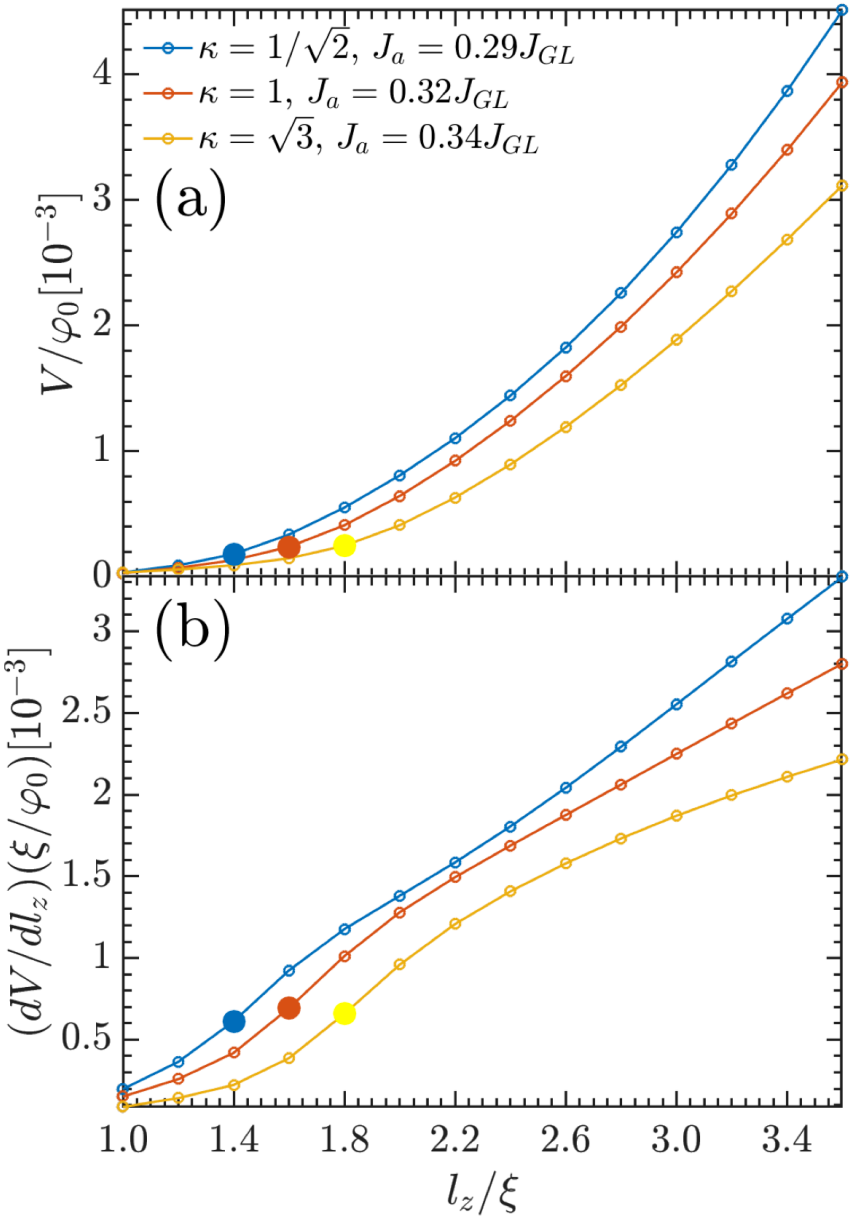

Figure 6 – *(a) Voltage across the z direction as a function of the thickness of the sample for three values of κ: the value of J_a for each case corresponds to the first critical current density when the resistive state sets in. The highlighted dots are the critical $l_{z,c}$ values for which the v-av pairs combine to make a closed vortex. (b) The derivative of the voltage: the dots separate the two regimes of straight to curved vortices; the inflection points coincide with $l_{z,c}$.*

where $n_y = l_y/\Delta y$, and $y_j = (j - n_y/2 - 1)\Delta y$ for are the y coordinates of the mesh points. The voltage is then calculated as a time average of $U(t)$. We have:

$$V = \frac{1}{T}\int_0^T U(t)\,dt, \tag{3.20}$$

where T is the time corresponding to an appropriate number of oscillations of $U(t)$.

The applied current density was adiabatically increased in steps of $\Delta J_a = 0.01 J_{GL}$

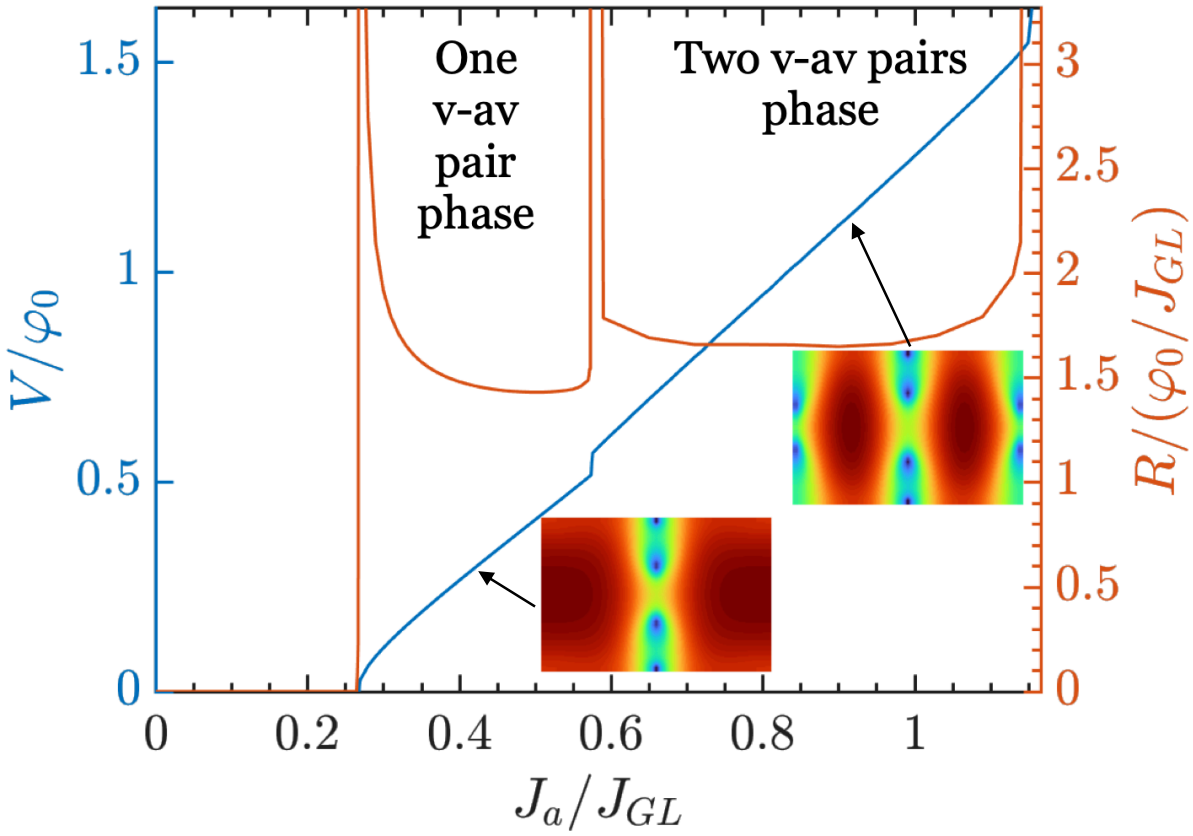

Figure 7 – *IV (blue line) and IR (red line) characteristic curves, respectively, for* $\kappa = 1$ *and* $l_z = 3\xi$*. The Meissner state (full superconductivity) survives up to* $J_a = J_{c1} = 0.27 J_{GL}$*. Above this current density, the resistive state sets in. The resistive state splits into two phases. In one of them the vortex and the antivortex nucleate only at the defects on the border of the superconductor. In the second phase, another set of v-av pairs nucleates at the frontiers between unit cells. The second jump in the IV characteristic is the signature of this crossover. The insets illustrate this scenario through the modulus of the order parameter in the xy plane (*$z = 0$ *plane).*

from the Meissner state until the superconductivity was fully destroyed. In the resistive state, we moved from value of J_a to $J_a + \Delta J_a$ only after the voltage $U(t)$ became periodic, which is the same periodicity with which the v-av pairs are formed and annihilated. When multiple nucleations of v-av (vortex-antivortex) pairs are present, the voltage looses its periodicity, and therefore we change the value of J_a only after 220 oscillations of $U(t)$ in order to obtain a more accurate value of the time averaged voltage. The results of all simulations are presented in the following Subsections.

3.3.2 Field Profile, Closed Vortex, and Current Distribution

In Fig. 2 we illustrate the vector field profile at $x = 0$ plane (in the middle of the unit cell, where the defects are located). The local field has symmetry as if the current density was uniform. Due to the geometric symmetry and the demagnetization effect, the local magnetic field is larger near the surface of the superconductor, and decreases deep inside. As can also be observed, the field is larger on the lateral sides of the sample. In this figure, we show the vector field for a value of the current density just before the first critical current $J_{c1} = 0.27 J_{GL}$. Therefore, once the resistive state sets in, it is on the lateral sides that the vortex and the antivortex sprout, move to the center, and finally annihilate each other at the center of the sample. Then, a periodic collapse of v-av pairs is established.

Next, we discuss the morphology of a closed vortex in the resistive state. The first works about closed vortices were conducted on long current-carrying superconducting cylinders, so that the vortex follows the geometry of the sample since from the surface until it collapses at the center [53, 70]. In the present scenario, we deal with a film of rectangular cross section. Thus, before the closed vortex is formed, two curved vortices (a vortex and an antivortex) nucleate in opposite sides of the sample (see panel (a) of Fig. 3) and move toward the center. Then, as they encounter each other, their ends join together forming a closed vortex (panel (b)). Once this ringlike vortex is formed, its radius starts decreasing (panel (c)) until it collapses at the center. After the transition from the Meissner state to the resistive one, the process is repeated periodically until superconductivity is suppressed throughout the sample.

It is conceivable that the closed vortex can exist for any thickness of the film, but for small values of l_z is very elongated when the ends of the v-av pair meet. In our simulations, we do not have sufficient resolution to detect a closed vortex for any l_z. Indeed, in Fig. 4 we show four panels of the color maps of the superconducting Cooper-pair density for $l_z = 1.6\xi$. As we can see, the shape of the closed vortex is much more elongated than for the previous case $l_z = 3\xi$ of Fig. 3. For $\kappa = 1$, and thickness below $l_z = 1.6\xi$, we do not observe any closed vortex; the v-av pair remains straight lines, from the nucleation of the vortex and the antivortex on the surfaces, until the pair is annihilated at the center of the sample. The formation of a closed vortex depends on the sample thickness because the current and the magnetic field concentrate near the surface of the superconductor, on a scale of the order of the London penetration depth. Therefore, for thicker samples, the ends of a vortex line are subjected to stronger Lorentz force and to a stronger horizontal magnetic field that facilitate the formation of a closed vortex.

Let us now discuss the current distribution of a closed vortex. When both curved vortex and antivortex touch their ends on the upper and lower surfaces, $z = +l_z/2$ and $z = -l_z/2$, respectively, they combine in order to make a single closed vortex. This new

vortex looks like a toroid with the superconducting currents flowing around its core. Fig. 5 exhibits four cuts of the toroid in the xz plane for $l_z = 3\xi$. As it can be seen, the currents in the internal parts of the toroid flow in the same direction for both the upper and lower segment of the closed vortex. Therefore, all v-av pairs opposedly positioned in the toroid attract one another, causing the closed vortex to collapse at the center of the sample.

3.3.3 Straight to Curved Vortex Crossover, and (IV,IR) Characteristics

As we mentioned previously, as the thickness of the sample is increased, there is a crossover between straight to curved v-av pair. In what follows, we show a consistence between the criterion based on the aspect ratio of the vortex (antivortex) and an important physical quantity, namely, the voltage across the z direction on the lateral side of the film; by *aspect ratio*, we mean the distance between the center of the vortex and the antivortex along the y direction when their tips first touch each other. For this purpose, we calculate the time average of the following voltage:

$$\begin{aligned} U(t) &= -\frac{2}{n_x}\sum_{i=n_x/2}^{n_x}\int_0^{l_z/2} E_z(x_i, l_y/2, z)dz \\ &= \frac{2}{n_x}\sum_{i=n_x/2}^{n_x}\int_0^{l_z/2} \frac{\partial A_z(x_i, l_y/2, z)}{\partial t}dz, \end{aligned} \tag{3.21}$$

where $n_x = l_x/\Delta x$, and $x_i = (i - n_x/2 - 1)\Delta x$ for all $\{i = 1, 2, \ldots, n_x + 1\}$ are the x coordinates of the mesh points. Here, we have not considered the branch $-l_z/2 \leq z \leq 0$. By symmetry, had we included this contribution, the voltage would vanish.

When a closed vortex appears, we will have a larger contribution for the current flowing in the vertical direction, and consequently an increase in the voltage. For a fixed value of κ and current density J_a, we determine the voltage for several values of l_z. We have done this for three distinct values of the Ginzburg-Landau parameter. The respective value of J_a is chosen to correspond to the critical current density J_{c1} for the lowest thickness, $l_z = 1\xi$. The results are summarized in Fig. 6. In panel (a) we present the voltage as a function of the thickness of the film. We find that, at a certain point, which we denote by $l_{z,c}$, there is a change of the behavior of the $V(l_z)$ curves. These points are highlighted in panel (a). They signal a crossover from linear to curved v-av pairs.

In order to make sure that this special point is correlated to the straight-to-curved vortex crossover, we calculate the derivative $dV(l_z)/dl_z$ for the three values of κ (see panel (b)). As can be seen, the derivatives have an inflection point which are highlighted in panel (b). These points correspond to $l_{z,c}$. We find the following critical values, $l_{z,c} = 1.4\xi, 1.6\xi, 1.8\xi$ for $\kappa = 1/\sqrt{2}, 1, \sqrt{3}$, respectively. We must emphasize that, first we determine the value of $l_{z,c}$ by inspecting the aspect ratio of the curvature of the vortex.

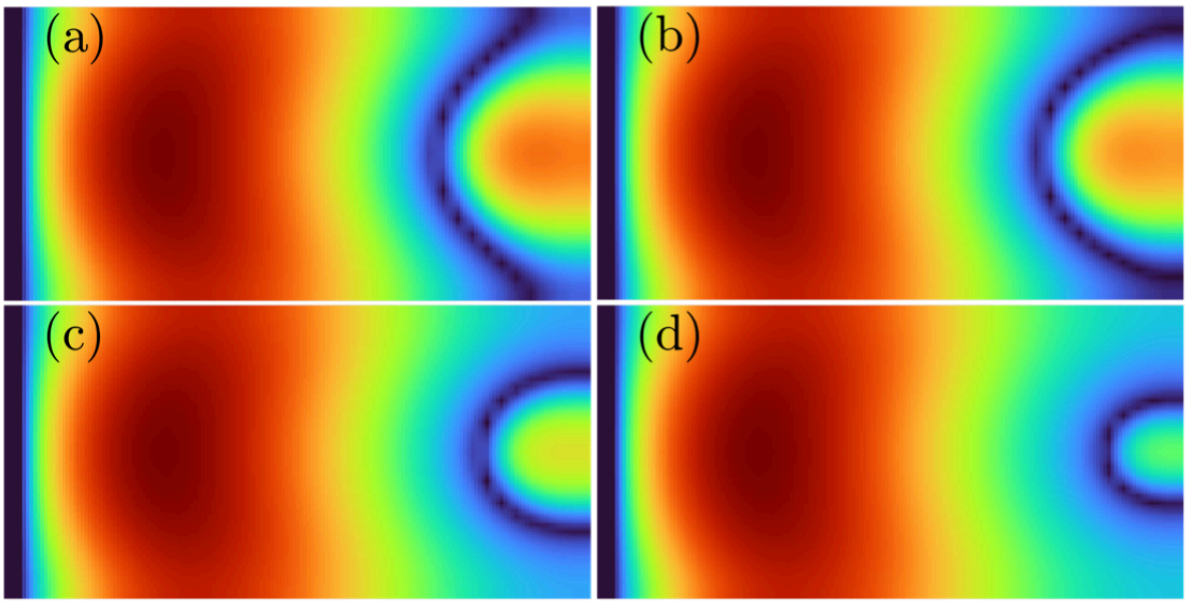

Figure 8 – *Color maps of the superconducting Cooper-pair density, $|\psi|$, for $\kappa = 1$, $l_z = 4\xi$, and $J_a = 0.26J_{GL}$ throughout the plane $x = 0$: (a) an av nucleates in the left edge of the sample and moves towards the opposite side; (b) the ends of the av touch the $y = l_y/2$ plane and form a half-closed vortex; (c) a half-closed vortex diminishing its radius; (d) the half-closed vortex shrinking down.*

Second, we check if the result is in agreement with the inflection point of $dV(l_z)/dl_z$. For all the three cases mentioned above they coincide.

Now we discuss the transport properties of the superconductor. The IV and IR characteristics are presented in Fig. 7 for $\kappa = 1$ and $l_z = 3\xi$. As we increase the applied current density, the system becomes unstable to the penetration of v-av pairs. When J_a achieves the value $J_{c1} = 0.27J_{GL}$ the superconductor goes to the resistive state, where a periodic formation v-av pairs occurs. Notice that J_{c1} is smaller than the depairing current density J_{GL}. This is a consequence of the defects deliberately introduced at the border of the superconducting film. If we further increase J_a, a second jump appears in the IV curve at $J_a = 0.575J_{GL}$. This is an indication that other two adjacent v-av pairs around the central one are nucleating (see insets). This is in correspondence with the experimental observations of multiple penetrations of kinematic vortices in Sn film by Sivakov *et. al.* [71]. Finally, when the current density reaches the value $J_a = J_{c2} = 1.155J_{GL}$ the superconductor goes straight to the normal state. We believe that for larger unit cells, additional jumps in the IV curve would occur.

3.3.4 Single Defect (Half-Closed Vortex)

We also have considered a single defect in the middle of a unit cell (in the middle of front edge in Fig. 1). In this configuration, only an antivortex nucleates on the $y = -l_y/2$ surface. Once the antivortex nucleates at $y = -l_y/2$ it moves directly towards the opposite side. As can be seen from Fig. 8, as the antivortex approaches the other side of the sample, it becomes significantly curved (see panel (a)). When it reaches the surface $y = l_y/2$, surprisingly, it does not escape the sample. Instead, its ends touch the surface giving rise to a *half-closed vortex* (see panels (b) and (c)). Then, it diminishes its ratio until it collapses (see panel (d)).

Due to its intrinsic nature, it is very difficult to observe experimentally the closed vortex. In addition, both the closed and half-closed vortex are very unstable. Therefore, we require an indirect method that signals either a v-av or a single half-closed vortex curves. Having this in mind, we propose a setup to detect the curvature of the v-av pair when it gives rise to a closed vortex with a non vanishing aspect ratio. Instead of doing this for a closed vortex, which is formed inside the sample, we think it should be much easier for a half-closed vortex, since its collapse occurs on the surface. For this purpose, we calculate the time average of the of the magnetic flux on the lateral side of the film. In order to calculate the magnetic flux, we focus in a small region where the antivortex tips touch the plane $y = l_y/2$, although we could extend it throughout the whole lateral side of the unit cell. We evaluate the following equation:

$$\Phi(t) = \int_0^{l_z/2} \int_{-\xi}^{\xi} h_y(x, \pm l_y/2, z)\, dxdz. \tag{3.22}$$

Here, the minus sign stands for the left edge where the antivortex nucleates, and the plus sign is for the opposite one where the antivortex ends touch the surface. We consider only half of the lateral edge, otherwise the total flux would vanish.

Fig. 9 presents the results for the time averaged magnetic flux by using the same parameters as those used in Fig. 8. As can be clearly seen, until the transition to the resistive state, the flux is approximately the same through both surfaces $y = \pm l_y/2$. Nevertheless, once the resistive state sets in, they become different as much as $\Delta\bar{\Phi} \approx 0.09\xi^2 H_{c2} \approx 0.02\Phi_0$. This is signaling that the antivortex is piercing the $y = +l_y/2$ surface. Therefore, for this to happen, the antivortex necessarily has to bend.

Since the creation and annihilation of the half-closed vortex is a dynamical process, the flux evolves periodically. The AC magnetic flux can be seen in the inset of Fig. 9. The period of the AC signal depends on the applied current density. For $J_a = 0.26 J_{GL}$ we find that the period is $\tau \approx 0.03 \times 10^4 t_{GL}$. For low-$T_c$ materials like Nb films [69], $t_{GL} \approx 6.72$ ps. This produces $\tau \approx 2$ ns, which is in the GHz frequency range.

As we can see, the measurement of the difference between the time averaged mag-

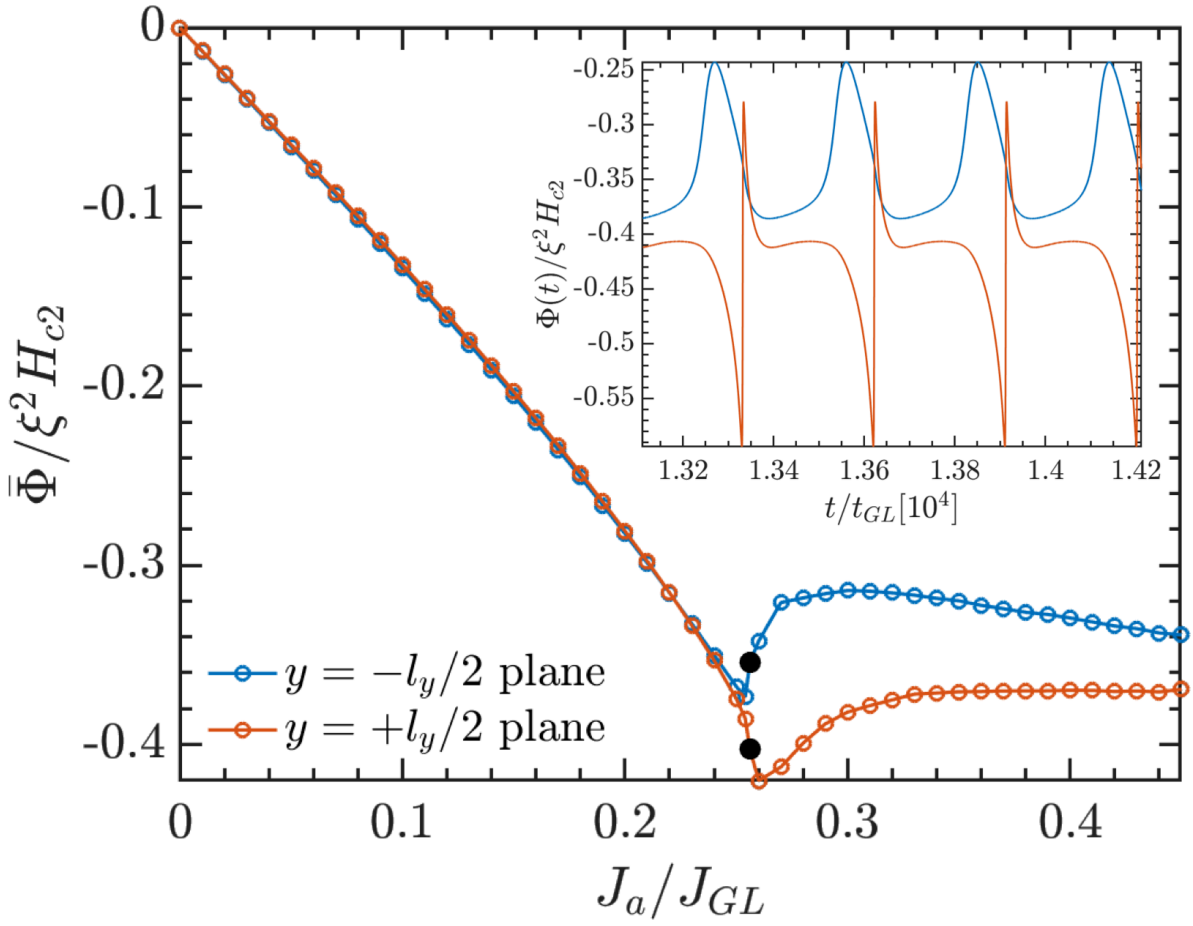

Figure 9 – *The main panel presents the time average of the magnetic flux, $\bar{\Phi}$, across the surfaces defined in Eq. 3.22; the black points correspond to the beginning of the resistive state. The inset shows the magnetic flux, Φ, as a function of time. The parameters used were $\kappa = 1$, $l_z = 4\xi$, and $J_a = 0.26 J_{GL}$.*

netic flux threading at each plane, as displayed in Fig. 9, can be an indirect method for the experimental detection of a closed vortex. Such measurement is experimentally feasible by using the recently developed nanoSQUIDs [72, 73, 74], which are capable of detecting the variation of the flux produced by the closed vortex in the time and length scale we used in our computations.

We must emphasize that for thin superconductors, the measurement of the flux in the region prescribed in the above setup can be experimentally challenging. For this reason, we also present another indirect method for the detection of a closed vortex. Fig 10 shows the difference between the averaged magnetic flux calculated at the lateral sides of our superconductor as a function of the applied current density, for different superconductor thicknesses. In contrast with the previous case, here the flux is calculated from the bottom of the superconductor up to a height well above the sample surface. The flux is evaluated across a vertical rectangular surface, located a coherence length away from the lateral

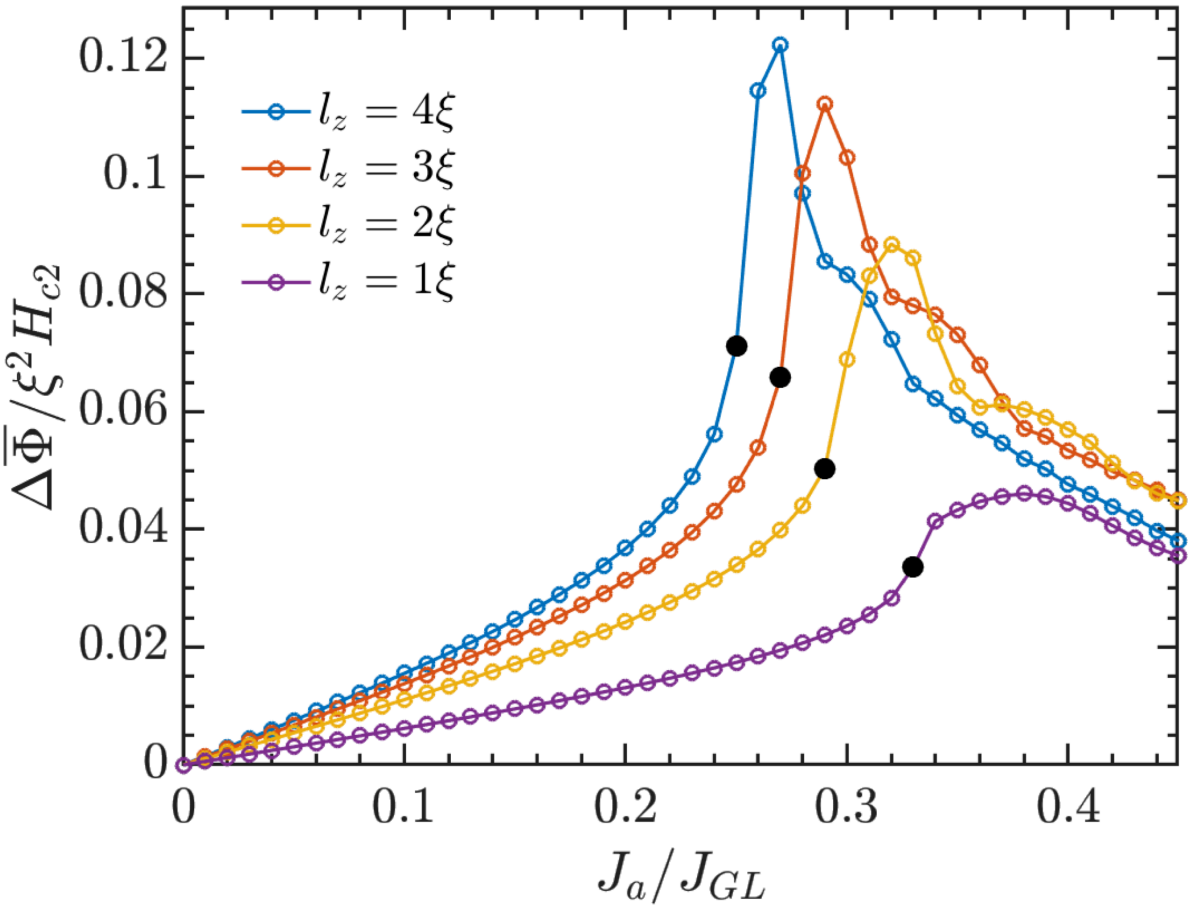

Figure 10 – *Difference between the average magnetic flux on both sides of the sample through two vertical circuits positioned on the planes* $y = \pm(l_y/2 + \xi)$*. The domain of the circuits is given by* $\{-\xi \leq x \leq \xi,\ -l_z/2 \leq z \leq L_z/2\}$*. The value of* L_z *was chosen such that the area of the circuit above the* $z = l_z/2$ *surface is the same for all thicknesses* l_z*. The points just before the onset of the resistive state are highlighted in black.*

surface. This makes the proposed experiment much more feasible.

The black dots in Fig. 10 represent the onset of the resistive state for each thickness. We are interested in current densities slightly above these values. In this region, the antivortex moves through the whole sample, being expelled at the other side. Due to its curvature, the antivortex produces a larger magnetic flux in the plane which it is moving into, increasing the flux difference between each plane. Since the curvature increases with the film thickness, this difference also increases with the sample thickness, as shown in Fig. 10. Nevertheless, for large values of the current density, a vortex also penetrates the superconductor at the opposite side, with the pair being annihilated inside the sample, reducing the impact of the curvature in the flux. The penetration of this vortex becomes easier as the superconductor thickness increases, which explains why the flux difference for $l_z = 4\xi$ is smaller than for $l_z = 2\xi$ or 3ξ at high current densities, for example. In

summary, by comparing the magnetic flux difference, at the onset of the resistive state, for films with different thicknesses, we can clearly demonstrate the existence of the half-closed vortex. Given the inherent complexity for the direct observation of a closed vortex, our indirect method brings a new possibility for the first detection of such objects.

3.4 Concluding remarks

To summarize, we have shown that the combination of the flux lines of a vortex and an antivortex during their annihilation gives origin to a closed vortex loop. As we show here, the formation of the closed vortex depends on how easily the flux lines can be bent due to the action of the applied current, with this bending increasing with the superconducting film thickness and decreasing with the Ginzburg-Landau parameter κ. Since the motion and annihilation of vortices are highly dissipative processes, understanding their behavior is of fundamental importance to the design of electronic devices.

Our findings suggest a new method to experimentally observe a closed vortex. As discussed here, closed vortices can be indirectly detected by the measuring the flux produced by their stray fields. We emphasize that the recently developed nanoSQUIDs are capable of performing such measurements in the time and length scales that our system requires.

4 Harnessing the superconducting diode effect through inhomogeneous magnetic fields

4.1 Introduction

One of the most important topics of both fundamental and applied research on electronic system is the search for faster and efficient devices, which would allow increased performance in a wide range of applications. One of such devices is the superconducting diode [75, 76], which has the practical advantage of presenting all the functionalities of a regular semiconductor diode while also being able to transport current without electrical resistance.

The fundamental characteristic of the superconducting diode is the lack of inversion symmetry for the current flow, which can be expressed as $I_c^+ \neq I_c^-$, where $I_c^\pm$ is the critical current that marks the emergence of a finite resistance for a given current polarity. The first idea for the realization of a superconducting diode focused on applying a pinning potential that breaks the inversion symmetry of the vortex lattice [77, 78]. In this manner, an alternate current would trigger vortex motion and the emergence of the resistive state for one current polarity, while the system would remain perfectly superconducting for the other one. This idea was executed experimentally in various different systems, with the inversion pinning landscape coming from regular arrays of asymmetric dots and antidots [79, 80, 81], asymmetric distributions of symmetric dots and antidots [82, 83, 84], regular arrays of nanosized magnetic dipoles [85, 86], and asymmetric weak-pinning channels [87].

The interest in the superconducting diode physics has witnessed a new increase in the recent years, with the emergence of a diverse amount of systems capable of displaying the diode effect. As examples of such systems we can cite heterostructures composed of superconducting materials and topological insulators or ferromagnetic materials [88, 89, 90, 91, 92, 93, 94], different superconducting systems with an applied magnetic field [95, 96, 97, 98, 99, 100, 101, 102], and even superconducting systems with no external field [103, 104, 105, 106]. Superconducting Josephson junctions have also been used to obtain the diode effect [107, 108, 109, 110, 111, 112], relaying on the asymmetric current-phase relation of specific junctions.

Here, it is interesting to define two types of superconducting diodes. The first of

them is the intrinsic superconducting diode, which occurs when an asymmetry inherent to the superconducting material leads to a different critical current for each polarity. The second is the vortex-based superconducting diode, briefly discussed above, where the current necessary to induce vortex motion in the superconductor is polarity dependent. Due to its nature, vortex-based diodes display a much higher degree of controllability than the intrinsic ones, once the critical currents for the vortex motion can be designed by a series of techniques. Moreover, one should note that in experimental conditions, vortex-based and intrinsic diodes can be hard to distinguish [113]. This occurs because the critical depairing current is always smaller than the theoretical one and vortex motion can trigger the onset of the normal state.

For vortex-based diodes, the dissipation emerges from the flux-flow and the superconducting state is not totally suppressed. Once the flux-flow resistance is smaller than the its normal state counterpart, the obtained DC voltage output is relatively small. A much more advantageous scenario occurs for diode systems where a completely dissipationless superconductor for one current polarity transits directly to the normal state when the polarity is switched. Hereafter, we will refer to these two distinct diode mechanisms as flux-flow dominated (FFD) and normal state dominated (NSD). Recently, Hou *et. al.* [90] demonstrated a highly efficient diode effect in superconducting stripes by introducing asymmetric conditions for vortex penetration at the system edges. In other words, there is a transition from FFD to NSD. In their work, however, there is no clear explanation for such transition. Ref. [114] possibly gives some insight to the physics. In this work, the authors studied the diode effect in a nonostructured superconducting stripe. As they show, the heat dissipated by the fast moving vortices *i.e.* the formation and propagation of hot spots, drives the system to the normal state, thus providing an explanation to the connection between FFD and NSD scenarios.

With these recent results, the necessity of a better understanding on the heating role in the emergence of the diode effect becomes evident. Moreover, the possibility of FFD conversion to NSD by heating effects suggests that a careful design of the vortex dynamics and the subsequent heat diffusion can serve as a platform for the optimization of diode efficiency $\epsilon = |I_c^- - I_c^+|/(I_c^- + I_c^+)$.

The focus of the present chapter is to study the interplay between the FFD and the NSD mechanisms in superconducting stripes subjected to asymmetric external magnetic fields. We do so by the numerical solution of the time-dependent Ginzburg-Landau equations coupled to the heat diffusion equations, for external field profiles that goes from fully positive to perfect antisymmetric. As we show, while both types of flux profile leads to the FFD scenario, the antisymmetric one displays the larger efficiency, with values surpassing 70%. As the magnitude of the transport current increases, vortex-antivortex (v-av) annihilation sends the system to the normal state, due to the hot spots formation

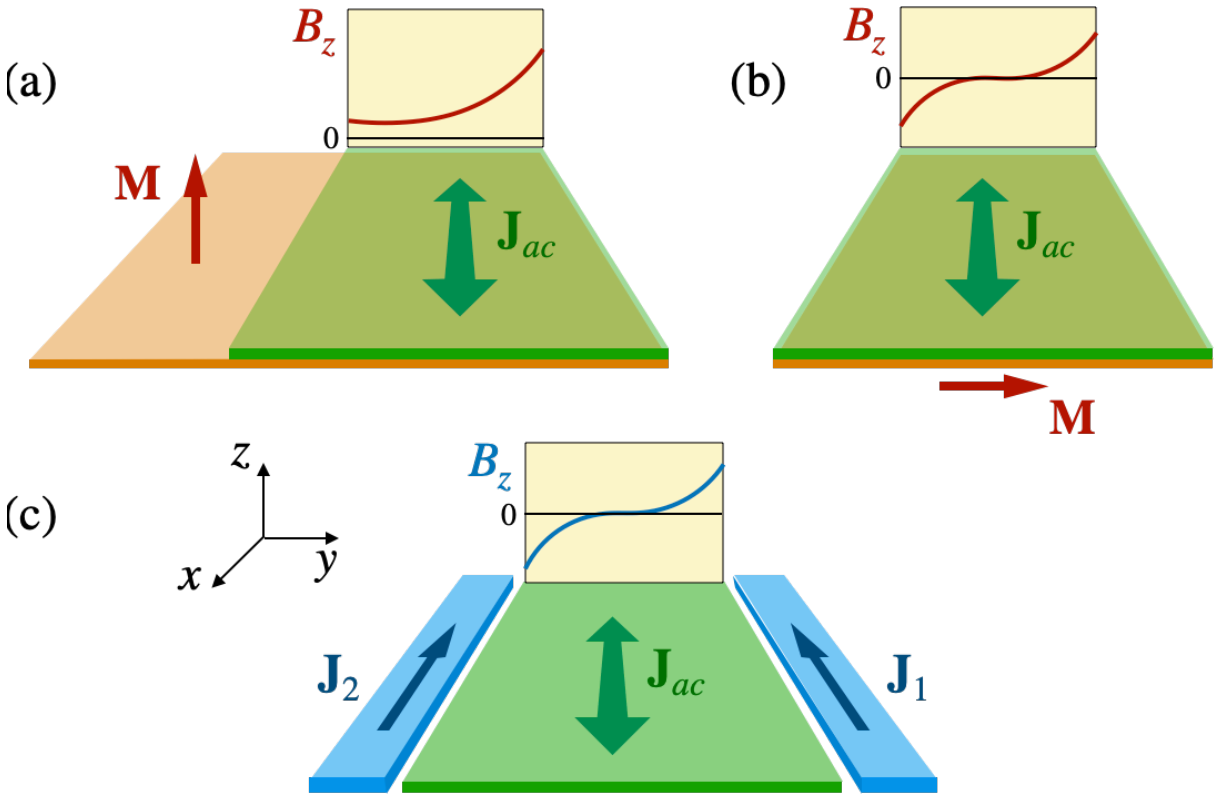

Figure 1 – *Schematic view of a superconducting film (green) subjected to asymmetric field profiles $B_z(y)$ induced by: (a) an asymmetrically lying ferromagnetic film (orange) with off-plane magnetization* $\mathbf{M}$*; (b) the same as (a) but with in-plane magnetization and symmetric arrangement of the bilayer; and (c) currents applied onto lateral superconducting stripes (blue).* $\mathbf{J}_1$ *and* $\mathbf{J}_2$ *can be adjusted to generate different field profiles. Here, setting* $\mathbf{J}_2 = \mathbf{J}_1 = -J\hat{\mathbf{x}}$ *emulates* $B_z(y)$ *similar to that induced by the magnet in (b). In all cases, an alternating current* $\mathbf{J}_{ac}$ *applied parallel to* x *induces nonreciprocal vortex penetration and motion.*

at the collision. We also show that reducing the heat removal strength accelerates this process, thus facilitating the conversion of FFD into NSD and enhancing the diode efficiency. Such results can help the physical interpretation of large efficiencies observed in recently discovered superconducting diode systems.

The organization of this chapter is as follows. In Sec. 4.2 we define our system and introduce the theoretical formalism used to study it. We present our results and discussion in Sec. 4.3 and our conclusions in Sec. 4.4.

4.2 Theoretical Formalism

The time dependent Ginzburg-Landau currents can be written, in dimensionless units as [66, 67]:

$$\frac{u}{\sqrt{1+\gamma^2|\psi|^2}}\left[\frac{\partial}{\partial t}+\frac{1}{2}\gamma^2\frac{\partial|\psi|^2}{\partial t}\right]\psi = (\boldsymbol{\nabla}-i\mathbf{A})^2\psi+\psi(1-T-|\psi|^2), \tag{4.1}$$

$$\sigma\frac{\partial\mathbf{A}}{\partial t} = \mathrm{Im}\left[\bar{\psi}(\boldsymbol{\nabla}-i\mathbf{A})\psi\right]-\kappa^2\boldsymbol{\nabla}\times\boldsymbol{\nabla}\times\mathbf{A}, \tag{4.2}$$

where ψ is the superconducting order parameter, $\mathbf{A}$ is the vector potential and σ is the normal conductivity. We also define the coherence length $\xi(0)$, the penetration length $\lambda(0)$ and the Ginzburg-Landau parameter $\kappa = \lambda(0)/\xi(0)$. In all calculations, the constants u and γ are fixed as 5.79 and 20, respectively. In these equations, lengths are in units of $\xi(0)$, T in units of the critical temperature, T_c, time in units of $t_{GL} = \pi\hbar/8uk_BT_c$, ψ in units of the field-free order parameter at $T = 0$, $\psi_\infty(0)$, $\mathbf{A}$ in units of $\xi(0)H_{c2}(0)$, with $H_{c2}(0)$ the upper critical field at $T = 0$, current densities are in units of $j_0 = \sigma V_0/\xi(0)$ and voltage in units of $V_0 = \hbar/2et_{GL}$.

The effects of heat dissipation are introduced through the heat diffusion equation [115, 116]:

$$\nu\frac{\partial T}{\partial t} = \zeta\nabla^2T+\sigma\left(\frac{\partial\mathbf{A}}{\partial t}\right)^2-\eta(T-T_0), \tag{4.3}$$

here, where ν, ζ, and η are the thermal capacity, thermal conductivity of the material, and the heat transfer coefficient of the substrate, respectively, with T_0 being the bath temperature. In what follows, we set $\nu = 0.03$, $\zeta = 0.06$ and varied η from 2.0×10^{-5} to 2.0×10^{-3}.

Panels (a) and (b) of Fig. 1 show two possible methods to the inclusion of the inhomogeneous field in the system. Here, we use a superconductor/ferromagnet heterostructure and the inhomogeneous field comes from the magnetization of the ferromagnet. We note that the system depicted in panel (b) was recently studied in Ref. [90]. In this chapter, we investigate a new system, presented in panel (c), which consists a central superconducting stripe under an AC current drive with two coplanar wires carrying a DC current being responsible for the creation of the inhomogeneous field profile. In the configurations shown in panels (b) and (c) display the particular behavior that their field profile matches the profile of the self-field generated by the AC current for one polarity but opposes it for the other one. In what follows, we discuss that this pattern leads to a larger diode efficiency. We choose panel (c) for our investigation of the diode effect, because it provides a suitable design to manipulate the inhomogeneous field profile through the tuning of the lateral currents J_1 and J_2.

In our calculations, the side stripes are defined with a width $w = 50\xi(0)$, a thickness $d_s = 5\xi(0)$ and its separated from the central superconducting film by a distance of

$s = 5\xi(0)$. The basic calculation of the field produced by two stripes carrying currents is simple, with its z component being given by:

$$\begin{aligned} H_{nh}(y) &= \frac{J_1 d_s}{2\pi\kappa^2} \ln\left(\frac{-y+w+s+L_y/2}{-y+s+L_y/2}\right) \\ &- \frac{J_2 d_s}{2\pi\kappa^2} \ln\left(\frac{y+w+s+L_y/2}{y+s+L_y/2}\right) \end{aligned} \tag{4.4}$$

The central superconductor has width $L_y = 200\xi(0)$ and thickness $d = \xi(0)$. An AC current $J_{ac}(t) = J_a \sin(2\pi t/\tau)$ is applied to this stripe, with τ being the period of oscillation.

Eqs. (4.1)-(4.3) are solved numerically solely for the central superconducting stripe, with periodic boundary conditions used along the x direction, with period $L_x = 400\xi(0)$. For the edges at $y = \pm L_y/2$, we must assure that no supercurrent leaves the system. This is done by the boundary condition $\hat{\mathbf{y}} \cdot (\boldsymbol{\nabla} - i\mathbf{A})\psi = 0$. For the local temperature, the following boundary condition is used $\hat{\mathbf{y}} \cdot \boldsymbol{\nabla} T = 0$ [115, 116]. To take into account the applied AC current [**??**], the magnetic field obeys the following boundary conditions $h_z(x, \pm L_y/2) = H_{nh}(\pm L_y/2) \pm L_y J(t)/2\kappa^2$.

4.3 Results and Discussion

To carefully investigate the conditions for the occurrence of the diode effect in our system, we have varied J_a, the magnitude of the applied AC current, and J_1 and J_2. In our analysis, we limit the values of J_1 and J_2 to be lower than 0.52. Here we note that, for the bath temperature fixed at $T_0 = 0.96T_c$, such currents would destroy the superconducting state if applied to the central stripe. Thus being, the lateral wires must be composed of a superconducting material with larger critical temperature and depairing current. For the remaining parameters, we have used $\kappa = 5$ and, unless stated otherwise, $\tau = \tau_0 = 10^5 t_{GL}$.

4.3.1 Fully Positive Asymmetric Flux Profiles ($J_1 \neq 0$, $J_2 = 0$)

Let us start our investigation by considering a fully positive field profile coming from the wires *i.e* $J_1 > 0$ and $J_2 = 0$ in Eq. (4.4). In Fig. 2, we show the color plot of time average DC signal V_{DC} as a function of the magnitude of the AC current and the value of J_1. As one can see, by increasing the magnitude of the AC current for a fixed J_1, we get three distinct V_{DC} regions. Namely, we start with a low V_{DC}, obtain a large V_{DC} value inside the red region of the figure and then go back to a low V_{DC}. Inside the large voltage region, the values of V_{DC} are ten times as large as the ones in the blue regions outside this domain. We note that the appearance of two separate islands of large V_{DC} for

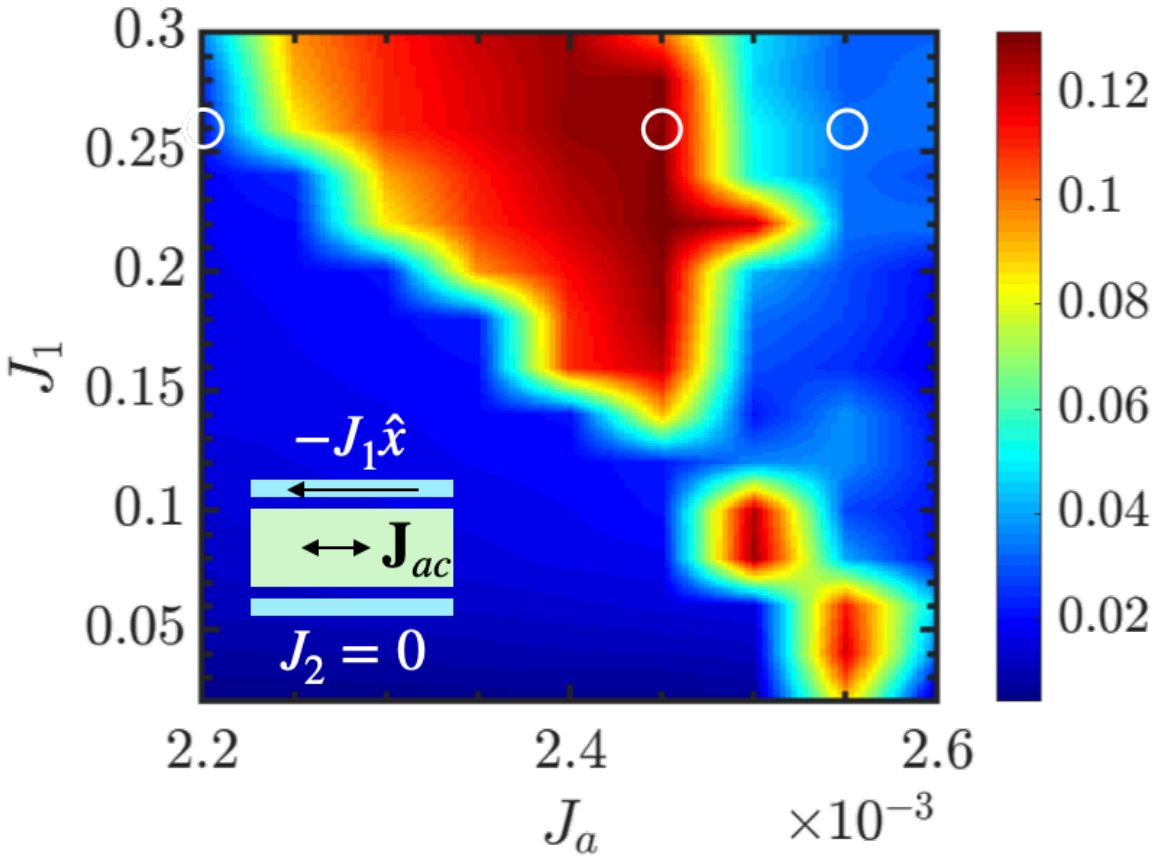

Figure 2 *– Phase-diagram displaying the color plot of the output voltage V_{DC} (in units of $V_0 = \hbar/2et_{GL}$) as a function of J_1 and the amplitude of the AC current (both in units of $j_0 = \sigma V_0/\xi(0)$). We fix $J_2 = 0$.*

small J_1 is a purely numerical result, which originates in the step that J_1 is being varied. For a smaller step, the two red regions would be connected.

To help us understand what occurs in each region of the V_{DC} phase diagram, Fig. 3 shows the voltage output (solid blue line) as a function of time for three selected values of J_a and $J_1 = 0.26$ fixed. The red dashed lines in each panel show the voltage of the system at the normal state, given by $V_n(t) = (J_a L_x/\sigma)\sin(2\pi t/\tau)$. Panel (a) depicts a case for the first region with low V_{DC}, before the red region. As can be seen, the vortex dynamics in the stripe is never sufficient to completely destroy the superconducting state, with the system displaying a finite resistance due to the vortex motion. The finite V_{DC} value occurs due to the presence of the inhomogeneous field. In this case, the external field is stronger at the top edge of the central stripe, thus nucleating vortices in this region. For positive current polarity, the AC current self-field is positive at the top edge and negative at the bottom edge, thus enhancing the inhomogeneous field at its stronger location. On the other hand, the self-field profile is opposite for negative current polarity, thus diminishing the external field. This difference leads to an asymmetric vortex dynamics for each current

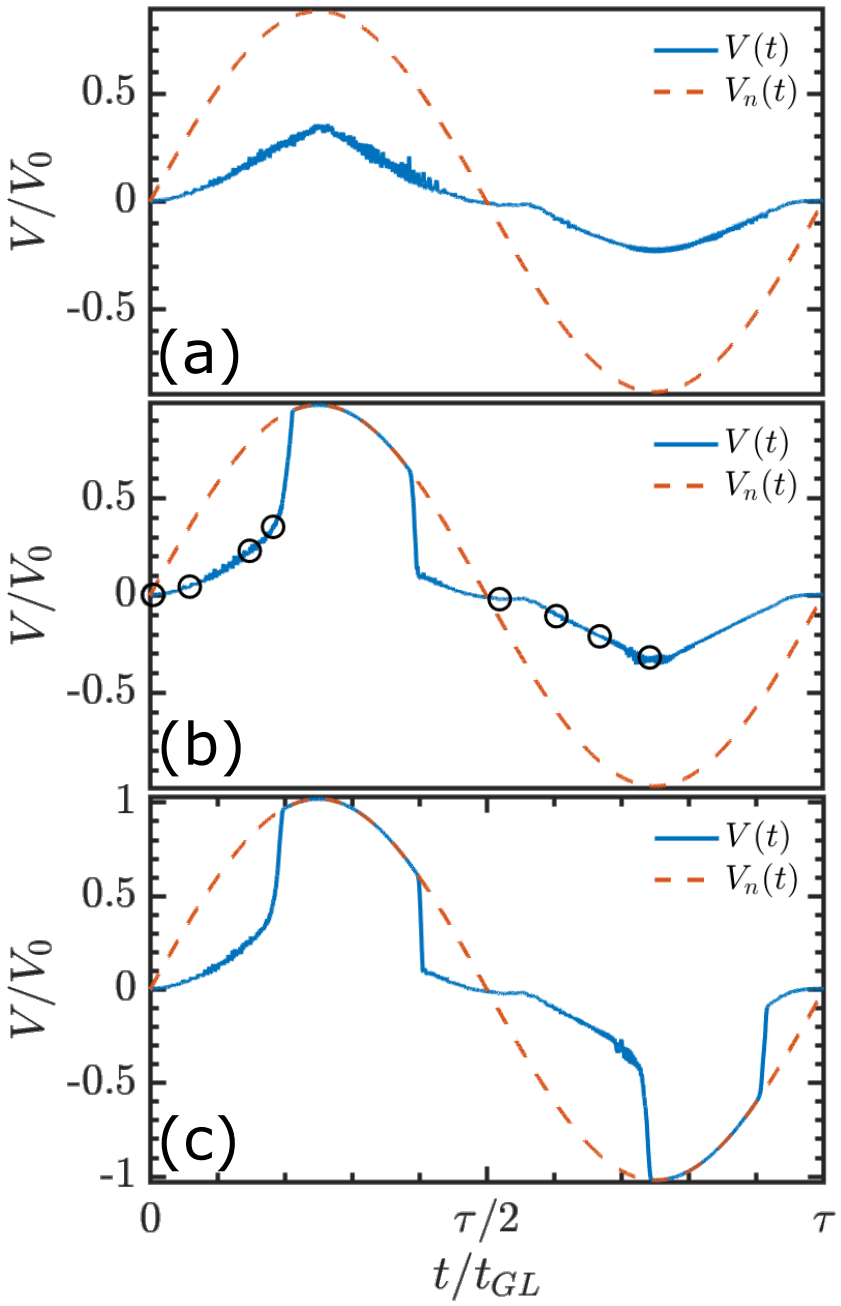

Figure 3 – *The voltage signal as a function of time (solid blue line) for* $J_1 = 0.26$ *and three current values,* $J_a = 2.20 \times 10^{-3}$ *(panel (a)),* $J_a = 2.45 \times 10^{-3}$ *(panel (b)) and* $J_a = 2.55 \times 10^{-3}$ *(panel (c)). In each panel, the red dashed lines represent the voltage if the system were in the normal state.*

polarity, thus originating the finite *DC* voltage output.

Panel (*b*) shows the voltage output as a function of time for one of the cases inside the red portion of Fig. 3. Here, the origin of the large V_{DC} value obtained becomes clear. As we can see, for positive current polarity, the heat dissipated by the vortex dynamics is sufficient to send the system to the normal state for a given time interval. We note that this behavior is similar to what was found by Ref. [114]. As the magnitude of the *AC*

current decreases, superconductivity once again nucleates in the sample and, for negative current polarity, the normal state is never achieved. This significant asymmetry between the system dynamics for the positive and negative current polarities leads to the large V_{DC} observed. The physical origin of the asymmetry between the two halves of the current period will be discussed later on this Chapter.

For the final case, panel (c) shows the voltage as a function of time for a case of low V_{DC} that occurs after the red region. As also happened in panel (b), the system transits to the normal state for positive current polarity. The fundamental difference is that now the amplitude of the AC current is large enough to trigger a vortex dynamics that also destroys the superconducting state for negative current polarity. This leads to a reduction of the asymmetry between the two halves of the current period and a consequent reduction in the value of V_{DC}, that remains finite, once the system expends more time in the normal state for positive current polarity.

From Fig. 3, the distinction between FFD and NSD mechanisms in our system becomes clear. Panel (a) is an example of the vortex diode effect, with the finite DC voltage output coming from the asymmetric vortex dynamics for each current polarity. In contrast, panels (b) and (c) represent examples of the superconducting diode effect, once the finite V_{DC} comes from the asymmetry in the critical currents to the onset of the normal state in each polarity.

Given that panel (b) presents the interesting case of a superconductor diode with large V_{DC}, we now analyze with greater detail the vortex dynamics behind such physics. This is depicted in Figs. 4 and 5, which show the order parameter and local temperature evolution for each current polarity. Each row in this figure shows the state of the system at a given instant of time marked by a black circle in Fig. 3(b). Panels (a) and (b) show the system configuration at $t = 0$, when the magnitude of the applied AC current is still zero. As can be seen from panel (a), vortices penetrate the superconductor where the inhomogeneous field is stronger *i.e.* at the top surface. The vortex pattern display in this panel resembles the conformal crystal configuration, shown in Refs. [117, 118]. When the time evolves and the AC current amplitude becomes finite, vortices begin to move towards the lower edge (see panels (c) and (d))), while new vortices penetrate at the top edge. This process of creation and annihilation of vortices dissipate energy, as can be seen from the temperature plots. The heating causes the local suppression of superconductivity, but for such small current magnitudes, the heat is promptly removed from the system and the normal state is never achieved.

At a later instant of time, the magnitude of the AC current increases and its self-field becomes sufficiently strong to initiate the penetration of antivortices at the bottom edge (panels (e) and (f)). As they mutually attract, vortices and antivortices annihilates themselves. Due to the field asymmetry, this occurs near the bottom edge of the super-

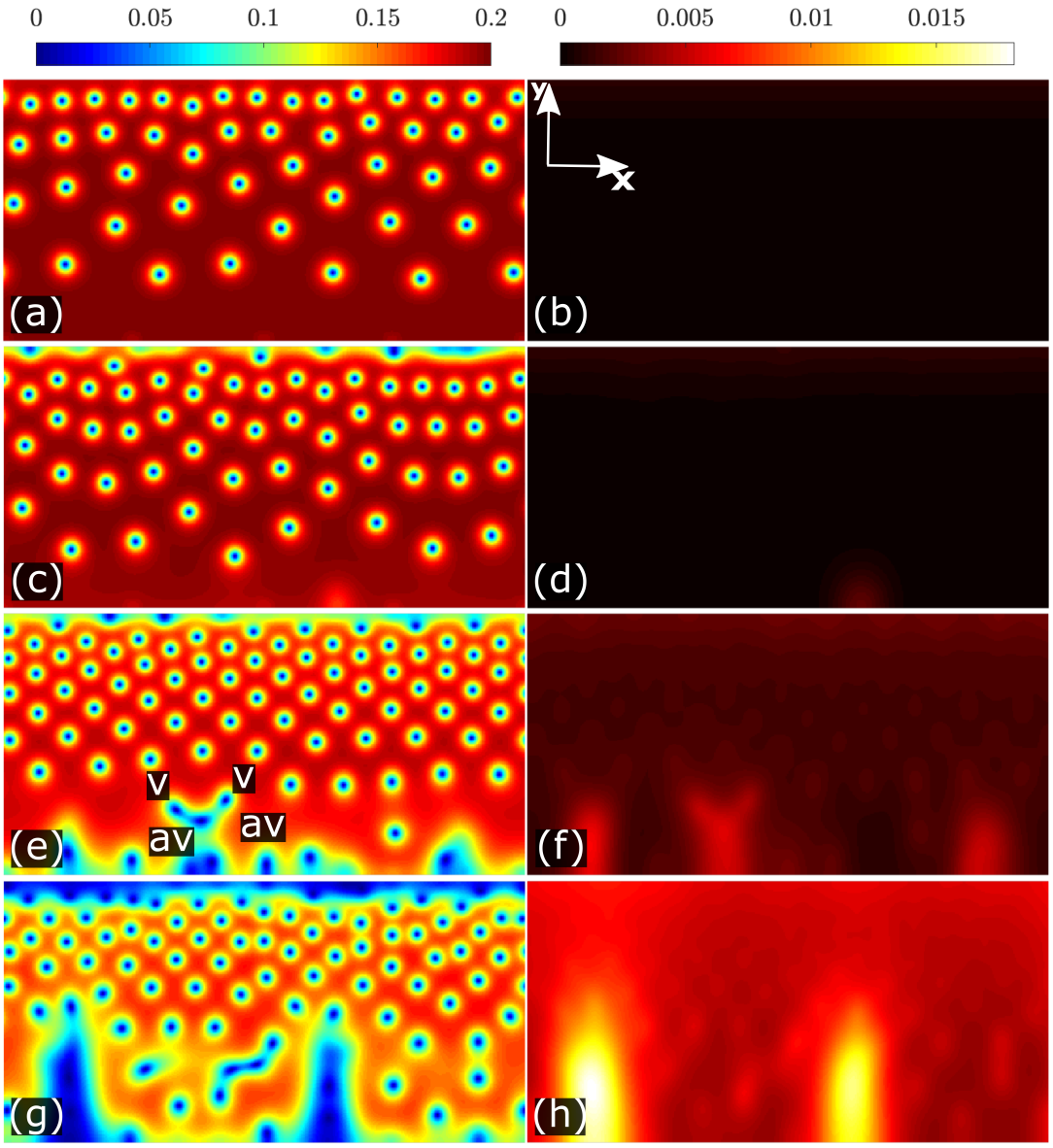

Figure 4 – *Color plot of the order parameter and local temperature difference $T - T_0$ at four different times for parameters corresponding to panel (b) in Fig. 3. Each line of the figure corresponds to a black circle in the positive current branch.*

conductor. To facilitate the visualization of each object, we have labeled a few vortices and antivortices with v and av. From the local temperature plot, we can see the hot spots that result from the v-av annihilation. For even larger AC current magnitudes (see panels (g) and (h)), the hot spots become supercritical and the heat cannot be removed from the superconductor at a sufficiently high rate. As a result, the superconducting state is suppressed in the whole system, only being recovered later, when the magnitude of the AC current decreases.

For the negative current polarity, the dynamics of the system is different. Exactly

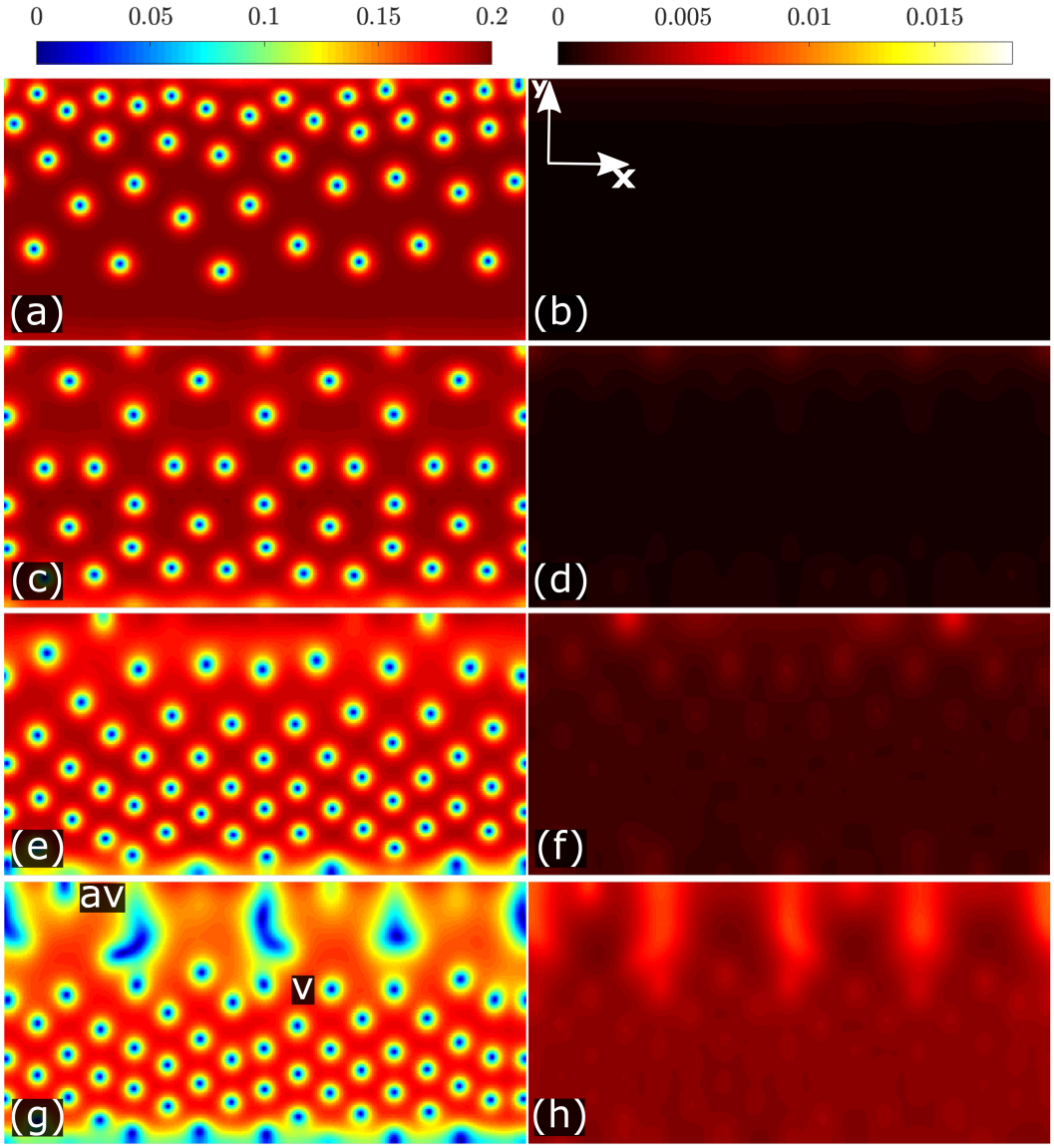

Figure 5 – *Color plot of the order parameter and local temperature difference $T - T_0$ at four different times for parameters corresponding to panel (b) in Fig. 3. Each line of the figure corresponds to a black circle in the negative current branch.*

at $t = \tau/2$, the conformal crystal like pattern of vortices is again reestablished (panels (a) and (b)). As the current becomes finite, the vortices leave the superconductor at the top edge, while new vortices are created at the bottom one (panels (c) and (d)). Once the external field is stronger at the top edge, surface barrier for vortex exit is larger, resulting in a smaller vortex velocity. Simultaneously, the field at the bottom edge is weaker, which means we have a smaller vortex density than what was obtained for positive current polarity. These effects diminish the dissipated heat and the hot spots are weaker (panels (e) and (f)). One can confirm this in panels (g) and (h), where the AC current magnitude is sufficiently strong to nucleate antivortices in the top edge and trigger the

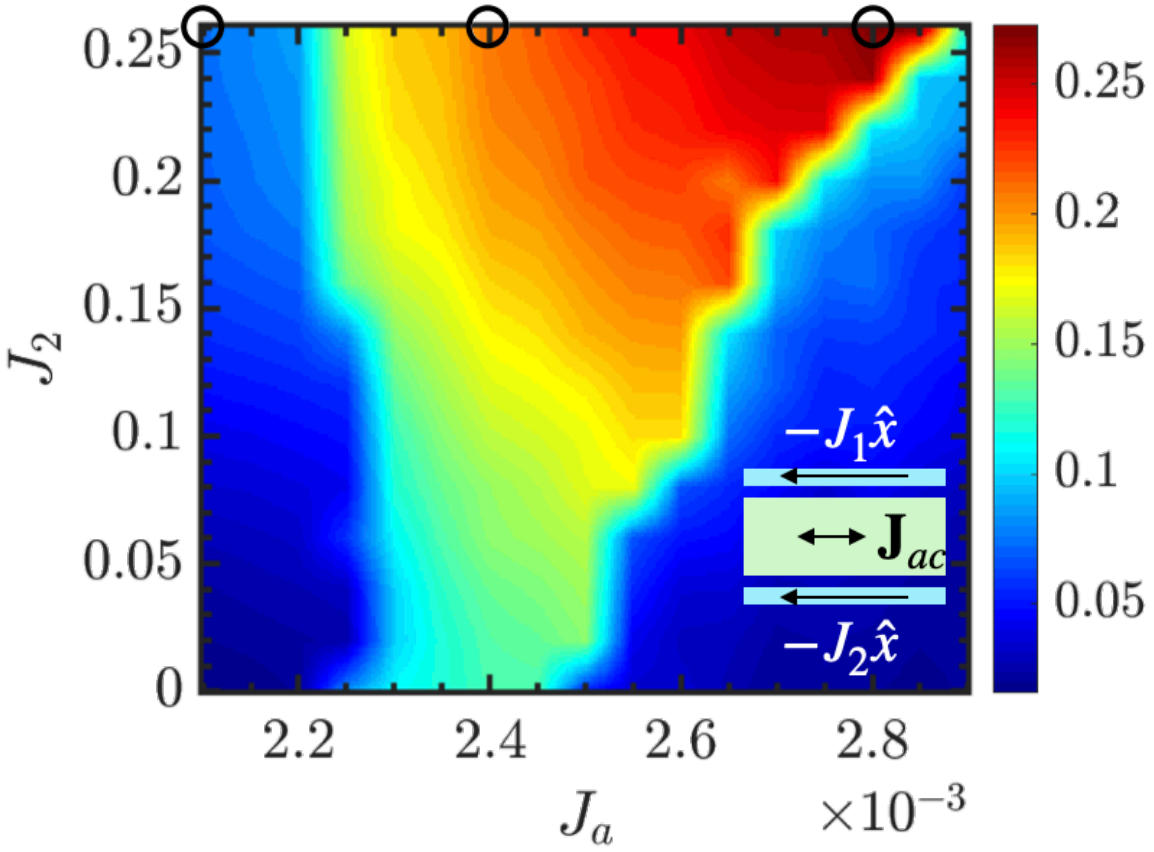

Figure 6 – *Phase-diagram displaying the color plot of the output voltage V_{DC} (in units of $V_0 = \hbar/2et_{GL}$) as a function of J_2 and the amplitude of the AC current (both in units of $j_0 = \sigma V_0/\xi(0)$). We fix $J_1 = 0.26$.*

v-av annihilation process, but the dissipated heat is never sufficient to send the system to the normal state.

4.3.2 Antisymmetric Flux Profiles ($J_1 = J_2$)

Although the physical system depicted in Figs. 4 and 5 displays the superconducting diode effect, the negative current polarity presents a finite resistance. This is in contradiction to the very aim of a superconducting diode, which is to present the functionalities of a semiconductor diode while allowing the flow of electrical current without energy dissipation. As we show in the following, one can overcome this by applying a finite J_2, such that the surface barrier for vortex penetration in the negative current polarity becomes large at a point where the self-field cannot overcome it, thus not allowing vortex penetration and producing a half-wave rectifier.

The phase diagram of the output voltage V_{DC} as a function of J_a and J_2 is shown in Fig. 6. In these calculations, we have fixed $J_1 = 0.26$. As a first feature, we can cite that the red region of large V_{DC} its wider when compared to Fig. 2, specially as J_2 increases.

For the perfectly antisymmetric case of $J_1 = J_2 = 0.26$, this feature is enhanced, with the red region being three times wider and V_{DC} twice as large as the results presented in Fig. 2. Fig. 7 helps us to understand the physics behind these enhancements by showing the voltage as a function of time for three values of J_a and $J_1 = J_2 = 0.26$. The positive current branch in panel (a) presents a case analogous to panel (a) of Fig. 3, as the voltage output becomes finite at an instant of time shortly after $t = 0$. As it was also the case before, the AC current magnitude is never sufficient to destroy the superconductivity state. The negative current branch, though, presents a completely new behavior, as the voltage output is zero for the whole half-period *i.e.* the system behaves as a half-wave rectifier.

The behavior of the negative current branch repeats itself in panel (b). Here, though, the v-av dynamics is capable of completely destroying the superconducting state for the positive current branch. This onset of the normal state also occurs in the positive current branch of panel (c). In this case, however, we can see that a region of finite voltage output appears for negative current polarity. This signals that the AC current self-field is strong enough to overcome the surface barrier imposed by the inhomogeneous field and vortices and antivortices penetrate the sample. The three voltage-time curves shown in Fig. 6 clearly explains the increment in V_{DC} observed for the perfectly antisymmetric inhomogeneous field profile. As the voltage output for the negative current polarity is always zero or very small, the asymmetry between the two current halves is much larger than the one obtained in Fig. 3, thus resulting in the significant DC voltage output. To conclude, we note that panel (b) presents the desired scenario for a superconducting diode, once it is able to display a large V_{DC} while maintaining half of the current period free from dissipation.

4.3.3 Hot Spot Dynamics

Let us now investigate in detail what is the physics behind the destruction of superconductivity due to vortex dynamics in the positive current branch. In Fig.8 we show the evolution of the order parameter (left column) and local temperature increment (right panel) for the positive current polarity of the case depicted in panel (b) of Fig. 7. Each line in this figure represents a given instant of time.

In panels (a) and (b), we can identify the processes of vortex creation, flow and annihilation. If we note that the hot spots associated with the v-av annihilation at the middle of the sample are stronger than the ones emerging from vortex nucleation and flow, we can conclude that it is v-av annihilation that commands the dissipation of heat in our system. Thus being, one of the advantages of the perfect antisymmetric inhomogeneous field profile is that it guarantees the occurrence of v-av collision, once they appear in the same number and meet at the center of the superconductor. For currents much smaller

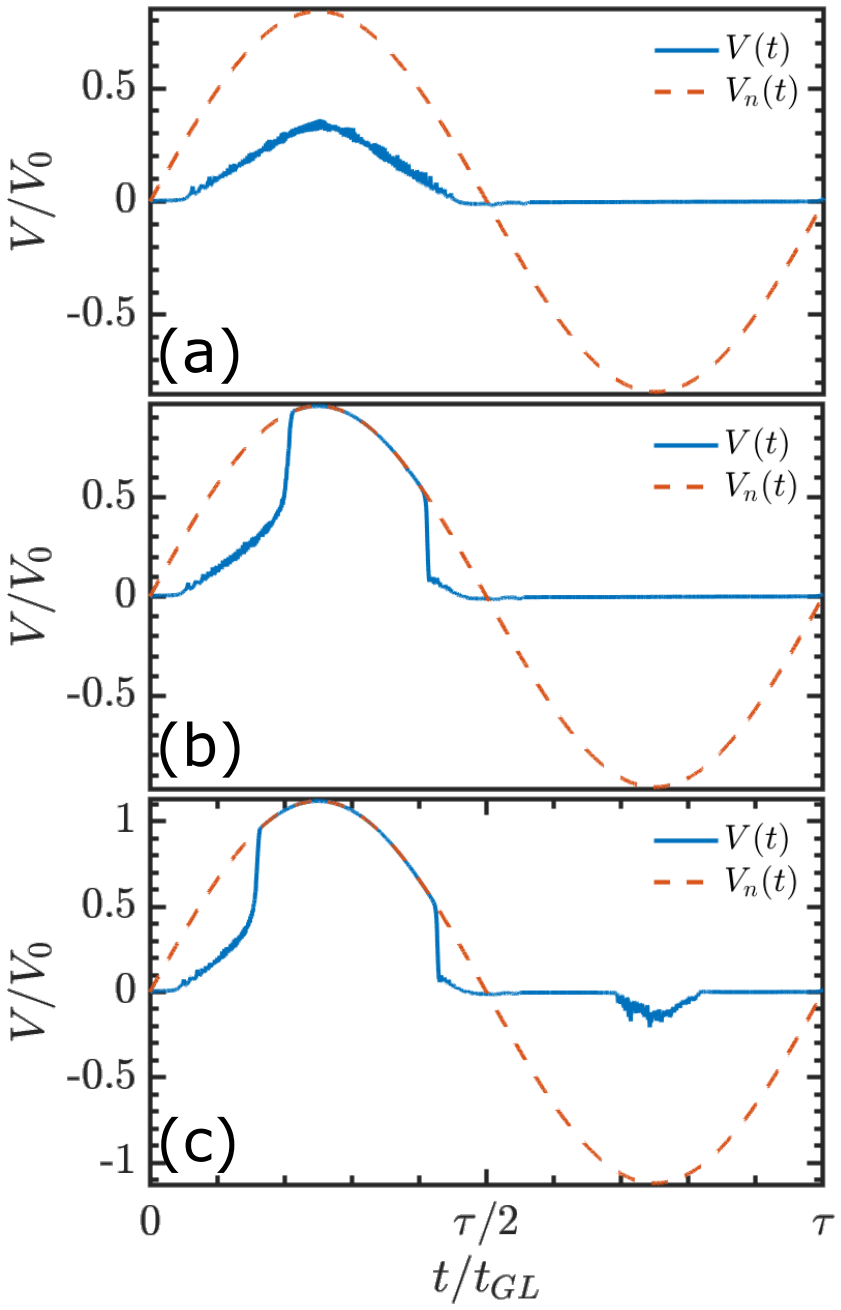

Figure 7 – *The voltage signal as a function of time (solid blue line) for* $J_1 = J_2 = 0.26$ *and three current values,* $J_a = 2.10 \times 10^{-3}$ *(panel (a)),* $J_a = 2.40 \times 10^{-3}$ *(panel (b)) and* $J_a = 2.80 \times 10^{-3}$ *(panel (c)). In each panel, the red dashed lines represent the voltage if the system was in the normal state.*

then I_c^+, the heat removal mechanism is sufficient to remove all the dissipated heat of the hot spots, which gradually disappears. By comparing panels (b) and (d), one can see that the three hot spots on the left side of panel (b) are examples of such dynamics. On the other hand, the mechanism behind the total suppression of superconductivity can be visualized in the hot spots on the right of panel (d). In this case, heat removal is not strong enough to completely remove the hot spots. As a consequence, the superconducting

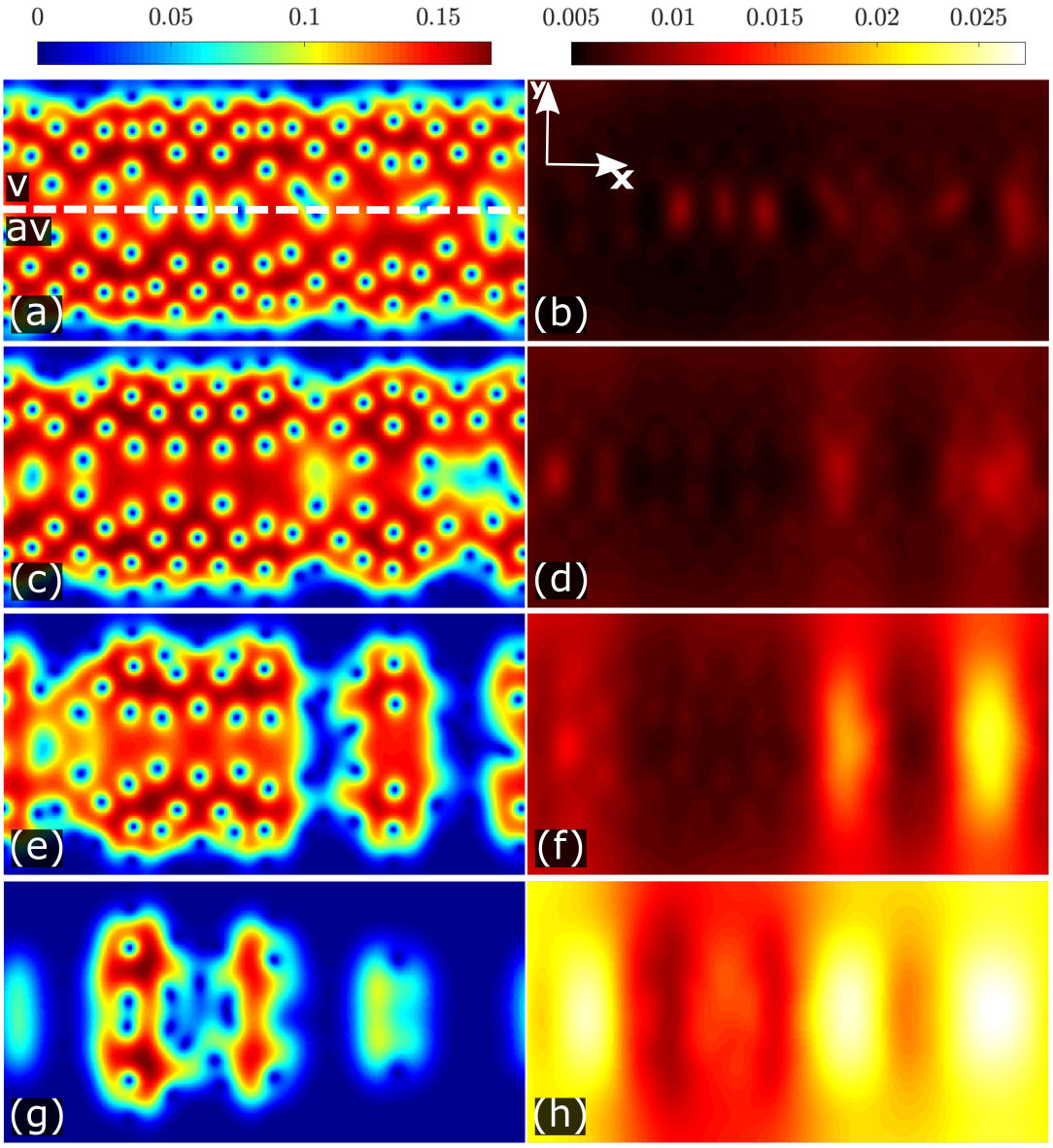

Figure 8 – *Evolution of the order parameter (panels in the left column) and the temperature increment $T - T_0$ (panels in the right column) before the destruction of the superconducting state for parameters of panel (b) in Fig. 7. The white dashed line depicted in panel (a) delineates the superconductor into two distinct halves, with the magnetic flux being composed by vortices in the top region and antivortices in the bottom one.*

state is locally suppressed in this region, attracting more v-av pairs. This triggers a chain reaction that leads to the formation of stripes with depleted superconductivity along the width of the system, as can be seen in panels (e) and (f). Such stripes spread across the entire system and eventually provoke the onset of the normal state, as depicted in panels (g) and (h).

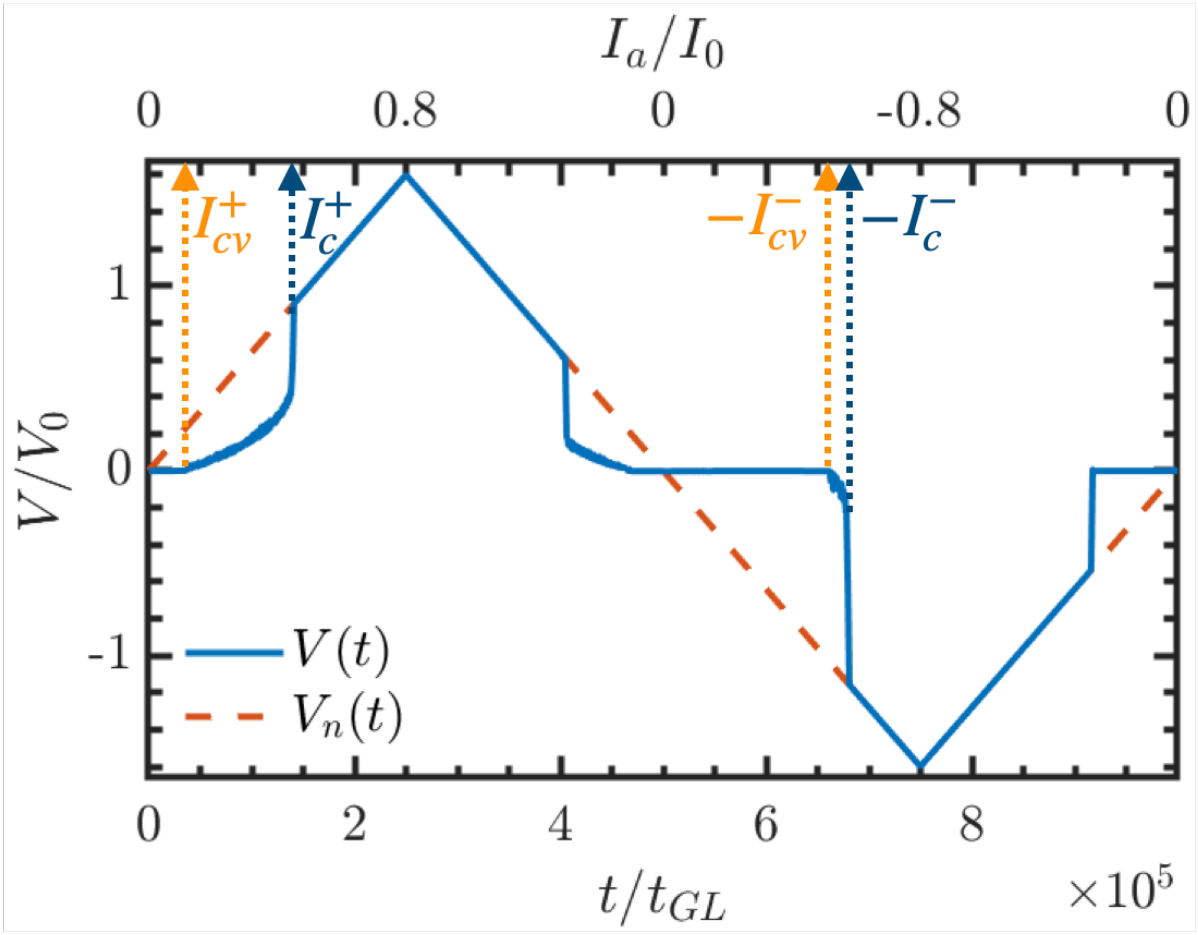

Figure 9 – *The voltage signal as a function of time (solid blue line) for a linear current cycle with $J_1 = J_2 = 0.26$ and total sweep time $\tau = 10^6 t_{GL}$). Red dashed curve represents the normal state voltage. The arrows represent the critical currents for the complete destruction of the superconducting state (dark blue) and the onset of vortex motion (orange) at each current polarity.*

4.3.4 Diode Efficiency

Once we have identified the physical behavior behind our superconducting diode, we now investigate the diode efficiency of our system, which is given by $\epsilon_{NSD} = (I_c^- - I_c^+) / (I_c^- + I_c^+)$, with $I_c^\pm$ being the critical current to the onset of the normal state in each current polarity. We do this by replacing our sine wave AC current by a linear AC current, with period equal to $\tau = 10\tau_0 = 10^5 t_{GL}$. This procedure approximates our simulations to real physical experiments where current is slowly swept. For all simulations presented in this subsection, we have fixed $J_1 = J_2 = 0.26$, thus exploring the most favorable scenarios for our superconducting diode. The voltage as a function of time for such system is presented in Fig. 9. In this figure, critical currents $I_c^\pm$ are indicated by blue arrows and their values give a diode efficiency of $\epsilon_{NSD} = 0.124$.

Let us now investigate the vortex diode effect. To do this, we define the critical

currents I_{cv} in Fig. 9 (marked by orange arrows), which mark the onset of the flux flow. The FFD efficiency is then defined as $\epsilon_{FFD} = (I_{cv}^{-} - I_{cv}^{+}) / (I_{cv}^{-} + I_{cv}^{+})$ and the values obtained in Fig. 9 give us $\epsilon_{FFD} = 0.619$. Clearly, this value is much larger than ϵ_{NSD}. The reason behind this disparity is the fact that the AC current self-field matches the inhomogeneous field profile for positive current polarity. This leads to the presence of several vortices and antivortices in the superconductor, which means that a small applied current is sufficient to trigger the flux flow. In contrast, the AC current self-field opposes the inhomogeneous field profile for the negative current polarity. As a consequence, a large current magnitude is necessary to allow vortex entry and motion. This large difference between the behavior of each current polarity is the origin of the large ϵ_{FFD} obtained. In cases where the system presents strong thermally activated processes, I_{cv} is not well defined and one should use ϵ_{NSD} as the measure of the diode efficiency.

To facilitate the visualization of the vortex and superconducting diode effect, Fig. 10 shows the absolute value of the output voltage $|V(t)|$ as a function of the total applied current $|I_a(t)|$. Blue and yellow regions highlighted in this figure represent the superconducting and vortex rectification, respectively, while green region depicts the overlap between the two effects. Here, the route to optimize the diode efficiency becomes clear. First, for the negative current polarity, one should increase I_c^{-}. This means that the Bean-Livingston barrier must be as large as possible for negative current polarity. Simultaneously, for the positive current polarity, I_c^{+} must be diminished, or, in other words, must approach the value of I_{cv}^{+}, anticipating the onset of the normal state due to the vortex dynamics.

4.3.5 Optimizing Diode Efficiencies: The Role of Heat Removal and Sweep Rate

Until this point in our analysis, we have kept $\eta = 2 \times 10^{-4}$ fixed in the heat diffusion equation. This mimics the behavior of a system with moderate heat removal efficiency. Now that we know that the heat generated in v-av annihilation is the key mechanism behind the diode effect, it is natural to assume that the heat removal capability of our system directly affects the diode efficiency, once it changes the hot spots dynamics. In Fig. 11, we show ϵ_{NSD} and ϵ_{FFD} as a function of η, with values representing weak ($\eta = 2 \times 10^{-5}$) and strong ($\eta = 2 \times 10^{-3}$) heat removal scenarios.

Since for currents near I_{cv}^{+} the heat generated by the slow moving vortices is rather small, the efficiency of the vortex diode effect weakly depends on η. On the other hand, as the current increases, the hot spots dynamics becomes more important to the behavior of the system. In this manner, for large η values, heat removal is strong and the formation of supercritical hot spots is delayed, thus increasing the current to the transition to the normal state. For small values of η, the behavior is the opposite and now even a small

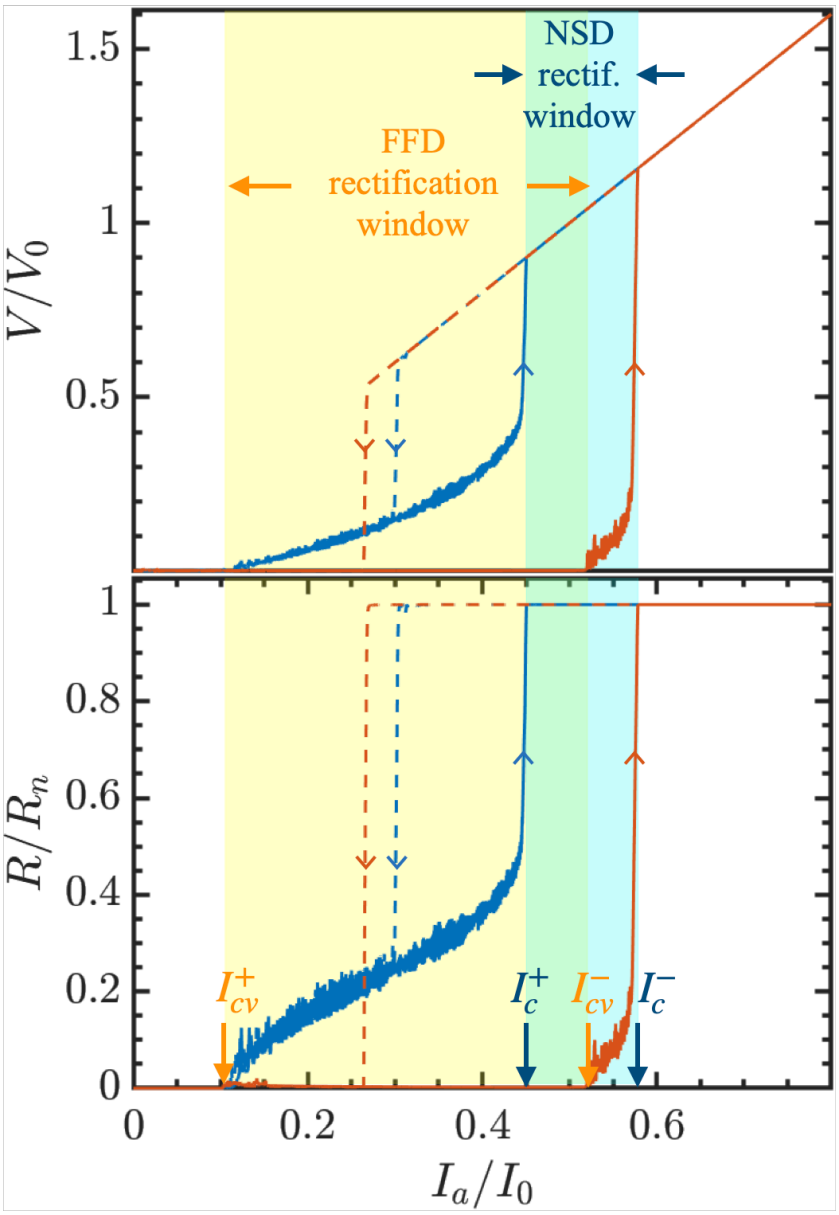

Figure 10 – *Top panel shows $|V(t)|$ as a function of $|I_a(t)|$. Blue and red curves represent the half period with positive and negative $J_a(t)$, respectively. Solid and dashed lines represent the regions where $|I_a(t)|$ is being increased and decreased, respectively. Yellow and blue background marks the current region of vortex and diode rectification, with green background depicting the region where they coexist. Bottom panel shows $R(t)$ as a function of $|I_a(t)|$, with the same definitions of the top panel following.*

hot spot can be sufficient to destroy the superconducting state, thus approaching I_c^+ to I_{cv}^+. For negative current polarity, though, both I_c^- to I_{cv}^- weakly depends on the value of η, once the system is free from vortices up to a large applied current and heat diffusion effects are not so important. Combining the behavior of the positive and negative current branch described above, lead to a significant increase of ϵ_{NSD} from 0.067 to 0.317 as η is

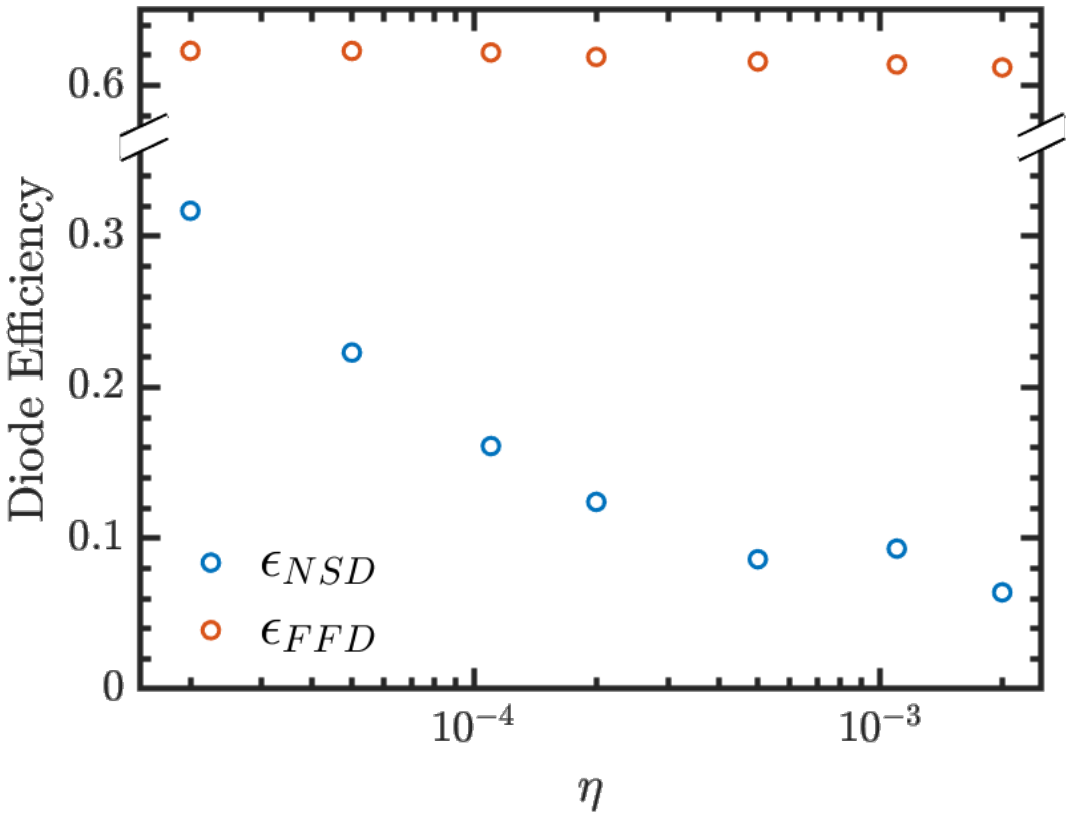

Figure 11 – *Efficiencies of the superconducting, ϵ_{NSD} (blue circles), and vortex, ϵ_{FFD} (red circles), diode effects as a function of the heat transfer coefficient η. Here, we set $\tau = 10^6 t_{GL}$.*

reduced from 2×10^{-3} to 2×10^{-5}. This signs to us that, to optimize our diode efficiency, one must use a substrate with weak heat removal capability.

It is important to mention that our $2D$ simulations do not take into account the heat diffusion along the thickness of the sample. If one consider a full $3D$ system, heat removal can be even weaker, which could trigger the normal state shortly after the beginning of the flux flow at I_{cv}^{+}. Such mechanism could be behind the diode superconducting diode investigated in Ref. [90]. In this case, the complete destruction of the superconducting state would occur due to the vortex and antivortex penetration in the system and the flux flow region would never be observed.

A quantity that is important from the experimental point of view is the total sweep time of the applied AC current, τ. In Fig. 12 we show how ϵ_{NSD} and ϵ_{FFD} changes with τ. For all cases, $\eta = 2 \times 10^{-5}$ is fixed. One can note that both efficiencies have the same qualitative behavior *i.e.* a rapid increase for small values of τ and the tendency to reach an asymptotic value at large τ. For this case all critical currents ($I_c^{\pm}$ and $I_{cv}^{\pm}$) decreases as τ increases. The in increment in efficiency is due to fact that critical currents at positive branch decreases more than the ones for the negative polarity. To understand this, note that small values of τ leads to larger I_c and I_{cv}, because the system has less time to evolve

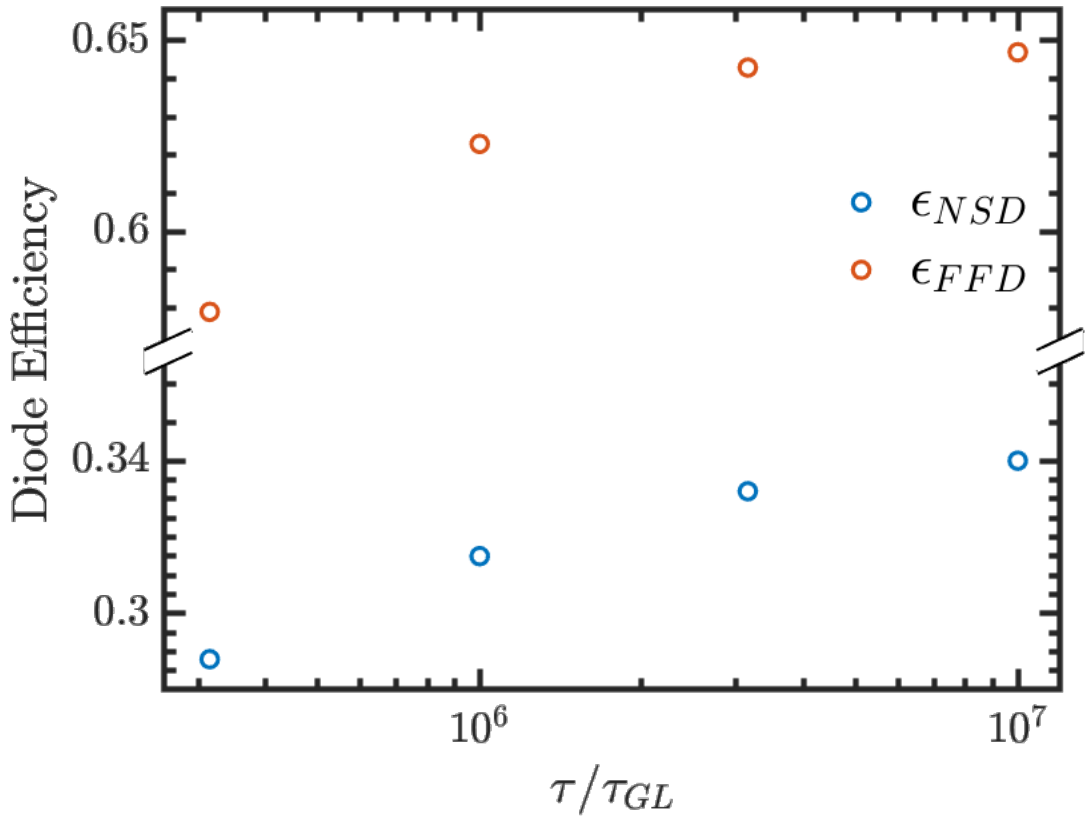

Figure 12 – *Efficiencies of the superconducting, ϵ_{NSD} (blue circles), and vortex, ϵ_{FFD} (red circles), diode effects as a function of total sweep time τ. Here, $\eta = 2\times10^{-5}$.*

to next state.

4.3.6 Optimizing Diode Efficiencies: The Role of the Inhomogeneous Field Amplitude and Shape

So far in our discussion for the perfect antisymmetric inhomogeneous field profile we have fixed $J_1 = J_2 = 0.26$ and the distance $s = 5\xi(0)$ between the central film and the lateral stripes. Let us now investigate how diode efficiency changes as the strength and shape of the magnetic field vary. To do this, we initially fix $s = 5\xi(0)$ and set $J_1 = J_2 = J$ and vary the value of J. Calculations are once again carried with a linear AC wave with time $\tau = 10^6 t_{GL}$ and $\eta = 2 \times 10^{-5}$. The critical currents $I_c^{\pm}$ (blue and red circles) and $I_{cv}^{\pm}$ (blue and red dots) are shown in panel (a) of Fig. 13. As one can see, the behavior of I_{cv}^{+} and I_c^{+} is rather simple, as they decrease with J. This is the case because, the larger the applied field, the larger the number of vortices for the positive current branch, which leads to a decrease in the necessary current to initiate vortex motion and, consequently, the onset of the normal state. On the other hand, for negative current polarity, a larger external field increases the Bean-Livingston barrier for the system, this increasing I_{cv}^{-} and I_c^{-}. But for strong enough values of J, the field becomes too strong and helps in the

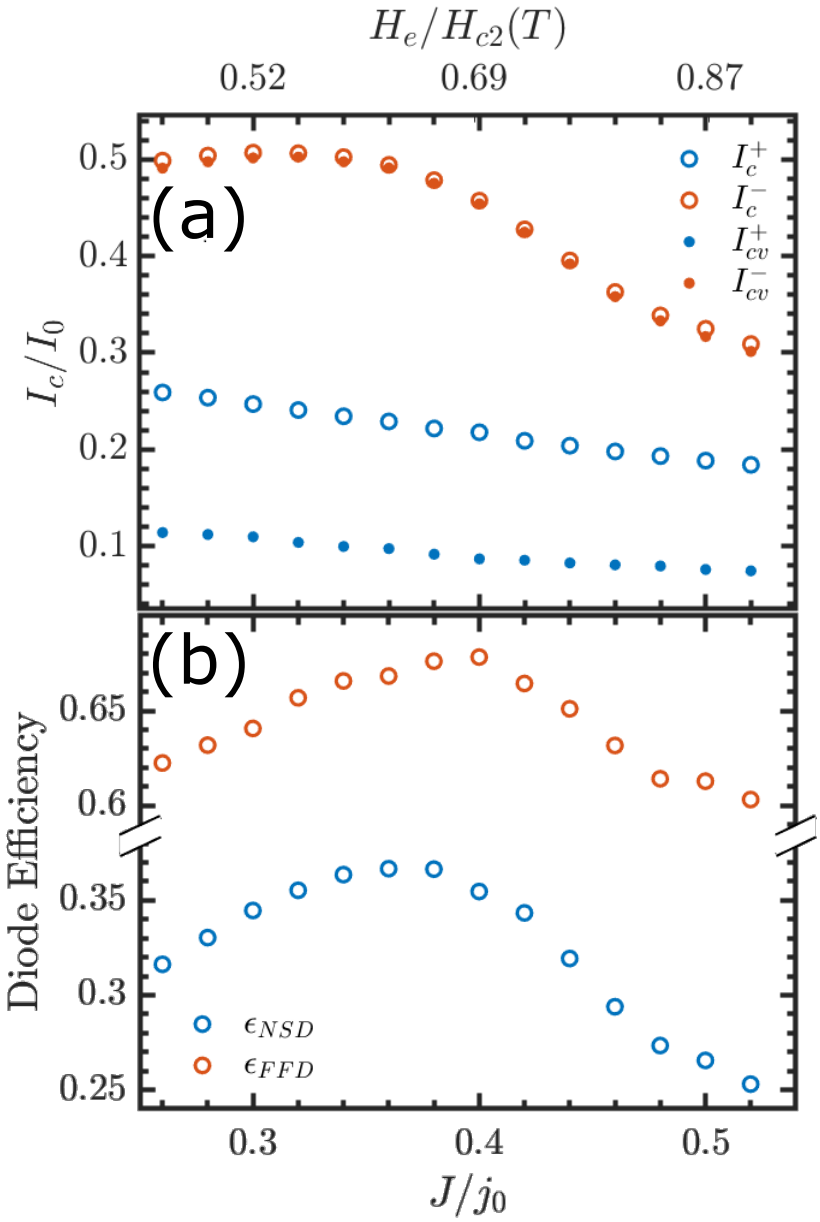

Figure 13 – *Panel (a) shows the critical currents I_c^+ (blue circles), I_c^- (red circles), I_{cv}^+ (blue dots) and I_{cv}^- (red dots) as a function of the current density in the side stripes J. Panel (b) shows ϵ_{NSD} (blue circles) and ϵ_{FFD} (red circles) as a function of J. Top x axis relates J with the value of the inhomogeneous field at the sample edges H_e.*

destruction of the superconducting state, then diminishing I_{cv}^- and I_c^-. This is the origin of the non-monotonic behavior of the critical currents for negative polarity.

This non-monotonic and asymmetric behavior leads to the existence of an optimal value of J at which the diode efficiency is the largest. ϵ_{NSD} (blue circles) and ϵ_{FFD} (red circles) as a function of J is shown in panel (b) of Fig. 13. This shows to us that $J \approx 0.36$ is the optimal value for the superconducting diode effect, while $J \approx 0.40$ maximizes the vortex diode effect.

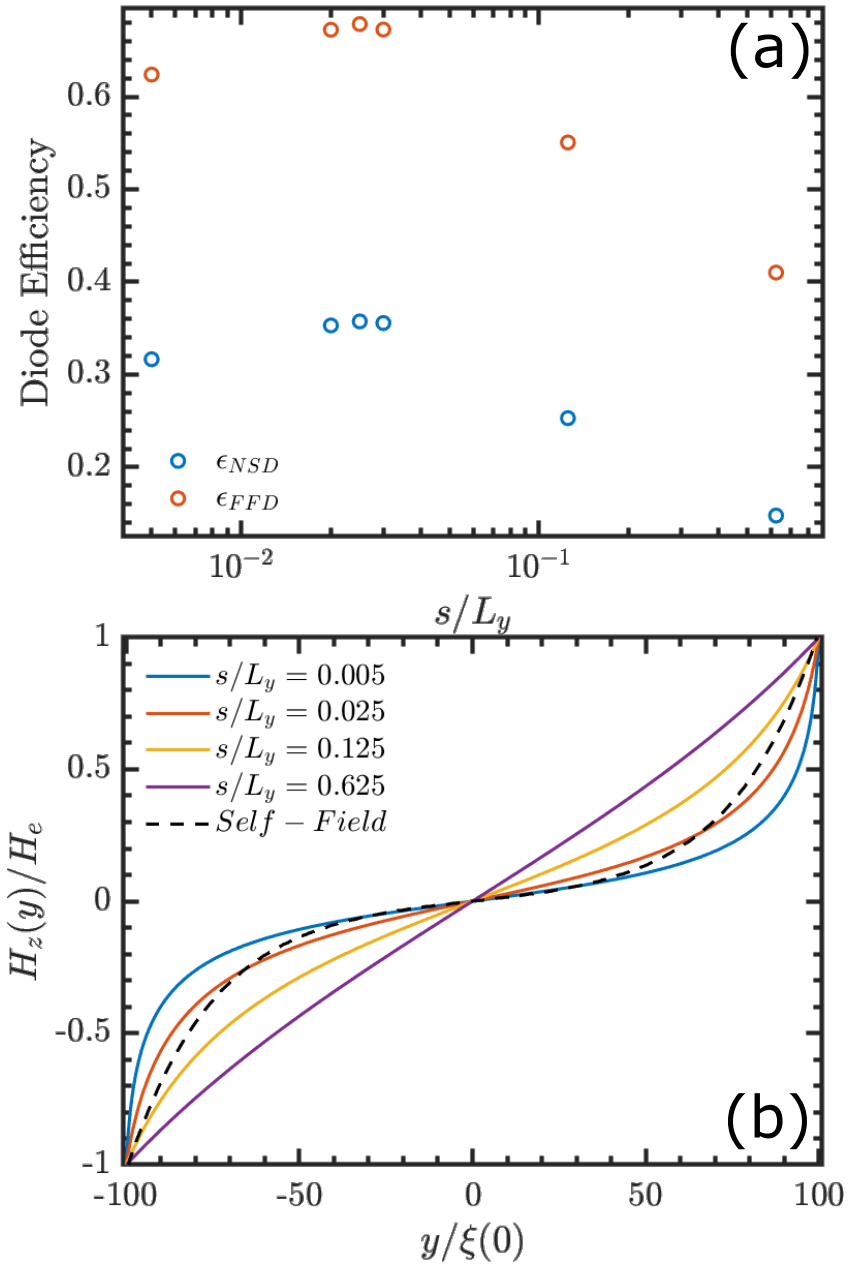

Figure 14 – *Panel (a) shows the diode efficiency as a function of the separation between the superconducting film and the lateral wires carrying a current chosen as to induce* $H_e = 0.69H_{c2}(T)$*. Panel (b) presents the inhomogeneous field profile for different values of* s/L_y *(solid lines) and the self-field profile of the central superconducting film (black dashed line). All curves are normalized by the field at the edges.*

In our simulations, the inhomogeneous field comes from the current carrying side stripes. However, we note that the existence of maximum values of ϵ_{NSD} and ϵ_{FFD} does not depend on the origin of the field, but solely on its strength. The same qualitative efficiency behavior could be found, for example, if the external field is produced by the ferromagnetic material depicted in Fig. 1. To facilitate such analysis, the top x axis in Fig. 13 represents

the value of the external field magnitude H_e at the superconductor edge for a given value of J. As can be seen, in terms of field magnitude, the maximum superconducting diode efficiency occurs for $H_e \approx 0.62H_{c2}(T)$ while the vortex diode efficiency presents its maximum for $H_e \approx 0.69H_{c2}(T)$. These results serve as a guide for the experimental realization of optimal superconducting diodes for systems that relay on inhomogeneous magnetic fields.

Finally, we investigate the role of the inhomogeneous field shape in the behavior of our system. Different shapes of the external field can be achieved by tuning the separation s, with small values of s resulting in a field profile more concentrated at the stripe edges, while large separations lead to a linear field profile (see solid lines in panel (b) of Fig. 14). We note that, for $s/L_y = 0.025$, the inhomogeneous field resembles the profile of the stripe self-field in the absence of vortices. The diode efficiencies as a function of s/L_y is shown in panel (a) of Fig. 14, where the value of J in each case is chosen such that we have $He = 0.69H_{c2}(T)$ at the film edges. As we can see, the largest efficiency occurs exactly for $s/L_y = 0.025$. We can conclude, then, that the optimal diode efficiency can be achieved by using a inhomogeneous field that most perfectly matches the profile of the stripe self-field, thus compensating the effect of the applied current in one polarity, maximizing its critical current.

4.4 Concluding Remarks

To conclude, in this chapter we have investigated the interplay between the different mechanisms of the superconducting diode effect in a superconducting film in the presence of external inhomogeneous fields. As we shown, such fields are capable of introducing highly asymmetric conditions for vortex dynamics, thus being excellent candidates for the design of efficient vortex diodes. As a great advantage, our proposed system does require complex nanofabrication, with the inhomogeneous field being introduced by two current carrying wires coplanar to the main superconducting film.

Furthermore, our simulations also review that an external field with a perfect antisymmetric profile leads to the optimization of the diode effect. This occurs because such flux profile maximizes the difference in the Bean-Livingston barrier for each current polarity. For positive current polarity, the profile of AC current self-field matches the external field, leading to the coexistence of vortices and antivortices in the superconductor. As the v-av pairs are annihilated at the center of the sample, hot spots are formed and eventually the system transits to the normal state. On the other hand, for negative current polarity, the profile of the AC self-field opposes the external flux, which enhances the Bean-Livingston barrier, protecting the existence of the Meissner state. as we have shown, such system leads to a half-wave rectifier for a wide range of parameters.

As a final remark, we have also provided experimental routes for the optimization of our diode system and other superconducting diodes in general. For instance, we have shown that the use of substrates with weak heat removal capability enhances the superconducting diode efficiency. Also, we demonstrated that the sweep rate of the current or the frequency of the AC current is important for the final result. Such findings help to understand and improve the physics of superconducting diode systems.

5 Stability limits of flux states in two-band superconducting rings

The existence of different overlapping sheets at the Fermi surface of a superconductor gives rise to the so called multiband superconductivity, characterized by more than one condensate. [119, 120] Since several of the novel superconducting materials that emerged in the last years are multiband superconductors, this topic has seen a revival of its interest in the literature, after beeing discussed for the first time in the late fifties. [121, 122] As examples of such materials, we can mention MgB_2, [123, 124] iron pnictides, [125] $NbSe_2$, [126, 127] iron arsenides, [128] among others.

The presence of different condensates has also rendered multiband superconductors of great interest due to their magnetic properties. One of them is the possibility of non-monotonic vortex-vortex interaction, with short-range repulsion and long-range attraction, arising through the competition between the coherence length of each condensate. [129] Such interaction leads to the formation of vortex clusters, separated by Meissner state regions in bulk specimens. [129] This vortex matter behavior is known as type-1.5 superconductivity [130] and has raised a great amount of discussion. [131, 132, 133, 134, 135] Recently, vortex stripes formation have been experimentally observed in the heavy fermion superconductor UTe_2. [136]

Another phenomenon observed in multiband superconductors is the possibility of vortices carrying a non-integer multiple of the flux quantum. [137, 138] Such objects can occur either when the phase winding of different condensates are not equal or when the phase singularities of each condensate occur at different points inside the superconductor. Fractional vortices have been extensively theoretically studied in the past [139, 140, 141, 142, 143, 144, 145, 146, 147, 148] and recently experimentally observed in different superconductor materials. [149, 150, 151] These recent experimental breakthroughs have renewed the interest in understanding how the presence of multiple order parameters influences the behavior of various superconducting systems. In this chapter, we explore two-band superconductor rings under an external magnetic field and establish the stability boundaries between different flux states. Specifically, we determine the critical flux at which the winding number of one or both order parameters changes.

It was also shown that the multiband superconductors have interesting properties in the presence of an external current [152]. For instance, two-band superconductors can display a state where the phase difference between their two condensates is neither locked at 0 or π, the so called phase soliton state. [153, 154, 155, 156, 157, 158, 159] In $1D$

two-band systems, it was shown that such states can emerge from the application of a current to the superconductor, [160, 161] with the detectable appearance of oscillations of the critical current with the length of the system, provided that the interband coupling is small. [162] In two-band systems with higher dimensions, the possibility of vortex formation and its subsequent motion give origin to nonequilibrium phase textures, which significantly affects the dissipation process. [163] Recently, the formation of phase-slips in quasi-one dimensional two-band superconductors, analogously to their one-band counterpart wires,[164, 165, 166, 167, 168, 169, 170] was studied and the time evolution of phase solitons and the conditions for their existence in such scenario were systematically described.

In the case of a superconducting loop that encloses an applied flux, the single-valuedness of the order parameters ensures that the fluxoid is quantized. The passage between different fluxoid numbers necessarily involves the vanishing of an order parameter at some instant and position, permitting the occurrence of a phase slip. Such a system was extensively studied for single band superconductors [171, 172, 173, 174, 175, 176, 177], with prospects of utilization in a number of applications, such as a superconducting qubit and several electronic devices [178, 179, 180, 181, 182, 183, 184, 185, 186, 187]. Of particular interest to the present study is the deterministic phase-slip, which occurs when the energy barrier separating two flux states vanishes. [176, 188] For single-band superconductors, analytical expressions for the conditions to the occurrence of a deterministic phase-slip have been found combining linear instability theory and Ginzburg-Landau formalism. [176, 177] In this study we use linear stability theory together with the Ginzburg-Landau formalism for two-band superconductors and derive a semi-analytical method to obtain the critical flux for the transition between two fluxoid states in a superconducting loop. Furthermore, we show that our analytical results are in agreement with the full Ginzburg-Landau theory and investigate how the system behavior depends on parameters such as the ring radius, the ratio between the diffusion coefficients of each band, and the temperature. In Refs. [176, 177], the stability of single-band superconductors was studied under the action of an external field varied at a finite rate. In the present chapter, when investigating the stability of different fluxoid states in two-band superconductors, the flux is either kept fixed or changed quasistatically.

The structure of this manuscript is as follows. In Sec. 5.1 we introduce the time-dependent Ginzburg-Landau equations for two-band superconductors. In Sec. 5.2 we detail how linear stability theory is used to obtain stability limits for our system and compare them with fully numerical results. We apply our method under different physical conditions in Sec. 5.3. Finally, we present our concluding remarks in Sec. 5.4.

5.1 Theoretical Formalism

The time dependent Ginzburg-Landau equations for a two-band system, in dimensionless units, are given as follows [24]:

$$\begin{aligned}\left(\frac{\partial}{\partial t}+i\varphi\right)\Delta_1 &= -\left(-i\boldsymbol{\nabla}-\mathbf{A}\right)^2\Delta_1 \\ &\quad +\left(\chi_1-|\Delta_1|^2\right)\Delta_1+\gamma\Delta_2\ , \qquad (5.1)\\ \left(\frac{\partial}{\partial t}+i\varphi\right)\Delta_2 &= -\frac{D_2}{D_1}\left(-i\boldsymbol{\nabla}-\mathbf{A}\right)^2\Delta_2 \\ &\quad +\left(\chi_2-|\Delta_2|^2\right)\Delta_2+\frac{\eta_1}{\eta_2}\gamma\Delta_1\ , \qquad (5.2)\end{aligned}$$

and the Ampère's law is:

$$\frac{1}{u}\left[1+\frac{\eta_2}{\eta_1}\frac{D_2}{D_1}\right]\left(\frac{\partial\mathbf{A}}{\partial t}+\boldsymbol{\nabla}\varphi\right)=\mathbf{J}_s-\kappa_1^2\boldsymbol{\nabla}\times\mathbf{h}\ , \qquad (5.3)$$

where the supercurrent density is given by:

$$\mathbf{J}_s=\sum_{j=1}^{2}\frac{\eta_j}{\eta_1}\frac{D_j}{D_1}\mathrm{Re}\left[\Delta_j^*\left(-i\boldsymbol{\nabla}-\mathbf{A}\right)\Delta_j\right]\ . \qquad (5.4)$$

In the equations above, D_j and η_j are the diffusion coefficient and the partial density of states of band j; χ_j is defined as $\chi_j=(T_{cj}-T)/T_c$, where the ratio between the critical temperature of the j band and the critical temperature of the coupled system (T_{cj}/T_c) is defined in Ref. [133]; γ is defined as $\gamma=\lambda_{12}/(\eta_1\delta)$, where $\delta=\lambda_{11}\lambda_{22}-\lambda_{12}^2$ is the determinant of the coupling constant matrix with components λ_{ij}. Finally, κ_1 is defined as the ratio between the coherence length at zero temperature $\xi_1=\sqrt{\pi\hbar D_1/8T_c}$ and the penetration length at zero temperature $\lambda_1=\sqrt{(1/N(0)\eta_jD_1)(7\zeta(3)\hbar c^2/32\pi^4e^2T_c)}$ of the first band. The order parameters Δ_j are in units of $8\pi^2T_c^2/7\zeta(3)$; lengths are expressed in units of the coherence length of the first band ξ_1; the magnetic field and the vector potential are given in units of $H_{c2}^{(1)}$ and $H_{c2}^{(1)}\xi_1$, respectively, where $H_{c2}^{(1)}=\Phi_0/(2\pi\xi_1^2)$, with $\Phi_0=hc/2e$ being the magnetic flux quantum unit; the scalar potential is in units of $\varphi_0=H_{c2}^{(1)}D_1/c$; the current densities in units of $j_0=4eN(0)\eta_1\pi^3T_cD_1/(7\zeta(3)\xi_1)$; and time in units of $t_0=\xi_1^2/D_1$. In Eq. (5.3), we have $u=5.79$, as in the case of single-band superconductors.

We have chosen the microscopic parameters of our two-band superconductor as follows. The coupling constants are given by $\lambda_{11}=2.0$, $\lambda_{22}=1.03$ and $\lambda_{12}=0.005$. The partial density of states of band 1 is $\eta_1=0.355$ ($\eta_2=1-\eta_1$). These parameters correspond to a critical temperature of each band given by $T_{c1}=0.9997T_c$ and $T_{c2}=0.903T_c$. The ratio D_1/D_2 is left as a free parameter for our subsequent analysis. Our problem consists of finding the local minimum of the system energy and then investigate at which critical

flux this minimum becomes a saddle point *i.e.* the flux at which it is no longer stable. To do so, we use the TDGL equations.

As derived in Ref. [24], the TDGL equations above are strictly valid only for gapless superconducting states. However, since we are using TDGL as a mathematical tool to find a local minimum, our procedure is valid as long as the Ginzburg-Landau expression for the free energy remains valid. As a by-product, we will obtain a qualitative description of the transient passage between states and the phase-slip that occurs during this passage.

In what follows, we consider a superconducting ring of radius R placed in an homogeneous applied field in such a manner that the ring in the normal state would enclose an amount of flux Φ. We consider that the ring width and thickness are much smaller than all characteristic lengths of the system (the coherence lengths of each band, the penetration length of the superconductor and R), thus the ring is effectively one-dimensional. This implies that the Ampère law (5.3) does not need to be solved, the vector potential can be taken uniform in the entire ring and is given by $\boldsymbol{A} = \Phi/(2\pi R)$.

When numerically solving the time dependent Ginzburg-Landau equations, we applied the link-variable method [189] which guarantees gauge invariance throughout the numerical procedure. In order to simulate the ring geometry for the one-dimensional system, we use periodic boundary conditions $\Delta_j(0) = \Delta_j(L)$, $\varphi(0) = \varphi(L)$, where L is the ring length $L = 2\pi R$. The use of periodic boundary condition gives rise to a numerical problem, since every single point of the grid is equivalent. In such scenario, nonuniform states would never be encountered, since there is no preferred position for the nucleation of this configuration. To overcome this difficulty, we randomly insert inhomogeneous spots in the ring by locally changing the temperature by a physically negligible amount in the order of $10^{-5}T_c$. The location of these spots and the specific value of the temperature increment do not alter the results presented here.

5.2 The Linear Stability Theory

In this section, we apply linear stability theory to the problem of passage between states with different winding number in a two-band superconductor. To our knowledge, this method has been used in the past only for single-band superconductors.

Our starting point is the first Ginzburg-Landau equation in the one-dimensional form:

$$\left(\frac{\partial}{\partial t}+i\varphi\right)\Delta_1 = -\left(-i\frac{\partial}{\partial x}-A\right)^2\Delta_1 + \left(\chi_1-|\Delta_1|^2\right)\Delta_1+\gamma\Delta_2\,, \tag{5.5}$$

$$\left(\frac{\partial}{\partial t}+i\varphi\right)\Delta_2 = -\frac{D_2}{D_1}\left(-i\frac{\partial}{\partial x}-A\right)^2\Delta_2 + \left(\chi_2-|\Delta_2|^2\right)\Delta_2+\frac{\eta_1}{\eta_2}\gamma\Delta_1\,, \tag{5.6}$$

where x represents an arbitrary arc-length and $A=\Phi/(2\pi R)$.

We then write each order parameter as a stationary term plus a small perturbation $\Delta_j=\Delta_j^0+\delta\Delta_j$, with the stationary unperturbed term given by $\Delta_j^0=a_j e^{in_i x/R}$, where n_i is the winding number of the initial state. At present, we have limited this analysis to the case in which both bands have the same winding number. However, in our later discussion on numerically solving Eqs. (5.1)-(5.2), we will show that the winding number of each order parameter after reaching the critical flux does not always equal unity, nor is it always the same for both bands. The values of a_j can be found from the procedure employed in Ref. [135]; for completeness, we reproduce it below.

Substituting Δ_j^0 in Eqs. (5.5) and (5.6), with $\varphi=0$, we obtain the following set of equations:

$$-\left(n_i/R-A\right)^2 a_1+\left(\chi_1-a_1^2\right)a_1+\gamma a_2=0\,, \tag{5.7}$$

$$-\frac{D_2}{D_1}\left(n_i/R-A\right)^2 a_2+\left(\chi_2-a_2^2\right)a_2+\frac{\eta_1}{\eta_2}\gamma a_1=0\,. \tag{5.8}$$

Defining $\rho=a_1/a_2$, a combination of Eqs. (5.7) and (5.8) produces the following polynomial equation for ρ:

$$\frac{\eta_1}{\eta_2}\gamma\rho^4+\left(\chi_2-\frac{D_2}{D_1}(n_i/R-A)^2\right)\rho^3 - \left(\chi_1-(n_i/R-A)^2\right)\rho-\gamma=0\,, \tag{5.9}$$

After ρ is known, a_1 and a_2 are given by:

$$a_1 = \sqrt{\gamma/\rho+\chi_1-(n_i/R-A)^2}$$

$$a_2 = \sqrt{\frac{\eta_1}{\eta_2}\gamma\rho+\chi_2-\frac{D_2}{D_1}(n_i/R-A)^2}\,. \tag{5.10}$$

To write down the perturbation, we follow the same procedures used for single-band systems. Since single-valuedness of the order parameters implies that the perturbation has to be periodic, we express it as a Fourier expansion:

$$\delta\Delta_j = \sum_{n_f} [\hat{a}^j_{n_f} e^{in_f x/R} + \hat{a}^{j*}_{-n_f} e^{i(2n_i - n_f)x/R}] e^{\lambda_{n_f} t} \,, \tag{5.11}$$

here λ_{n_f} is real and n_f is the winding number of the final state. We remind that n_f is also set to be the same for both bands. As we can see, the parameter λ_{n_f} determines the stability of the the n_f mode of the perturbation, since it decreases exponentially if λ_{n_f} is negative and grows exponentially otherwise. To determine the value of λ_{n_f} for a given applied flux, we need to substitute $\Delta_j = \Delta^0_j + \delta\Delta_j$ in Eqs. (5.5) and (5.6) and linearize the resulting expressions with respect to $\delta\Delta_j$. Making use of Eqs. (5.7) and (5.8), we find:

$$\begin{aligned}
&\frac{\partial\delta\Delta_1}{\partial t} + i\varphi\Delta^0_1 = -\left(-i\frac{\partial}{\partial x} - A\right)^2 \delta\Delta_1 \\
&+ \left(\chi_1 - 2a_1^2\right)\delta\Delta_1 - a_1^2 e^{2in_i x/R}\delta\Delta_1^* + \gamma\delta\Delta_2 \,, \qquad (5.12)\\
&\frac{\partial\delta\Delta_2}{\partial t} + i\varphi\Delta^0_2 = -\frac{D_2}{D_1}\left(-i\frac{\partial}{\partial x} - A\right)^2 \delta\Delta_2 \\
&+ \left(\chi_2 - 2a_2^2\right)\delta\Delta_2 - a_2^2 e^{2in_i x/R}\delta\Delta_2^* + \frac{\eta_1}{\eta_2}\gamma\delta\Delta_1 \,. \qquad (5.13)
\end{aligned}$$

The scalar potential can be obtained from the expression $\sigma_n \boldsymbol{\nabla}\varphi = -\boldsymbol{J}_n$, where $\sigma_n = (1/u)\,(1 + \eta_2 D_2/(\eta_1 D_1))$ is the normal conductivity. Using charge conservation and assuming there is no charge accumulation, we have $\boldsymbol{\nabla}\cdot(\boldsymbol{J}_n + \boldsymbol{J}_s) = 0$, from which the equation for the scalar potential in our one-dimensional system can be written as:

$$\sigma_n \frac{\partial^2\varphi}{\partial x^2} = \frac{\partial J_s}{\partial x} \,. \tag{5.14}$$

Since the stability limits of our system depend on its energy landscape but not on its dynamical parameter, we can take the limit $\sigma_n \to \infty$, which allows us to take $\varphi = 0$. With this result and using Eqs. (5.12)-(5.13), we are now able to write down an eigenvalue-eigenvector equation for each λ_{n_f}, which is given by:

$$\begin{bmatrix} M_{11} & M_{12} & M_{13} & M_{14} \\ M_{21} & M_{22} & M_{23} & M_{24} \\ M_{31} & M_{32} & M_{33} & M_{34} \\ M_{41} & M_{42} & M_{43} & M_{44} \end{bmatrix} \begin{bmatrix} \hat{a}^1_{n_f} \\ \hat{a}^{1*}_{-n_f} \\ \hat{a}^{2*}_{-n_f} \\ \hat{a}^2_{n_f} \end{bmatrix} = \lambda_{n_f} \begin{bmatrix} \hat{a}^1_{n_f} \\ \hat{a}^{1*}_{-n_f} \\ \hat{a}^{2*}_{-n_f} \\ \hat{a}^2_{n_f} \end{bmatrix} \tag{5.15}$$

with the coefficients M_{ij} obtained as follows. Substituting Eq.5.11 in Eq.5.13, we have for the first order parameter and specific value of n_f:

$$\begin{aligned}\lambda_{n_f}\hat{a}^1_{n_f} = &- (n_f/R - A)^2\hat{a}^1_{n_f} + \left(\chi_1 - 2a_1^2\right)\hat{a}^1_{n_f} \\ &- a_1^2\hat{a}^{1*}_{-n_f} + \gamma\hat{a}^2_{n_f} \,, \end{aligned} \tag{5.16}$$

and:

$$\begin{aligned}\lambda_{n_f}\hat{a}^{1*}_{-n_f} = &- (-n_f/R + 2n_i/R - A)^2\hat{a}^{1*}_{-n_f} \\ &+ \left(\chi_1 - 2a_1^2\right)\hat{a}^{1*}_{-n_f} - a_1^2\hat{a}_{n_f} + \gamma\hat{a}^{2*}_{-n_f} \,, \end{aligned} \tag{5.17}$$

From Eq. 5.16, we can identify that the coefficients M_{11}, M_{12}, M_{13} and M_{14} are equal to the terms multiplying $\hat{a}^1_{n_f}$, $\hat{a}^1_{-n_f}$, $\hat{a}^2_{-n_f}$ and $\hat{a}^2_{n_f}$, respectively. The same follows for Eq. 5.17 and the analogous equations for the second order parameter.

The coefficients M_{ij} in Eq. (5.15) can then be written as:

$$\begin{aligned}
M_{11} &= -(n_f/R - A)^2 + (\chi_1 - 2a_1^2) \,, \\
M_{12} &= -a_1^2 \,, \\
M_{13} &= 0 \,, \\
M_{14} &= \gamma \,, \\
M_{21} &= -a_1^2 \,, \\
M_{22} &= -(-n_f/R + 2n_i/R - A)^2 + (\chi_1 - 2a_1^2) \,, \\
M_{23} &= \gamma \,, \\
M_{24} &= 0 \,, \\
M_{31} &= 0 \,, \\
M_{32} &= \frac{\eta_1}{\eta_2}\gamma \,, \\
M_{33} &= -\frac{D_2}{D_1}(-n_f/R + 2n_i/R - A)^2 + (\chi_2 - 2a_2^2) \,, \\
M_{34} &= -a_2^2 \,, \\
M_{41} &= \frac{\eta_1}{\eta_2}\gamma \,, \\
M_{42} &= 0 \,, \\
M_{43} &= -a_2^2 \,, \\
M_{44} &= -\frac{D_2}{D_1}(n_f/R - A)^2 + (\chi_2 - 2a_2^2) \,.
\end{aligned} \tag{5.18}$$

A detailed and cumbersome analysis of the matrix M can show that its determinant ($det(M)$) depends on the applied flux only through $(n_i - A)^2$. Also, since the determinant of a matrix equals the product of its eigenvalues, we have that $det(M) = 0$ at a critical flux. Combined, these two results mean that the critical points for the transitions $n \to n+1$ and $n+1 \to n+2$ are separated by Φ_0, as physically expected. In addition, we conclude that

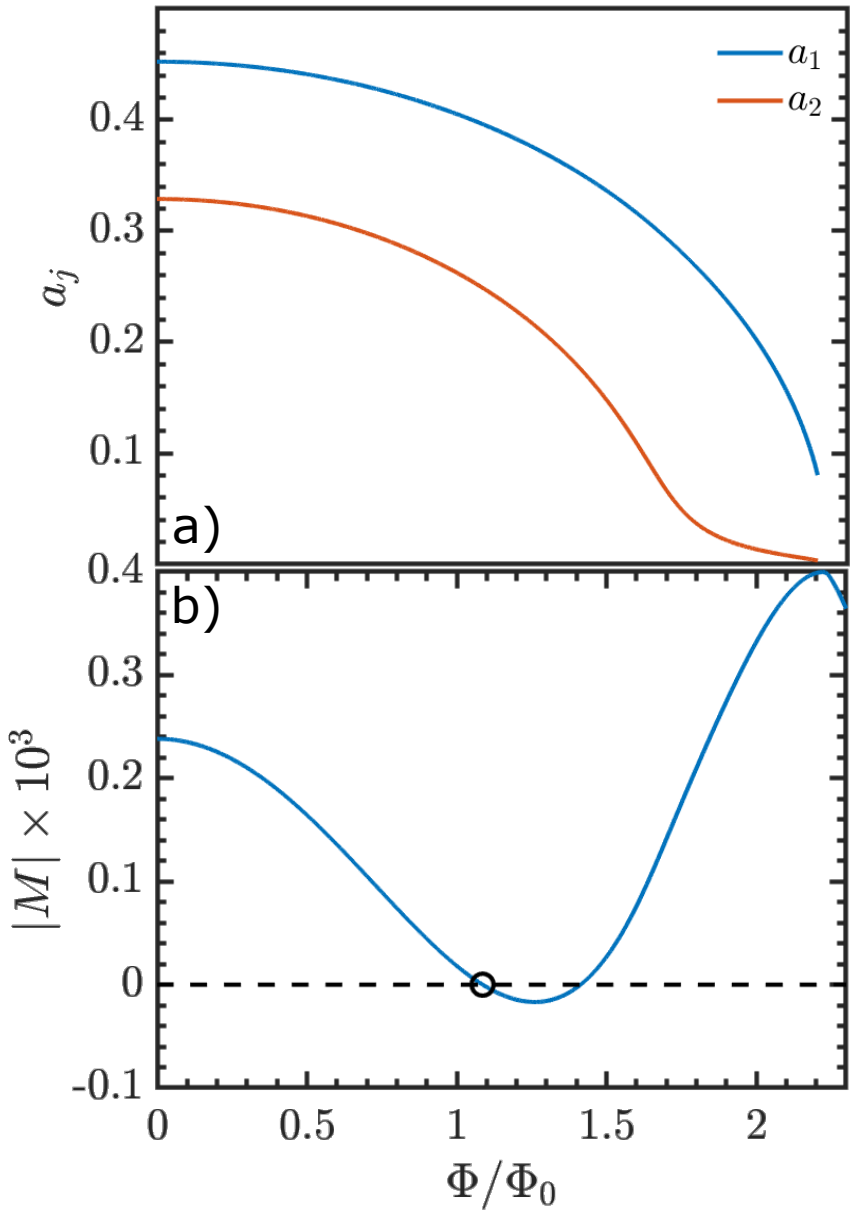

Figure 1 – *The upper panel shows the values of a_1 and a_2 for $n_i = 0$ as functions of the applied flux. The lower panel presents $det(M)$ as a function of Φ; the black circle indicates the critical flux $\Phi = 1.087\Phi_0$, above which the state with winding number 0 is unstable.*

the upper and the lower stability limits of a state with winding number n are equidistant from $n\Phi_0$.

Furthermore, we can now clearly see the reason for assuming n_f to be equal in both bands. Since we solve Eq. (5.15) for each n_f separately, n_f must be the same in the two bands. Nevertheless, it will be shown that the results from our method are still valid even if the winding number of each band is not the same at the final state *i.e.* even if the final state presents a phase soliton.

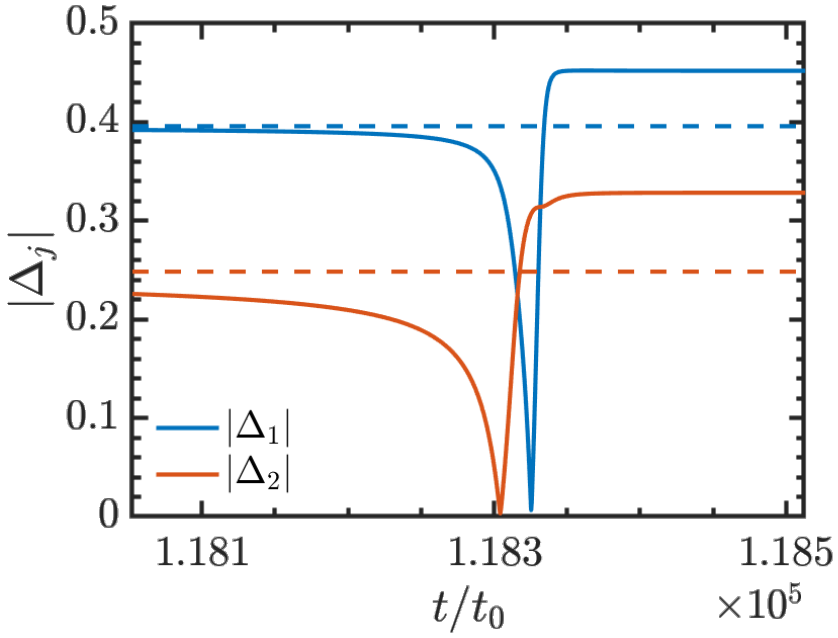

Figure 2 – *Time evolution of the minimum values of the order parameters of a state initially prepared with winding number 0, close to the limit of stability,* $\Phi_c = 1.087\Phi_0$. $R = 5\xi_1$, $D_1 = D_2$, $T = 0.8T_c$. *Solid and dashed lines represent the evolution for* $\Phi = \Phi_c + 0.001\Phi_0$ *and* $\Phi = \Phi_c - 0.001\Phi_0$, *respectively.*

At this point, we introduce a compromise into our previously entirely analytical procedure by adopting numerical routines moving forward. This is done because, in order to get the final value of Φ_c, one needs first to solve the fourth order polynomial Eq. (5.9) for ρ and subsequently for a_1 and a_2. With this result, $det(M)$ must then be calculated for different values of Φ, until $det(M) = 0$ is found. In principle, while it is possible to carry on this procedure analytically, the laborious work required to do so is not worth, since we can reach the same results with an almost negligible computational effort. In addition, given the complexity of these equations, we probably would obtain intractable results.

To exemplify our method, we apply it to the problem of finding the critical flux at which the Meissner state of a two-band superconducting ring with radius $R = 5\xi_1$ and $D_1/D_2 = 1.00$ is unstable against a perturbation with winding number n_f. As is the case for single-band superconductors, the first mode to become unstable corresponds to $n_f = 1$. Therefore, in the following we solve Eq. (5.15) with $n_i = 0$ and $n_f = 1$.

Panel *a*) of Fig. 1 presents the values of a_1 and a_2 as functions of the applied flux. The region of high applied flux shows an important feature for our future discussions. As can be seen, there is a pronounced change in the behavior of the curve corresponding to a_2, which acquires an elongated tail. As can be easily visualized from Eqs. (5.7)-(5.8), this occurs because the applied flux reaches a value higher than the critical flux at which the second band goes to the normal state in the decoupled regime. In other to avoid confusion

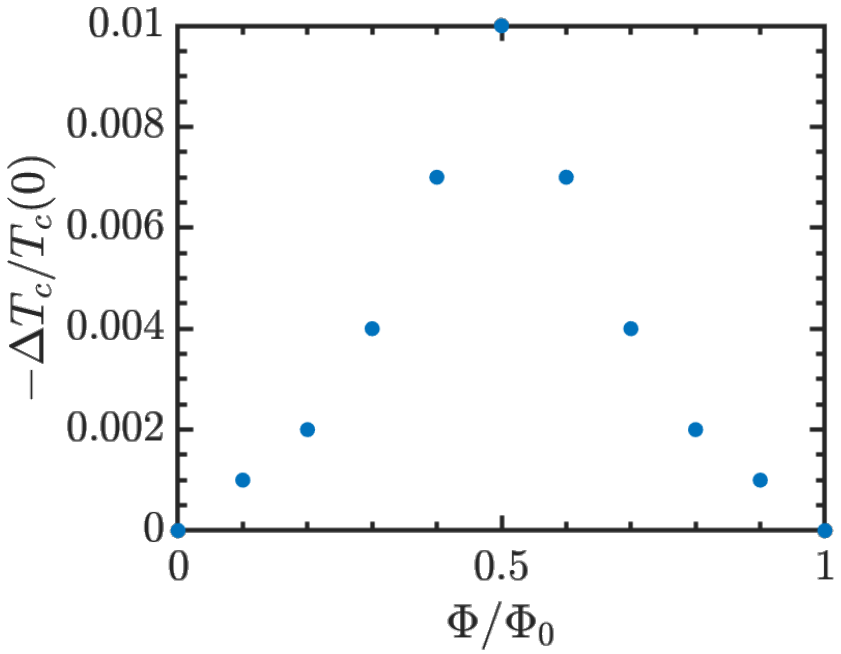

Figure 3 – $-\Delta T_c/T_c(0)$ *as a function of the applied flux for a two-band ring with* $R = 5\xi_1$ *and* $D_1/D_2 = 1.00$.

between this critical flux and the critical flux at which the initial state becomes unstable, hereafter we refer to the former as the "upper critical flux of the second band". Above this flux, the second band stays superconducting due only to coupling with the first band. Eq. (5.8) and the expression of the vector potential show that the upper critical flux of the second band increases with D_1/D_2 and with the radius of the ring R.

The panel *b*) of Fig. 1 shows $det(M)$ as a function of Φ, with the black circle indicating the value of flux ($\Phi_c = 1.087\Phi_0$) at which the first eigenvalue of M changes its sign. This is the critical flux value, above which the system is unstable against decay into a state with winding number 1.

While our semi-analytical method allows us to calculate the flux at which a state becomes unstable, the full numerical solution of Eqs. (5.1)-(5.2) gives us the time evolution of both order parameters for a given applied flux. Fig. 2 exemplifies the above analysis by showing the time evolution of the minimum values of each order parameter for a system with the same parameters described in Fig. 1. Here, dashed lines represent a case with $\Phi < \Phi_c$, while solid lines show the order parameter evolution for $\Phi > \Phi_c$. For $\Phi < \Phi_c$, the system just stays the whole time in the Meissner state, without major modifications. However, if $\Phi > \Phi_c$, the system initially sits practically unperturbed in the Meissner state. Eventually, the perturbation becomes noticeable, and the system transits to a state with winding number greater than 0. As expected, the occurrence of a phase-slip is not simultaneous in both bands, with the time interval between them depending on D_1/D_2, the applied flux and temperature. Although both phase slips are not simultaneous, they

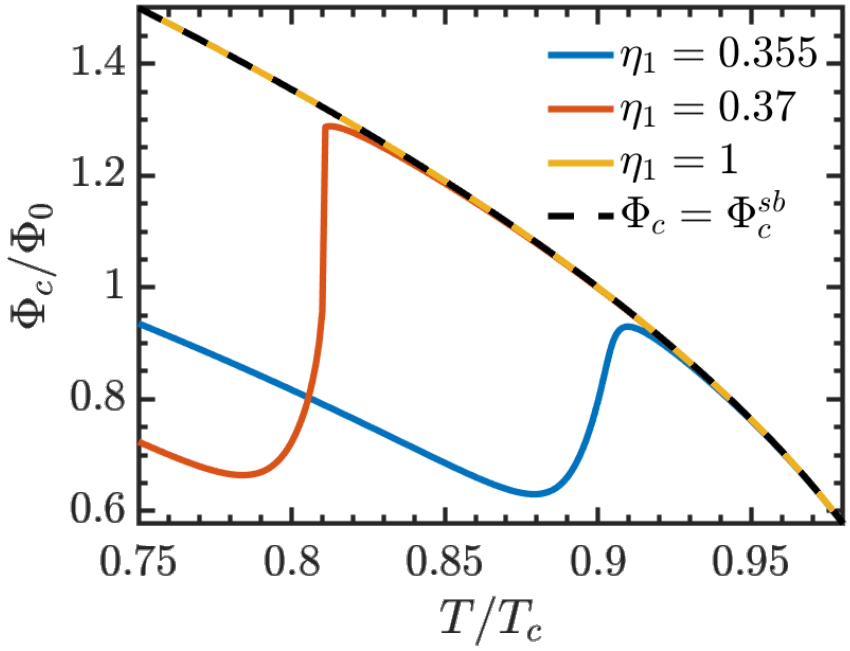

Figure 4 – *Critical flux for the emergence of a phase slip as a function of temperature for different values of* η_1*. The black dashed curve shows the single-band limit* $\Phi_c^{sb} = \sqrt{(1-T)R^2 + 1/2}/\sqrt{3}$.

do occur at the same place, i.e. they are a case of time-connected phase-slips. [190] After this couple of phase-slips, the system stabilizes at a new state, with winding number 1.

As a test of our semi-analytical method we compare the results that it yields with the well known expression for the single-band limit [191, 176, 177] $\Phi_c^{sb} = \sqrt{(1-T)R^2 + 1/2}/\sqrt{3}$. Fig. 4 shows this comparison, by presenting the critical flux Φ_c as a function of the temperature for different values of η_1. As we can see, as η_1 increases and the importance of the second band to the physical behavior of the system decreases, the curve approaches the single-band limit, represented by the black dashed curve. In particular, for $\eta_1 = 1$, both models coincide, supporting the correctness of our semi-analytical method.

As a last comment before the discussion of the main results of this Chapter, we would like to emphasize that the Little-Parks oscillations in T_c due to the external flux are fully taken into account in our method. This is shown in Fig. 3, where we present the T_c variation as function of Φ for a ring with radius $R = 5\xi_1$ and $D_1/D_2 = 1.00$. As can be seen, the result is very similar to the well-known one band-limit, with the largest critical temperature variation occurring at $\Phi = 0.5\Phi_0$.

5.3 Results and Discussion

Having presented our semi-analytical method and an example of its application, let us now apply it to a specific study. We will investigate how the critical flux, above

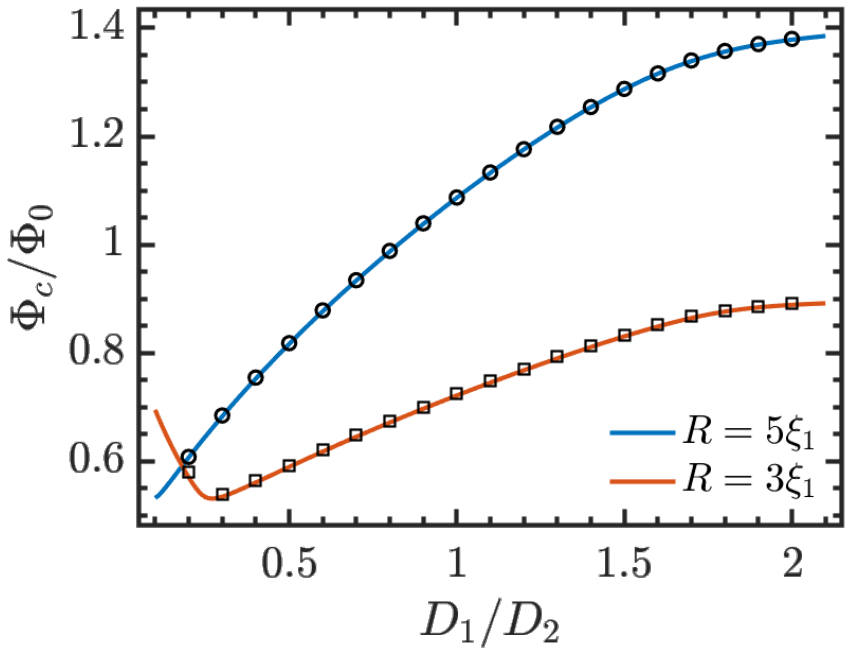

Figure 5 – *Critical flux above which the system becomes unstable as a function of the ratio D_1/D_2. The blue (red) line presents the results obtained from our method developed in Section 5.2 for a ring with radio $R = 5\xi_1$ ($R = 3\xi_1$). Black circles (squares) show the values of the critical flux obtained numerically directly from the TDGL.*

which the Meissner state first becomes unstable against decay into a state with winding number 1, depends on the ratio between the diffusion coefficients in each band and on the bath temperature.

5.3.1 The Critical Flux Dependence on D_1/D_2

We have already seen that our linear stability analysis is correct in the single-band limit, let us now compare its results with the direct numerical solution of Eqs. (5.1)-(5.2) when both bands are active. In Fig. 5, we present the critical flux at which the two-band system first becomes unstable, as a function of the ratio of the diffusion coefficients D_1/D_2. The blue (red) line shows the critical flux obtained from our semi-analytical method for a ring with radius $R = 5\xi_1$ ($3\xi_1$), whereas the black circles (squares) indicate the critical flux obtained by solving numerically the TDGL equations for a ring with $R = 5\xi_1$ ($3\xi_1$). The black circles indicate the critical flux obtained by numerically solving the TDGL equations for the system with $R = 5\xi_1$, and the black squares represent the results for $R = 3\xi_1$. As can be seen, the agreement between our semi-analytical method and the numerical results fully verifies the validity of our procedure. In fact, the largest deviation between them is of the order of $10^{-3}\Phi_0$.

Analyzing the curve corresponding to $R = 5\xi_1$, one can see that the critical flux

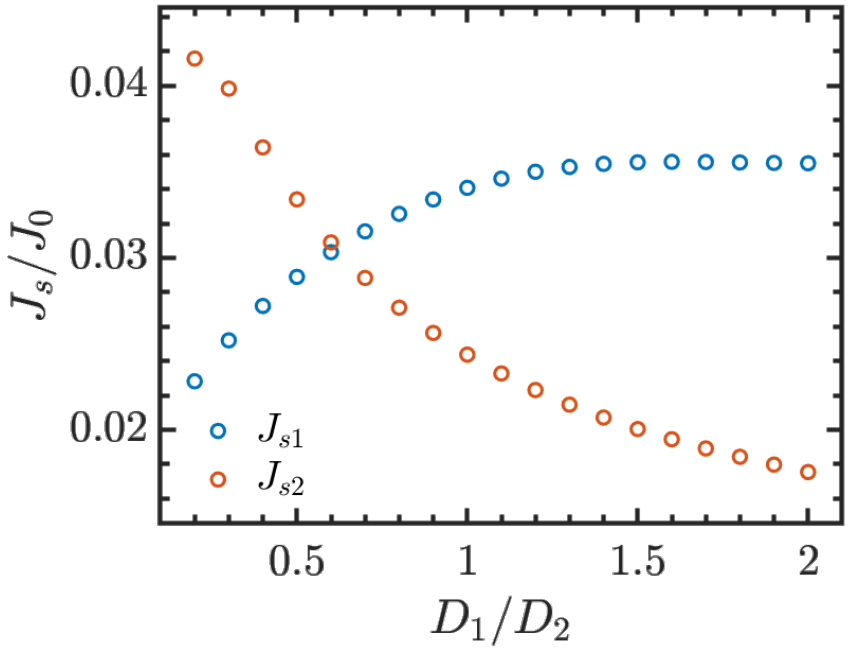

Figure 6 – *Supercurrent carried by the first (blue circles) and second band (red circles) in the Meissner state for an applied flux equals to the critical flux of the given D_1/D_2 as a function of D_1/D_2, for $R = 5\xi_1$*

increases with D_1/D_2, reaching an asymptotic value for large diffusion coefficient ratio. This can be explained by the amount of current carried by each condensate, which depends on the relative strength of the bands and the values of D_1 and D_2. Since all microscopic constants are held fixed and D_1 is used in the definition of our units, the proportion of current in each condensate is determined by the ratio D_1/D_2. An increase in this ratio (decrease in D_2) means a decrease in the amount of current carried by the second condensate. This can be seen in Fig. 6, where we show the amount of current carried by each band (calculated exactly at $\Phi_c(D_1/D_2)$) as a function of D_1/D_2.

As the current in the second band decreases, the phase-slip formation process becomes more dependent on the dynamics of the first band. Since the first band has a higher critical temperature, the critical flux for the formation of a phase-slip increases, explaining the general behavior of the curve. If the ratio D_1/D_2 becomes too large, the dynamics of the system is determined solely by the first band and thus the critical flux tends to a constant value, which is also in agreement with our results.

If we now examine the curve corresponding to $R = 3\xi_1$, we see that a special feature, that is, a minimum in the critical flux is now present. Here, for small values of D_1/D_2, the critical flux for phase-slip formation decreases, contrary to increasing, as the diffusion coefficient ratio increases.

The behavior of the curve resumes the previously described pattern for the $R = 5\xi_1$ case only after reaching a minimum in this flux. This occurs due the relationship between

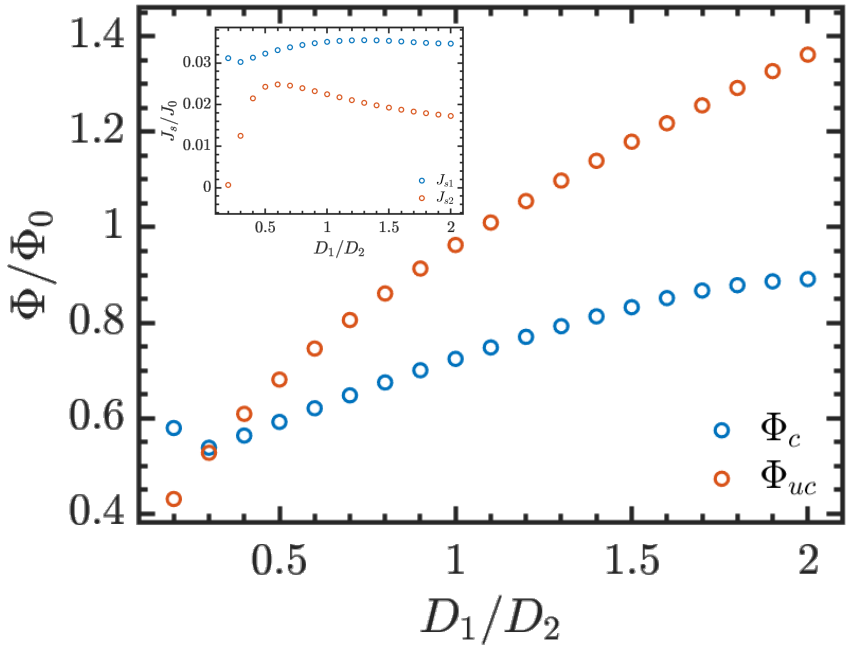

Figure 7 – *The main panel shows the critical flux for the formation of a phase-slip (blue circles) and the upper critical field of the second band (red circles) as functions of D_1/D_2. The inset presents the supercurrent carried by the first (blue circles) and second (red circles) band in the Meissner state, calculated at an applied flux equals to $\Phi_c(D_1/D_2)$, as functions of D_1/D_2. In both curves $R = 3\xi_1$.*

the critical flux for the formation of a phase-slip Φ_c and the "upper critical flux of the second band" Φ_{uc}, defined in the previous Section. As shown in the main panel of Fig. 7, Φ_c is larger than Φ_{uc} for small values of the ratio D_1/D_2. As a consequence, at the stability limit, the second band is superconducting due only to the coupling with the first band. As presented in the inset of Fig. 7, this implies that for these values of D_1/D_2, a very small portion of current is carried by the second band. As we have seen in the previous discussion, this means that the stronger band dominates the process of phase-slip formation and results in a larger critical flux. Increasing D_1/D_2, the curves Φ_c and Φ_{uc} intersect, activating the second band. This leads to a recurrence of the behavior observed for $R = 5\xi_1$. As we can see then, the minimum in Φ_c originates from the transition of the weaker band from passive to active. This behavior is absent is the curve for $R = 5\xi_1$ in Fig. 5 because $\Phi_{uc} > \Phi_c$ in the entire region of D_1/D_2 displayed in this figure.

Our method is also capable of calculating the critical flux for the inverse transition *i.e.* between an initial state winding number equals to 1 in and a final state with winding number equals to 0. When the external flux is being swept down, Φ_c for such transition is defined as the first flux at which the initial state with $n_i = 1$ becomes unstable against a perturbation with $n_f = 0$. In Fig. 8, this Φ_c as a function of D_1/D_2 is shown for $R = 5\xi_1$ (blue curve) and $R = 3\xi_1$ (red curve). As can be seen, for $R = 5\xi_1$ the critical flux

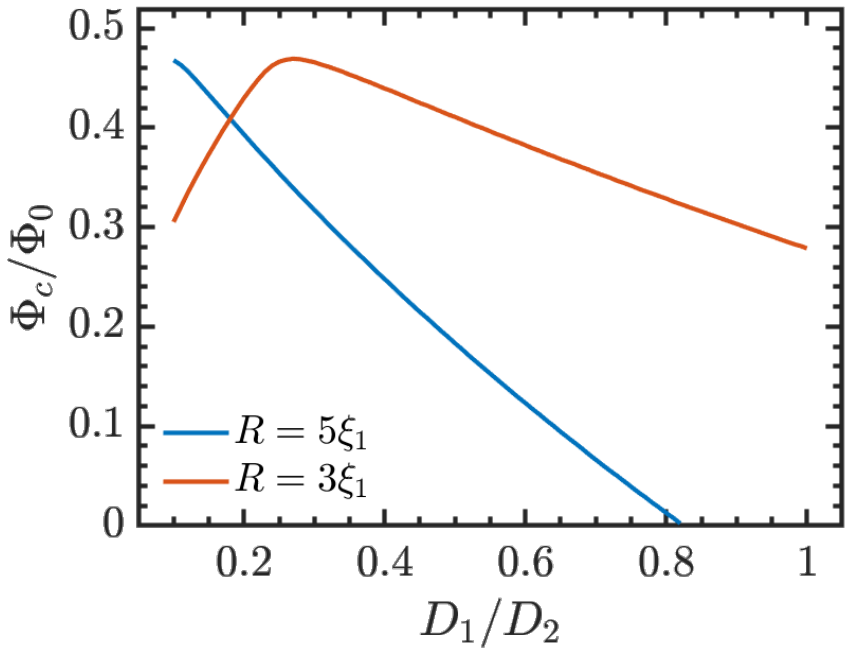

Figure 8 *– Critical flux for the transition $n_i = 1 \rightarrow n_f = 0$ as a function of D_1/D_2.*

monotonically decreases with D_1/D_2 and at a certain point reaches 0. This means that is necessary to invert the flux sign to get an unstable $n_i = 1$. The ring with $R = 3\xi_1$ behaves at large D_1/D_2, but present the same non-monotonically behavior discussed in Fig. 5 at small D_1/D_2.

5.3.2 Critical Flux Dependence on the Bath Temperature

Let us now investigate how the critical flux behaves with temperature. Fig. 9 depicts Φ_c for three different values of D_1/D_2 with temperature ranging from $T = 0.8T_c$ to $T = 0.95T_c$. Panel *a*) shows the critical flux for $D_1/D_2 = 1.0$ (blue curve), $D_1/D_2 = 0.5$ (red curve) and $D_1/D_2 = 0.1$ (yellow curve).

As we can see, the blue and red curves exhibit similar behavior; namely, for small values of T, the critical flux decreases as the temperature increases. This is the expected behavior in a superconducting system. On the other hand, the yellow curve presents the intriguing behavior of an increasing critical flux with temperature value. This occurs because, for such small values of D_1/D_2, the weaker band is passive throughout this temperature region. As the amount of supercurrent carried by the weaker condensate decreases, the system becomes more dominated by the stronger condensate, leading to an increase in the critical flux. This behavior lasts until superconductivity in the weaker band is completely destroyed, after which the critical flux decreases with temperature, a typical behavior of single band superconductors. As can be seen, the blue and red curves also display regions where Φ_c increases with the temperature. The mechanism behind this is exactly the same one detailed for the yellow curve. Finally, we note that superconducting

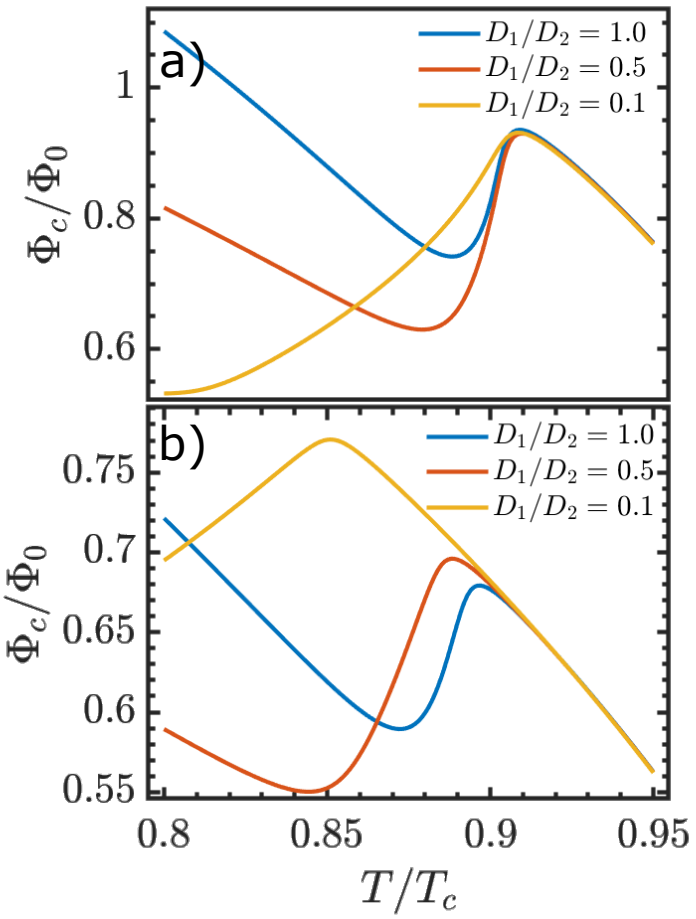

Figure 9 – *The critical flux as a function of temperature for* $R = 5\xi_1$ *(panel a)) and* $R = 3\xi_1$ *(panel b)). In each panel, we show the critical flux for* $D_1/D_2 = 1.0$, 0.5 *and* 0.1 *(blue, red and yellow curves, respectively).*

rings with radius $3\xi_1$ depicted in panel b) presents the same qualitative behavior of the yellow curve. In this case, the temperature values where the maximum and minimum of the critical flux occurs are smaller than the ones obtained in panel a). As we have discussed above, this occurs because a smaller radius makes the suppression of superconductivity easier for both condensates.

5.3.3 The Phase Soliton State

In order to maintain the previous discussion as straightforward as possible, up to this point we have not described how the final state varies as we change the value D_1/D_2. In other words, we have not investigated what the winding numbers are in the final state for the various values of D_1/D_2 presented in Fig. 5.

Given the small radii and the relatively high temperature employed in the cases of Fig. 5, the critical flux we found is never larger than $1.5\Phi_0$. This means that winding

numbers larger than 1 are thermodynamically unfavorable. Nevertheless, as stated earlier, it is still possible to obtain a state with a phase-slip in only one of the bands.

For $R = 5\xi_1$ ($R = 3\xi_1$), for instance, $D_1/D_2 \geq 0.8$ ($D_1/D_2 \geq 1.1$) the system always transits from the Meissner state ($\Delta_j = a_j^{MS}$) to a phase-locked state ($\Delta_j = a_j^{PS} e^{ikx}$), where $k = 1/R$ for both bands. In other words, both bands display the same winding number. For $D_1/D_2 < 0.8$ ($D_1/D_2 < 1.1$) the Meissner state may be succeeded by a less trivial state with a different phase winding at each band, which is known as a phase soliton. The formation or not of the phase soliton depends on the exact value of the applied flux. For instance, if the flux is much larger than the critical flux, the system will go to a phase-locked state, even if its diffusion coefficient ratio allows for the formation of a soliton.

On the other hand, if the applied flux is close enough to Φ_c in this region of diffusion coefficient ratio, the system transits from the Meissner state to the a phase soliton state. In panel *a*) of Fig. 10 we show the spatial dependence of the magnitude of the order parameters and their phases in a typical soliton state. Since we have a periodic system, we have taken the center of the x-axis at the phase-slip position. The parameters used are $R = 5\xi_1$, $D_1/D_2 = 0.5$, with an applied flux slightly above the critical flux obtained for these parameters, $\Phi_c = 0.82\Phi_0$. Unfortunately, our semi-analytical method is not able to predict whether the final state will be phase-locked or the phase soliton state. We note that, even though $n_1 = 0$ and $n_2 = 1$ in the final state, Φ_c is obtained from a initial perturbation with winding number equal to 1 fro both bands.

The possible stabilization of a phase soliton (as a metastable state) can be characterized by the time difference between the formation of phase-slips in each condensate, hereafter referred as t_γ. For states with $n_1 = n_2$, t_γ is finite, while for the soliton state, where the phase-slip never occurs in one of the order parameters, $t_\gamma \to \infty$. We now investigate how t_γ depends on D_1/D_2 and on the applied flux. To do this, we numerically solve the Ginzburg-Landau equations for different flux values, always initializing the system with $n_1 = n_2 = 0$. The results are shown in Fig. 11, where we present t_γ as a function of $\Phi - \Phi_c$ (with Φ_c being the critical flux for correspondent value of D_1/D_2) in order to compare different values of D_1/D_2 on equal footing. As can be seen, as Φ gets closer to Φ_c, t_γ varies slowly for $D_1/D_2 = 1.00$, but presents a sharp increase that eventually leads to a divergence at an appropriately small Φ for $D_1/D_2 = 0.25$ and 0.50. This is in agreement with our previous result that a phase soliton is only possible for $D_1/D_2 < 0.8$ and a phase soliton is only possible for parameters that result in $t_\gamma \to \infty$.

Let us now investigate the stability of our soliton state for different values of applied flux. To do so, we start with the system in a state with no flux threading the superconducting loop and with winding number zero in both order parameters, and gradually change the applied flux in units of $\Delta\Phi = 0.001\Phi_0$. For each value of the applied flux

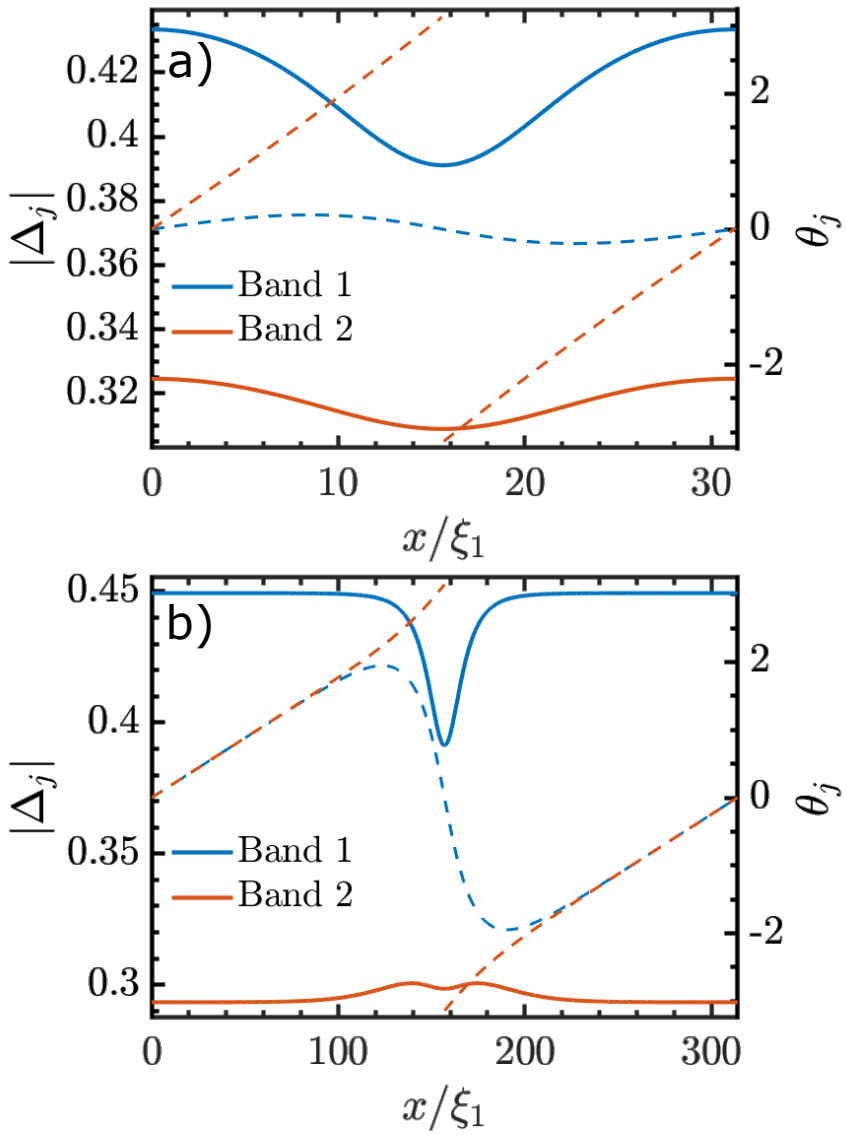

Figure 10 – *The spatial dependence of the magnitudes (solid lines) and phases (dashed lines) of the order parameters correspondent to the first (blue) and second (red) band in a soliton state. The left and the right vertical axes give the magnitudes and the phases, respectively. In panel a)* $R = 5\xi_1$, $D_1/D_2 = 0.5$ *and* $\Phi = 0.82\Phi_0$. *In panel b)* $R = 50\xi_1$, $D_1/D_2 = 0.1$ *and* $\Phi = 3.27\Phi_0$. *In both panels,* $T = 0.8T_c$.

we let the system relax to its equilibrium state. In Fig. 12 we show the system energy as a function of the applied flux in the range $0 \leq \Phi \leq 1.2\Phi_0$, for a superconducting ring with $R = 5\xi_1$ and $D_1/D_2 = 0.25$. Solid blue and dashed red lines correspond to the regimes where the flux is being swept up and down, respectively. The expression for the free energy density of our system can be written as: [24]

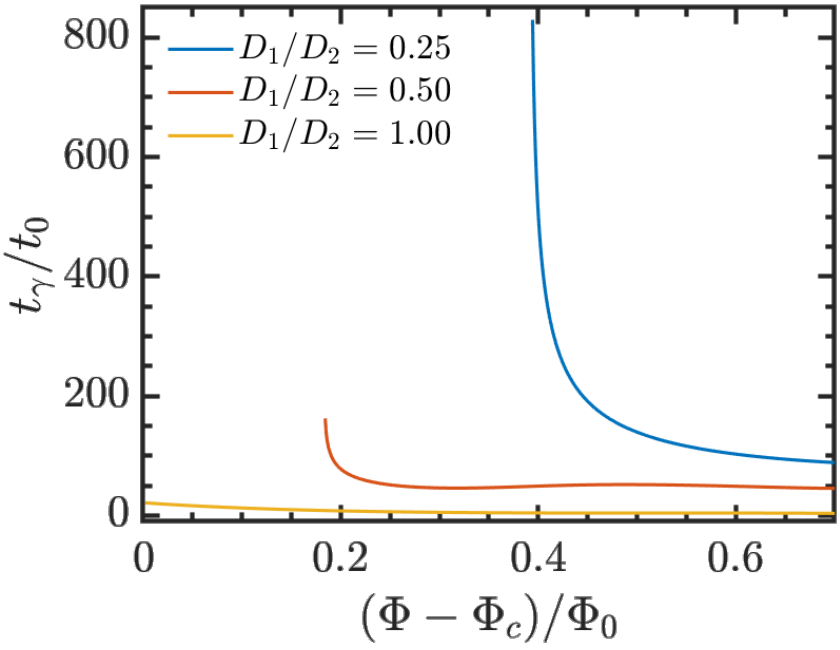

Figure 11 *– t_γ as a function of $(\Phi - \Phi_c)$ for $D_1/D_2 = 0.25$ (blue curve), 0.50 (red curve) and 1.00 (yellow curve). Here $R = 5\xi_1$ and $T = 0.8T_c$.*

$$\begin{aligned} F &= \left(-\chi_1 + \frac{1}{2}|\Delta_1|^2\right)|\Delta_1|^2 + \frac{\eta_2}{\eta_1}\left(-\chi_2 + \frac{1}{2}|\Delta_2|^2\right)|\Delta_2|^2 \\ &+|\left(-i\boldsymbol{\nabla} - \mathbf{A}\right)\Delta_1|^2 + \frac{\eta_2 D_2}{\eta_1 D_1}|\left(-i\boldsymbol{\nabla} - \mathbf{A}\right)\Delta_2|^2 \\ &-\gamma\left(\Delta_1\Delta_2^* + \Delta_1^*\Delta_2\right) \end{aligned} \tag{5.19}$$

In an equilibrium situation, we can take GL equations with $\partial\Delta_j/\partial t = 0$ and $\varphi = 0$. Multiplying by Δ_j and integrating by parts, one can obtain a simple expression for the free energy density:

$$F = -\frac{1}{2}|\Delta_1|^4 - \frac{1}{2}\frac{\eta_2}{\eta_1}|\Delta_2|^4 \tag{5.20}$$

As can be seen from the blue curve, the system stays at the zero winding number state up to the critical flux $\Phi_c = 0.647\Phi_0$, as predicted from our semi-analytical method, and transits to a phase soliton state. During the transition a phase-slip occurs only in the second order parameter. The soliton state remains stable up to $\Phi = 1.037\Phi_0$. As we can see, the soliton state can be stable for a large window of the applied flux values, making it important to the behavior of the system. We note, though, that such window depends on the rate at which the applied flux is being increased, decreasing if the flux step is too large. If we now decrease the applied flux, as shown in the red curve, we see that the state $n_1 = n_2 = 1$ is stable down to $\Phi = 0.356\Phi_0$, where it transits to a different soliton state, with $n_1 = 1$ and $n_2 = 0$, which still remains stable at zero applied flux.

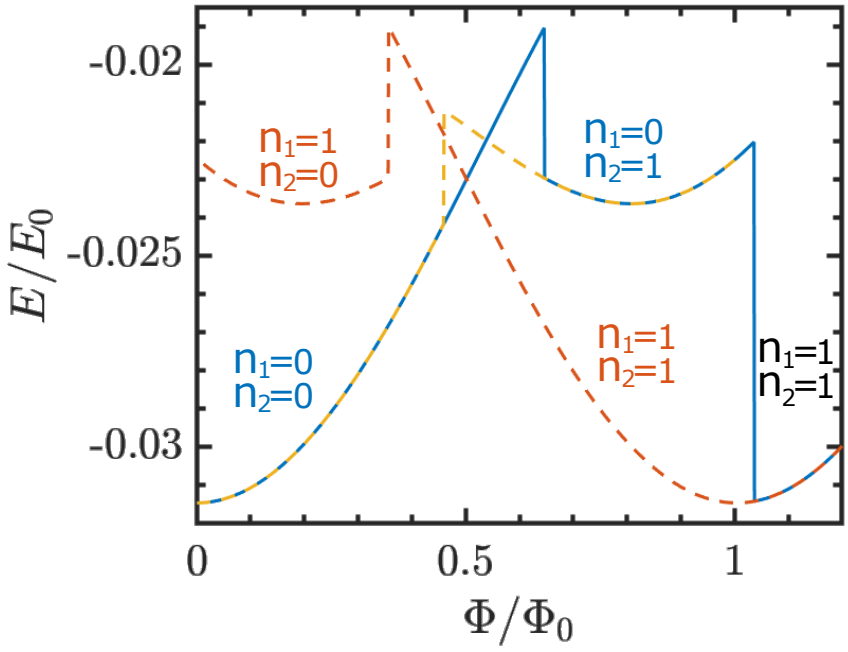

Figure 12 – *Energy as a function of the applied flux for $R = 5\xi_1$ and $D_1/D_2 = 0.25$. The numbers n_1 and n_2 denotes the winding number of each order parameter. Solid blue and dashed red lines depict the regimes where the flux is being swept up and down in the range $0 \leq \Phi \leq 1.2\Phi_0$, respectively. In the dashed yellow curve, the flux is decreased from $\Phi = \Phi_0$ down to $\Phi = 0$.*

In the dashed yellow curve, on the other hand, we start from the soliton state at $\Phi = \Phi_0$ and the external flux is decreased. In this case, when we decrease the flux, the system transits from the soliton state $n_1 = 0$ and $n_2 = 1$ to the state $n_1 = n_2 = 0$ at $\Phi = 0.459\Phi_0$. From the comparison of the different curves in Fig. 12 it becomes clear that a soliton state can be metastable for a large range of applied flux, with its occurrence being highly dependent on the system history. Note that, although the previous analysis considered superconducting rings with small R the same conclusions are valid for more realistic system sizes. For instance, we numerically obtained that for $R = 25\xi_1$ ($R = 50\xi_1$) the phase soliton state can be found for $D_1/D_2 < 0.3$, ($D_1/D_2 < 0.2$) and the same behavior can be expected for even larger values of R. The spatial dependence of the order parameters magnitude and phase are shown in panel *b*) of Fig. 10.

Finally, it is expected that the strength of the interband coupling significantly affects the stability of the soliton state. To see this, we investigated superconducting rings with larger values of λ_{12}. We note that changing λ_{12} also affects the critical temperature of each band T_{ci}. To keep this effect small and focus solely on how the coupling strength influences the soliton state, we choose $\lambda_{12} = 0.01$ and $\lambda_{12} = 0.05$, which render $T_{c1} = 0.9989$, $T_{c2} = 0.9022$ and $T_{c1} = 0.9783$, $T_{c2} = 0.8814$, close to the original values obtained for $\lambda_{12} = 0.005$. Fig. 13 shows the critical flux as a function of D_1/D_2 for the different values of λ_{12}. As can be seen, Φ_c slightly increases with the interband coupling, but the

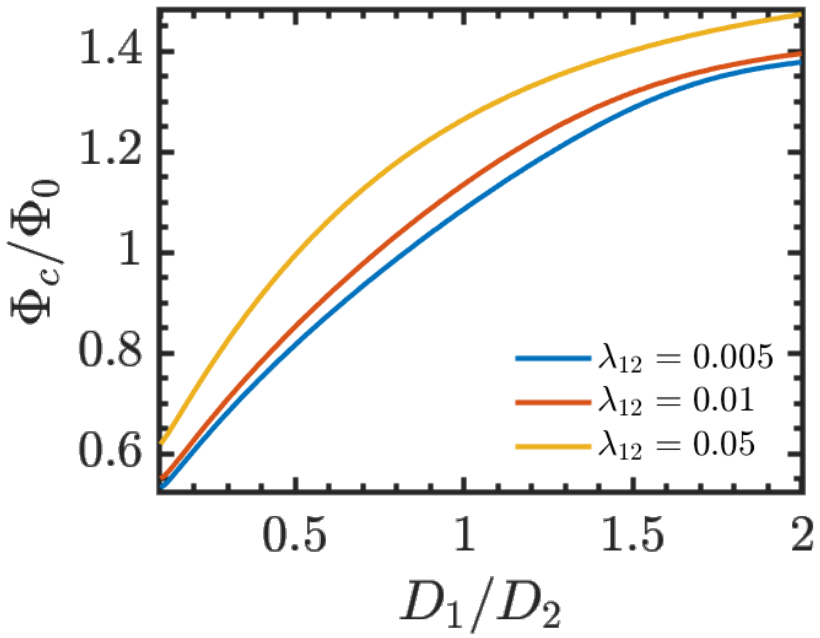

Figure 13 – *Critical flux as a function of D_1/D_2 for three different values of λ_{12}. In all cases $R = 5\xi_1$ and $T = 0.8T_c$.*

overall behavior of the curves remains the same. Nevertheless, the limiting values of D_1/D_2 above which the phase soliton state can no longer be encountered are significantly affected. As previously stated, for $\lambda_{12} = 0.005$, the phase soliton exists for $D_1/D_2 < 0.8$. For $\lambda_{12} = 0.01$ this condition changes to $D_1/D_2 < 0.5$ and, more dramatically, for $\lambda_{12} = 0.05$ the phase soliton state was not found down to $D_1/D_2 = 0.01$. As physically expected, we can conclude that stronger interband couplings favor states with the same winding number in each order parameter, thus suppressing the formation of a phase soliton.

5.4 Concluding Remarks

In this chapter, we have studied the process of phase-slip mediated transitions in two-band superconducting rings under an applied flux. By combining linear stability theory with the time dependent Ginzburg-Landau equations for superconducting systems with two condensates, we have developed a semi-analytical method to determine the critical flux above which a transition must occur. We have validated our new method by comparing it with the results of the numerical solution of the Ginzburg-Landau equations. As we show, the agreement between the two methods is excellent.

Having verified the validity of our model, we used it to study how the behavior of our system depends on the diffusion coefficient ratio of each band and the temperature. A number of distinct features were shown, such as the unexpected increase of the critical flux with temperature for certain system parameters. Another unique behavior of such

systems is the possibility of a phase soliton state, which displays order parameters with different winding numbers. We note that, with a suitable modification in the parameters, our model could be applied to a bilayer composed of two single-band superconductors. We note that these characteristic physical phenomena can also be investigated in superconducting layered rings, as shown in Ref. [192]. In such a case, an effectively two order parameters system emerges due to the coupling between the order parameter of each layer. In particular, the non-monotonic behavior of the critical flux with temperature can be accomplished in bilayer ring composed of different superconducting materials.

6 Vortical and Skyrmionic States in a Twisted-Bilayer with d-wave Superconducting Pairing

6.1 Introduction

Chiral superconductivity [193] has been a topic of tremendous interest in the recent literature due to its rich phenomenology [194, 195], including appearance of nontrivial surface currents [196] and half-quantum vortices [197, 198, 199, 200, 201], to name a few examples. Being mostly characterized by several Fermi surfaces, chiral superconductors often present multiple superconducting gaps, and are thereby prone to a plethora of interesting physics typical of multicomponent superconductivity [202, 120, 129, 203, 153]. Arguably, chiral superconductors gained a special relevance due to the increasing interest in topological superconductivity [14] and its promise towards use in modern quantum technologies [204]. With its highly non-trivial topology, the chiral state of superconductors is known to present the uniquely associated phenomena, such as the gapless edge states [205] and Majorana bound states localized in the vortex cores [206], which obey the non-Abelian statistics [207] fundamental to future applications in quantum computing.

Recently, Can *et al.* [1] showed that a twisted bilayer composed of two monolayers of the high-temperature superconductor $Bi_2Sr_2CaCu_2O_{8+\delta}$ [208] (Bi-2212) can display a chiral topological phase which breaks time-reversal symmetry for twist angles near 45°. As they argued, at a twist angle equal to 45°, the $d_{x^2-y^2}$ order parameter of each layer, characteristic of Bi-2212, induces a significant d_{xy} component in the order parameter of the other layer. This results in a superconducting state with $d + id'$ pairing symmetry. Note that, given the Josephson coupling between the two monolayers of such a system, the state in question bears physics related to φ-Josephson junctions [209, 210, 211].

The above arguments were developed in Ref. [1] considering a homogeneous superconducting state. IN what follows we go beyond this premise and investigate how such system responds to applied magnetic field, i.e. how the vortex matter of such bilayers evolves with the twist angle between the monolayers. As we will show, the emergent typical vortex configurations can be used as a smoking gun for the detection of the chiral topological phase. Recently, it was proposed that edge currents can be used as a probe of the topological phase [212, 213], although the small magnitude of such currents renders their detection experimentally challenging. In the case of vortices, due to the broken time-reversal symmetry, skyrmionic vortex states [214, 215, 216, 217, 218, 219, 201, 220, 221]

arise in the topological phase, and exhibit a distinct magnetic signature that can be detected in scanning imaging experiments. The skyrmionic nature of these states is identified through the topology of the pseudospin texture defined by the local correlations between the superconducting order parameters in the two layers. Furthermore, we show that the vortex matter changes even *within* the topological phase itself. Namely, as one varies the twist angle in the range where topological phase is stable, two different skyrmionic states are found. In one of them, states with unit topological charge are favored (presenting as a lattice of vortex pairs), while in the second one, states with large topological charge become energetically favorable, causing formation of extended vortex chains with a distinct appearance and magnetic signature.

The outline of this chapter is as follows. In Sec. 6.2 we present our theoretical formalism and show how we deal with the twisted bilayer system at hand within the framework of the Ginzburg-Landau theory. In Sec. 6.3 we present and discuss our main results. We start by showing the existence of a topological phase for certain values of the twist angle in a homogeneous system, to subsequently reveal and characterize the vortical and skyrmionic matter, as well as transitions between them, inside the topological phase. Our concluding remarks are given in Sec. 6.2.

6.2 Theoretical Formalism

To study a material with d-wave pairing within the Ginzburg-Landau framework, one need to consider also a second order parameter with s-wave pairing, once it is impossible to obtain a Ginzburg-Landau free energy with pure d-wave pairing due to symmetry reasons. The free energy of this $s+d$ system is given by [222, 27]:

$$\begin{aligned} F_1 \;=\; & -2\alpha_s|\Delta_{s1}|^2 - |\Delta_{d1}|^2 + \frac{4}{3}|\Delta_{s1}|^4 + \frac{1}{2}|\Delta_{d1}|^4 + \frac{8}{3}|\Delta_{s1}|^2|\Delta_{d1}|^2 + \frac{2}{3}(\Delta_{s1}^{*2}\Delta_{d1}^2 + H.c.) \\ & +2|\mathbf{\Pi}\Delta_{s1}^*|^2 + |\mathbf{\Pi}\Delta_{d1}^*|^2 + (\Pi_x\Delta_{s1}^*\Pi_x^*\Delta_{d1} - \Pi_y\Delta_{s1}^*\Pi_y^*\Delta_{d1} + H.c.)\,, \end{aligned} \tag{6.1}$$

with α_s determining the relative strength between the s and d-wave components and $\mathbf{\Pi} = (\mathrm{i}\boldsymbol{\nabla} - \boldsymbol{A})$. Note that the fourfold symmetry characteristic of d-wave superconductors is introduced in this model through the mixed gradient terms in the free energy contribution coming from the kinetic energy of the system. To focus on the d-wave order parameter, the value $\alpha_s = 0.7$ is taken such to make the s component of the order parameter very small *i.e.* not having a significant role in the physics of the system. In this case, we found the s-wave order parameter to be less than 20% of the d-wave component. Hereafter, the sub index 1 will refers to the unrotated layer.

Minimizing Eq. 6.1 with respect to both components of the order parameter, we find the following set of coupled equations:

$$-\alpha_s\Delta_{s1}+\frac{4}{3}|\Delta_{s1}|^2\Delta_{s1}+\frac{4}{3}|\Delta_{d1}|^2\Delta_{s1}+\frac{2}{3}\Delta_{d1}^2\Delta_{s1}^*+\Pi^{*2}\Delta_{s1}$$
$$+\frac{1}{2}(\Pi_x^{*2}-\Pi_y^{*2})\Delta_{d1}=0\ , \tag{6.2}$$

for the s-wave component, and:

$$-\Delta_{d1}+|\Delta_{d1}|^2\Delta_{d1}+\frac{8}{3}|\Delta_{s1}|^2\Delta_{d1}+\frac{4}{3}\Delta_{s1}^2\Delta_{d1}^*+\Pi^{*2}\Delta_{d1}+(\Pi_x^{*2}-\Pi_y^{*2})\Delta_{s1}=0 \tag{6.3}$$

for the d-wave component.

To use this formalism to investigate the twisted-bilayer we need two adaptations. The first of them is to write Eqs. 6.1-6.3 for a rotated coordinate frame, for the description of the twisted layer. Secondly, we need to add to the free energy the contribution coming from the Josephson coupling between the two layers.

Beginning with the first task, the transformation of coordinates to the the rotated frame is given as follows:

$$\begin{pmatrix}x'\\y'\end{pmatrix}=\begin{pmatrix}\cos(\theta) & \sin(\theta)\\ -\sin(\theta) & \cos(\theta)\end{pmatrix}\begin{pmatrix}x\\y\end{pmatrix}\ , \tag{6.4}$$

where x' and y' are the coordinates in the new rotated frame and θ is the angle of rotation.

To adapt Eqs. 6.1-6.3 to the new frame, we then need to find how the rotation affects the operator $\mathbf{\Pi}$. It is straightforward to see that the rotation operation given by Eq. 6.4 leads to the following relations:

$$\Pi_x'^2+\Pi_y'^2=\Pi_x^2+\Pi_y^2\ , \tag{6.5}$$

$$\Pi_x'^2-\Pi_y'^2=\cos(2\theta)\Pi_x^2-\cos(2\theta)\Pi_y^2-\sin(2\theta)\Pi_x\Pi_y-\sin(2\theta)\Pi_y\Pi_x\ . \tag{6.6}$$

With this, Eqs. 6.1-6.3 are written for the rotated frame as:

$$\begin{aligned}F_2 \;=\;& -2\alpha_s|\Delta_{s2}|^2-|\Delta_{d2}|^2+\frac{4}{3}|\Delta_{s2}|^4+\frac{1}{2}|\Delta_{d2}|^4+\frac{8}{3}|\Delta_{s2}|^2|\Delta_{d2}|^2+\frac{2}{3}(\Delta_{s2}^{*2}\Delta_{d2}^2+H.c.)\\ &+2|\mathbf{\Pi}\Delta_{s2}^*|^2+|\mathbf{\Pi}\Delta_{d2}^*|^2+(\cos(2\theta)\Pi_x\Delta_{s2}^*\Pi_x^*\Delta_{d2}-\cos(2\theta)\Pi_y\Delta_{s2}^*\Pi_y^*\Delta_{d2}\\ &-\sin(2\theta)\Pi_x\Delta_{s2}^*\Pi_y^*\Delta_{d2}-\sin(2\theta)\Pi_y\Delta_{s2}^*\Pi_x^*\Delta_{d2}+H.c.)\ ,\end{aligned} \tag{6.7}$$

with the Ginzburg-Landau equations for the order parameters:

$$
\begin{aligned}
&-\alpha_s\Delta_{s2}+\frac{4}{3}|\Delta_{s2}|^2\Delta_{s2}+\frac{4}{3}|\Delta_{d2}|^2\Delta_{s2}+\frac{2}{3}\Delta_{d2}^2\Delta_{s2}^*+\Pi^{*2}\Delta_{s2}\\
&+\frac{1}{2}\left(\cos(2\theta)\Pi_x^{*2}-\cos(2\theta)\Pi_y^{*2}\right)\Delta_{d2}-\frac{1}{2}\sin(2\theta)\Pi_x^*\Pi_y^*\Delta_{d2}\\
&-\frac{1}{2}\sin(2\theta)\Pi_y^*\Pi_x^*\Delta_{d2}=0\ ,
\end{aligned}
\tag{6.8}
$$

$$
\begin{aligned}
&-\Delta_{d2}+|\Delta_{d2}|^2\Delta_{d2}+\frac{8}{3}|\Delta_{s2}|^2\Delta_{d2}+\frac{4}{3}\Delta_{s2}^2\Delta_{d2}^*+\Pi^{*2}\Delta_{d2}\\
&+(\cos(2\theta)\Pi_x^{*2}-\cos(2\theta)\Pi_y^{*2})\Delta_{s2}-\sin(2\theta)\Pi_x^*\Pi_y^*\Delta_{s2}-\sin(2\theta)\Pi_y^*\Pi_x^*\Delta_{s2}=0\ ,
\end{aligned}
\tag{6.9}
$$

where sub index 2 refers to the rotated layer.

Finally the free energy contribution coming from the Josephson coupling between the two layers, as derived by Ref. [1], is given by:

$$
\begin{aligned}
F_{12} &= A|\Delta_{(d1)}|^2|\Delta_{(d2)}|^2-B\cos(2\theta)(\Delta_{(d1)}\Delta_{(d2)}^*+H.c.)\\
&\quad +C(\Delta_{(d1)}^2\Delta_{(d2)}^{*2}+H.c.)\ ,
\end{aligned}
\tag{6.10}
$$

with A, B and C taken as free phenomenological parameters. Note, however, that closed expressions for these parameters are microscopically derived in Ref. [1]. Given the d-wave symmetry of this component of the order parameter, the term proportional to B, representing the tunneling of Cooper pairs between each layer, must be proportional to $\cos(2\theta)$. With the same reasoning, authors of Ref. [1] state that the term proportional to C can be interpreted as the coherent tunnelling of two Cooper pairs between the layers.

The final set of equations for each component of the order parameter for both layers are then by minimizing the total energy $F=F_1+F_2+F_{12}$. This gives us:

$$
\begin{aligned}
&-\alpha_s\Delta_{(s1)}+\frac{4}{3}|\Delta_{(s1)}|^2\Delta_{(s1)}+\frac{4}{3}|\Delta_{(d1)}|^2\Delta_{(s1)}+\frac{2}{3}\Delta_{(d1)}^2\Delta_{(s1)}^*+\Pi^{*2}\Delta_{(s1)}\\
&+\frac{1}{2}(\Pi_x^{*2}-\Pi_y^{*2})\Delta_{(d1)}=0\ ,
\end{aligned}
\tag{6.11}
$$

$$
\begin{aligned}
&-\Delta_{(d1)}+|\Delta_{(d1)}|^2\Delta_{(d1)}+\frac{8}{3}|\Delta_{(s1)}|^2\Delta_{(d1)}+\frac{4}{3}\Delta_{(s1)}^2\Delta_{(d1)}^*+A|\Delta_{(d2)}|^2\Delta_{(d1)}\\
&-B\cos(2\theta)\Delta_{(d2)}+2C\Delta_{(d2)}^2\Delta_{(d1)}^*+\Pi^{*2}\Delta_{(d1)}+(\Pi_x^{*2}-\Pi_y^{*2})\Delta_{(s1)}=0\ ,
\end{aligned}
\tag{6.12}
$$

$$
\begin{aligned}
&-\alpha_s\Delta_{(s2)}+\frac{4}{3}|\Delta_{(s2)}|^2\Delta_{(s2)}+\frac{4}{3}|\Delta_{(d2)}|^2\Delta_{(s2)}+\frac{2}{3}\Delta_{(d2)}^2\Delta_{(s2)}^*\\
&+\frac{1}{2}(\cos(2\theta)\Pi_x^{*2}-\cos(2\theta)\Pi_y^{*2})\Delta_{(d2)}-\frac{1}{2}\sin(2\theta)\Pi_x^*\Pi_y^*\Delta_{(d2)}-\frac{1}{2}\sin(2\theta)\Pi_y^*\Pi_x^*\Delta_{(d2)}\\
&+\Pi^{*2}\Delta_{(s2)}=0\ ,
\end{aligned}
\tag{6.13}
$$

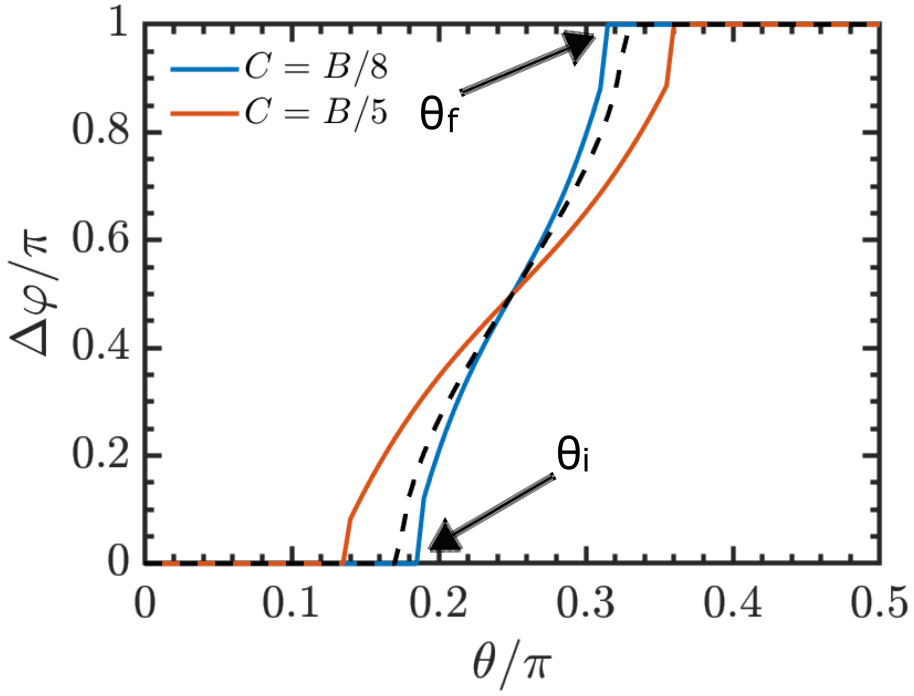

Figure 1 – *Phase difference between the d-wave components of the order parameters of two layers as a function of the twist angle θ. Blue and red curves represent the phase difference for $C = B/8$ and $C = B/5$, respectively, while $A = B = 0.1$. Dashed line shows the phase difference given by the analytical expression* $\arccos(B\cos(2\theta)/4C)$ *from Ref. [1], for $C = B/8$. The nontrivial values of the phase difference ($\neq 0$ or π) indicate existence of a topological phase for a particular twist angle.*

and:

$$
\begin{aligned}
&-\Delta_{(d2)} + |\Delta_{(d2)}|^2\Delta_{(d2)} + \frac{8}{3}|\Delta_{(s2)}|^2\Delta_{(d2)} + \frac{4}{3}\Delta_{(s2)}^2\Delta_{(d2)}^* + A|\Delta_{(d1)}|^2\Delta_{(d2)} \\
&-B\cos(2\theta)\Delta_{(d1)} + 2C\Delta_{(d1)}^2\Delta_{(d2)}^* + \Pi^{*2}\Delta_{(d2)} + (\cos(2\theta)\Pi_x^{*2} - \cos(2\theta)\Pi_y^{*2})\Delta_{(s2)} \\
&-\sin(2\theta)\Pi_x^*\Pi_y^*\Delta_{(s2)} - \sin(2\theta)\Pi_y^*\Pi_x^*\Delta_{(s2)} = 0\ . \qquad (6.14)
\end{aligned}
$$

In these equations, the order parameters are in units of $\Delta_0 = \sqrt{(4/3W)\ln(T_d/T)}$; lengths are in units of $\xi = (\nu_F/2)\sqrt{W/\ln(T_d/T)}$, where ξ is the coherence length of a single layer and $W = 7\zeta(3)/(8\pi^2T^2)$; magnetic field is in units of $H_{c2} = \Phi_0/(2\pi\xi^2)$, where the magnetic flux quantum is $\Phi_0 = hc/2e$; the free energy is in units of $E_0 = (4N(0)/3W)\ln(T_d/T)$.

Eqs. 6.11-6.14 are then solved for different twist angles θ, assuming periodic boundary conditions [223]. As the Ginzburg-Landau parameter κ for Bi-2212 is typically much greater than 1, we disregard the contribution of the supercurrents to the total magnetic

field and use a vector potential solely due to the applied magnetic field to solve the above set of equations.

For a given θ, we initialize the calculations from dozens of different initial conditions for the order parameters, which include the Meissner state, conventional vortex lattices and skyrmionic states, while also varying the aspect ratio of the unit cell of the simulation in order to identify the lowest-energy solutions for the vortex states. From a given initial state, the system is relaxed through the numerical solution of the time-dependent Ginzburg-Landau equations, which by construction guarantees the decrease of the system energy with time. In what follows, we display the ground-state found for an external applied magnetic field that corresponds to the flux of $24\Phi_0$ threading the shown unit cell, without loss of generality. Namely, for other values of the applied magnetic field we obtained qualitatively equivalent results. When plotting the magnetic field profile in different figures, we will show only the contribution of the supercurrents, after subtracting the (strongly dominating) homogeneous external field from the total calculated field. To obtain the field correspondent to each vortex configuration, we take the supercurrent $\boldsymbol{J}_s$ calculated through the solution of Eqs. 6.11-6.14 and numerically solve for the magnetic vector potential $\boldsymbol{\nabla} \times \boldsymbol{\nabla} \times \boldsymbol{A} = \boldsymbol{J}_s/\kappa^2$. In this solution, the periodic boundary conditions for the vector potential [223] are respected in our unit cell. The spatial distribution of the field shown in the figures is calculated at the plane of the superconducting film, taking into account the displaced Meissner currents in two layers as well as the Josephson current between them. We note, though, that the resulting vector potential is not fed back into the GL equations for the order parameters, since the system at hand is an extreme type-II one and the effect of the generated magnetic field on the superconducting condensate is negligible compared to the effect of the applied magnetic field.

6.3 Results and Discussion

As shown in Ref. [[1]] in the case of homogeneous superconductivity, for a certain range of θ the competition between the terms proportional to B and C in F_{12} yields a non-trivial phase difference between the d-wave components of the order parameters of the two layers. Let us start by discussing the homogeneous solutions of our free-energy model and show that it analogously allows for the existence of a topological phase.

To do this, we minimize the free energy density $\mathcal{F} = F_1 + F_2 + F_{12}$ with respect to the modulus and phase of the s and d components of the order parameter in both layers. Fig. 1 shows the phase difference between $\Delta_{(d1)}$ and $\Delta_{(d2)}$ ($\Delta\varphi = \varphi_{(d1)} - \varphi_{(d2)}$) which minimizes the free energy as a function of θ. As can be seen from the figure, for small twist angles up to a critical angle θ_i, the free energy is minimal when the order parameters have the same phase. For twist angles larger than a critical value θ_f, the phase difference

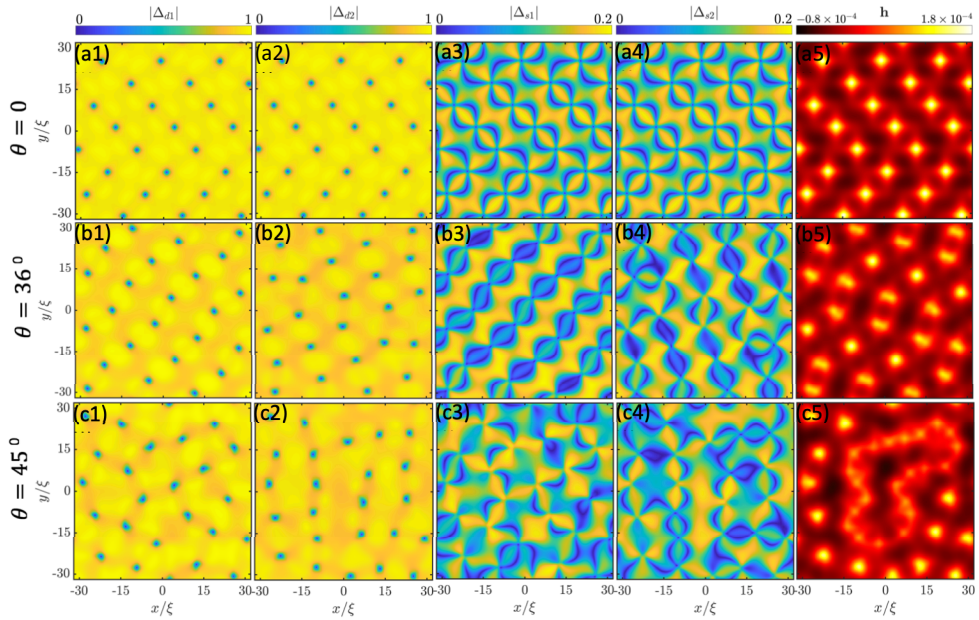

Figure 2 – *Vortex configurations in the d-wave component of the order parameter of the unrotated layer (first column) and the rotated layer (second column), for the s-wave component of the order parameter of the unrotated layer (third column) and the rotated layer (fourth column), and the magnetic response of the system (fifth column), for three selected twist angles between the layers. The applied magnetic field was* $H = 0.0368H_{c2}$*, corresponding to the magnetic flux of* $24\Phi_0$ *through the shown area of the sample.*

that yields minimal energy equals π.

On the other hand, for angles between θ_i and θ_f, one obtains a non-trivial phase difference between the condensates of the two layers, which means a superconducting state that breaks time-reversal symmetry. In particular, for $\theta = \pi/4$, the phase difference is equal to $\pi/2$, i.e. a $d + id'$ superconducting state is found [1]. The values of θ_i and θ_f depend on the particular values chosen for the parameters A, B and C, as can be seen from the two examples shown in Fig. 1. Nevertheless, the features of the superconducting state that we discuss below are always present in the range $\theta_i < \theta < \theta_f$, for any choice of the aforementioned parameters. Therefore, without loss of generality of our results, in what follows we will use the parameters correspondent to the blue curve in Fig. 1. In that case, $\theta_i \approx 34°$ and $\theta_f \approx 56°$.

Let us now go beyond these results and show how the twist angle affects the vortex matter of such bilayers. In Fig. 2 we show the spatial distribution of the d-wave and s-wave component of the order parameter for both layers, together with the magnetic field distribution in the system, for $\theta = 0$, 36° and 45°. Once the value of α_s is fixed, we expect no qualitative changes for the s-wave components when we change the twist angle. This is promptly confirmed in the third and fourth columns of Fig. 2. Moreover, as stated

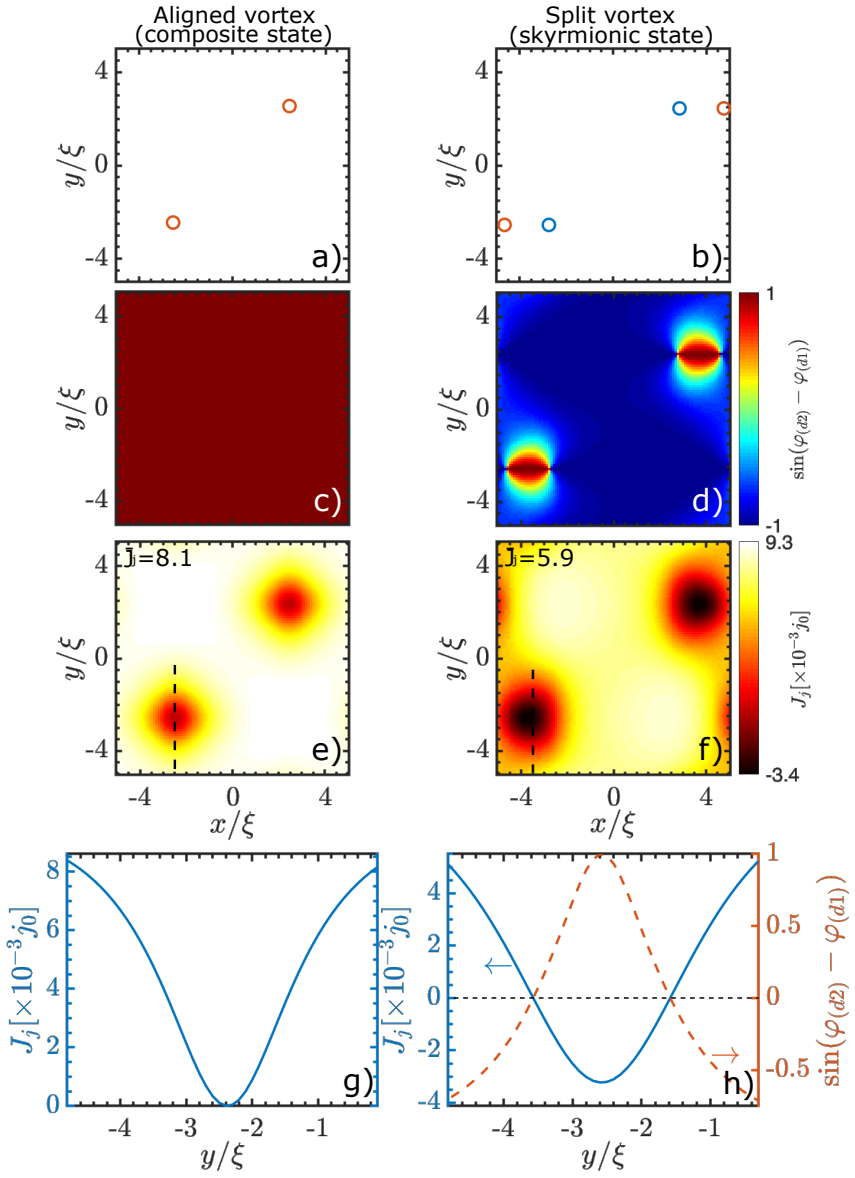

Figure 3 – *Zoom on the composite (phase shifted, $\Delta\varphi = \pi/2$, left column) and skyrmionic (minimum energy, right column) vortex states for a bilayer twisted with $\theta = 45°$, in applied magnetic field $H = 0.12H_{c2}$ (simulation region $36 \times 36\xi^2$). Panels a) and b) present the vortex positions in the first and the second layer (blue and red circles, respectively). Panels c) and d) show the sine of the phase difference between the condensates. Panels e) and f) plot the Josephson current profile, with the average Josephson current displayed in each panel. Panels e) and f) show the Josephson current profile along the black dashed lines in panels g) and h), respectively. Red dashed line in panel h) show the sine of phase difference between the layers along the same line as the current shown.*

previously, the magnitudes of the *s*-wave components are much smaller than the magnitudes for the *d*-wave components. Thus, the contribution of the *s*-wave order-parameters

to the supercurrents is very small, having no effect in the field profiles presented here. For $\theta = 0$, as discussed above, the phase difference between the order parameters is locked at zero. It is therefore energetically favorable for the vortices in the two layers to organize in a composite configuration, where the vortex cores are vertically aligned between the unrotated and the rotated layer. In this case, the magnetic field profile of the vortices exhibits well defined peaks at vortex locations and one can clearly distinguish the fourfold symmetry characteristic of $d_{x^2-y^2}$ superconductors. Note that, for a finite θ, the vortex lattice orientation would not be the same in each layer if they were decoupled. For the coupled case studied here, though, we found that the Josephson coupling leads to the alignment of the lattices and the vortex configurations remain qualitatively unchanged for the non-zero twist angles outside the topological phase, i.e. for $\theta < \theta_i$ or $\theta > \theta_f$.

Next, we increase the twist angle to 36°, larger than θ_i, to enter the topological phase in the ground state of the system (cf. Fig. 1). The composite vortex configuration is no longer the most energetically favorable state, as the vortex cores in two layers no longer coincide. As a consequence, the field of the vortex is now distributed over the two displaced cores in two layers (see Fig. 2), reflecting a magnetic field profile of a dimer rather than one clear peak. Notably, some vortices within the configuration remain seemingly composite. The situation radically changes as we increase the twist angle further, to $\theta = 45°$ (bottom row of Fig. 2). Here one sees that not only vortex cores displace between the layers, they also organize into extended closed vortex chains. As will be discussed in the following paragraphs, such a vortex chain is formed along a domain wall separating sample regions with different phase differences between the layers. Moreover, such chains will exhibit skyrmionic topology, with an integer topological charge equal to the total vorticity of the chain. Last but not least, the overall shape and the magnetic signature of these chains are uniquely distinct which facilitates their experimental observation.

The vortex splitting in the topological phase occurs in order to reduce the Josephson current between the layers and thereby minimize the energy. This is shown in Fig. 3, where we compare the composite (left column) and skyrmionic (right column) vortex state for a system with twist angle $\theta = 45°$. In the composite state, the phase difference between the d-wave component of the order parameters in each layer is fixed at $\pi/2$, which is an energetically favorable phase difference in absence of vortices. Panels a) and b) present the vortex core position in layers 1 (blue circle) and 2 (red circle). The sine of the phase difference between the d-wave component of the order parameter in each layer is shown in panels c) and d), to highlight the spatial phase changes. Panels e) and f) present the profile of the Josephson current, with its average value given in the top left corner of each panel. Finally, panels g) and h) show the Josephson current profile along the black dashed lines shown in panels e) and f). As seen in panels e) and f), the phase texture that emerges from the vortex splitting decreases the overall Josephson current between the layers, consequently lowering the system energy and rendering the skyrmionic

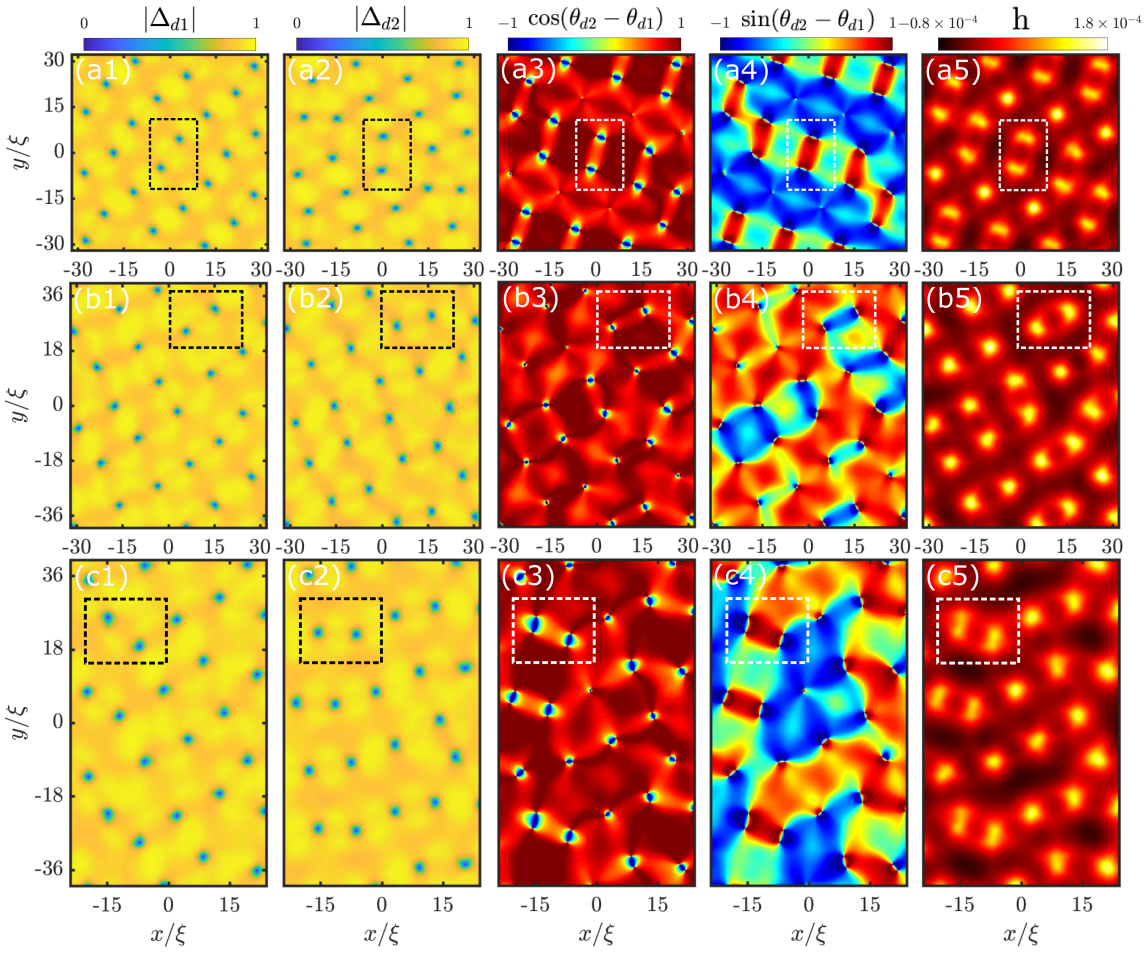

Figure 4 – *Vortex configurations for twist angle $\theta = 36° \gtrsim \theta_i$ at three values of applied magnetic field. Each row corresponds to a different system size (lateral sizes are shown), for same magnetic flux of $24\Phi_0$. From left to right, the columns respectively show the magnitude of the d-wave component of the order parameter for unrotated and rotated layers, the cosine and sine of the phase difference between the order parameters in two layers, and the magnetic field distribution across the system.*

state energetically favorable. From the current profile presented in panels *g*) and *h*) one can better relate the vortex splitting to the profiles of phase and the Josephson currents around a vortex. While for the composite vortex the Josephson current is always positive and vanishes only at the vortex core, the skyrmionic state presents Josephson current with opposite polarities in the domains of phase difference $\pm\pi/2$, with zero Josephson current at the phase domain wall (cf. dashed red line in panel *h*) of Fig. 3. The line profiles along the black dashed line in this panel help visualize the correspondence between the zero Josephson current and $\Delta\varphi = 0$). We note that during the numerical solution of the Ginzburg-Landau equations, the aligned vortex state transits to a split vortex state, reconfirming the latter as the most stable and minimal energy solution for our system.

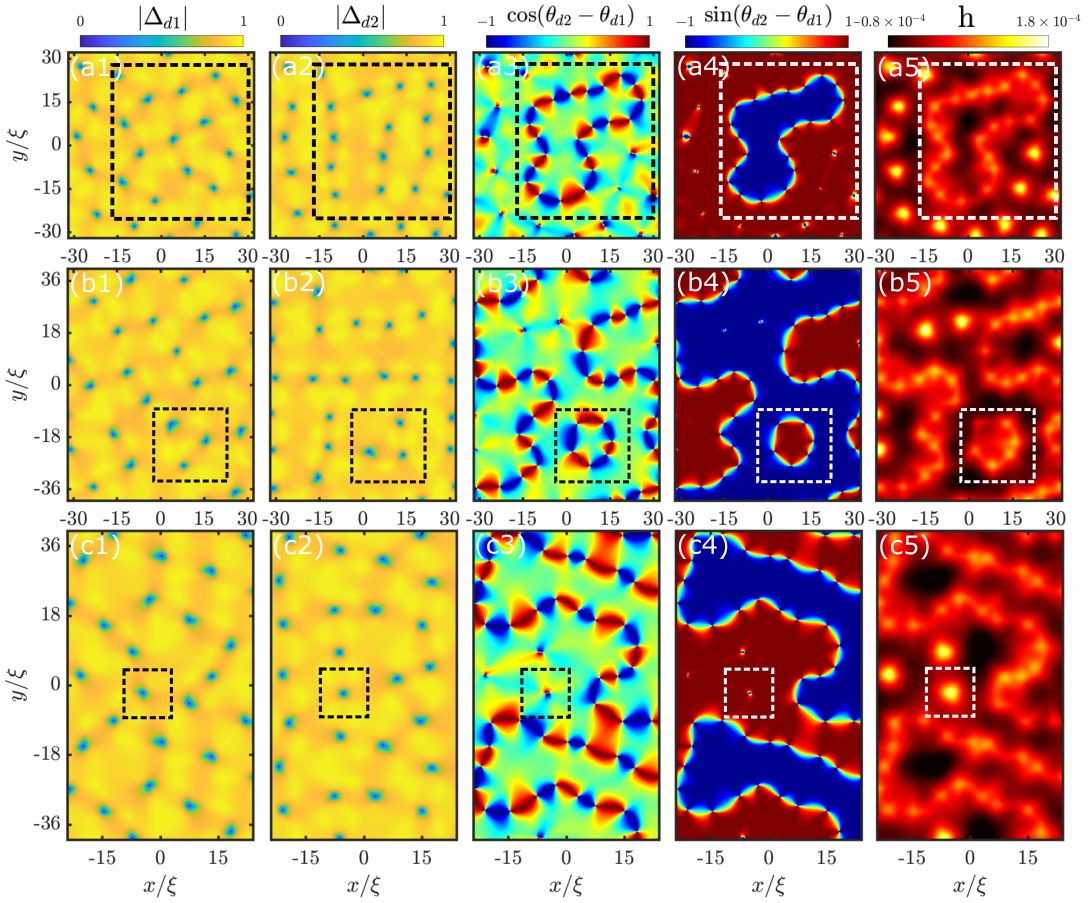

Figure 5 – *Vortex configurations for $\theta = 45°$, deep inside the topological phase, for three values of applied magnetic field. Each row corresponds to a different system size (lateral sizes are shown), for same magnetic flux of $24\Phi_0$. From left to right, the columns respectively show the magnitude of the d-wave component of the order parameter for unrotated and rotated layers, the cosine and sine of the phase difference between the order parameters in two layers, and the magnetic field distribution across the system.*

These results demonstrate that the twist angle and the onset of a topological phase strongly influence the vortex matter of the system, with detectable consequences in the magnetic profile at the onset of the topological phase and within the topological phase itself. Due to the very large effective penetration depth of this ultrathin superconducting system, a detailed characterization of the field profile is a difficult experimental task. Even so, we note that the significant symmetry differences between the magnetic profile of the composite vortex lattice and the vortex chains can be experimentally detected, especially if the scanning probe can be brought in close proximity to the surface of the crystalline 2D material. This feature can therefore be used as a smoking gun for the detection of topological superconductivity in such and similar bilayers. In what follows, we further detail the vortex configurations for $\theta = 36°$ and $\theta = 45°$, which are the representative examples of two different types of behavior we encountered in the vortex matter inside

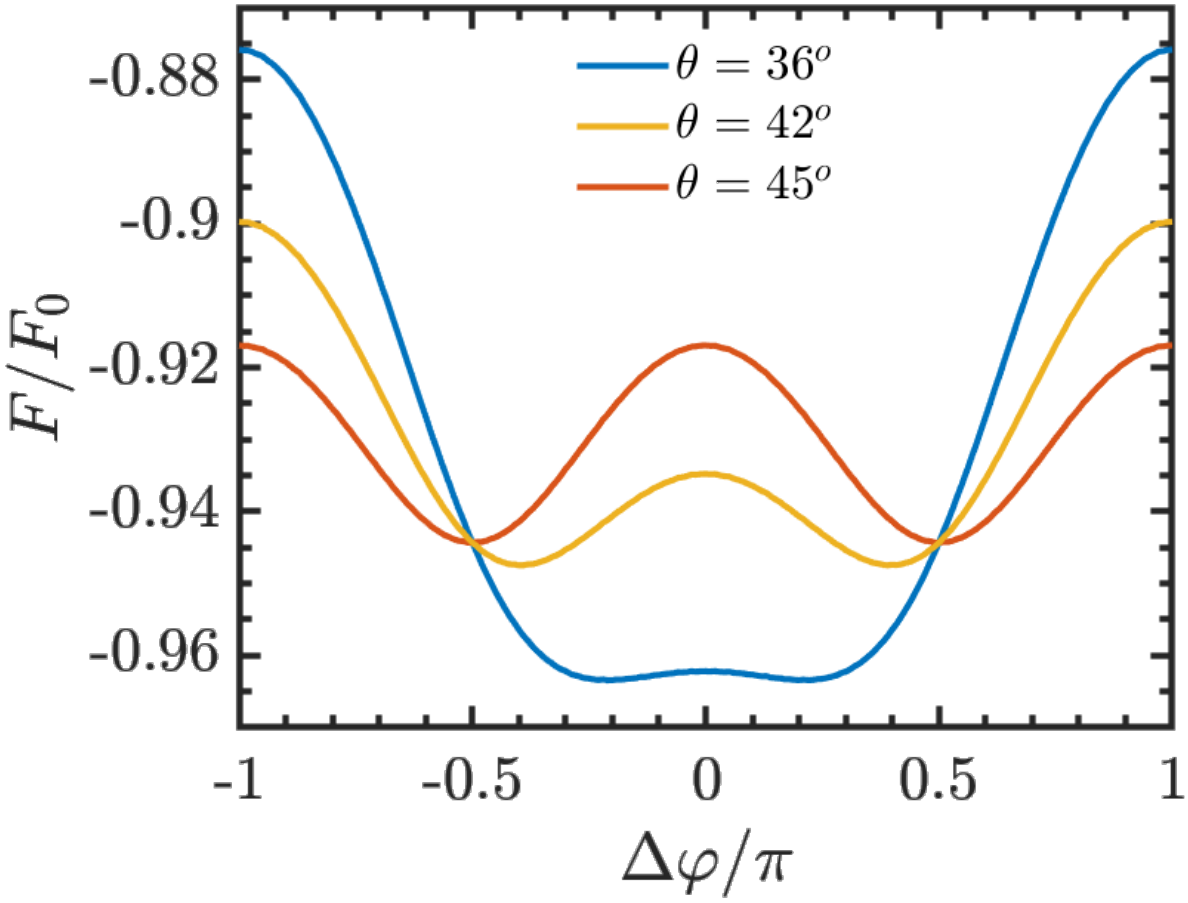

Figure 6 – *Energy of the homogeneous system (without vortices) as a function of the phase difference between the d-wave components of the order parameter in two twisted layers. The blue, yellow and red curves show the energy for the twist angle* $\theta = 36°$, $\theta = 42°$ *and* $\theta = 45°$, *respectively.*

the topological phase.

6.3.1 Vortex Matter at the Onset of the Topological Phase

We start the description of the vortex matter for an angle close to θ_i (equivalent results are obtained for angles close to θ_f). In Fig. 4 we show vortex configurations found for $\theta = 36°$, each row displaying minimum energy solutions for a different size of the unit cell. As discussed previously, the vortex cores in two layers are displaced from each other inside the topological phase, but each vortex of a given layer remains connected to its counterpart in the other layer. This is visible in the phase difference profile, suggesting the existence of a phase soliton between the two vortex cores. Hereafter, we refer to this pair of connected vortices as the interlayer vortex pair. As can be seen in Fig. 4, inside the interlayer vortex pair we find the phase difference $\Delta\varphi = \pi$ between the condensates in two layers, and $\Delta\varphi = 0$ outside of the pair.

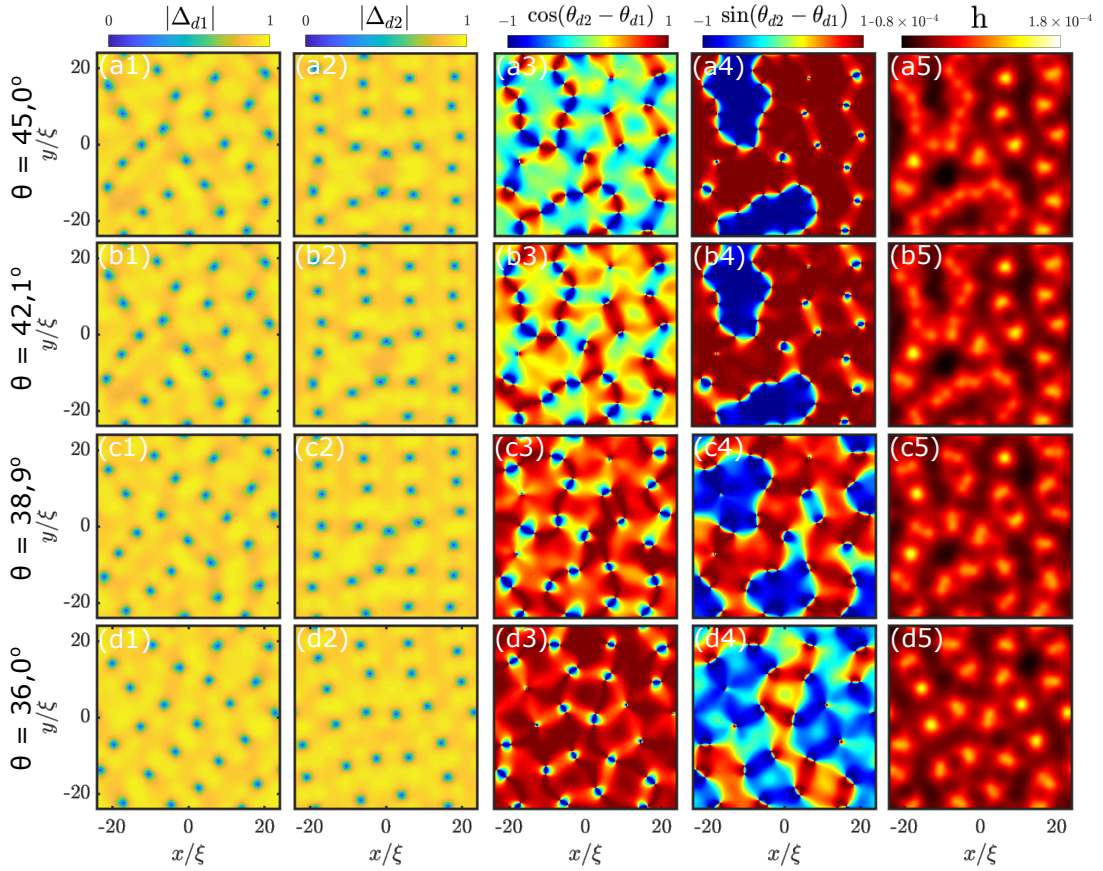

Figure 7 – *Evolution of the vortex configuration when adiabatically decreasing the twist angle from $\theta = 45°$ to 36°. From left to right, the columns respectively show the magnitude of the d-wave component of the order parameter for unrotated and rotated layers, the cosine and sine of the phase difference between the order parameters in two layers, and the magnetic field distribution across the system.*

As an object, the interlayer vortex pair displays skyrmionic properties. To better see this, we map our GL model to a σ model, as done in Refs. [219, 198] in the context of multicomponent systems, defining the pseudo-spin

$$\boldsymbol{n} = \frac{\Delta_d^\dagger \boldsymbol{\sigma} \Delta_d}{\Delta_d^\dagger \Delta_d}, \tag{6.15}$$

with $\Delta_d = (\Delta_{(d1)}, \Delta_{(d2)})$ and $\boldsymbol{\sigma} = (\sigma_1, \sigma_2, \sigma_3)$, where σ_i is the Pauli matrix. We note that, although $\Delta_{(d1)}$ and $\Delta_{(d2)}$ describe the superconducting order parameter in different layers, here they are defined in the same plane, to allow the introduction of the pseudo-spin.

With such pseudo-spin profile, one then calculates the topological charge of the system, defined as

$$Q = \frac{1}{4\pi} \int \boldsymbol{n} \cdot \left(\frac{\partial \boldsymbol{n}}{\partial x} \times \frac{\partial \boldsymbol{n}}{\partial y} \right) dxdy. \tag{6.16}$$

If we calculate the total topological charge for the three different configurations

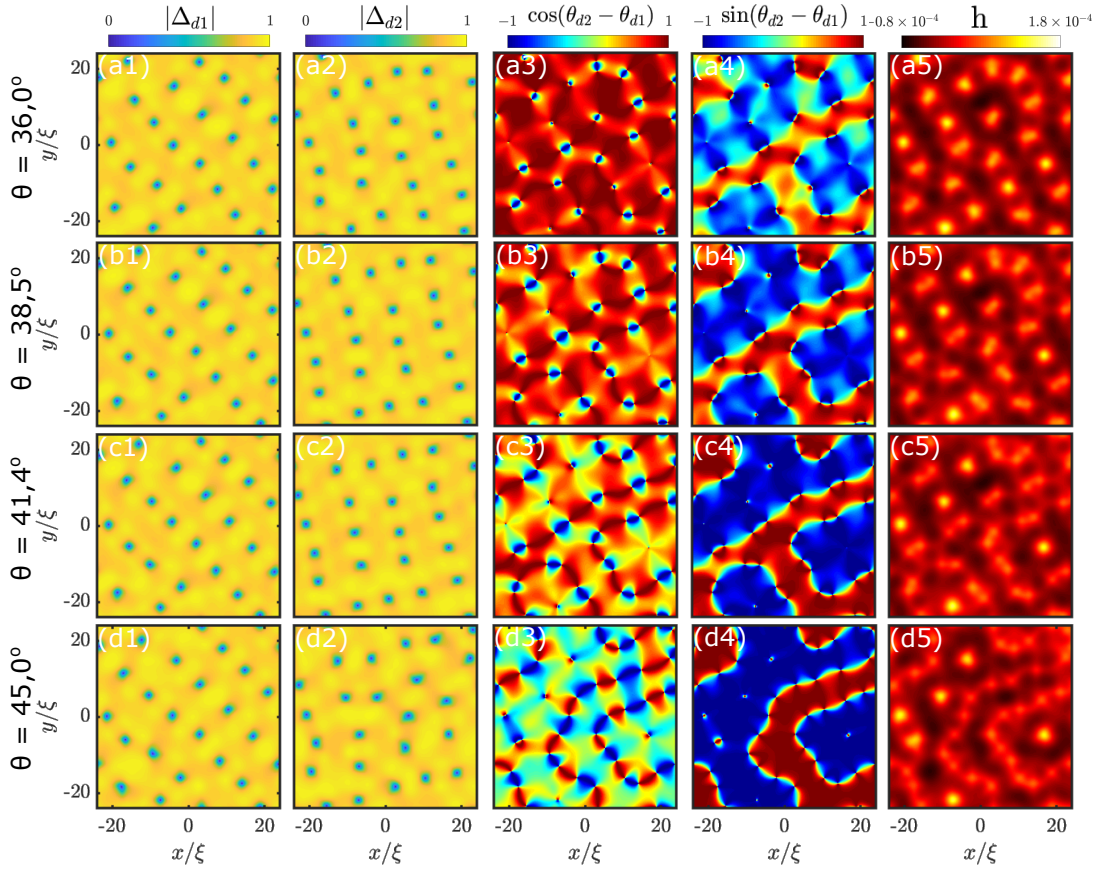

Figure 8 – *Evolution of the vortex configuration when adiabatically increasing the twist angle from $\theta = 36°$ to $45°$. From left to right, the columns respectively show the magnitude of the d-wave component of the order parameter for unrotated and rotated layers, the cosine and sine of the phase difference between the order parameters in two layers, and the magnetic field distribution across the system.*

shown in Fig. 4, we obtain $Q = 24$ for each of them. As the same number of flux quanta (24) are threading the shown unit cells, we conclude that each interlayer vortex pair is actually a skyrmionic object with a topological charge equal to 1 (for a truly composite vortex, $Q = 0$). We confirmed this further by calculating the topological charge not over the entire unit cell, but only around isolated interlayer pairs.

Within the dashed rectangles shown in Fig. 4 we highlight vortex configurations characteristic of the topological phase for twist angles close to θ_i. As can be seen from the cosine and sine of the phase difference between the condensate of each layer, two adjacent interlayer vortex pairs typically organize themselves into a larger correlated object. Inside the dashed rectangles in panels $(a1)-(a2)$ of Fig. 4, we can see that in one of the interlayer vortex pairs (the one near the top of the rectangle) the vortex of the unrotated layer is on the right and the vortex of the rotated layer is on the left. In the interlayer pair near the bottom of the rectangle, the vortex positions are interchanged. In other words, adjacent

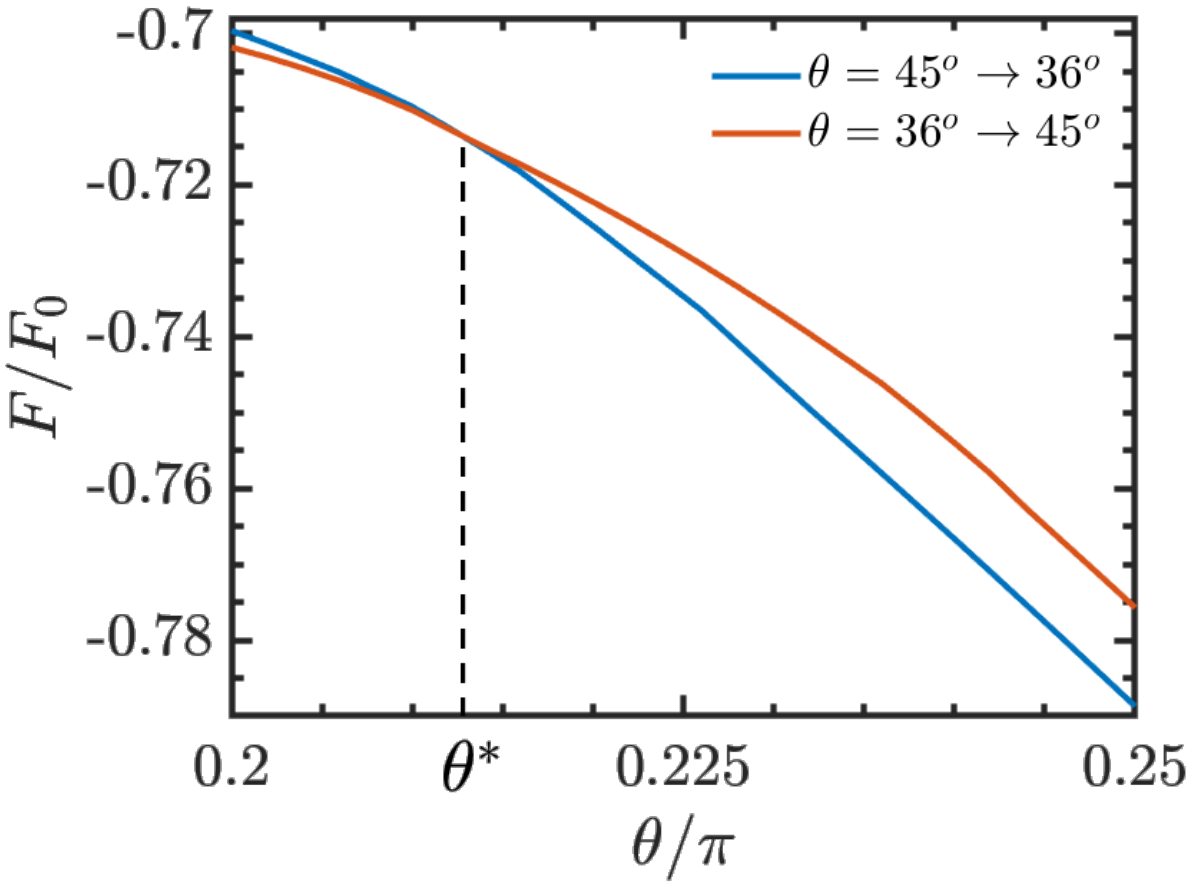

Figure 9 – *Energy as a function of the twist angle θ. The blue and red lines show the energy curves for the twist angle being decreased from $\theta = 45°$ to $36°$ and increased from $36°$ to $45°$, respectively.*

pairs of vortices in two layers are twisted with respect to each other. The same behavior can be easily verified in panels $(b1) - (b2)$ and $(c1) - (c2)$. After such an organization of interlayer vortex pairs, their interlayer phase solitons become visibly connected, as seen in the dashed rectangle of the cosine of the phase difference in Fig. 4. Due to proximity and strong overlap between different phase domains, a supercurrent emerges surrounding the two interlayer vortex pairs, yielding a rather weak magnetic field. As a consequence, while the field profile of each pair is strong and the spatial correlation between them is rather obvious, the consequence of the phase connection between them is difficult to spot in the last column of Fig. 4.

6.3.2 Vortex Matter Deep Inside the Topological Phase

Finally we reveal the evolution of the vortex matter when the twisted bilayer is deeply inside the topological phase, i.e. for twist angle $\theta \approx 45°$ in the present case. As previously shown, for this θ the phase difference between the d-wave components of the order parameters in two layers is $\pi/2$ and we have a $d+id'$ superconducting state. Despite

this particularity, the characteristics encountered in the vortex matter in this case can be related to those exhibited for other twist angles within the topological phase in the vicinity of $\theta = 45°$.

Fig. 5 shows the order parameters of both layers, the cosine and the sine of the phase difference between the layers and the magnetic field profile for $\theta = 45°$. In this case, formation of interlayer vortex pairs with topological charge $Q = 1$ is still favorable, as highlighted by dashed rectangles in panels $(c1) - (c5)$ of Fig. 5. However, as highlighted by dashed rectangles in panels $(a1) - (a5)$, the organization of interlayer vortex pairs into larger objects is preferable. As a consequence, a new vortex configuration emerges - the skyrmionic chain. In this uniquely distinct state, instead of the small interlayer phase domains within individual interlayer vortex pairs, much larger domains are formed. Interlayer vortex pairs are interconnected along the domain wall, with a vortex core from one layer being in between two vortex cores of the other one, forming a closed chain of interlayer vortex pairs. Dashed rectangles in panels $(a1) - (a5)$ of Fig. 5 exemplify one such structure, containing 11 interlayer vortex pairs in a single closed chain. In panel $(a5)$, one can see that such vortex chain is a very laterally extended object (nearly $40\xi \times 40\xi$ in this case), and leaves a very clear and rather unusual signature in the magnetic field profile of the system. Here, the peaks of the magnetic field along the vortex chain are smaller in comparison with the isolated interlayer vortex pairs due to the fact that the distance between the vortex cores in two layers is significantly larger in the former case.

Once again, and as can be seen from the third and fourth columns in Fig. 5, the closed vortex chain separates two regions with different phase differences between the layers. Inside the vortex chain, the phase difference between the condensates is $\Delta\varphi = -\pi/2$, while outside the chain $\Delta\varphi = \pi/2$. The opposite is also possible: panels $(b1) - (b5)$ show such an example, where $\Delta\varphi = \pi/2$ inside the chain, while $\Delta\varphi = -\pi/2$ outside. We note the difference from the case of the individual interlayer vortex pairs, harboring phase difference π within them, with zero phase difference away from the pair.

If we now calculate the total topological charge around the vortex chains seen in panels $(a1) - (a5)$ and $(b1) - (b5)$, we obtain $Q = 11$ and $Q = 3$, respectively, reflecting the number of interlayer vortex pairs interconnected in the chain. These large values for the topological charge of such a novel object contrast the exclusively $Q = 1$ of the individual interlayer vortex pairs found for $\theta = 36°$. This very different behavior for different twist angles emerges from the fact that, as discussed before, the domain wall separates regions with a phase difference equal to 0 and π for $\theta = 36°$ and $-\pi/2$ and $\pi/2$ for $\theta = 45°$.

To understand how the value of the phase difference inside the domains affects the topological charge, Fig. 6 shows the energy of the homogeneous system as a function of the phase difference between the layers $\Delta\varphi$ for different values of the twist angle θ. At the onset of the topological phase (blue curve in Fig. 6), the energy of the system is largest

when the phase difference is π. Therefore, larger splitting within each formed interlayer vortex pair costs energy, and their interconnection into larger objects is not energetically favorable. Notice that, as discussed in Fig. 1, the phase difference equal to 0 does not yield the free energy minimum in the homogeneous state of the system for θ at which the topological state is stable. In the presence of magnetic field, the formation of interlayer vortex pairs re-stabilizes the zero phase difference in a large part of the superconductor for θ close to θ_i and θ_f.

On the other hand, deep in the topological phase (for $\theta = 45°$), a degenerate lowest energy homogeneous state is found for phase difference equal to either $-\pi/2$ or $\pi/2$, explaining the tendency to formation of coexisting domains with such phase differences. The resulting long domain walls would cost energy, but not in the presence of magnetic field when they are decorated by the skyrmionic vortex chains.

For θ values in the vicinity of 45°, represented in Fig. 6 by $\theta = 42°$, the free-energy minima no longer occur at $-\pi/2$ and $\pi/2$ but shift to lower phase differences and become shallower (cf. Fig. 6). Nevertheless, the system still presents the vortex chains dividing the superconductor in regions with phase differences $-\pi/2$ and $\pi/2$, since vortices require a total phase difference π across the domain wall on which they reside. Once both values of the phase difference possess the same free energy, the long domain walls described above are also present, with the same size as the ones for $\theta = 45°$.

6.3.3 Transitions Between the Topological Vortex Matter with the Interlayer Twist

Complementary, it seems relevant to discuss in which manner the above-described characteristic skyrmionic states in the topological phase evolve as one continuously varies the twist angle. To capture this behavior, we follow two distinct procedures. In the first, we start deep in the topological phase, i.e. at a twist angle $\theta = 45°$ and a skyrmionic vortex chain as the initial state of the simulation. We then "adiabatically" decrease the twist angle down to 36°, in decrements of 0.1°, recording the evolution of the stable solution (which is no longer necessarily the lowest-energy state). In Fig. 7 we show the selected vortex configurations obtained during this procedure. Starting from the skyrmionic vortex chain (panels $(a1) - (a5)$), we see that when the twist angle is decreased to $\theta = 42.1°$ (panels $(b1) - (b5)$), the contour of the chain can still be seen in the magnetic field profile of the system. At the same time, the sine of the phase difference shows that the vortex chain still splits the superconducting landscape in regions with interlayer phase difference equal to either $\pi/2$ and $-\pi/2$. However, vortices in each layer start to group in pairs, as reflected in double peaks appearing in the magnetic field profile along the chain. This indicates the onset of the transition from the skyrmionic vortex chain to the skyrmionic state with separate interlayer vortex pairs. Such a transition is more apparent for $\theta = 38.9°$

(panels $(c1)-(c5)$). Although the magnetic field contour of the vortex chain can still be visualized in this case, the separation of the superconductor into regions with different interlayer phase differences becomes less clear. Finally, at $\theta = 36°$ (panels $(d1)-(d5)$) the transition between the two skyrmionic states is completed and the system displays an arrangement of dissociated individual interlayer vortex pairs, surrounded by a landscape of near-zero interlayer phase difference.

Along the opposite route, we start with the lowest-energy state with interlayer vortex pairs for $\theta = 36°$ (shown in panels $(a1)-(a5)$ of Fig. 8) as the initial state of our system and then gradually increase the twist angle up to $\theta = 45°$. As can be conveniently seen from the third and fourth columns of Fig. 8, the state gradually changes from the topological phase with regions of interlayer phase difference either 0 or π to another one with regions of interlayer phase differences either $\pi/2$ or $-\pi/2$. As the twist angle is increased, the vortices forming an interlayer vortex pair slowly separate from each other. One sees this by comparing the magnetic profile in panels $(b5)$ and $(c5)$, where the double peak characteristic of a vortex pair becomes smeared. For twist angles in the vicinity of $\theta = 45°$, this culminates in the formation of the skyrmionic vortex chain state, as we display in panels $(d1)-(d5)$.

Both discussed transitions between the two different topological skyrmionic vortex states occur through the second-order relocation of vortex cores in each layer. This is further evidenced in Fig. 9, where we show the energy of the system as a function of the twist angle for the cases where θ is decreased from 45° to 36° (blue line, cf. Fig. 7), and increased from 36° to 45° (red line, cf. Fig. 8). In other words, we evolve the two characteristic skyrmionic vortex states found at two ends of the θ-range of the topological phase of the system by gradually changing the twist angle across the topological phase. As seen in Fig. 9, the energies of those states cross in energy at a twist angle $\theta^* \approx 38°$, i.e. the states dominated by interlayer vortex pairs are energetically preferred for interlayer twist below this angle, whereas the states containing extended skyrmionic vortex chains become favorable for $\theta > \theta^*$. Obviously the exact value of θ^* will depend on the details of the simulation (size of the unit cell, magnetic field), but we can safely generalize this result to conclude that skyrmionic vortex chains should be observable in the larger portion of the twist range where topological phase is expected.

6.4 Concluding Remarks

To summarize, we have analyzed the vortex configurations emerging in a twisted bilayer composed of superconducting monolayers with d-wave pairing - motivated by prospects of such realizations using e.g. $Bi_2Sr_2CaCu_2O_{8+\delta}$. In such a system, the phase difference between the superconducting order parameters in two layers depends on the twist

angle θ, with a topological state with a non-trivial phase difference emerging for a range of angles around $\theta = 45°$. In that topological phase, the superconducting state exhibits broken time-reversal symmetry, giving rise to skyrmionic vortex configurations with topological charge not equal to zero. We revealed and characterized those nontrivial vortex states, and discussed their detectable differences when compared to usual vortex lattice found for twist angles outside the topological range. Based on those clearly discernible differences, we argue that direct experimental observation of skyrmionic vortex states can be used as a smoking gun to detect topological superconductivity in such systems.

In addition, we showed that the skyrmionic vortex matter also evolves with the twist angle inside the topological phase. Namely, we have identified two distinct types of skyrmionic states. At the onset of the topological state, the system prefers to preserve same phase of the order parameter in two layers, so the broken reversal symmetry reflects solely in formation of the interlayer vortex pairs. Each of this pairs carries a unit of topological charge, and hosts phase difference π between the coupled superconducting layers. As the twist angle is varied towards 45° and one is deeper in the topological state, the phase difference of $\pm\pi/2$ becomes energetically favorable. As a consequence, the interlayer vortex pairs interconnect into extended closed chains, separating the regions of the sample with phase difference either $-\pi/2$ or $\pi/2$. Such chains can easily exhibit lateral extent on the micron scale, and carry topological charge equal to the number of vortices interconnected in the chain. Once again, we emphasize that each of the two types of skyrmionic flux objects leaves a clear signature in the spatial profile of the magnetic field across the system, but will also host uniquely related local density of states and bound states detectable by e.g. Scanning Tunneling Microscopy, as also suggested in Refs. [147, 224] for the case of chiral *d*-wave superconductors. The calculation of such states is left as a prospect for further work, being beyond the capability of the present Ginzburg-Landau analysis (with Bogolyubov-de Gennes approach as a viable alternative [225, 226]. Another interesting outlook is to adapt the here-presented Ginzburg-Landau formalism to the cases of other pairing symmetries that may arise in the twisted bilayers of present interest, so to classify the emergent vortex matter according to the symmetries at hand - and thereby enable conclusive identification of the pairing symmetry in experimental systems through visualization of the vortex states - complementary to other existing efforts (see e.g. [227]). Finally, we note that recent experimental breakthroughs [228, 229] readily realized high-quality Josephson junctions of twisted $Bi_2Sr_2CaCu_2O_{8+\delta}$ flakes, promoting such devices for further technological applications, rendering the analysis of the vortex states presented in this chapter timely and relevant even from an applied point of view.

7 Summary and outlook

7.1 Summary

In the preceding chapters, we explored both the stationary and dynamic characteristics of superconducting vortex matter, uncovering properties that are intriguing from both a fundamental and practical perspective. Throughout this study, we examined various superconducting systems, including conventional mesoscopic and nanostripes of type I and II under the influence of applied magnetic fields and currents, two-band superconducting rings subjected to external magnetic flux, and twisted bilayer heterostructures composed of superconductors exhibiting *d*-wave pairing.

In **Chapter 2**, we revisited the longstanding issue of classifying superconductors into type I and type II. Specifically, we examined how the presence of superconductor/insulator surfaces alters the conventional Ginzburg-Landau (GL) classification, where materials are defined as type I when the GL parameter $\kappa_c < 1/\sqrt{2}$, and type II when $\kappa_c > 1/\sqrt{2}$. Our analysis focused on mesoscopic superconducting squares, where the small volume-to-area ratio amplifies these effects. We discovered that, unlike bulk superconductors which have a single critical κ_c, mesoscopic systems exhibit three distinct critical κ values, each marking a different regime in the superconductor's response to an applied magnetic field. For $\kappa < \kappa_{c1}$, we observe *genuine* type I behavior, where vortices are entirely absent, regardless of whether the magnetic field is increased (from 0 to H_{c2} starting from the Meissner state) or decreased (from H_{c2} to 0 starting from the normal state). In the range $\kappa_{c1} < \kappa < \kappa_{c3}$, the system exhibits an *intermediate* type I behavior. Here, vortices remain forbidden during the ascending field protocol, but may nucleate during the descending protocol. Within this *intermediate* type I regime, two distinct responses can be identified during the descending field protocol: for $\kappa_{c1} < \kappa < \kappa_{c2}$, the response is consistently diamagnetic, while for $\kappa_{c2} < \kappa < \kappa_{c3}$, a paramagnetic response can emerge in certain field ranges. Lastly, for $\kappa > \kappa_{c3}$, the system enters a *quasi* type II regime, where vortices can also appear during the ascending field protocol.

In **Chapter 3**, we shifted our focus to the dynamic properties of thin superconducting nanostripes under the influence of an applied current. Specifically, we investigated how the stripe's thickness influences the creation and annihilation of vortex-antivortex pairs. In circular superconducting wires, due to the symmetry of the magnetic field generated by the transport current, it was theorized that flux penetrates the superconductor in the form of a closed loop. Although this closed vortex line was predicted theoretically, it has remained elusive in experiments, as its weak stray magnetic field and short lifetime pre-

vent detection via techniques such as STM measurements. In our study, we demonstrated that a new type of closed vortex state can emerge in rectangular stripes with sufficient thickness. We showed that as vortex and antivortex lines approach each other during the annihilation process, the endpoints of these lines—located near the top and bottom surfaces of the superconducting film—move at higher velocities. Consequently, these points meet first, forming a closed vortex loop that gradually contracts until it collapses entirely. To conclude our study, we proposed two potential experimental protocols for detecting this closed vortex state.

Continuing our exploration of superconducting materials under transport currents, in **Chapter 4**, we investigated how a superconducting stripe subjected to an inhomogeneous magnetic field can function as a superconducting diode. We proposed a device configuration consisting of a central superconducting film flanked by two superconducting wires carrying a DC bias. This setup breaks both inversion and time-reversal symmetries in the system, leading to a polarity-dependent critical current in the central stripe. By carefully tuning the DC bias in each wire, we demonstrated that it is possible to achieve an optimal condition where vortex entry is facilitated for one current polarity and entirely suppressed for the opposite polarity, effectively resulting in half-wave rectification. Upon studying different inhomogeneous magnetic field profiles, we found that the diode's efficiency is maximized with an antisymmetric inhomogeneous field that closely resembles the self-field profile of the current in the central superconductor. In this scenario, the Bean-Livingston barrier is maximized for one current polarity, preventing flux penetration and increasing the critical current. Conversely, for the opposite polarity, the constructive combination of the external and inhomogeneous fields promotes the entry of vortices and antivortices, which annihilate at the stripe's center, creating hot spots and leading to a lower critical current. Finally, we examined how the diode's efficiency is influenced by heat removal efficiency and the sweep rate of the applied current. Our results revealed that smaller values for both parameters significantly enhance the diode's performance.

In **Chapter 5**, we began our investigation into superconducting systems characterized by multiple order parameters by examining the stability of flux states in two-band superconductor rings. It is well-known that, when subjected to a sufficiently strong external magnetic flux, a conventional single-band superconductor ring transitions to a lower-energy state via a phase-slip, where each phase-slip alters the phase winding of the superconducting order by 2π. The critical flux Φ_c required for a transition between states with winding numbers n and $n \pm 1$ can be determined using a combination of Ginzburg-Landau theory and Linear stability analysis. In this chapter, we extended this approach to two-band superconductors and developed a semi-analytical method to quickly determine Φ_c for any desired transition. We applied this method to explore how Φ_c depends on factors such as the ring radius, system temperature, and the ratio of diffusion coefficients between the two bands. Notably, we discovered that the coupling between the two

bands induces a non-monotonic dependence of Φ_c on temperature, a feature that can be leveraged to probe the existence of multiple order parameters in newly discovered superconducting materials. Furthermore, we employed the time-dependent Ginzburg-Landau formalism to investigate the conditions necessary for the stability of soliton states, where the winding number differs between the two condensates in the system.

Finally, in **Chapter 6**, we explored vortical and skyrmionic states in twisted bilayers with d-wave pairing symmetry. Recent breakthroughs in high-temperature superconductivity in two-dimensional cuprate superconductors, as well as the creation of twisted heterostructures using these materials, have generated significant interest in the physics of these systems. It has been shown that the symmetry mismatch in the nodal gaps of twisted bilayers suppresses Cooper pair tunneling at twist angles close to 45°, with Josephson coupling between the layers primarily driven by second-order processes. The competition between first- and second-order tunneling mechanisms results in a non-trivial phase difference between the layers, leading to the breaking of time-reversal symmetry. In our study, we demonstrated that within this time-reversal symmetry-breaking phase, the vortex matter transitions from conventional vortical states to skyrmionic states. Additionally, we identified two distinct types of skyrmionic states and showed how the characteristic patterns in their magnetic field profiles could serve as a smoking gun for detecting the topological phase of these heterostructures. This finding provides a novel way to probe the intricate topological properties emerging in twisted bilayer superconductors with d-wave pairing.

7.2 Outlook

The work presented in the previous chapters opens several avenues for further exploration of the problems addressed in this thesis. For instance, in Chapter 7, we focused on how the vortex matter in twisted bilayer d-wave superconductors evolves with the twist angle under static equilibrium. A logical extension of this work would be to examine how the different skyrmionic states we identified behave under the influence of a transport current. This introduces an intriguing challenge even in the case of a single layer system, as the applied current can be oriented at various angles relative to the nodal directions of the superconductor. It would therefore be insightful to study how the system's response varies with the orientation of the sample.

An additional interesting direction involves investigating how the sample's orientation affects the critical current of a single layer as a function of an applied magnetic field. Once the behavior of the single layer is fully understood, a second layer can be introduced, allowing the study of how the twist angle and the resulting skyrmionic states influence the superconductor's response. Any distinctive features in the voltage versus time curves under

such conditions could be experimentally tested using transport measurements, providing a concrete means to validate theoretical predictions about the dynamics of skyrmions in twisted bilayer systems.

So far, our discussion of twisted bilayers has primarily centered on their macroscopic properties, such as magnetic field profiles and their response to transport currents. However, as noted in the conclusion of Chapter 7, the skyrmionic states predicted to emerge in the topological phase are also expected to exhibit distinct local density of states (LDOS) and bound states, which can be detected through STM measurements. Exploring these local properties presents an intriguing direction for further study. The theoretical calculation of such states could be pursued using the Bogoliubov-de Gennes framework, providing a detailed microscopic view of the skyrmionic states. This approach would allow us to investigate how the intricate electronic structure and bound states near the vortex cores manifest at the local scale, offering direct signatures that can complement macroscopic measurements and further our understanding of the topological phases in twisted bilayer superconductors.

Finally, as demonstrated in Chapter 5 during our investigation of the superconducting diode, the time-dependent Ginzburg-Landau (TDGL) theory provides a robust framework for the numerical exploration of various superconducting devices. An exciting direction for future work could involve applying this theory to more complex systems. For instance, as recently proposed experimentally [230], multiple superconducting diodes could be combined to achieve full-wave rectification. TDGL simulations would be highly valuable for exploring the conditions needed to optimize such devices for practical applications.

Another promising application of TDGL simulations is modeling superconducting nanowire artificial neurons, as described in [231]. These devices consist of a shunted superconducting wire, where the dynamic oscillation of electrical current between the superconductor and the shunt resistor produces voltage spikes that emulate the behavior of biological neurons. By coupling the TDGL equations with those governing the associated electric circuit, it would be possible to thoroughly characterize and optimize the operation of these artificial neurons.

Additionally, several recent proposals for electronic applications based on superconducting vortices could be investigated using TDGL simulations. These include vortex-based memory devices [232] and vortex-driven spintronics in superconductor/ferromagnet heterostructures [233]. The TDGL framework, as discussed in this thesis, offers a powerful tool for studying and optimizing the dynamics and performance of these innovative superconducting technologies.

Bibliography

1 CAN, O. et al. High-temperature topological superconductivity in twisted double-layer copper oxides. *Nature Physics*, Nature Publishing Group, v. 17, n. 4, p. 519–524, 2021.

2 GORTER, C. J.; TACONIS, K. W. The world of cryogenics. i: The kamerlingh onnes laboratory. *Cryogenics*, Elsevier, v. 4, n. 6, p. 345–353, 1964.

3 ONNES, H. K. *Through measurement to knowledge: The selected papers of Heike Kamerlingh Onnes 1853–1926*. [S.l.]: Springer Science & Business Media, 2012. v. 124.

4 MEISSNER, W.; OCHSENFELD, R. Ein neuer effekt bei eintritt der supraleitfähigkeit. *Naturwissenschaften*, Springer-Verlag Berlin/Heidelberg, v. 21, n. 44, p. 787–788, 1933.

5 DAHL, P. F. Superconductivity after world war i and circumstances surrounding the discovery of a state b= 0. *Historical Studies in the Physical and Biological Sciences*, JSTOR, v. 16, n. 1, p. 1–58, 1986.

6 GINZBURG, V. L.; GINZBURG, V. L.; LANDAU, L. *On the theory of superconductivity*. [S.l.]: Springer, 2009.

7 COOPER, L. N. et al. *BCS: 50 years*. [S.l.]: World scientific, 2011.

8 BARDEEN, J.; COOPER, L. N.; SCHRIEFFER, J. R. Theory of superconductivity. *Physical review*, APS, v. 108, n. 5, p. 1175, 1957.

9 BEDNORZ, J. G.; MÜLLER, K. A. Possible high t c superconductivity in the ba-la- cu- o system. *Zeitschrift für Physik B Condensed Matter*, Springer, v. 64, n. 2, p. 189–193, 1986.

10 WU, M.-K. et al. Superconductivity at 93 k in a new mixed-phase y-ba-cu-o compound system at ambient pressure. *Physical review letters*, APS, v. 58, n. 9, p. 908, 1987.

11 MAKSIMOV, E. G. High-temperature superconductivity: the current state. *Physics-Uspekhi*, IOP Publishing, v. 43, n. 10, p. 965, 2000.

12 KORDYUK, A. Iron-based superconductors: Magnetism, superconductivity, and electronic structure. *Low temperature physics*, AIP Publishing, v. 38, n. 9, p. 888–899, 2012.

13 WHITE, B.; THOMPSON, J.; MAPLE, M. Unconventional superconductivity in heavy-fermion compounds. *Physica C: superconductivity and its applications*, Elsevier, v. 514, p. 246–278, 2015.

14 SATO, M.; ANDO, Y. Topological superconductors: a review. *Reports on Progress in Physics*, IOP Publishing, v. 80, n. 7, p. 076501, 2017.

15 LEIJNSE, M.; FLENSBERG, K. Introduction to topological superconductivity and majorana fermions. *Semiconductor Science and Technology*, IOP Publishing, v. 27, n. 12, p. 124003, 2012.

16 PICKARD, C. J.; ERREA, I.; EREMETS, M. I. Superconducting hydrides under pressure. *Annual Review of Condensed Matter Physics*, Annual Reviews, v. 11, n. 1, p. 57–76, 2020.

17 EREMETS, M. I. The current status and future development of high-temperature conventional superconductivity. *National Science Review*, Oxford Academic, v. 11, n. 7, 2024.

18 BARDEEN, J.; STEPHEN, M. Theory of the motion of vortices in superconductors. *Physical Review*, APS, v. 140, n. 4A, p. A1197, 1965.

19 TINKHAM, M. *Introduction to superconductivity*. [S.l.]: Courier Corporation, 2004.

20 GENNES, P.-G. D. *Superconductivity of metals and alloys*. [S.l.]: CRC press, 2018.

21 PARKS, R. D. *Superconductivity: In Two Volumes: Volume 1*. [S.l.]: Routledge, 2018. v. 1.

22 FETTER, A. L.; WALECKA, J. D. *Quantum theory of many-particle systems*. [S.l.]: Courier Corporation, 2012.

23 GOR'KOV, L. P. Microscopic derivation of the ginzburg-landau equations in the theory of superconductivity. *Sov. Phys. JETP*, v. 9, n. 6, p. 1364–1367, 1959.

24 VARGUNIN, A.; SILAEV, M.; BABAEV, E. Unusual resistive states of multiband superconductors in the effective field theory approach. *EPL (Europhysics Letters)*, IOP Publishing, v. 130, n. 1, p. 17001, 2020.

25 SILAEV, M.; BABAEV, E. Microscopic derivation of two-component ginzburg-Landau model and conditions of its applicability in two-band systems. *Physical Review B*, APS, v. 85, n. 13, p. 134514, 2012.

26 KOMENDOVÁ, L. et al. Two-band superconductors: Hidden criticality deep in the superconducting state. *Physical Review Letters*, APS, v. 108, n. 20, p. 207002, 2012.

27 REN, Y.; XU, J.-H.; TING, C. Ginzburg-landau equations and vortex structure of a d x 2- y 2 superconductor. *Physical review letters*, APS, v. 74, n. 18, p. 3680, 1995.

28 CADORIM, L. R. et al. Intermediate type-i superconductors in the mesoscopic scale. *Physical Review B*, APS, v. 103, n. 1, p. 014504, 2021.

29 CADORIM, L. R. et al. Closed vortex state in three-dimensional mesoscopic superconducting films under an applied transport current. *Phys. Rev. B*, American Physical Society, v. 107, p. 094515, Mar 2023. Disponível em: <https://link.aps.org/doi/10.1103/PhysRevB.107.094515>.

30 CADORIM, L. R.; SARDELLA, E.; SILVA, C. C. d. S. Harnessing the superconducting diode effect through inhomogeneous magnetic fields. *Physical Review Applied*, APS, v. 21, n. 5, p. 054040, 2024.

31 CADORIM, L. R. et al. Stability limits of flux states in two-band superconductor rings. *Phys. Rev. B*, American Physical Society, v. 110, p. 144513, Oct 2024. Disponível em: <https://link.aps.org/doi/10.1103/PhysRevB.110.144513>.

32 CADORIM, L. R.; SARDELLA, E.; MILOŠEVIĆ, M. V. Vortical versus skyrmionic states in the topological phase of a twisted bilayer with d-wave superconducting pairing. *Physical Review B*, APS, v. 110, n. 6, p. 064508, 2024.

33 BUCHANAN, J.; CHANG, G.; SERIN, B. The ginzburg-landau parameter of tantalum. *J. Phys. Chem. Solids*, v. 26, n. 7, p. 1183 – 1184, 1965. ISSN 0022-3697. Disponível em: <http://www.sciencedirect.com/science/article/pii/0022369765900168>.

34 MCEVOY, J.; JONES, D.; PARK, J. Supercooling of superconductors below the surface nucleation field. *Solid State Commun.*, v. 5, n. 8, p. 641 – 644, 1967. ISSN 0038-1098. Disponível em: <http://www.sciencedirect.com/science/article/pii/003810986790083X>.

35 MALONEY, M. D.; CRUZ, F. de la; CARDONA, M. Superconducting parameters and size effects of aluminum films and foils. *Phys. Rev. B*, American Physical Society, v. 5, p. 3558–3572, May 1972. Disponível em: <https://link.aps.org/doi/10.1103/PhysRevB.5.3558>.

36 BLOT, J.; PELLAN, Y.; ROSENBLATT, J. Metastable states of superconducting indium films. *J. Low Temp. Phys.*, v. 30, n. 5, p. 669–695, Mar 1978. ISSN 1573-7357. Disponível em: <https://doi.org/10.1007/BF00116205>.

37 FEDER, J. Comments of the supercooling field for superconductors with k values near 0.4. *Solid State Commun.*, v. 5, n. 4, p. 299 – 301, 1967. ISSN 0038-1098. Disponível em: <http://www.sciencedirect.com/science/article/pii/0038109867902773>.

38 PARK, J. Metastable states of the superconducting surface sheath in decreasing fields. *Solid State Commun.*, v. 5, n. 8, p. 645 – 648, 1967. ISSN 0038-1098. Disponível em: <http://www.sciencedirect.com/science/article/pii/0038109867900841>.

39 GOTTLIEB, U. et al. Superconductivity in $tasi_2$ single crystals. *Phys. Rev. B*, American Physical Society, v. 45, p. 4803–4806, Mar 1992. Disponível em: <https://link.aps.org/doi/10.1103/PhysRevB.45.4803>.

40 KRIENER, M. et al. Superconductivity in heavily boron-doped silicon carbide. *Sci. Technol. Adv. Mater.*, v. 9, n. 4, p. 044205, Jan 2008.

41 ZHAO, L. L. et al. Type-I superconductivity in $ybsb_2$ single crystals. *Phys. Rev. B*, American Physical Society, v. 85, p. 214526, Jun 2012. Disponível em: <https://link.aps.org/doi/10.1103/PhysRevB.85.214526>.

42 ARANTES, F. R.; ARISTIZÁBAL-GIRALDO et al. Superconductivity in monocrystalline $ynisi_3$ and $lunisi_3$. *Phys. Rev. B*, American Physical Society, v. 99, p. 224505, Jun 2019. Disponível em: <https://link.aps.org/doi/10.1103/PhysRevB.99.224505>.

43 de C. Romaguera, A. R.; DORIA, M. M.; PEETERS, F. M. Vortex pattern in a nanoscopic cylinder. *Physica C*, v. 460-462, p. 1234 – 1235, 2007. ISSN 0921-4534. Disponível em: <http://www.sciencedirect.com/science/article/pii/S0921453407005941>.

44 BAELUS, B. J. et al. Multivortex and giant vortex states near the expulsion and penetration fields in thin mesoscopic superconducting squares. *Phys. Rev. B*, American Physical Society, v. 73, p. 024514, Jan 2006. Disponível em: <https://link.aps.org/doi/10.1103/PhysRevB.73.024514>.

45 CÓRDOBA-CAMACHO, W. Y. et al. Between types I and II: Intertype flux exotic states in thin superconductors. *Phys. Rev. B*, American Physical Society, v. 94, p. 054511, Aug 2016. Disponível em: <https://link.aps.org/doi/10.1103/PhysRevB.94.054511>.

46 CÓRDOBA-CAMACHO, W. Y. et al. Quasi-one-dimensional vortex matter in superconducting nanowires. *Phys. Rev. B*, American Physical Society, v. 98, p. 174511, Nov 2018. Disponível em: <https://link.aps.org/doi/10.1103/PhysRevB.98.174511>.

47 CÓRDOBA-CAMACHO, W. Y. et al. Spontaneous pattern formation in superconducting films. *J. Phys. Condens. Matter*, IOP Publishing, v. 32, n. 7, p. 075403, nov 2019. Disponível em: <https://doi.org/10.1088%2F1361-648x%2Fab5379>.

48 SHANENKO, A. A. et al. Extended ginzburg-landau formalism for two-band superconductors. *Phys. Rev. Lett.*, American Physical Society, v. 106, p. 047005, Jan 2011. Disponível em: <https://link.aps.org/doi/10.1103/PhysRevLett.106.047005>.

49 VAGOV, A. et al. Superconductivity between standard types: Multiband versus single-band materials. *Phys. Rev. B*, American Physical Society, v. 93, p. 174503, May 2016. Disponível em: <https://link.aps.org/doi/10.1103/PhysRevB.93.174503>.

50 OLIVEIRA, I. G. de et al. The spike state in type-i mesoscopic superconductor. *Physics Letters A*, Elsevier, v. 406, p. 127457, 2021.

51 ABRIKOSOV, A. A. On the magnetic properties of superconductors of the second group. *Soviet Physics-JETP*, v. 5, p. 1174–1182, 1957.

52 KOZLOV, V.; SAMOKHVALOV, A. Closed abrikosov vortices in type-ii superconductors. *JETP letters*, v. 53, n. 3, p. 158–161, 1991.

53 KOZLOV, V.; SAMOKHVALOV, A. Closed abrikosov vortices in a superconducting cylinder. *Physica C: Superconductivity and its Applications*, Elsevier, v. 213, n. 1-2, p. 103–108, 1993.

54 KOZLOV, V.; SAMOKHVALOV, A. Stabilization of toroidal abrikosov vortex in a nonuniform superconductor. *Journal of superconductivity*, Springer, v. 6, p. 63–68, 1993.

55 GENENKO, Y. A. Relaxation of magnetic vortex rings in a superconducting cylinder: some universal features. *Physica C: Superconductivity*, Elsevier, v. 215, n. 3-4, p. 343–349, 1993.

56 GENENKO, Y. A. Vortex helicoid in a superconducting cylinder in a longitudinal magnetic field. *JETP LETTERS C/C OF PIS'MA V ZHURNAL EKSPERIMENTAL'NOI TEORETICHESKOI FIZIKI*, AMERICAN INSTITUTE OF PHYSICS, v. 59, p. 841–841, 1994.

57 GENENKO, Y. A. Magnetic self-field entry into a current-carrying type-ii superconductor. *Physical Review B*, APS, v. 49, n. 10, p. 6950, 1994.

58 GENENKO, Y. A. Magnetic self-field entry into a current-carrying type-ii superconductor. ii. helical vortices in a longitudinal magnetic field. *Physical Review B*, APS, v. 51, n. 6, p. 3686, 1995.

59 GENENKO, Y. A. et al. Magnetic self-field entry into a current-carrying type-ii superconductor. iii. general criterion of penetration for an external field of arbitrary direction. *Physical Review B*, APS, v. 57, n. 2, p. 1164, 1998.

60 SAMOKHVALOV, A. V. Vortex loops entry into type-ii superconductors. *Physica C: Superconductivity*, Elsevier, v. 259, n. 3-4, p. 337–348, 1996.

61 SAMOKHVALOV, A. Abrikosov vortex loop near the surface of superconductor. *Physica C: Superconductivity and its applications*, Elsevier, v. 282, p. 2163–2164, 1997.

62 SAMOKHVALOV, A. V. Expanding vortex rings in a current-carrying superconducting cylinder. *Physica C: Superconductivity*, Elsevier, v. 308, n. 1-2, p. 74–84, 1998.

63 NIEDZIELSKI, B.; BERAKDAR, J. Vortex ring and helical current formation in superconductors driven by a thz-field-induced toroidal vector potential. *physica status solidi (b)*, Wiley Online Library, p. 2100622, 2022.

64 BERDIYOROV, G. et al. Josephson vortex loops in nanostructured josephson junctions. *Scientific reports*, Nature Publishing Group, v. 8, n. 1, p. 1–17, 2018.

65 FYHN, E. H.; LINDER, J. Controllable vortex loops in superconducting proximity systems. *Physical Review B*, APS, v. 100, n. 21, p. 214503, 2019.

66 KRAMER, L.; WATTS-TOBIN, R. Theory of dissipative current-carrying states in superconducting filaments. *Physical Review Letters*, APS, v. 40, n. 15, p. 1041, 1978.

67 WATTS-TOBIN, R.; KRÄHENBÜHL, Y.; KRAMER, L. Nonequilibrium theory of dirty, current-carrying superconductors: Phase-slip oscillators in narrow filaments near T_c. *Journal of Low Temperature Physics*, v. 42, n. 5, p. 459–501, 1981.

68 DU, Q.; GRAY, P. High-κ limits of the time-dependent Ginzburg-Landau model. *SIAM Journal on Applied Mathematics*, SIAM, v. 56, n. 4, p. 1060–1093, 1996.

69 BERDIYOROV, G.; MILOŠEVIĆ, M.; PEETERS, F. Kinematic vortex-antivortex lines in strongly driven superconducting stripes. *Physical Review B*, APS, v. 79, n. 18, p. 184506, 2009.

70 GENENKO, Y. A. Magnetic self-field entry into a current-carrying type-ii superconductor. *Phys. Rev. B*, American Physical Society, v. 49, p. 6950–6957, Mar 1994. Disponível em: <https://link.aps.org/doi/10.1103/PhysRevB.49.6950>.

71 SIVAKOV, A. G. et al. Josephson behavior of phase-slip lines in wide superconducting strips. *Phys. Rev. Lett.*, American Physical Society, v. 91, p. 267001, Dec 2003. Disponível em: <https://link.aps.org/doi/10.1103/PhysRevLett.91.267001>.

72 EMBON, L. et al. Imaging of super-fast dynamics and flow instabilities of superconducting vortices. *Nature Communications*, Nature Publishing Group, v. 8, n. 1, p. 1–10, 2017.

73 ANAHORY, Y. et al. Squid-on-tip with single-electron spin sensitivity for high-field and ultra-low temperature nanomagnetic imaging. *Nanoscale*, Royal Society of Chemistry, v. 12, n. 5, p. 3174–3182, 2020.

74 VASYUKOV, D. et al. A scanning superconducting quantum interference device with single electron spin sensitivity. *Nature nanotechnology*, Nature Publishing Group, v. 8, n. 9, p. 639–644, 2013.

75 MOLL, P. J.; GESHKENBEIN, V. B. Evolution of superconducting diodes. *Nature Physics*, Nature Publishing Group UK London, p. 1–2, 2023.

76 NADEEM, M.; FUHRER, M. S.; WANG, X. The superconducting diode effect. *Nature Reviews Physics*, Nature Publishing Group UK London, p. 1–20, 2023.

77 LEE, C.-S. et al. Reducing vortex density in superconductors using the 'ratchet effect'. *Nature*, Nature Publishing Group UK London, v. 400, n. 6742, p. 337–340, 1999.

78 OLSON, C. J. et al. Collective interaction-driven ratchet for transporting flux quanta. *Phys. Rev. Lett.*, American Physical Society, v. 87, p. 177002, Oct 2001. Disponível em: <https://link.aps.org/doi/10.1103/PhysRevLett.87.177002>.

79 VILLEGAS, J. et al. A superconducting reversible rectifier that controls the motion of magnetic flux quanta. *Science*, American Association for the Advancement of Science, v. 302, n. 5648, p. 1188–1191, 2003.

80 VONDEL, J. Van de et al. Vortex-rectification effects in films with periodic asymmetric pinning. *Physical Review Letters*, APS, v. 94, n. 5, p. 057003, 2005.

81 SILVA, C. C. de S. et al. Controlled multiple reversals of a ratchet effect. *Nature*, Nature Publishing Group UK London, v. 440, n. 7084, p. 651–654, 2006.

82 WÖRDENWEBER, R.; DYMASHEVSKI, P.; MISKO, V. Guidance of vortices and the vortex ratchet effect in high-t c superconducting thin films obtained by arrangement of antidots. *Physical Review B*, APS, v. 69, n. 18, p. 184504, 2004.

83 GILLIJNS, W. et al. Origin of reversed vortex ratchet motion. *Phys. Rev. Lett.*, American Physical Society, v. 99, p. 247002, Dec 2007. Disponível em: <https://link.aps.org/doi/10.1103/PhysRevLett.99.247002>.

84 LARA, D. P. D. et al. Vortex ratchet reversal at fractional matching fields in kagomélike array with symmetric pinning centers. *Physical Review B*, APS, v. 82, n. 17, p. 174503, 2010.

85 SILVA, C. C. de S. et al. Dipole-induced vortex ratchets in superconducting films with arrays of micromagnets. *Physical review letters*, APS, v. 98, n. 11, p. 117005, 2007.

86 SILHANEK, A. et al. Manipulation of the vortex motion in nanostructured ferromagnetic/superconductor hybrids. *Applied physics letters*, AIP Publishing, v. 90, n. 18, 2007.

87 YU, K. et al. Asymmetric weak-pinning superconducting channels: Vortex ratchets. *Phys. Rev. B*, American Physical Society, v. 76, p. 220507, Dec 2007. Disponível em: <https://link.aps.org/doi/10.1103/PhysRevB.76.220507>.

88 YASUDA, K. et al. Nonreciprocal charge transport at topological insulator/superconductor interface. *Nature communications*, Nature Publishing Group UK London, v. 10, n. 1, p. 2734, 2019.

89 NARITA, H. et al. Field-free superconducting diode effect in noncentrosymmetric superconductor/ferromagnet multilayers. *Nature Nanotechnology*, Nature Publishing Group UK London, v. 17, n. 8, p. 823–828, 2022.

90 HOU, Y. et al. Ubiquitous superconducting diode effect in superconductor thin films. *Physical Review Letters*, APS, v. 131, n. 2, p. 027001, 2023.

91 LEGG, H. F.; LOSS, D.; KLINOVAJA, J. Superconducting diode effect due to magnetochiral anisotropy in topological insulators and rashba nanowires. *Physical Review B*, APS, v. 106, n. 10, p. 104501, 2022.

92 MEHRNEJAT, A. et al. Flux-pinning mediated superconducting diode effect in nbse2/crgete3 heterostructure. *2D Materials*, 2023.

93 KARABASSOV, T. et al. Phase diagrams of the diode effect in superconducting heterostructures. *Physica Scripta*, IOP Publishing, v. 99, n. 1, p. 015010, 2023.

94 GUTFREUND, A. et al. Direct observation of a superconducting vortex diode. *Nature Communications*, Nature Publishing Group UK London, v. 14, n. 1, p. 1630, 2023.

95 WAKATSUKI, R. et al. Nonreciprocal charge transport in noncentrosymmetric superconductors. *Science advances*, American Association for the Advancement of Science, v. 3, n. 4, p. e1602390, 2017.

96 HOSHINO, S. et al. Nonreciprocal charge transport in two-dimensional noncentrosymmetric superconductors. *Physical Review B*, APS, v. 98, n. 5, p. 054510, 2018.

97 ANDO, F. et al. Observation of superconducting diode effect. *Nature*, Nature Publishing Group UK London, v. 584, n. 7821, p. 373–376, 2020.

98 ZHANG, E. et al. Nonreciprocal superconducting nbse2 antenna. *Nature communications*, Nature Publishing Group UK London, v. 11, n. 1, p. 5634, 2020.

99 BAURIEDL, L. et al. Supercurrent diode effect and magnetochiral anisotropy in few-layer nbse2. *Nature communications*, Nature Publishing Group UK London, v. 13, n. 1, p. 4266, 2022.

100 MARGINEDA, D. et al. Sign reversal diode effect in superconducting dayem nanobridges. *Communications Physics*, Nature Publishing Group UK London, v. 6, n. 1, p. 343, 2023.

101 CHAHID, S. et al. High-frequency diode effect in superconducting nb 3 sn microbridges. *Physical Review B*, APS, v. 107, n. 5, p. 054506, 2023.

102 YUAN, N. F.; FU, L. Supercurrent diode effect and finite-momentum superconductors. *Proceedings of the National Academy of Sciences*, National Acad Sciences, v. 119, n. 15, p. e2119548119, 2022.

103 GOLOD, T.; KRASNOV, V. M. Demonstration of a superconducting diode-with-memory, operational at zero magnetic field with switchable nonreciprocity. *Nature Communications*, Nature Publishing Group UK London, v. 13, n. 1, p. 3658, 2022.

104 WU, H. et al. The field-free josephson diode in a van der waals heterostructure. *Nature*, Nature Publishing Group UK London, v. 604, n. 7907, p. 653–656, 2022.

105 LIN, J.-X. et al. Zero-field superconducting diode effect in small-twist-angle trilayer graphene. *Nature Physics*, Nature Publishing Group UK London, v. 18, n. 10, p. 1221–1227, 2022.

106 JIANG, J. et al. Field-free superconducting diode in a magnetically nanostructured superconductor. *Physical Review Applied*, APS, v. 18, n. 3, p. 034064, 2022.

107 GHOSH, S. et al. High-temperature josephson diode. *Nature Materials*, Nature Publishing Group UK London, p. 1–7, 2024.

108 STEINER, J. F. et al. Diode effects in current-biased josephson junctions. *Physical Review Letters*, APS, v. 130, n. 17, p. 177002, 2023.

109 ZAZUNOV, A. et al. Nonreciprocal charge transport and subharmonic structure in voltage-biased josephson diodes. *Physical Review B*, APS, v. 109, n. 2, p. 024504, 2024.

110 CHENG, Q.; SUN, Q.-F. Josephson diode based on conventional superconductors and a chiral quantum dot. *Physical Review B*, APS, v. 107, n. 18, p. 184511, 2023.

111 ZINKL, B.; HAMAMOTO, K.; SIGRIST, M. Symmetry conditions for the superconducting diode effect in chiral superconductors. *Physical Review Research*, APS, v. 4, n. 3, p. 033167, 2022.

112 GUPTA, M. et al. Gate-tunable superconducting diode effect in a three-terminal josephson device. *Nature communications*, Nature Publishing Group UK London, v. 14, n. 1, p. 3078, 2023.

113 QIAO, J.; LIU, H.; ZHANG, D. Electric tuning of vortex ratchet effect in nbse2. *Nano Letters*, ACS Publications, 2023.

114 LYU, Y.-Y. et al. Superconducting diode effect via conformal-mapped nanoholes. *Nature communications*, Nature Publishing Group UK London, v. 12, n. 1, p. 2703, 2021.

115 VODOLAZOV, D. Y. et al. Masking effect of heat dissipation on the current-voltage characteristics of a mesoscopic superconducting sample with leads. *Physical Review B*, APS, v. 71, n. 18, p. 184502, 2005.

116 DUARTE, E. et al. Dynamics and heat diffusion of abrikosov's vortex-antivortex pairs during an annihilation process. *Journal of Physics: Condensed Matter*, IOP Publishing, v. 29, n. 40, p. 405605, 2017.

117 MENEZES, R. M.; SILVA, C. C. de S. Conformal vortex crystals. *Scientific reports*, Nature Publishing Group UK London, v. 7, n. 1, p. 12766, 2017.

118 MENEZES, R. M. et al. Self-assembled vortex crystals induced by inhomogeneous magnetic textures. *Journal of Physics: Condensed Matter*, IOP Publishing, v. 31, n. 17, p. 175402, 2019.

119 XI, X. Two-band superconductor magnesium diboride. *Reports on Progress in Physics*, IOP Publishing, v. 71, n. 11, p. 116501, 2008.

120 TANAKA, Y. Multicomponent superconductivity based on multiband superconductors. *Superconductor Science and Technology*, IOP Publishing, v. 28, n. 3, p. 034002, 2015.

121 SUHL, H.; MATTHIAS, B.; WALKER, L. Bardeen-cooper-schrieffer theory of superconductivity in the case of overlapping bands. *Physical Review Letters*, APS, v. 3, n. 12, p. 552, 1959.

122 MOSKALENKO, V. Superconductivity in metals with overlapping energy bands. *Fiz. Metal. Metalloved*, Citeseer, v. 8, n. 503513, p. 2518–2520, 1959.

123 NAGAMATSU, J. et al. Superconductivity at 39 K in magnesium diboride. *nature*, Nature Publishing Group, v. 410, n. 6824, p. 63–64, 2001.

124 BOUQUET, F. et al. Specific heat of $Mg^{11}B_2$: evidence for a second energy gap. *Physical review letters*, APS, v. 87, n. 4, p. 047001, 2001.

125 PAGLIONE, J.; GREENE, R. L. High-temperature superconductivity in iron-based materials. *Nature physics*, Nature Publishing Group, v. 6, n. 9, p. 645–658, 2010.

126 YOKOYA, T. et al. Fermi surface sheet-dependent superconductivity in 2H-$NbSe_2$. *Science*, American Association for the Advancement of Science, v. 294, n. 5551, p. 2518–2520, 2001.

127 ROSSNAGEL, K. et al. Fermi surface of 2H-$NbSe_2$ and its implications on the charge-density-wave mechanism. *Physical Review B*, APS, v. 64, n. 23, p. 235119, 2001.

128 ROTTER, M.; TEGEL, M.; JOHRENDT, D. Superconductivity at 38 k in the iron arsenide $(Ba_{1-x}K_x)Fe_2As_2$. *Physical Review Letters*, APS, v. 101, n. 10, p. 107006, 2008.

129 BABAEV, E.; SPEIGHT, M. Semi-meissner state and neither type-i nor type-ii superconductivity in multicomponent superconductors. *Physical Review B*, APS, v. 72, n. 18, p. 180502, 2005.

130 MOSHCHALKOV, V. et al. Type-1.5 superconductivity. *Physical Review Letters*, APS, v. 102, n. 11, p. 117001, 2009.

131 BABAEV, E.; CARLSTRÖM, J.; SPEIGHT, M. Type-1.5 superconducting state from an intrinsic proximity effect in two-band superconductors. *Physical review letters*, APS, v. 105, n. 6, p. 067003, 2010.

132 CARLSTRÖM, J.; GARAUD, J.; BABAEV, E. Length scales, collective modes, and type-1.5 regimes in three-band superconductors. *Physical Review B*, APS, v. 84, n. 13, p. 134518, 2011.

133 KOGAN, V.; SCHMALIAN, J. Ginzburg-Landau theory of two-band superconductors: Absence of type-1.5 superconductivity. *Physical Review B*, APS, v. 83, n. 5, p. 054515, 2011.

134 BABAEV, E.; SILAEV, M. Comment on "Ginzburg-Landau theory of two-band superconductors: Absence of type-1.5 superconductivity". *Physical Review B*, APS, v. 86, n. 1, p. 016501, 2012.

135 CHAVES, A. et al. Conditions for nonmonotonic vortex interaction in two-band superconductors. *Physical Review B*, APS, v. 83, n. 21, p. 214523, 2011.

136 WANG, Y. et al. Observation of vortex stripes in ute _2. *arXiv preprint arXiv:2408.06209*, 2024.

137 BABAEV, E. Vortices with fractional flux in two-gap superconductors and in extended faddeev model. *Physical Review Letters*, APS, v. 89, n. 6, p. 067001, 2002.

138 BABAEV, E.; JÄYKKÄ, J.; SPEIGHT, M. Magnetic field delocalization and flux inversion in fractional vortices in two-component superconductors. *Physical Review Letters*, APS, v. 103, n. 23, p. 237002, 2009.

139 CHIBOTARU, L.; DAO, V. H. Stable fractional flux vortices in mesoscopic superconductors. *Physical Review B*, APS, v. 81, n. 2, p. 020502, 2010.

140 GEURTS, R.; MILOŠEVIĆ, M.; PEETERS, F. Vortex matter in mesoscopic two-gap superconducting disks: influence of josephson and magnetic coupling. *Physical Review B*, APS, v. 81, n. 21, p. 214514, 2010.

141 SILAEV, M. Stable fractional flux vortices and unconventional magnetic state in two-component superconductors. *Physical Review B*, APS, v. 83, n. 14, p. 144519, 2011.

142 PIÑA, J. C.; SILVA, C. C. de S.; MILOŠEVIĆ, M. V. Stability of fractional vortex states in a two-band mesoscopic superconductor. *Physical Review B*, APS, v. 86, n. 2, p. 024512, 2012.

143 YANAGISAWA, T. et al. Vortices and chirality in multi-band superconductors. *Journal of the Physical Society of Japan*, The Physical Society of Japan, v. 81, n. 2, p. 024712, 2012.

144 SILVA, R. da et al. Distinct magnetic signatures of fractional vortex configurations in multiband superconductors. *Applied Physics Letters*, AIP Publishing LLC, v. 105, n. 23, p. 232601, 2014.

145 GILLIS, S.; JÄYKKÄ, J.; MILOŠEVIĆ, M. V. Vortex states in mesoscopic three-band superconductors. *Physical Review B*, APS, v. 89, n. 2, p. 024512, 2014.

146 MAIANI, A.; BENFENATI, A.; BABAEV, E. Vortex nucleation barriers and stable fractional vortices near boundaries in multicomponent superconductors. *Physical Review B*, APS, v. 105, n. 22, p. 224507, 2022.

147 HOLMVALL, P.; BLACK-SCHAFFER, A. M. Coreless vortices as direct signature of chiral d-wave superconductivity. *Physical Review B*, APS, v. 108, n. 10, p. L100506, 2023.

148 JI, H.; YUAN, N. F. Fractional vortices and ising superconductivity in multiband superconductors. *arXiv preprint arXiv:2408.02120*, 2024.

149 IGUCHI, Y. et al. Superconducting vortices carrying a temperature-dependent fraction of the flux quantum. *Science*, American Association for the Advancement of Science, v. 380, n. 6651, p. 1244–1247, 2023.

150 ZHENG, Y. et al. Direct observation of quantum vortex fractionalization in multiband superconductors. *arXiv preprint arXiv:2407.18610*, 2024.

151 ZHOU, Q. et al. Observation of single-quantum vortex splitting in the ba _{1 − x} k _x fe _2 as _2 superconductor. *arXiv preprint arXiv:2408.05902*, 2024.

152 FENCHENKO, V.; YERIN, Y. Phase slip centers in a two-band superconducting filament: application to mgb2. *Physica C: Superconductivity*, Elsevier, v. 480, p. 129–136, 2012.

153 TANAKA, Y. Soliton in two-band superconductor. *Physical Review Letters*, APS, v. 88, n. 1, p. 017002, 2001.

154 KUPLEVAKHSKY, S.; OMELYANCHOUK, A.; YERIN, Y. Soliton states in mesoscopic two-band-superconducting cylinders. *Low Temperature Physics*, American Institute of Physics, v. 37, n. 8, p. 667–677, 2011.

155 LIN, S.-Z.; HU, X. Phase solitons in multi-band superconductors with and without time-reversal symmetry. *New Journal of Physics*, IOP Publishing, v. 14, n. 6, p. 063021, 2012.

156 VAKARYUK, V. et al. Topological defect-phase soliton and the pairing symmetry of a two-band superconductor:<? format?> role of the proximity effect. *Physical Review Letters*, APS, v. 109, n. 22, p. 227003, 2012.

157 SAMOKHIN, K. Phase solitons and subgap excitations in two-band superconductors. *Physical Review B—Condensed Matter and Materials Physics*, APS, v. 86, n. 6, p. 064513, 2012.

158 LIN, S.-Z. Ground state, collective mode, phase soliton and vortex in multiband superconductors. *Journal of Physics: Condensed Matter*, IOP Publishing, v. 26, n. 49, p. 493202, 2014.

159 YERIN, Y.; DRECHSLER, S.-L. Phase solitons in a weakly coupled three-component superconductor. *Physical Review B*, APS, v. 104, n. 1, p. 014518, 2021.

160 GUREVICH, A.; VINOKUR, V. Interband phase modes and nonequilibrium soliton structures in two-gap superconductors. *Physical review letters*, APS, v. 90, n. 4, p. 047004, 2003.

161 GUREVICH, A.; VINOKUR, V. Phase textures induced by dc-current pair breaking in weakly coupled multilayer structures and two-gap superconductors. *Physical Review Letters*, APS, v. 97, n. 13, p. 137003, 2006.

162 MARYCHEV, P.; VODOLAZOV, D. Y. Soliton-induced critical current oscillations in two-band superconducting bridges. *Physical Review B*, APS, v. 97, n. 10, p. 104505, 2018.

163 POLO, A. M. et al. Nonequilibrium interband phase textures induced by vortex splitting in two-band superconductors. *Physical Review B*, APS, v. 96, n. 5, p. 054517, 2017.

164 LANGER, J. S.; AMBEGAOKAR, V. Intrinsic resistive transition in narrow superconducting channels. *Physical Review*, APS, v. 164, n. 2, p. 498, 1967.

165 IVLEV, B.; KOPNIN, N. Dynamic phase-slip centers and the resistive state of a strong-nonequilibrium superconductor. *Journal of Low Temperature Physics*, Springer, v. 39, p. 137–150, 1980.

166 RUBINSTEIN, J.; STERNBERG, P.; MA, Q. Bifurcation diagram and pattern formation of phase slip centers<? format?> in superconducting wires driven with electric currents. *Physical review letters*, APS, v. 99, n. 16, p. 167003, 2007.

167 BARANOV, V.; BALANOV, A.; KABANOV, V. Dynamics of resistive state in thin superconducting channels. *Physical Review B—Condensed Matter and Materials Physics*, APS, v. 87, n. 17, p. 174516, 2013.

168 YERIN, Y.; FENCHENKO, V.; IL'ICHEV, E. Phase diagram of the resistive state of a narrow superconducting channel in the voltage-driven regime. *Low Temperature Physics*, AIP Publishing, v. 39, n. 2, p. 125–132, 2013.

169 BERDIYOROV, G. et al. Dynamics of current-driven phase-slip centers in superconducting strips. *Physical Review B*, APS, v. 90, n. 5, p. 054506, 2014.

170 CADORIM, L. R.; JUNIOR, A. de O.; SARDELLA, E. Ultra-fast kinematic vortices in mesoscopic superconductors: the effect of the self-field. *Scientific reports*, Nature Publishing Group UK London, v. 10, n. 1, p. 18662, 2020.

171 VODOLAZOV, D. Y. et al. Multiple flux jumps and irreversible behavior of thin al superconducting rings. *Physical Review B*, APS, v. 67, n. 5, p. 054506, 2003.

172 VODOLAZOV, D. Y.; PEETERS, F. Dynamic transitions between metastable states in a superconducting ring. *Physical Review B*, APS, v. 66, n. 5, p. 054537, 2002.

173 KENAWY, A. et al. Electronically tunable quantum phase slips in voltage-biased superconducting rings as a base for phase-slip flux qubits. *Superconductor Science and Technology*, IOP Publishing, v. 33, n. 12, p. 125002, 2020.

174 LU-DAC, M.; KABANOV, V. V. Multiple phase slips phenomena in mesoscopic superconducting rings. *Physical Review B*, APS, v. 79, n. 18, p. 184521, 2009.

175 BERGER, J. Flux transitions in a superconducting ring. *Physical Review B*, APS, v. 67, n. 1, p. 014531, 2003.

176 TARLIE, M. B.; ELDER, K. Metastable state selection in one-dimensional systems with a time-ramped control parameter. *Physical review letters*, APS, v. 81, n. 1, p. 18, 1998.

177 KARTTUNEN, M. et al. Instabilities and resistance fluctuations in thin accelerated superconducting rings. *Physical Review E*, APS, v. 66, n. 2, p. 026115, 2002.

178 MOOIJ, J.; HARMANS, C. Phase-slip flux qubits. *New Journal of Physics*, IOP Publishing, v. 7, n. 1, p. 219, 2005.

179 MOOIJ, J.; NAZAROV, Y. V. Superconducting nanowires as quantum phase-slip junctions. *Nature Physics*, Nature Publishing Group UK London, v. 2, n. 3, p. 169–172, 2006.

180 ASTAFIEV, O. et al. Coherent quantum phase slip. *Nature*, Nature Publishing Group UK London, v. 484, n. 7394, p. 355–358, 2012.

181 GÜMÜŞ, E. et al. Calorimetry of a phase slip in a josephson junction. *Nature Physics*, Nature Publishing Group UK London, v. 19, n. 2, p. 196–200, 2023.

182 GRAAF, S. D. et al. Charge quantum interference device. *Nature Physics*, Nature Publishing Group UK London, v. 14, n. 6, p. 590–594, 2018.

183 LIGATO, N. et al. Thermal superconducting quantum interference proximity transistor. *Nature Physics*, Nature Publishing Group UK London, v. 18, n. 6, p. 627–632, 2022.

184 MURPHY, A.; AVERIN, D. V.; BEZRYADIN, A. Nanoscale superconducting memory based on the kinetic inductance of asymmetric nanowire loops. *New Journal of Physics*, IOP Publishing, v. 19, n. 6, p. 063015, 2017.

185 HONGISTO, T.; ZORIN, A. Single-charge transistor based on the charge-phase duality of a superconducting nanowire circuit. *Physical review letters*, APS, v. 108, n. 9, p. 097001, 2012.

186 CHENG, R.; GOTETI, U. S.; HAMILTON, M. C. Spiking neuron circuits using superconducting quantum phase-slip junctions. *Journal of Applied Physics*, AIP Publishing, v. 124, n. 15, 2018.

187 PAOLO, A. D. et al. Efficient modeling of superconducting quantum circuits with tensor networks. *npj Quantum Information*, Nature Publishing Group UK London, v. 7, n. 1, p. 11, 2021.

188 PETKOVIĆ, I. et al. Deterministic phase slips in mesoscopic superconducting rings. *Nature communications*, Nature Publishing Group UK London, v. 7, n. 1, p. 13551, 2016.

189 GROPP, W. D. et al. Numerical simulation of vortex dynamics in type-II superconductors. *Journal of Computational Physics*, v. 123, n. 2, p. 254 – 266, 1996. ISSN 0021-9991. Disponível em: <http://www.sciencedirect.com/science/article/pii/S0021999196900224>.

190 DOMINGUEZ, D.; BERGER, J. Time-connected phase slips in current-driven two-band superconducting wires. *arXiv preprint arXiv:2405.09671*, 2024.

191 TUCKERMAN, L. S.; BARKLEY, D. Bifurcation analysis of the eckhaus instability. *Physica D: Nonlinear Phenomena*, Elsevier, v. 46, n. 1, p. 57–86, 1990.

192 BLUHM, H. et al. Magnetic response of mesoscopic superconducting rings with two order parameters. *Physical review letters*, APS, v. 97, n. 23, p. 237002, 2006.

193 KALLIN, C.; BERLINSKY, J. Chiral superconductors. *Reports on Progress in Physics*, IOP Publishing, v. 79, n. 5, p. 054502, 2016.

194 SIGRIST, M.; UEDA, K. Phenomenological theory of unconventional superconductivity. *Reviews of Modern physics*, APS, v. 63, n. 2, p. 239, 1991.

195 VOJTA, M.; ZHANG, Y.; SACHDEV, S. Quantum phase transitions in d-wave superconductors. *Physical review letters*, APS, v. 85, n. 23, p. 4940, 2000.

196 STONE, M.; ROY, R. Edge modes, edge currents, and gauge invariance in p x+ i p y superfluids and superconductors. *Physical Review B*, APS, v. 69, n. 18, p. 184511, 2004.

197 READ, N.; GREEN, D. Paired states of fermions in two dimensions with breaking of parity and time-reversal symmetries and the fractional quantum hall effect. *Physical Review B*, APS, v. 61, n. 15, p. 10267, 2000.

198 GARAUD, J.; BABAEV, E. Skyrmionic state and stable half-quantum vortices in chiral p-wave superconductors. *Physical Review B*, APS, v. 86, n. 6, p. 060514, 2012.

199 JANG, J. et al. Observation of half-height magnetization steps in sr2ruo4. *Science*, American Association for the Advancement of Science, v. 331, n. 6014, p. 186–188, 2011.

200 ZYUZIN, A.; GARAUD, J.; BABAEV, E. Nematic skyrmions in odd-parity superconductors. *Physical review letters*, APS, v. 119, n. 16, p. 167001, 2017.

201 BECERRA, V. F. et al. Vortical versus skyrmionic states in mesoscopic p-wave superconductors. *Physical Review B*, APS, v. 93, n. 1, p. 014518, 2016.

202 MILOŠEVIĆ, M. V.; PERALI, A. Emergent phenomena in multicomponent superconductivity: an introduction to the focus issue. *Superconductor Science and Technology*, IOP Publishing, v. 28, n. 6, p. 060201, apr 2015. Disponível em: <https://doi.org/10.1088/0953-2048/28/6/060201>.

203 LIN, S.-Z.; HU, X. Vortex states and the phase diagram of a multiple-component ginzburg-landau theory with competing repulsive and attractive vortex interactions. *Physical Review B*, APS, v. 84, n. 21, p. 214505, 2011.

204 SARMA, S. D.; FREEDMAN, M.; NAYAK, C. Majorana zero modes and topological quantum computation. *npj Quantum Information*, Nature Publishing Group, v. 1, n. 1, p. 1–13, 2015.

205 VOLOVIK, G. On edge states in superconductors with time inversion symmetry breaking. *Journal of Experimental and Theoretical Physics Letters*, Springer, v. 66, n. 7, p. 522–527, 1997.

206 VOLOVIK, G. Fermion zero modes on vortices in chiral superconductors. *Journal of Experimental and Theoretical Physics Letters*, Springer, v. 70, n. 9, p. 609–614, 1999.

207 IVANOV, D. A. Non-abelian statistics of half-quantum vortices in p-wave superconductors. *Physical review letters*, APS, v. 86, n. 2, p. 268, 2001.

208 YU, Y. et al. High-temperature superconductivity in monolayer bi2sr2cacu2o8+ δ. *Nature*, Nature Publishing Group, v. 575, n. 7781, p. 156–163, 2019.

209 BUZDIN, A.; KOSHELEV, A. Periodic alternating 0-and π-junction structures as realization of φ-josephson junctions. *Physical Review B*, APS, v. 67, n. 22, p. 220504, 2003.

210 GOLDOBIN, E. et al. Josephson junctions with second harmonic in the current-phase relation: Properties of φ junctions. *Physical Review B*, APS, v. 76, n. 22, p. 224523, 2007.

211 BAKURSKIY, S. et al. Josephson φ-junctions based on structures with complex normal/ferromagnet bilayer. *Superconductor science and technology*, IOP Publishing, v. 26, n. 1, p. 015005, 2012.

212 HOLMVALL, P.; BLACK-SCHAFFER, A. M. Enhanced chiral edge currents and orbital magnetic moment in chiral d-wave superconductors from mesoscopic finite-size effects. *Physical Review B*, APS, v. 108, n. 17, p. 174505, 2023.

213 PATHAK, V.; CAN, O.; FRANZ, M. Edge currents as probe of topology in twisted cuprate bilayers. *Physical Review B*, APS, v. 110, n. 1, p. 014506, 2024.

214 SALOMAA, M.; VOLOVIK, G. Vortices with spontaneously broken axisymmetry in b 3. *Physical review letters*, APS, v. 56, n. 4, p. 363, 1986.

215 THUNEBERG, E. Identification of vortices in superfluid b 3. *Physical review letters*, APS, v. 56, n. 4, p. 359, 1986.

216 VOLOVIK, G. On the vortex lattice transition in heavy-fermionic upt3. *Journal of Physics C: Solid State Physics*, IOP Publishing, v. 21, n. 8, p. L221, 1988.

217 BARASH, Y. S.; MEL'NIKOV, A. Possible existence of nonsingular-vortex in upt3. *ZhETF Pisma Redaktsiiu*, v. 51, p. 511, 1990.

218 MEL'NIKOV, A. et al. Nonsingular vortices in (d+ s)-wave superconductors. *Physical Review B*, APS, v. 62, n. 17, p. 11820, 2000.

219 BABAEV, E.; FADDEEV, L. D.; NIEMI, A. J. Hidden symmetry and knot solitons in a charged two-condensate bose system. *Physical Review B*, APS, v. 65, n. 10, p. 100512, 2002.

220 GARAUD, J. et al. Chiral $\mathbb{C}P^2$ skyrmions in three-band superconductors. *Phys. Rev. B*, American Physical Society, v. 87, p. 014507, Jan 2013. Disponível em: <https://link.aps.org/doi/10.1103/PhysRevB.87.014507>.

221 BENFENATI, A.; BARKMAN, M.; BABAEV, E. Demonstration of $\mathbb{C}P^2$ skyrmions in three-band superconductors by self-consistent solutions to a bogoliubov-de gennes model. *arXiv preprint arXiv:2204.05242*, 2022.

222 ZHANG, L.-F. et al. Skyrmionic chains and lattices in s+ i d superconductors. *Physical Review B*, APS, v. 101, n. 6, p. 064501, 2020.

223 DORIA, M. M.; GUBERNATIS, J.; RAINER, D. Virial theorem for ginzburg-landau theories with potential applications to numerical studies of type-ii superconductors. *Physical Review B*, APS, v. 39, n. 13, p. 9573, 1989.

224 HOLMVALL, P.; WALL-WENNERDAL, N.; BLACK-SCHAFFER, A. M. Robust and tunable coreless vortices and fractional vortices in chiral d-wave superconductors. *Physical Review B*, APS, v. 108, n. 9, p. 094511, 2023.

225 ZHANG, L.-F. et al. Electronic properties of emergent topological defects in chiral p-wave superconductivity. *Phys. Rev. B*, American Physical Society, v. 94, p. 024520, Jul 2016. Disponível em: <https://link.aps.org/doi/10.1103/PhysRevB.94.024520>.

226 SU, Y.; LIN, S.-Z. Pairing symmetry and spontaneous vortex-antivortex lattice in superconducting twisted-bilayer graphene: Bogoliubov-de gennes approach. *Phys. Rev. B*, American Physical Society, v. 98, p. 195101, Nov 2018. Disponível em: <https://link.aps.org/doi/10.1103/PhysRevB.98.195101>.

227 WU, F.; SARMA, S. D. Identification of superconducting pairing symmetry in twisted bilayer graphene using in-plane magnetic field and strain. *Phys. Rev. B*, American Physical Society, v. 99, p. 220507, Jun 2019. Disponível em: <https://link.aps.org/doi/10.1103/PhysRevB.99.220507>.

228 LEE, Y. et al. Encapsulating high-temperature superconducting twisted van der waals heterostructures blocks detrimental effects of disorder. *Advanced Materials*, Wiley Online Library, v. 35, n. 15, p. 2209135, 2023.

229 MARTINI, M. et al. Twisted cuprate van der waals heterostructures with controlled josephson coupling. *Materials Today*, Elsevier, v. 67, p. 106–112, 2023.

230 CASTELLANI, M. et al. A superconducting full-wave bridge rectifier. *arXiv preprint arXiv:2406.12175*, 2024.

231 TOOMEY, E. et al. Superconducting nanowire spiking element for neural networks. *Nano letters*, ACS Publications, v. 20, n. 11, p. 8059–8066, 2020.

232 GOLOD, T.; MORLET-DECARNIN, L.; KRASNOV, V. M. Word and bit line operation of a $1\times$ 1 μm2 superconducting vortex-based memory. *Nature Communications*, Nature Publishing Group UK London, v. 14, n. 1, p. 4926, 2023.

233 CAI, R.; ŽUTIĆ, I.; HAN, W. Superconductor/ferromagnet heterostructures: a platform for superconducting spintronics and quantum computation. *Advanced Quantum Technologies*, Wiley Online Library, v. 6, n. 1, p. 2200080, 2023.

APPENDIX A – Numerical Methods for the Ginzburg-Landau equations

A.1 Introduction

In this section, we outline the numerical methods employed to solve the Ginzburg-Landau equations. The specific details depend on the nature of the problem at hand—for instance, whether the system is two- or three-dimensional, whether an external magnetic field or current is applied, or whether the superconductor is periodic in one or more dimensions, which would necessitate the use of periodic boundary conditions. Additionally, factors such as heat dissipation due to vortex motion, the presence of multiple order parameters in the superconductor, and other scenarios must also be considered. Below, we describe the method used for each of these situations.

A.2 Infinite Superconductor with Rectangular Cross Section under an Applied Magnetic Field

Let us begin with the simplest case: a very long superconductor, which can be considered infinite along the z direction in the presence of an external magnetic field. First, we rewrite the Ginzburg-Landau equations in dimensionless form. For this example, we will express the equations using the following dimensionless units:

$$\begin{aligned} \tilde{\mathbf{r}} &= \frac{\mathbf{r}}{\xi} \\ \tilde{\psi}^2 &= \frac{\psi^2}{(\alpha/\beta)} \\ \tilde{\mathbf{h}} &= \frac{\mathbf{h}}{H_{c2}} \\ \tilde{\mathbf{A}} &= \frac{\mathbf{A}}{H_{c2}\xi} \,, \end{aligned} \tag{A.1}$$

where the quantities with a tilde on top represent dimensionless quantities.

By substituting Eq. A.1 into the first Ginzburg-Landau equation, we obtain:

$$\alpha\sqrt{(\alpha/\beta)}\left(-\tilde{\psi}+|\tilde{\psi}|^2\tilde{\psi}\right)+\frac{\hbar^2}{2m^*\xi^2}\sqrt{(\alpha/\beta)}\left(-\mathrm{i}\tilde{\boldsymbol{\nabla}}-\frac{2\pi\xi^2 H_{c2}}{\Phi_0}\tilde{\mathbf{A}}\right)^2\tilde{\psi}=0\,. \tag{A.2}$$

Using the definitions of ξ and H_{c2}, we can see that the factor $\alpha\sqrt{(\alpha/\beta)}$ is common to all terms in the equation and can therefore be dropped. The resulting equation is:

$$-\tilde{\psi} + |\tilde{\psi}|^2\tilde{\psi} + \left(-\mathrm{i}\tilde{\boldsymbol{\nabla}} - \tilde{\mathbf{A}}\right)^2 \tilde{\psi} = 0 \; . \tag{A.3}$$

In the same manner, we can rewrite the second Ginzburg-Landau equation using the new quantities as:

$$\frac{c}{4\pi}\frac{H_{c2}}{\xi}\tilde{\boldsymbol{\nabla}} \times \tilde{\mathbf{h}} = \frac{e^*\hbar}{m^*\xi}\frac{\alpha}{\beta}\tilde{\mathbf{J}}_s \; , \tag{A.4}$$

with the definitions of λ and H_{c2}, this is finally written as:

$$\kappa^2\tilde{\boldsymbol{\nabla}} \times \tilde{\mathbf{h}} = \tilde{\mathbf{J}}_s \; , \tag{A.5}$$

where the supercurrent, in dimensionless units, is given by:

$$\tilde{\mathbf{J}}_s = \mathrm{Re}\left[\tilde{\psi}^*\left(-\mathrm{i}\tilde{\boldsymbol{\nabla}} - \tilde{\mathbf{A}}\right)\tilde{\psi}\right] \; . \tag{A.6}$$

In this specific situation, we can assume the system is invariant along the z direction and take $\tilde{\psi} = \tilde{\psi}(x,y)$, $\tilde{\mathbf{A}} = (\tilde{A}_x(x,y), \tilde{A}_y(x,y), 0)$ and $\tilde{\mathbf{h}} = (0, 0, \tilde{h}_z(x,y))$. From this point forward, we drop the tilde over the dimensionless quantities to simplify our notation.

Before continuing with our method, it is important to note that Eqs. A.3 and A.5 are invariant under the following gauge transformation:

$$\begin{aligned} \psi &= \psi e^{\mathrm{i}\chi} \\ \mathbf{A} &= \mathbf{A} + \boldsymbol{\nabla}\chi \; . \end{aligned} \tag{A.7}$$

This feature is important because, while numerically solving the Ginzburg-Landau equations, we must ensure that the discretized version remains gauge invariant under the same transformations. To achieve this, we employ the link variable method, also known as the $U - \psi$ method, developed by Gropp *et. al.* [189]. In this method, the following auxiliary fields are defined:

$$\begin{aligned} \mathcal{U}_x(x,y) &= \exp\left(-\mathrm{i}\int_{x_0}^{x} A_x(x',y)dx'\right) \\ \mathcal{U}_y(x,y) &= \exp\left(-\mathrm{i}\int_{y_0}^{y} A_y(x,y')dy'\right) \; . \end{aligned} \tag{A.8}$$

These auxiliary fields have the following property:

$$\begin{aligned} \mathcal{U}_x^* \mathcal{U}_x &= 1 \\ \frac{\partial \mathcal{U}_x}{\partial x} &= -\mathrm{i} A_x \mathcal{U}_x \ , \end{aligned} \tag{A.9}$$

with the same being true for $\mathcal{U}_y$. Thus, we can conclude that the following expression is also valid:

$$\frac{\partial (\mathcal{U}_x f)}{\partial x} = \mathcal{U}_x \left(\frac{\partial f}{\partial x} - \mathrm{i} A_x f \right) \ , \tag{A.10}$$

for an arbitrary function f.

From Eq. A.10, we can obtain:

$$\frac{\partial^2 (\mathcal{U}_x f)}{\partial x^2} = -\mathrm{i} A_x \mathcal{U}_x \left(\frac{\partial f}{\partial x} - \mathrm{i} A_x f \right) + \mathcal{U}_x \left(\frac{\partial^2 f}{\partial x^2} - \mathrm{i} \frac{\partial A_x}{\partial x} f - \mathrm{i} A_x \frac{\partial f}{\partial x} \right) \ . \tag{A.11}$$

Rearranging the terms, we have:

$$\frac{\partial^2 (\mathcal{U}_x f)}{\partial x^2} = -\mathcal{U}_x \left(-\mathrm{i} \frac{\partial}{\partial x} - A_x \right)^2 f \ . \tag{A.12}$$

With this result, the third term in Eq. A.3 can be written as:

$$\left(-\mathrm{i} \boldsymbol{\nabla} - \mathbf{A} \right)^2 \psi = \left(-\mathrm{i} \frac{\partial}{\partial x} - A_x \right)^2 \psi + \left(-\mathrm{i} \frac{\partial}{\partial y} - A_y \right)^2 \psi = -\mathcal{U}_x^* \frac{\partial^2 (\mathcal{U}_x \psi)}{\partial x^2} - \mathcal{U}_y^* \frac{\partial^2 (\mathcal{U}_y \psi)}{\partial y^2} \ , \tag{A.13}$$

where we have used Eq. A.9.

The final equation to be discretized is then:

$$\mathcal{U}_x^* \frac{\partial^2 (\mathcal{U}_x \psi)}{\partial x^2} + \mathcal{U}_y^* \frac{\partial^2 (\mathcal{U}_y \psi)}{\partial y^2} + \left(1 - |\psi|^2 \right) \psi = 0 \ . \tag{A.14}$$

To proceed, we must define where each quantity is calculated in our discrete grid, which is shown in Fig.1 As we can see, the order parameter and $\mathcal{U}_i$ are computed at the grid points, while the supercurrent and the vector potential are calculated between two consecutive grid points in the x or y directions, according to their components and h_z is calculated at the center of a square cell of the grid.

We are now ready to discretize Eq. A.14. The third term in this equation is straightforward and is given as:

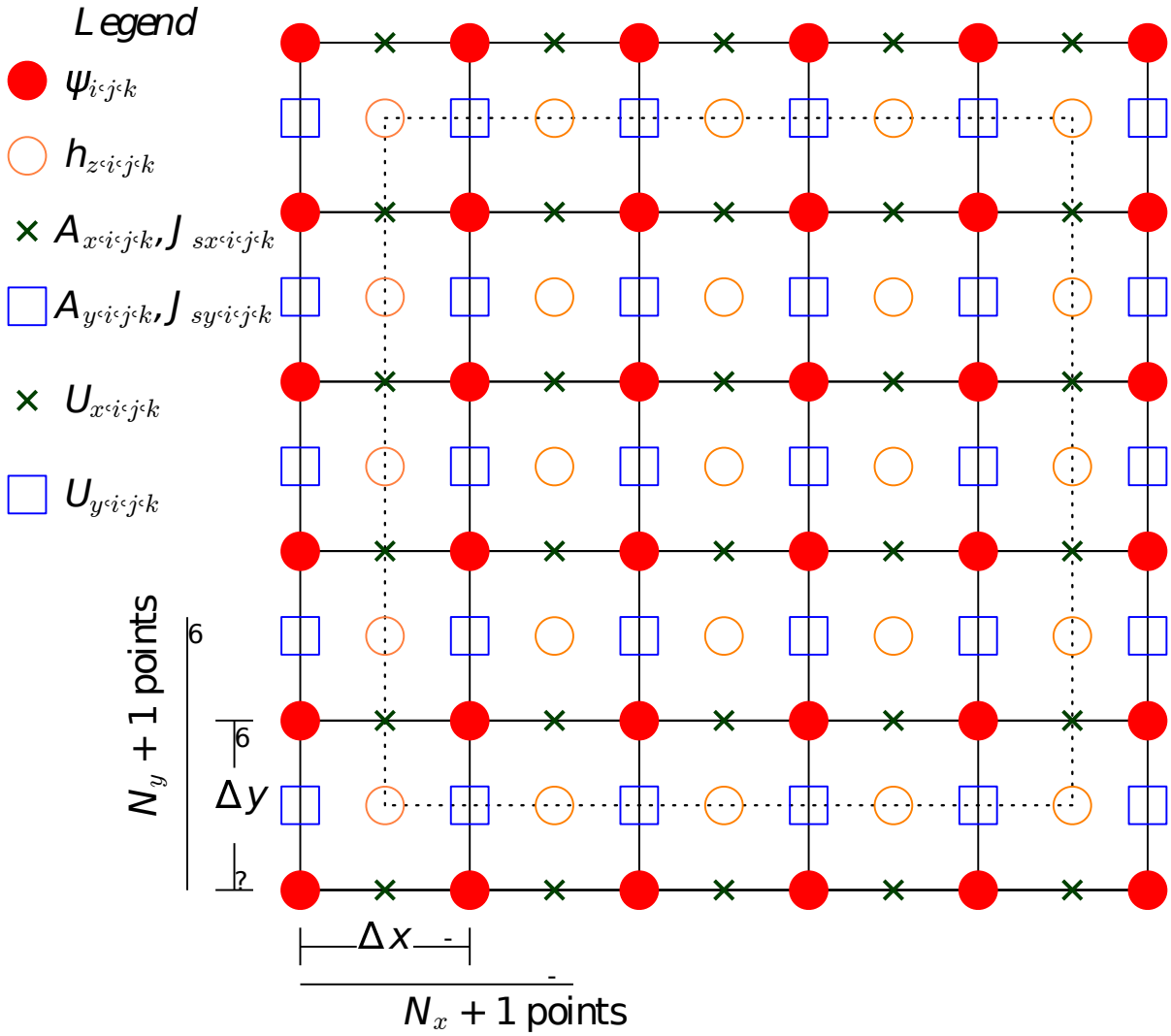

Figure 1 – *Schematic view of the points where each quantity is computed in the simulation grid.*

$$\left(1 - |\psi|^2\right)\psi \rightarrow \left(1 - |\psi_{i,j}|^2\right)\psi_{i,j} \ , \tag{A.15}$$

where $i = 1, ..., N_x + 1$ and $j = 1, ..., N_y + 1$ give the position of the grid point, with $N_x = L_x/\Delta x$, $N_y = L_y/\Delta y$, L_i being the length of the superconductor in the i direction and Δ_i the distance between two grid points at i direction.

For the discretized version of the second order derivative, we use the following expression:

$$\frac{d^2 f}{dx^2} \rightarrow \frac{f_{i+1} - 2f_i + f_{i-1}}{\Delta x^2} \ , \tag{A.16}$$

the first term in Eq. A.14 then becomes:

$$\mathcal{U}_x^* \frac{\partial^2(\mathcal{U}_x\psi)}{\partial x^2} \rightarrow \mathcal{U}_{xi,j}^* \frac{\mathcal{U}_{xi+1,j}\psi_{i+1,j} - 2\mathcal{U}_{xi,j}\psi_{i,j} + \mathcal{U}_{xi-1,j}\psi_{i-1,j}}{\Delta x^2} \ , \tag{A.17}$$

with the y component being obtained by the same procedure.

We now define the following link variable, which is calculated between two grid points:

$$\begin{aligned} U_{xi,j} &= \mathcal{U}_{xi+1,j}\mathcal{U}^*_{xi,j} = \exp\left(-iA_{xi,j}\Delta x\right) \\ U_{yi,j} &= \mathcal{U}_{yi,j+1}\mathcal{U}^*_{yi,j} = \exp\left(-iA_{yi,j}\Delta y\right) , \end{aligned} \tag{A.18}$$

where we have used Eq. A.9 and approximated the integral as the value of the vector potential component times the interval length. With this definition, Eq. A.17 can be rewritten as:

$$\mathcal{U}^*_x \frac{\partial^2(\mathcal{U}_x\psi)}{\partial x^2} \rightarrow \frac{U_{xi,j}\psi_{i+1,j} - 2\psi_{i,j} + U^*_{xi-1,j}\psi_{i-1,j}}{\Delta x^2} . \tag{A.19}$$

And the final discretized form of Eq. A.14 is given by:

$$\frac{U_{xi,j}\psi_{i+1,j} - 2\psi_{i,j} + U^*_{xi-1,j}\psi_{i-1,j}}{\Delta x^2} + \frac{U_{yi,j}\psi_{i,j+1} - 2\psi_{i,j} + U^*_{yi,j-1}\psi_{i,j-1}}{\Delta y^2} + \left(1 - |\psi_{i,j}|^2\right)\psi_{i,j} = 0 . \tag{A.20}$$

To discretize Eq. A.5 we first establish that we are using a central scheme for first order spatial derivatives, such as:

$$\frac{df}{dx} = \frac{f_{i+1} - f_{i-1}}{2\Delta x} . \tag{A.21}$$

The two components of Eq. A.5 we need to discretize are:

$$\begin{aligned} J_{sx} - \kappa^2\frac{\partial h_z}{\partial y} &= 0 \\ J_{sy} + \kappa^2\frac{\partial h_z}{\partial x} &= 0 . \end{aligned} \tag{A.22}$$

Since h_z is calculated at the center of a square cell, the central scheme described in Eq. A.21, gives the following result:

$$\begin{aligned} J_{sxi,j} - \kappa^2\frac{h_{zi,j} - h_{zi,j-1}}{\Delta y} &= 0 \\ J_{syi,j} + \kappa^2\frac{h_{zi,j} - h_{zi-1,j}}{\Delta x} &= 0 . \end{aligned} \tag{A.23}$$

The supercurrent, defined in Eq. A.6, can be rewritten with the help of Eq. A.10:

$$J_{sx} = \mathrm{Re}\left[-\mathrm{i}\mathcal{U}_x^*\psi^*\frac{\partial(\mathcal{U}_x\psi)}{\partial x}\right] = \mathrm{Im}\left[\mathcal{U}_x^*\psi^*\frac{\partial(\mathcal{U}_x\psi)}{\partial x}\right] , \tag{A.24}$$

where we have used the mathematical identity $\mathrm{Re}(-\mathrm{i}z) = \mathrm{Im}(z)$.

The discretized version of Eq. A.24 is given by:

$$\begin{aligned} J_{sxi,j} &= \mathrm{Im}\left[\left(\frac{\mathcal{U}^*_{xi+1,j}\psi^*_{i+1,j} + \mathcal{U}^*_{xi,j}\psi^*_{i,j}}{2}\right)\left(\frac{\mathcal{U}_{xi+1,j}\psi_{i+1,j} - \mathcal{U}_{xi,j}\psi_{i,j}}{\Delta x}\right)\right] = \\ &= \mathrm{Im}\left[\frac{|\psi_{i+1,j}|^2 + |\psi_{i,j}|^2 + U_{xi,j}\psi_{i+1,j}\psi^*_{i,j} - U^*_{xi,j}\psi^*_{i+1,j}\psi_{i,j}}{2\Delta x}\right] , \end{aligned} \tag{A.25}$$

where we have used Eq. A.18.

The first two terms are entirely real and so can be dropped from our expression. Using the identity $\mathrm{Im}(z^*) = -\mathrm{Im}(z)$, the final form of the discretized supercurrent is:

$$J_{sxi,j} = \mathrm{Im}\left[\frac{U_{xi,j}\psi_{i+1,j}\psi^*_{i,j}}{\Delta x}\right] . \tag{A.26}$$

In a similar fashion, the discretized y component of the supercurrent is given by:

$$J_{syi,j} = \mathrm{Im}\left[\frac{U_{yi,j}\psi_{i,j+1}\psi^*_{i,j}}{\Delta y}\right] . \tag{A.27}$$

Eqs. A.20 and A.23 are then used as a relaxation method for the order parameter and vector potential. Starting from a given initial state, these quantities are updated until convergence according to the following procedure:

$$\begin{aligned} \psi^{(n+1)}_{i,j} &= \psi^{(n)}_{i,j} + \frac{\Delta t}{\Delta x^2}\left(U^{(n)}_{xi,j}\psi^{(n)}_{i+1,j} - 2\psi^{(n)}_{i,j} + U^{*(n)}_{xi-1,j}\psi^{(n)}_{i-1,j}\right) \\ &+ \frac{\Delta t}{\Delta y^2}\left(U^{(n)}_{yi,j}\psi^{(n)}_{i,j+1} - 2\psi^{(n)}_{i,j} + U^{*(n)}_{yi,j-1}\psi^{(n)}_{i,j-1}\right) \\ &+ \Delta t\left(1 - |\psi^{(n)}_{i,j}|^2\right)\psi^{(n)}_{i,j} , \end{aligned} \tag{A.28}$$

for $i = 2, ..., N_x$ and $j = 2, ..., N_y$.

$$A^{(n+1)}_{xi,j} = A^{(n)}_{xi,j} + \Delta t J^{(n)}_{sxi,j} - \frac{\Delta t\kappa^2}{\Delta y}\left(h^{(n)}_{zi,j} - h^{(n)}_{zi,j-1}\right) , \tag{A.29}$$

for $i = 1, ..., N_x$ and $j = 2, ..., N_y$.

$$A^{(n+1)}_{yi,j} = A^{(n)}_{yi,j} + \Delta t J^{(n)}_{syi,j} + \frac{\Delta t\kappa^2}{\Delta x}\left(h^{(n)}_{zi,j} - h^{(n)}_{zi-1,j}\right) , \tag{A.30}$$

for $i = 2, ..., N_x$ and $j = 1, ..., N_y$.

In the equations above, $f^{(n)}$ denotes the value of quantity f at the nth iteration step. The factor Δt mimics the role of a time step between each iteration. To secure that the solution will not diverge, we must limit $\Delta t = \min(\delta/4, \delta/4\kappa^2)$, where $\delta = 2/\Delta x^2 + 2/\Delta y^2$.

We now need to define the physical quantities at the grid points not specified by Eqs. A.28-A.30. To do this, we must define the spatial boundary conditions for such quantities. Let us start by the local magnetic field. In the case treated here, of a very long superconductor, we can assume that the demagnetization effects caused by the supercurrents do not affect the field at the system edge. Thus being, we have:

$$\begin{aligned} h_{zi,1} &= H_a \\ h_{zi,N_y} &= H_a \ , \end{aligned} \tag{A.31}$$

for $i = 1, ..., N_x$, and:

$$\begin{aligned} h_{z1,j} &= H_a \\ h_{zN_x,j} &= H_a \ , \end{aligned} \tag{A.32}$$

for $j = 1, ..., N_y$, where H_a is the modulus of the applied field.

With this, the vector potential also must satisfy the condition for the field at the borders. We then have:

$$\begin{aligned} A_{xi,1} &= A_{xi,2} - \frac{\Delta y}{\Delta x}\left(A_{yi+1,1} - A_{yi,1}\right) + \Delta y H_a \\ A_{xi,N_y+1} &= A_{xi,N_y} + \frac{\Delta y}{\Delta x}\left(A_{yi+1,N_y} - A_{yi,N_y}\right) - \Delta y H_a \ , \end{aligned} \tag{A.33}$$

for $i = 2, ..., N_x - 1$, and:

$$\begin{aligned} A_{y1,j} &= A_{y2,j} - \frac{\Delta x}{\Delta y}\left(A_{x1,j+1} - A_{x1,j}\right) - \Delta x H_a \\ A_{yN_x+1,j} &= A_{yN_x,j} + \frac{\Delta x}{\Delta y}\left(A_{xN_x,j+1} - A_{xN_x,j}\right) + \Delta x H_a \ , \end{aligned} \tag{A.34}$$

for $j = 2, ..., N_y - 1$.

For the boundary condition of the order parameter we impose the physical condition that no supercurrent flows in or out the superconductor. Analyzing Eq. A.6, one can see that the following expression satisfies this condition:

$$\left(-\mathrm{i}\boldsymbol{\nabla} - \mathbf{A}\right)\psi\Big|_n = \frac{\mathrm{i}\psi}{b} \ , \tag{A.35}$$

where b is a real constant and it is known as the de Gennes extrapolation length. If the interface is of a superconductor/insulator type, b goes to infinity, whereas if the surface is superconductor/magnetic, b goes to zero. With such expression, one can find the following boundary condition for the order parameter:

$$\begin{aligned} \psi_{i,1} &= \left(1-\frac{\Delta y}{b}\right)\mathcal{U}_{yi,1}\psi_{i,2} \\ \psi_{i,N_y+1} &= \left(1-\frac{\Delta y}{b}\right)\mathcal{U}^{*}_{yi,N_y}\psi_{i,N_y}\ , \end{aligned} \tag{A.36}$$

for $i = 2, ..., N_x$, and:

$$\begin{aligned} \psi_{1,j} &= \left(1-\frac{\Delta x}{b}\right)\mathcal{U}_{x1,j}\psi_{2,j} \\ \psi_{N_x+1,j} &= \left(1-\frac{\Delta x}{b}\right)\mathcal{U}^{*}_{xN_x,j}\psi_{N_x,j}\ , \end{aligned} \tag{A.37}$$

for $j = 2, ..., N_y$.

A.3 Superconducting Film under an Applied Magnetic Field

Let us now extend our previous analysis to the case of a finite superconducting film, where all three spatial dimensions must be considered, along with the demagnetization effects caused by the supercurrents. To achieve this, we introduce the concept of a simulation box, which extends beyond the superconductor. This box is used to simulate the variation of the magnetic field from its value at the boundaries of the superconductor to its value far away from the system, *i.e.*, the applied field.

In this method, the simulation box has dimensions equal to (L_x, L_y, L_z), while the dimensions of the superconductor are (l_x, l_y, l_z). In terms of grid points, the simulation box extends from $i = 1, ..., N_x + 1$, $j = 1, ..., N_y + 1$ and $k = 1, ..., N_z + 1$. In contrast, the superconductor goes from for $i = i_{x1} + 1, ..., i_{x2} - 1$, $j = j_{y1} + 1, ..., j_{y2} - 1$ and $k = k_{z1} + 1, ..., k_{z2} - 1$, where $i_{x1} = N_x/2 + 1 - l_x/(2\Delta x)$, $i_{x2} = N_x/2 + 1 + l_x/(2\Delta x)$, $j_{y1} = N_y/2 + 1 - l_y/(2\Delta y)$, $j_{y2} = N_y/2 + 1 + l_y/(2\Delta y)$, $k_{z1} = N_z/2 + 1 - l_z/(2\Delta z)$ and $k_{z2} = N_z/2 + 1 + l_z/(2\Delta z)$.

The adaptation of Eq. A.28 to three dimensions is straightforward, resulting in the new expression governing the relaxation of the order parameter:

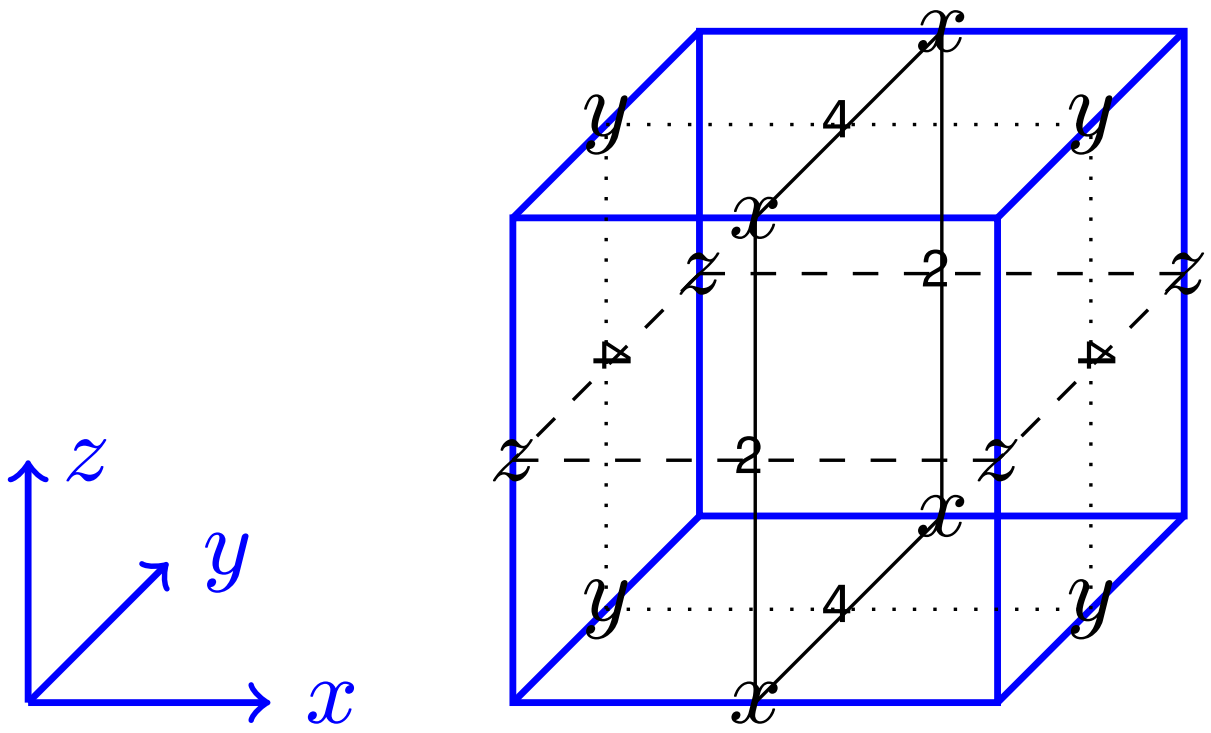

Figure 2 – *Schematic view of the three-dimensional version of the simulation grid introduced in Fig. 1*

$$\begin{aligned}
\psi_{i,j,k}^{(n+1)} &= \psi_{i,j,k}^{(n)} + \frac{\Delta t}{\Delta x^2}\left(U_{xi,j,k}^{(n)}\psi_{i+1,j,k}^{(n)} - 2\psi_{i,j,k}^{(n)} + U_{xi-1,j,k}^{*(n)}\psi_{i-1,j,k}^{(n)}\right) \\
&+ \frac{\Delta t}{\Delta y^2}\left(U_{yi,j,k}^{(n)}\psi_{i,j+1,k}^{(n)} - 2\psi_{i,j,k}^{(n)} + U_{yi,j-1,k}^{*(n)}\psi_{i,j-1,k}^{(n)}\right) \\
&+ \frac{\Delta t}{\Delta z^2}\left(U_{zi,j,k}^{(n)}\psi_{i,j,k+1}^{(n)} - 2\psi_{i,j,k}^{(n)} + U_{zi,j,k-1}^{*(n)}\psi_{i,j,k-1}^{(n)}\right) \\
&+ \Delta t\left(1 - |\psi_{i,j,k}^{(n)}|^2\right)\psi_{i,j,k}^{(n)} \,, \qquad \text{(A.38)}
\end{aligned}$$

for $i = i_{x1}+1, ..., i_{x2}-1$, $j = j_{y1}+1, ..., j_{y2}-1$ and $k = k_{z1}+1, ..., k_{z2}-1$. The new link variable U_z is defined in the same manner as in Eq. A.18, being calculated between two grid points along the z direction.

In addressing a three-dimensional problem, we must consider the three components of the vector potential and the three components of the local magnetic field. In two dimensions, we noted that the z component of the magnetic field was calculated at the center of a unit cell in the xy plane. Similarly, the x and y components are calculated at the center of a unit cell in the yz and xz planes, respectively. In mathematical terms, we have $h_{xi,j,k} = h_x(x_i, y_j + \Delta y/2, z_k + \Delta z/2)$, $h_{yi,j,k} = h_y(x_i + \Delta x/2, y_j, z_k + \Delta z/2)$ and $h_{zi,j,k} = h_z(x_i \Delta x/2, y_j + \Delta y/2, z_k)$, where x_i, y_j and z_k correspond to the positions of the grid points at indices i, j and k, respectively. 2 provides a schematic view of the numerical grid in three-dimensions.

With this, the equations governing the relaxation of each component of the vector potential are given by:

$$A^{(n+1)}_{xi,j,k} = A^{(n)}_{xi,j,k} + \Delta t J^{(n)}_{sxi,j,k} - \frac{\Delta t \kappa^2}{\Delta y}\left(h^{(n)}_{zi,j,k} - h^{(n)}_{zi,j-1,k}\right) + \frac{\Delta t \kappa^2}{\Delta z}\left(h^{(n)}_{yi,j,k} - h^{(n)}_{yi,j,k-1}\right) \ , \quad \text{(A.39)}$$

for $i = 1, ..., N_x$, $j = 2, ..., N_y$ and $k = 2, ..., N_z$, and:

$$A^{(n+1)}_{yi,j,k} = A^{(n)}_{yi,j,k} + \Delta t J^{(n)}_{syi,j,k} - \frac{\Delta t \kappa^2}{\Delta z}\left(h^{(n)}_{xi,j,k} - h^{(n)}_{xi,j,k-1}\right) + \frac{\Delta t \kappa^2}{\Delta x}\left(h^{(n)}_{zi,j,k} - h^{(n)}_{zi-1,j,k}\right) \ , \quad \text{(A.40)}$$

for $i = 2, ..., N_x$, $j = 1, ..., N_y$ and $k = 2, ..., N_z$, and:

$$A^{(n+1)}_{zi,j,k} = A^{(n)}_{zi,j,k} + \Delta t J^{(n)}_{szi,j,k} - \frac{\Delta t \kappa^2}{\Delta x}\left(h^{(n)}_{yi,j,k} - h^{(n)}_{yi-1,j,k}\right) + \frac{\Delta t \kappa^2}{\Delta y}\left(h^{(n)}_{xi,j,k} - h^{(n)}_{xi,j-1,k}\right) \ , \quad \text{(A.41)}$$

for $i = 2, ..., N_x$, $j = 2, ..., N_y$ and $k = 1, ..., N_z$.

In the same manner as we did for the two-dimensional case, we must impose that no supercurrent flows in or out of the faces of the superconductor. This results in the following boundary conditions for the order parameter:

$$\begin{aligned} \psi_{i_{x1},j,k} &= \left(1 - \frac{\Delta x}{b}\right) \mathcal{U}_{xi_{x1},j,k} \psi_{i_{x1}+1,j,k} \\ \psi_{i_{x2},j,k} &= \left(1 - \frac{\Delta x}{b}\right) \mathcal{U}^*_{xi_{x2}-1,j,k} \psi_{i_{x2}-1,j,k} \ , \end{aligned} \quad \text{(A.42)}$$

for $j = j_{y1} + 1, ..., j_{y2} - 1$ and $k = k_{z1} + 1, ..., k_{z2} - 1$, and:

$$\begin{aligned} \psi_{i,j_{y1},k} &= \left(1 - \frac{\Delta y}{b}\right) \mathcal{U}_{yi,j_{y1},k} \psi_{i,j_{y1}+1,k} \\ \psi_{i,j_{y2},k} &= \left(1 - \frac{\Delta y}{b}\right) \mathcal{U}^*_{yi,j_{y2}-1,k} \psi_{i,j_{y2}-1,k} \ , \end{aligned} \quad \text{(A.43)}$$

for $i = i_{x1} + 1, ..., i_{x2} - 1$ and $k = k_{z1} + 1, ..., k_{z2} - 1$, and:

$$\begin{aligned} \psi_{i,j,k_{z1}} &= \left(1 - \frac{\Delta y}{b}\right) \mathcal{U}_{zi,j,k_{z1}} \psi_{i,j,k_{z1}+1} \\ \psi_{i,j,k_{z2}} &= \left(1 - \frac{\Delta y}{b}\right) \mathcal{U}^*_{zi,j,k_{z2}-1} \psi_{i,j,k_{z2}-1} \ , \end{aligned} \quad \text{(A.44)}$$

for $i = i_{x1} + 1, ..., i_{x2} - 1$ and $j = j_{y1} + 1, ..., j_{y2} - 1$.

At the boundaries of the simulation box, the local magnetic field must equal the externally applied magnetic field, which leads to boundary conditions analogous to Eqs. A.31 and A.32. An important distinction is that there is no need to impose boundary conditions on the vector potential, as its values at the border of the superconductor are not utilized.

A.4 Superconductor Periodic in One Direction

Let us return to a two-dimensional system to discuss a different type of boundary condition, specifically for a two-dimensional superconductor that is periodic in one of its directions. In practice, such systems can mimic long superconducting stripes or superconductors with a unit cell that repeats itself along one direction.

Assuming that the system is periodic along the y direction, the equations governing the relaxation of the order parameter and of the vector potential do not change and remain equal to Eq. A.28 and Eqs. A.29 and A.30, respectively.

While for the x direction the boundary condition from Eq. A.37, forbidding the flow of supercurrent in or out the superconductor, still holds, we now must assure the periodicity along the y direction. This is done through the following boundary condition:

$$\begin{aligned} \psi_{i,1} &= \psi_{i,N_y} \\ \psi_{i,N_y+1} &= \psi_{i,2} \ , \end{aligned} \tag{A.45}$$

for $i = 2, ..., N_x$.

Similarly, the vector potential must also be periodic along the y direction. A_y is only calculated within the periodic unit cell, thus being, we only need to impose periodic boundary conditions to the x component of the vector potential, which are:

$$\begin{aligned} A_{xi,1} &= A_{xi,N_y} \\ A_{xi,N_y+1} &= A_{xi,2} \ , \end{aligned} \tag{A.46}$$

for $i = 1, ..., N_x$. It is important to note that the boundary condition Eq. A.34 still holds for A_y.

Finally, the local magnetic field can be calculated without the need for boundary conditions at $j = 1$ and $j = N_y$, while the boundary condition from Eq. A.32 still applies.

A.5 Superconductor Periodic in Two Directions

Suppose we now want to describe a very large superconducting system, where the effects of the boundaries can be completely neglected far from them. In this case, we need to apply periodic boundary conditions along both spatial dimensions.

Here, the straightforward generalization of the procedure outlined above for a system that is periodic in only one direction is not sufficient. We need to specify the flux that crosses through our unit cell, as well as how the phase of the order parameter

changes. In other words, we must define the number of vortices present in our system. The correct numerical procedure for this situation was described in Ref. [223]. The authors demonstrate that the order parameter and the vector potential must satisfy the following boundary conditions:

$$\begin{aligned} \mathbf{A}(\mathbf{r}+\mathbf{a}_v) &= \mathbf{A}(\mathbf{r}) + \boldsymbol{\nabla}\chi_v \\ \psi(\mathbf{r}+\mathbf{a}_v) &= \psi(\mathbf{r}) exp\left(\mathrm{i}\chi_v\right) \ , \end{aligned} \tag{A.47}$$

where $\mathbf{a}_v$ are lattice vectors denoting the periodicity of our system and χ_v are functions associated with them. This type of boundary condition ensures that our physical quantities remain gauge invariant when translated by one of the vectors $\mathbf{a}_v$. Since the order parameter must be single-valued, the following relation can be obtained:

$$(\chi_\alpha(\mathbf{r}) + \chi_\beta(\boldsymbol{r}+\mathbf{a}_{\boldsymbol{\alpha}}) - \chi_\alpha(\boldsymbol{r}+\mathbf{a}_{\boldsymbol{\beta}}) - \chi_\beta(\mathbf{r})) = -2\pi N \ , \tag{A.48}$$

where α and β denotes the two vectors that gives our unit cell. By adding this result to Eq. A.47, we can obtain that the total magnetic flux that cuts through our unit cell is equal to $N\Phi_0$, which means the factor N appearing in Eq. A.48 is the number of vortices in our system.

Let us give an example of this procedure in practice. Suppose the vectors are $\mathbf{a}_\alpha = L_x\hat{\boldsymbol{x}}$ and $\mathbf{a}_\beta = L_y\hat{\boldsymbol{y}}$, with the functions associated to them being $\chi_\alpha = 2N\pi y/L_y$ and $\chi_\beta = 0$. This functions obey the condition of Eq. A.48 and gives the following boundary conditions for the order parameter:

$$\begin{aligned} \psi_{i,1} &= \psi_{i,N_y} \\ \psi_{i,N_y+1} &= \psi_{i,2} \ , \end{aligned} \tag{A.49}$$

for $i = 2, ..., N_x$, and:

$$\begin{aligned} \psi_{1,j} &= exp\left(-\mathrm{i}\frac{2\pi N}{L_y}y_j\right)\psi_{N_x,j} \\ \psi_{N_x+1,j} &= exp\left(\mathrm{i}\frac{2\pi N}{L_y}y_j\right)\psi_{2,j} \ , \end{aligned} \tag{A.50}$$

for $j = 2, ..., N_y$.

While for the vector potential, we have:

$$\begin{aligned} A_{xi,1} &= A_{xi,N_y} \\ A_{xi,N_y+1} &= A_{xi,2} \ , \end{aligned} \tag{A.51}$$

for $i = 1, ..., N_x$, and:

$$\begin{aligned} A_{y1,j} &= A_{yN_x,j} - \frac{2\pi N}{L_y} \\ A_{yN_x+1,j} &= A_{y2,j} + \frac{2\pi N}{L_y} \, , \end{aligned} \tag{A.52}$$

for $j = 1, ..., N_y$.

In this case, there is no need to impose boundary conditions on the local magnetic field, as it can be calculated for all grid points.

A.6 Superconductor under an Applied Current

Having examined several scenarios of a superconducting system in an external magnetic field, let us now describe our numerical methods for simulating systems under the influence of an applied current. Since this is inherently a dynamical process, we must employ the time-dependent Ginzburg-Landau equations, which, in dimensionless units, are given by:

$$u\left(\frac{\partial}{\partial t} + \mathrm{i}\varphi\right)\psi = \psi - |\psi|^2\psi - (-\mathrm{i}\boldsymbol{\nabla} - \mathbf{A})^2\,\psi \, , \tag{A.53}$$

where we have introduced the scalar potential φ and u is a parameter that comes from the microscopic theory and it is equal to 5.79.

The Ampère law now reads:

$$\sigma_n\left(\frac{\partial \mathbf{A}}{\partial t} + \boldsymbol{\nabla}\varphi\right) = \mathbf{J}_s - \kappa^2\boldsymbol{\nabla}\times\mathbf{h} \, , \tag{A.54}$$

where σ_n represents the normal conductivity in dimensionless units and $\mathbf{J}_s$ is the supercurrent given in Eq. A.6.

In addition to these two equations, we need to find an expression that gives us the scalar potential at each instant of time. To do this, we first note that our system must obey the continuity equation:

$$\boldsymbol{\nabla}\cdot\mathbf{J} + \frac{\partial\rho}{\partial t} = 0 \, , \tag{A.55}$$

with ρ being the electric charge density. Assuming there is no accumulation of electric charge in our system, this is, ρ does not depend on time, we have:

$$\boldsymbol{\nabla}\cdot\mathbf{J} = \boldsymbol{\nabla}\cdot(\mathbf{J}_s + \mathbf{J}_n) = 0 \, . \tag{A.56}$$

With the help of Eq. A.54 for the definition of the normal current density $\mathbf{J}_n$, we reach the final equation for the scalar potential:

$$\nabla^2\varphi = \frac{1}{\sigma_n}\boldsymbol{\nabla}\cdot\mathbf{J}_s \ . \tag{A.57}$$

To obtain this equation, we have used the fact that our equations are invariant under the following gauge transformations:

$$\begin{aligned} \psi &= \psi e^{\mathrm{i}\chi} \\ \mathbf{A} &= \mathbf{A} + \boldsymbol{\nabla}\chi \\ \varphi &= \varphi + \frac{\partial\chi}{\partial t} \ , \end{aligned} \tag{A.58}$$

and have chosen χ such that $\boldsymbol{\nabla}\cdot\mathbf{A} = 0$.

Once we have the expression for the scalar potential, we can start to discretize the equations and detail our numerical method. To do this, let us suppose our system consists of a finite superconducting stripe with two metallic contacts located at $x = 0$ and $x = L_x$, covering the whole width of the sample, which are responsible for the injection and removal of the applied current.

For the time evolution of the order parameter, the discretization of the right-hand side of Eq. A.53 is equivalent to Eq. A.28. For the left-hand side, we also need to define a link variable for the time derivative:

$$U_{ti,j}^{(n,n+1)} = exp(\mathrm{i}\varphi_{i,j}^{(n)}\Delta t) \ , \tag{A.59}$$

given this expression, the discrete version of the left side of Eq. A.53 is:

$$u\left(\frac{\partial}{\partial t} + \mathrm{i}\varphi\right)\psi = \frac{U_{ti,j}^{(n,n+1)}\psi_{i,j}^{(n+1)} - \psi_{i,j}^{(n)}}{\Delta t} \ . \tag{A.60}$$

Combining Eq. A.28 and Eq. A.60 we then have:

$$\begin{aligned} \psi_{i,j}^{(n+1)} &= \left[\psi_{i,j}^{(n)} + \frac{\Delta t}{u\Delta x^2}\left(U_{xi,j}^{(n)}\psi_{i+1,j}^{(n)} - 2\psi_{i,j}^{(n)} + U_{xi-1,j}^{*(n)}\psi_{i-1,j}^{(n)}\right)\right. \\ &+ \frac{\Delta t}{u\Delta y^2}\left(U_{yi,j}^{(n)}\psi_{i,j+1}^{(n)} - 2\psi_{i,j}^{(n)} + U_{yi,j-1}^{*(n)}\psi_{i,j-1}^{(n)}\right) \\ &+ \left.\frac{\Delta t}{u}\left(1 - |\psi_{i,j}^{(n)}|^2\right)\psi_{i,j}^{(n)}\right] exp(-\mathrm{i}\varphi_{i,j}^{(n)}\Delta t) \ , \end{aligned} \tag{A.61}$$

for $i = 2, ..., N_x$ and $j = 2, ..., N_y$. Note that the scalar potential is calculated at the grid points.

similarly, the evolution of the two components of the vector potential are given by:

$$A_{xi,j}^{(n+1)} = A_{xi,j}^{(n)} + \frac{\Delta t}{\sigma_n} J_{sxi,j}^{(n)} - \frac{\Delta t \kappa^2}{\sigma_n \Delta y}\left(h_{zi,j}^{(n)} - h_{zi,j-1}^{(n)}\right) - \frac{\Delta t}{\Delta x}\left(\varphi_{i+1.j}^{(n)} - \varphi_{i,j}^{(n)}\right) , \tag{A.62}$$

for $i = 1, ..., N_x$ and $j = 2, ..., N_y$, and:

$$A_{yi,j}^{(n+1)} = A_{yi,j}^{(n)} + \frac{\Delta t}{\sigma_n} J_{syi,j}^{(n)} + \frac{\Delta t \kappa^2}{\sigma_n \Delta x}\left(h_{zi,j}^{(n)} - h_{zi-1,j}^{(n)}\right) - \frac{\Delta t}{\Delta y}\left(\varphi_{i.j+1}^{(n)} - \varphi_{i,j}^{(n)}\right) , \tag{A.63}$$

for $i = 2, ..., N_x$ and $j = 1, ..., N_y$, with the supercurrent being given by Eqs. A.26 and A.27. In this case, to assure convergence, we must impose $\Delta t = \min\left(u\delta^2/4, \beta\delta^2/4\kappa^2\right)$, with $\delta^2 = 2/(1/\Delta x^2 + 1/\Delta y^2)$.

As can be seen from Eq. A.57, we do not have an equation for the evolution of the scalar potential. Instead, this equation must be solve at each iteration n. One can apply different numerical methods to complete this task. The simplest of them (not the optimal in terms of computational time), the Jacobi's method, is given by:

$$\begin{aligned} \varphi_{i,j}^{(m+1)} &= \varphi_{i,j}^{(m)} + \frac{\Delta t'}{\Delta x^2}\left(\varphi_{i+1,j}^{(m)} - 2\varphi_{i,j}^{(m)} + \varphi_{i-1,j}^{(m)}\right) \\ &+ \frac{\Delta t'}{\Delta y^2}\left(\varphi_{i,j+1}^{(m)} - 2\varphi_{i,j}^{(m)} + \varphi_{i,j-1}^{(m)}\right) \\ &- \frac{\Delta t'}{\Delta x}\left(J_{sxi,j}^{(m)} - J_{sxi-1,j}^{(m)}\right) - \frac{\Delta t'}{\Delta y}\left(J_{syi,j}^{(m)} - J_{syi,j-1}^{(m)}\right) , \end{aligned} \tag{A.64}$$

where we have used m to differentiate this iteration step to the time steps of the previous equations. Also, $\Delta t'$ can be different from Δt and have the optimal value $\Delta t' = \delta^2/4$.

Now, we need to specify the boundary conditions for the scalar potential. At the normal contacts, they are given by:

$$\begin{aligned} \varphi_{1,j} &= \varphi_{2,j} + J_a \Delta x \\ \varphi_{N_x+1,j} &= \varphi_{N_x,j} - J_a \Delta x , \end{aligned} \tag{A.65}$$

for $j = 2, ..., N_y$. For the other two boundaries, we have:

$$\begin{aligned} \varphi_{i,1} &= \varphi_{i,2} \\ \varphi_{i,N_y+1} &= \varphi_{i,N_y} , \end{aligned} \tag{A.66}$$

for $i = 2, ..., N_x$.

Since we are now in the presence of an applied current, the boundary conditions for the local magnetic field must be changed accordingly. Applying the Ampère law, it is simple to obtain the following equations:

$$\begin{aligned} h_{zi,1} &= -\frac{J_a L_y}{2\kappa^2} \\ h_{zi,N_y} &= \frac{J_a L_y}{2\kappa^2} \ , \end{aligned} \tag{A.67}$$

for $i = 2, ..., N_x - 1$, and:

$$\begin{aligned} h_{z1,j} &= \frac{J_a y_j}{\kappa^2} \\ h_{zN_x,j} &= \frac{J_a y_j}{\kappa^2} \ , \end{aligned} \tag{A.68}$$

for $j = 2, ..., N_y - 1$.

The other boundary conditions remain unaltered, wiht the expressions derived previously still holding.

Another possibility for the description of the superconducting state carrying current is to consider an infinite superconducting stripe. In this case, instead of working in the gauge where $\boldsymbol{\nabla} \cdot \mathbf{A} = 0$ it is more convenient to work in the gauge $\varphi = 0$. The procedure is the same outlined for the superconductor periodic in one direction under an applied field, with the difference that the boundary conditions for the local magnetic field at $y = -L_y/2$ and $y = L_y/2$, must be the ones given in Eq. A.67.

A.7 Superconductor under an Applied Current Described by the Generalized Time Dependent Ginzburg-Landau Equation

Let us now treat the problem of a finite superconducting stripe driven by an external current injected through normal contacts, but this time using the generalized time-dependent Ginzburg-Landau equation (GTDGL), which, in dimensionless units, is given by:

$$\frac{u}{\sqrt{1+\gamma^2|\psi|^2}}\left(\frac{\partial\psi}{\partial t} + \frac{\gamma^2\psi}{2}\frac{\partial|\psi|^2}{\partial t} + \mathrm{i}\varphi\psi\right) = \psi - |\psi|^2\psi - \left(-\mathrm{i}\boldsymbol{\nabla} - \mathbf{A}\right)^2\psi \ , \tag{A.69}$$

where γ is a constant related to the electron-phonon inelastic collision time and to the superconducting gap.

As can be seen from Eq. A.69, before writing a discrete version of this equation, we need to obtain a closed expression for the time derivative of the order parameter, thus obtaining its evolution in each iteration. To do this, let us define:

$$\Delta = \psi - |\psi|^2\psi - \left(-\mathrm{i}\boldsymbol{\nabla} - \mathbf{A}\right)^2\psi \,, \tag{A.70}$$

which allows us to rewrite Eq. A.69, as well as its complex conjugate as:

$$\begin{aligned} \frac{\partial\psi}{\partial t} + \frac{\gamma^2\psi}{2}\frac{\partial|\psi|^2}{\partial t} &= \frac{\sqrt{1+\gamma^2|\psi|^2}}{u}\Delta - \mathrm{i}\varphi\psi \\ \frac{\partial\psi^*}{\partial t} + \frac{\gamma^2\psi^*}{2}\frac{\partial|\psi|^2}{\partial t} &= \frac{\sqrt{1+\gamma^2|\psi|^2}}{u}\Delta^* + \mathrm{i}\varphi\psi^* \,. \end{aligned} \tag{A.71}$$

These equations can be combined in a matrix equation given by:

$$\begin{pmatrix} 1+\frac{\gamma|\psi|^2}{2} & \frac{\gamma^2\psi^2}{2} \\ \frac{\gamma^2\psi^{*2}}{2} & 1+\frac{\gamma|\psi|^2}{2} \end{pmatrix} \begin{pmatrix} \frac{\partial\psi}{\partial t} \\ \frac{\partial\psi^*}{\partial t} \end{pmatrix} = \begin{pmatrix} \frac{\sqrt{1+\gamma^2|\psi|^2}}{u}\Delta - \mathrm{i}\varphi\psi \\ \frac{\sqrt{1+\gamma^2|\psi|^2}}{u}\Delta^* + \mathrm{i}\varphi\psi^* \end{pmatrix} \,. \tag{A.72}$$

From linear algebra we know that, in the general matrix equation:

$$\begin{pmatrix} a_1 & b_1 \\ a_2 & b_2 \end{pmatrix} \begin{pmatrix} x \\ y \end{pmatrix} = \begin{pmatrix} k_1 \\ k_2 \end{pmatrix} \,, \tag{A.73}$$

the solution for x is given by:

$$x = \frac{\begin{vmatrix} k_1 & b_1 \\ k_2 & b_2 \end{vmatrix}}{D} \,, \tag{A.74}$$

where D is the determinant of the first of the 2×2 matrix:

$$D = \begin{vmatrix} a_1 & b_1 \\ a_2 & b_2 \end{vmatrix} \,. \tag{A.75}$$

Applying this procedure to Eq. A.72, we have:

$$D = \begin{vmatrix} 1+\frac{\gamma|\psi|^2}{2} & \frac{\gamma^2\psi^2}{2} \\ \frac{\gamma^2\psi^{*2}}{2} & 1+\frac{\gamma|\psi|^2}{2} \end{vmatrix} = 1+\gamma^2|\psi|^2;, \tag{A.76}$$

and:

$$\frac{\partial\psi}{\partial t} = \frac{\begin{vmatrix} \frac{\sqrt{1+\gamma^2|\psi|^2}}{u}\Delta - \mathrm{i}\varphi\psi & \frac{\gamma^2\psi^2}{2} \\ \frac{\sqrt{1+\gamma^2|\psi|^2}}{u}\Delta^* + \mathrm{i}\varphi\psi^* & 1+\frac{\gamma|\psi|^2}{2} \end{vmatrix}}{1+\gamma^2|\psi|^2};. \tag{A.77}$$

Solving the determinant in Eq. A.77 finally gives us the the expression for the time evolution of the order parameter:

$$\left(\frac{\partial}{\partial t}+\mathrm{i}\varphi\right)\psi=\frac{\sqrt{1+\gamma^2|\psi|^2}}{u}\Delta-\gamma^2\frac{\mathrm{Re}\left[\psi^*\Delta/u\right]}{\sqrt{1+\gamma^2|\psi|^2}};. \tag{A.78}$$

The iteration procedure, in the discretized form, is given by:

$$\psi_{i,j}^{(n+1)}=\left(\psi_{i,j}^{(n)}+\Delta t\sqrt{1+\gamma^2|\psi_{i,j}^{(n)}|^2}\frac{\Delta_{i,j}^{(n)}}{u}-\Delta t\gamma^2\frac{\mathrm{Re}\left[\psi_{i,j}^{*(n)}\Delta_{i,j}^{(n)}/u\right]}{\sqrt{1+\gamma^2|\psi_{i,j}^{(n)}|^2}}\right)exp(-\mathrm{i}\varphi_{i,j}^{(n)}\Delta t)\ , \tag{A.79}$$

with:

$$\begin{aligned}\Delta_{i,j}^{(n)} &= \frac{1}{\Delta x^2}\left(U_{xi,j}^{(n)}\psi_{i+1,j}^{(n)}-2\psi_{i,j}^{(n)}+U_{xi-1,j}^{*(n)}\psi_{i-1,j}^{(n)}\right)\\ &+ \frac{1}{\Delta y^2}\left(U_{yi,j}^{(n)}\psi_{i,j+1}^{(n)}-2\psi_{i,j}^{(n)}+U_{yi,j-1}^{*(n)}\psi_{i,j-1}^{(n)}\right)\\ &+ \left(1-|\psi_{i,j}^{(n)}|^2\right)\psi_{i,j}^{(n)};,\end{aligned} \tag{A.80}$$

The remaining steps of the iteration procedure are exactly the same as the ones described for the standard time-dependent Ginzburg-Landau equation.

A.8 $d_{x^2-y^2}$ Superconductor

Let us now consider a superconductor with d-wave pairing. The Ginzburg-Landau equations for such system were given in the last chapter. Below, we give them in discretized form, detailing the iteration procedure to solve them numerically:

$$\begin{aligned}\Delta_{si,j}^{(n+1)} &= \Delta_{si,j}^{(n)}+\frac{\Delta t}{\Delta x^2}\left(U_{xi,j}^{(n)}\Delta_{si+1,j}^{(n)}-2\Delta_{si,j}^{(n)}+U_{xi-1,j}^{*(n)}\Delta_{si-1,j}^{(n)}\right)\\ &+ \frac{\Delta t}{\Delta y^2}\left(U_{yi,j}^{(n)}\Delta_{si,j+1}^{(n)}-2\Delta_{si,j}^{(n)}+U_{yi,j-1}^{*(n)}\Delta_{si,j-1}^{(n)}\right)\\ &+ \frac{\Delta t}{2\Delta x^2}\left(U_{xi,j}^{(n)}\Delta_{di+1,j}^{(n)}-2\Delta_{di,j}^{(n)}+U_{xi-1,j}^{*(n)}\Delta_{di-1,j}^{(n)}\right)\\ &- \frac{\Delta t}{2\Delta y^2}\left(U_{yi,j}^{(n)}\Delta_{di,j+1}^{(n)}-2\Delta_{di,j}^{(n)}+U_{yi,j-1}^{*(n)}\Delta_{di,j-1}^{(n)}\right)\\ &+ \Delta t\left[\left(\alpha_s-\frac{4}{3}|\Delta_{si,j}^{(n)}|^2-\frac{4}{3}|\Delta_{di,j}^{(n)}|^2\right)\Delta_{si,j}^{(n)}-\frac{2}{3}\Delta_{si,j}^{*(n)}\Delta_{di,j}^{(n)2}\right]\ ,\end{aligned} \tag{A.81}$$

and:

$$\begin{aligned}
\Delta_{di,j}^{(n+1)} &= \Delta_{di,j}^{(n)} + \frac{\Delta t}{\Delta x^2}\left(U_{xi,j}^{(n)}\Delta_{di+1,j}^{(n)} - 2\Delta_{di,j}^{(n)} + U_{xi-1,j}^{*(n)}\Delta_{di-1,j}^{(n)}\right) \\
&+ \frac{\Delta t}{\Delta y^2}\left(U_{yi,j}^{(n)}\Delta_{di,j+1}^{(n)} - 2\Delta_{di,j}^{(n)} + U_{yi,j-1}^{*(n)}\Delta_{di,j-1}^{(n)}\right) \\
&+ \frac{\Delta t}{\Delta x^2}\left(U_{xi,j}^{(n)}\Delta_{si+1,j}^{(n)} - 2\Delta_{si,j}^{(n)} + U_{xi-1,j}^{*(n)}\Delta_{si-1,j}^{(n)}\right) \\
&- \frac{\Delta t}{\Delta y^2}\left(U_{yi,j}^{(n)}\Delta_{si,j+1}^{(n)} - 2\Delta_{si,j}^{(n)} + U_{yi,j-1}^{*(n)}\Delta_{si,j-1}^{(n)}\right) \\
&+ \Delta t\left[\left(1 - |\Delta_{di,j}^{(n)}|^2 - \frac{8}{3}|\Delta_{si,j}^{(n)}|^2\right)\Delta_{di,j}^{(n)} - \frac{4}{3}\Delta_{di,j}^{*(n)}\Delta_{si,j}^{(n)2}\right] . \qquad \text{(A.82)}
\end{aligned}$$

Eqs. A.81 and A.82 are then iterated simultaneously until both components of the order parameter reach convergence. The boundary conditions are applied in the same manner we detailed for a *s*-wave superconductor.